Equilibrium and nonequilibrium dynamics close to impurity quantum phase transitions

Dissertation
zur Erlangung des Doktorgrades
der Naturwissenschaften
der Fakultät Physik an der
Technischen Universität Dortmund

vorgelegt von

Benedikt Lechtenberg
aus Borken

Dezember 2015

Erster Gutachter	Prof. Dr. Frithjof B. Anders
Zweiter Gutachter	Prof. Dr. Joachim Stolze
Tag der mündlichen Prüfung	19. Februar 2016

Kontakt zum Autor benedikt.lechtenberg@tu-dortmund.de

Contents

Publication list v

Table of Abbreviations vii

1 Introduction 1

2 Quantum phase transitions and quantum impurity models 5
- 2.1 Quantum phase transitions . . . 6
- 2.2 Kondo model . . . 7
- 2.3 Two impurity Kondo model . . . 10
- 2.4 Single impurity Anderson model . . . 14

3 Methods 19
- 3.1 Numerical renormalization group . . . 19
  - 3.1.1 Structure of the Hamiltonian . . . 20
  - 3.1.2 Logarithmic discretization . . . 21
  - 3.1.3 Mapping on a semi-infinite chain . . . 23
  - 3.1.4 Iterative diagonalization . . . 25
  - 3.1.5 Calculation of impurity properties . . . 27
- 3.2 Time-dependent numerical renormalization group . . . 28
  - 3.2.1 Complete basis set . . . 29
  - 3.2.2 Time-evolution of a local Operator . . . 30
  - 3.2.3 Reduced density matrix . . . 32
  - 3.2.4 TD-NRG algorithm . . . 34
  - 3.2.5 Restoring the continuous bath: the z-trick . . . 35
- 3.3 NRG Green's functions . . . 35
  - 3.3.1 Derivation of the NRG Green's function . . . 35
  - 3.3.2 Broadening . . . 37
  - 3.3.3 Self-energy of the single impurity Anderson model . . . 39
- 3.4 Parameters of an effective low energy Hamiltonian . . . 41
  - 3.4.1 Effective low energy Hamiltonian . . . 41
  - 3.4.2 Algorithm . . . 43

3.4.3 Benchmark calculations . . . 44

4 Spatial and temporal propagation of Kondo correlations 49
4.1 Theory . . . 51
4.1.1 The Hamiltonian and the spin density . . . 51
4.1.2 Sum rules of the spatial correlation function . . . 54
4.1.3 Effective densities of states in 1D, 2D and 3D . . . 55
4.2 Equilibrium . . . 57
4.2.1 Kondo regime (J>0): short distance versus large distance behavior 57
4.2.2 Ferromagnetic couplings $J < 0$ . . . 60
4.2.3 Spin correlation function in 2D and 3D . . . 61
4.3 Nonequilibrium . . . 62
4.3.1 Time-dependent spatial correlation function in the Kondo regime 63
4.3.2 Perturbation theory . . . 68
4.3.3 Intrinsic correlations of the Fermi sea . . . 70
4.3.4 Local moment regime: ferromagnetic coupling $J < 0$ . . . 73
4.3.5 Finite temperature: cutoff of the Kondo correlations . . . 74
4.4 Response . . . 76
4.4.1 Retarded host susceptibility $\chi^r_{c-c}(R,t)$ . . . 77
4.4.2 Retarded susceptibility $\chi^r_{\mathrm{imp}-c}(R,t)$ . . . 80
4.5 Summary . . . 83

5 Metal-molecule complexes on an Au(111) surface 85
5.1 Monomer . . . 86
5.1.1 Experiment and DFT: setup and theory . . . 87
5.1.2 Experiment and DFT: results . . . 88
5.1.3 NRG studies of the electronic properties . . . 94
5.1.4 Monomer: Summary . . . 103
5.2 Dimer . . . 104
5.2.1 Dimer: Experiment and DFT . . . 105
5.2.2 NRG mapping and transmission function . . . 109
5.2.3 NRG results . . . 115
5.2.4 Dimer: Summary . . . 121

6 Two impurity Kondo model 123
6.1 Restoring the quantum critical point . . . 124
6.2 Nonequilibrium TIKM: constant densities of states . . . 130
6.2.1 Parallel aligned impurity spins . . . 130
6.2.2 Antiparallel aligned impurity spins . . . 138
6.3 Nonequilibrium TIKM with restored QCP . . . 143
6.3.1 Parallel aligned impurity spins . . . 143

6.3.2 Antiparallel aligned impurity spins 147
6.4 Summary and outlook 150

7 Conclusion **153**

A Mapping the TIKM to even and odd parity states **157**

B RKKY interaction **160**

C Perturbative approach of spin-spin correlation function $\chi(\vec{r},t)$ **163**

D Intrinsic spin-spin correlation function of the Fermi sea $\langle\vec{s}(0)\vec{s}(R)\rangle$ **165**

E Retarded host spin-spin susceptibility $\chi^r_{c-c}(R,t)$ **167**

F The long-time value of the spin polarization $\langle s^z(R,t)\rangle$ **169**

G Derivation of NRG parameters from a mean field spectrum **171**

Bibliography **173**

Acknowledgments **185**

Publication list

During the course of the work for this thesis several articles have been published or submitted.

- Greuling, A.; Temirov, R.; Lechtenberg B.; Anders, F. B.; Rohlfing, M.; Tautz, F. S.: *Spectral properties of a molecular wire in the Kondo regime*.
  In: physica status solidi (b) **250**, 2386 (2013), November
- Lechtenberg B.; Anders F. B.: *Spatial and temporal propagation of Kondo correlations*. In: Phys. Rev. B **90**, 045117 (2014), July
- Esat T.; Deilmann T.; Lechtenberg B.; Wagner C.; Krüger P.; Temirov R.; Anders F. B.; Rohlfing M.; Tautz F. S.: *Transfering spin into an extended π-orbital of a large molecule*. In: Phys. Rev. B **91**, 144415 (2015), April
- Esat T.; Lechtenberg B.; Deilmann T.; Wagner C.; Krüger P.; Temirov R.; Rohlfing M.; Anders F. B.; Tautz F. S.: *A chemically driven quantum phase transition in a two-molecule Kondo system*. Submitted to Nature Physics.

Table of Abbreviations

DFT	density functional theory
DMFT	dynamical mean field theory
DMRG	density matrix renormalization group
DOS	density of states
FWHM	full width at half maximum
GGA	generalized gradient approximation
GMR	giant magnetoresistance
HDD	hard disk drive
HOMO	highest occupied molecular orbital
LDA	local density approximation
LM	local moment
LSDA	local spin density approximation
LUMO	lowest unoccupied molecular orbital
MBPT	many-body perturbation theory
NRG	numerical renormalization group
PDOS	projected density of states
PTCDA	perylene-tetracarboxylic dianhydride
QCP	quantum critical point
QIS	quantum impurity system
QMC	quantum Monte Carlo
QP	quasiparticle
QPT	quantum phase transition
RG	renormalization group
RKKY	Ruderman-Kittel-Kasuya-Yosida
SC	strong coupling
SIAM	single impurity Anderson model
STM	scanning tunneling microscopy
STS	scanning tunneling spectroscopy
TD-NRG	time-dependent numerical renormalization group
TMR	tunnel magnetoresistance
TIAM	two impurity Anderson model
TIKM	two impurity Kondo model

Chapter 1

Introduction

In solid-state physics one typically has to deal with a large number of particles of the order 10^{23}. For such a large number of particles it is not possible to solve the Schrödinger equation anymore, and one must find a different approach to handle the problem. One of the most successful methods is the density functional theory (DFT) [1, 2] which is based on the Hohenberg-Kohn theorem [3]. This theorem states that a nondegenerate ground state of a system is unambiguously defined by the electron density. An approximation of this electron density is self-consistently determined by solving the Kohn-Sham equations [4] which are similar to a one-particle Schrödinger equation with an effective potential. Since in this set of equations the particles are noninteracting, the computational effort to solve the problem is significantly reduced. All many-particle interactions are comprised in an exchange-correlation potential V_{xc} which cannot be denoted exactly. The most common approximations for V_{xc} are the local density approximation (LDA) where the potential is only a function of the electron density and the generalized gradient approximation (GGA) where the potential is a function of the electron density and its first derivative. By use of the DFT it is possible to compute bond lengths, binding energies and band structures of many systems. For the development of the DFT Walter Kohn has been rewarded with the Nobel prize in chemistry in 1998 [5].

However, the DFT often fails to describe strongly correlated systems which are particularly interesting due to their unusual properties. An example of such an correlation effect is superconductivity [6, 7] where the electrical resistivity of an material suddenly vanishes below a critical transition temperature. This superconducting phase was first discovered by Kamerlingh Onnes in 1911. It took more than four decades until Bardeen, Cooper and Schrieffer could give an explanation of this effect with their BCS theory. An electron-phonon interaction leads to an effective attractive electron-electron interaction causing the binding of two electrons to a Cooper pair of bosonic-like nature. For temperatures below the transition temperature these Cooper pairs form a Bose-Einstein condensate [8, 9] where a large fraction of bosons occupy the ground state forming a macroscopic quantum state. For the explanation of superconductivity Bardeen, Cooper

and Schrieffer have been rewarded with the Nobel prize in physics in 1972.
Another prominent example of a strongly correlated system is the Mott insulator [10–13] where a material becomes insulating due to strong correlation effects. The Mott insulator is a classic example where the DFT fails to capture the correct physics [14]. In contrast to a band insulator, the Fermi energy is located within a conduction band instead of a gap, however, strong Coulomb repulsions prevent the motions of the electrons.
A third well-known example of a strong correlation effect is the Kondo effect [15]. In 1934 de Haas, de Boer and van den Berg observed the increase of the electrical resistivity of a gold probe contaminated with iron atoms upon lowering the temperature [16]. This is unusual since typically the resistivity only decreases if the temperature is lowered. Jun Kondo has been able to ascribe this effect to the interactions between the magnetic moments of impurity spins and the electron spins of the conduction band [17]. The Kondo effect will be discussed in more detail later on in Sec. 2.2. As for the Mott insulator, the DFT is not able to describe the Kondo effect correctly.
Besides impurities diluted in host materials, the Kondo effect is often observed in quantum dots [18–23]. Quantum dots are zero-dimensional structures which confine a charge in all three space dimensions and, hence, exhibit discrete energy levels [24] similar to a particle in a box. Theoretically, such a system can be described by the single impurity Anderson model (SIAM) [25–27] where an energy level with an on-site Coulomb repulsion couples to a fermionic bath.
In recent years quantum dots have received much attention since a confined spin in the quantum dot may be used as a qubit for quantum computers [28–31]. With a quantum computer one hopes to simulate a quantum many-body system more efficiently than with a classical computer. Furthermore, it is known that some algorithms can be implemented faster on a quantum computer [32, 33] where the most prominent example is the Shor algorithm [34, 35] which is used for integer factorization. For the use of a spin as a qubit it is very important to have a long coherence time and that the spin relaxes slowly [28], therefore, the time-dynamics of quantum dots are particularly interesting [36–38].
Another reason why quantum dots are currently in the focus of intense research is that their magnetic properties may be used for spintronic devices [39–41]. In a spintronic device the magnetic moment of an electron alone or in addition to the electronic charge is used in order to increase data processing speed or to decrease the power consumption compared to conventional charged-based devices [42].
Up until now, the most common device that makes use of the spin is a hard disk drive (HDD) where the spins are used to store information. In a HDD the read heads use the giant magnetoresistance (GMR) [43, 44] or tunnel magnetoresistance (TMR) [45, 46] effect to readout the stored information. Both effects are based on the fact that the electric resistance through two adjacent ferromagnetic layers is dependent on

whether the spins in the layers are parallel or antiparallel aligned. For the discovery of the GMR effect Albert Fert and Peter Grünberg have been awarded with the Nobel prize in physics in 2007.
For the application of quantum dots as qubits or for spintronic devices it is crucial to gain a better understanding of the spin and charge properties of quantum impurity systems (QISs).
In this thesis we will investigate the equilibrium and nonequilibrium properties of different QISs. At first, we will consider the Kondo model where a local magnetic moment of an impurity is coupled via a Heisenberg interaction to a fermionic bath. We will examine how the Kondo correlations are built up and propagate through the conduction band. For this purpose we will study the spin-spin correlation function between the impurity spin and the spin density of the conduction band at a certain distance. To set the stage for the nonequilibrium calculations, we will first investigate the equilibrium properties and improve the results found in the literature [47] in the way that the spin-spin correlation function now fulfills an analytically known sum-rule. The nonequilibrium results will show that most of the correlations propagate within a light cone defined by the Fermi velocity. Interestingly, we will also observe the buildup of correlations outside the light cone which do not decay exponentially. With a second-order perturbation theory in the coupling, we will be able to reveal that these correlations are connected to the intrinsic correlations of the Fermi sea which are already present before the coupling between the impurity and the conduction band is switched on. Furthermore, we will compute the retarded susceptibility that describes the response of the conduction band spin density at a certain distance to a small magnetic field applied to the impurity spin. Using this susceptibility, we will clarify that for a real response no correlations outside the light cone are observed.
Moreover, we will present an experiment where a metal-molecule complex is formed by reacting a perylene-tetracarboxylic dianhydride (PTCDA) molecule, adsorbed on an Au(111) surface, with a single Au atom leading to the emergence of a radical. The observed Kondo effect in the scanning tunneling spectroscopy (STS) spectrum is an unambiguous proof of a local moment formation. A DFT calculation shows that the local moment resides in a π-orbital that is extended over almost the entire Au-PTCDA complex. This makes this system very interesting for the investigation of interactions between magnetic molecules and for the usability as spintronic devices since the delocalized character of the π-orbital increases the probability of the local moments to interact with adjacent complexes. However, a correct physical description of the local moment formation and the Kondo effect is not possible with the DFT. Therefore, we employ a combined DFT+NRG approach where we use the projected density of states (PDOS) of the π-orbital and the Coulomb repulsion, both obtained from a combination of many-body perturbation theory (MBPT) and DFT calculation, as a first principle input for our numerical renormalization group (NRG) calculations. We will

show that the results of the experiment and NRG are in perfect agreement without any fitting parameters. In particular, the Kondo temperatures, which are extracted by a temperature-dependent fit of the zero-bias conductance from both spectra, deviate by only 1 K. In order to provide a reliable method to experimentally extract the Kondo temperature in a particle-hole asymmetric system, we will make a careful scaling analysis of various definitions of the Kondo temperature and will demonstrate that indeed the fit to the zero-bias conductance is the best method.
If two Au atoms are adsorbed on adjacent PTCDA molecules, the STS spectrum exhibits in some cases a gap around the Fermi energy rather than a Kondo peak. By mapping the system onto a two impurity Anderson model (TIAM), we will reveal that this gap is caused by a strong nonmagnetic chemical interaction between the π-orbitals of both complexes. The DFT calculations show that the strength of this interaction depends on the precise adsorption position of the Au atoms on the PTCDA molecules. Only for certain configurations the interaction is sufficient to produce the gap in the spectrum. Using our NRG results we will provide a detailed analysis of the occurring quantum phase transition (QPT) which is caused by a competition between the gain of kinetic energy due to the entanglement with the substrate and the binding energy gain due to the chemical interaction between the π-orbitals. We will also discuss the relevance of parity-symmetry breaking for the observation of the gap in the STS spectrum.
At the end, we will consider the equilibrium and nonequilibrium properties of the two impurity Kondo model (TIKM) which exhibits a QPT if the energy dependence of the couplings to the conduction bands are artificially neglected. We will demonstrate that it is possible to restore this QPT in the full energy-dependent model with appropriate potential scattering terms. Afterwards, the time-dynamics of the spin polarization and the spin-spin correlation function of both impurity spins after a quench in the direct spin-spin interaction between the impurity spins will be investigated. For this purpose, we will examine the two different initial conditions of parallel and antiparallel aligned spins in the case of constant as well as energy-dependent couplings. We will explain that the main differences between both initial conditions are caused by the fact that for antiparallel aligned spins local oscillations between both impurity spins can occur even without a coupling to the conduction band. It will be shown that a sufficiently large antiferromagnetic spin-spin interaction prevents a thermalization of the correlation function since in this case the impurities decouple from the conduction band. To conclude our investigations, we will reveal that the time-dependent behavior of the full energy-dependent model is essentially the same as the one for the model with constant couplings. The slight differences originate from details of the energy-dependent model such as the emergence of potential scattering terms.

Chapter 2

Quantum phase transitions and quantum impurity models

In this chapter we will briefly discuss the concept of quantum phase transitions (QPTs) and present the quantum impurity models that are used throughout this thesis.
The following section 2.1 is devoted to the QPTs and explains the different existing types. In contrast to "conventional" phase transitions, a QPT occurs upon variation of a nonthermal control parameter at zero temperature and order is not destroyed by thermal fluctuations but by quantum fluctuations. We will consider the properties of the Kondo model which describes a local magnetic moment that is coupled via a Heisenberg interaction to the spin density of a conduction band in Sec. 2.2. The Kondo effect will be explained and we will discuss the QPT that arises in the Kondo model. For this purpose, we will analyze how the coupling to the conduction band in an effective low energy Hamiltonian changes upon lowering the temperature. In Sec. 2.3 the two impurity Kondo model (TIKM) will be introduced which is an extension of the Kondo model. In the TIKM two impurity spins are coupled to one conduction band which gives rise to the Ruderman-Kittel-Kasuya-Yosida (RKKY) interaction that is an indirect spin-spin interaction between both impurity spins mediated by the conduction band electrons. A competition between the Kondo effect and an antiferromagnetic spin-spin interaction may lead to the emergence of a QPT, and we will clarify under which conditions this QPT occurs. Furthermore, we will consider the single impurity Anderson model (SIAM) which also includes charge fluctuations instead of only spin fluctuations in Sec. 2.4. The SIAM describes an energy level with an on-site Coulomb repulsion that hybridizes with a conduction band. We will analyze the different unstable and stable fixed points the SIAM passes through upon lowering the temperature and will reveal that for a large Coulomb repulsion the SIAM can be mapped onto a Kondo model at low temperature via a Schrieffer Wolff transformation. Afterwards, the impurity spectral function for small and large Coulomb repulsions will be shown. The spectral function is of great relevance for scanning tunneling microscopy (STM) measurements on quantum dots since the differential conductance of a current through the quantum dot at low temperatures is directly proportional to the spectral function.

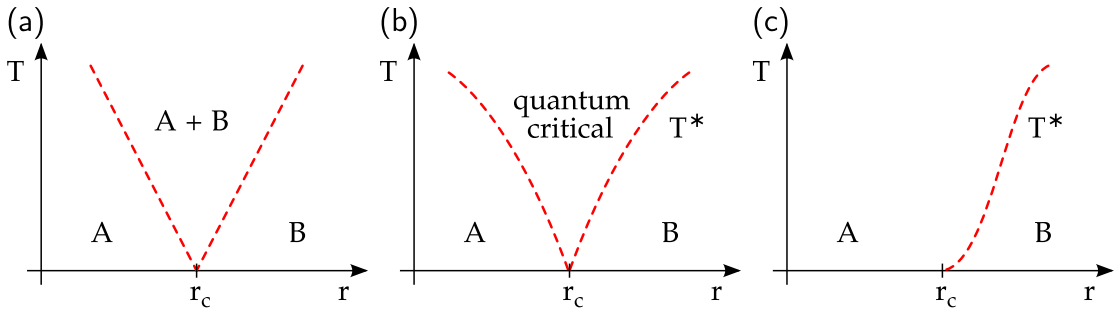

Figure 2.1: Schematic representation of the finite-temperature phase diagrams of impurity QPT near the QCP. A and B are both stable phases, r is a nonthermal tuning parameter and r_c the position of the QCP. (a) First-order transition: the finite-temperature region A+B is a simple thermodynamic mixture of the two phases. (b) Second-order transition: the quantum critical region is bounded by $T^* \propto |t|^{\nu}$, where $t = (r - r_c)/r_c$ is a dimensionless parameter measuring the distance to the QCP and ν is the correlation length exponent. (c) A transition of Kosterlitz-Thouless type, sometimes also called an infinite-order transition. In contrast to (b), the two phases are not separated by an unstable fixed point.

2.1 Quantum phase transitions

Phase transitions cause a qualitative change of the properties of a system and arise from a variation of an external control parameter. In a "traditional" phase transition, which occurs at finite temperature, a macroscopic order is destroyed by thermal fluctuations. In contrast, a quantum phase transition (QPT) [48–50] takes place at zero temperature and emerges upon variation of a nonthermal control parameter. In a QPT order is destroyed solely by quantum fluctuations which always appear according to the Heisenberg uncertainty principle. A QPT results from a competition between different ground state phases and can be classified into first-order and continuous transitions. The transition point of a continuous transition between the two phases is called quantum critical point (QCP) and can lead to unconventional behavior of the system such as non-Fermi liquid behavior.

One type of QPTs are the so-called bulk transitions where the whole system shows critical behavior. In this thesis, however, we focus on the class of boundary transitions where only degrees of freedom of a subsystem become critical. In particular, we consider zero-dimensional boundaries where only the contribution of an impurity shows critical behavior. These types of transitions are called impurity quantum phase transitions. A first example of such an impurity QPT is the anisotropic Kondo model [15, 51] that will be discussed in the following section 2.2. Note that an impurity QPT is completely independent of a possible bulk phase transition in the bath.

The interplay between the quantum and classical fluctuations leads in the vicinity of the QCP to phase diagrams that are schematically depicted in Fig. 2.1.

Figure 2.1a shows the phase diagram of a first-order transition which is a simple level crossing in the ground state of the system. Here, A and B indicate two distinct sta-

ble phases while the finite-temperature region A+B above the transition point is just a thermodynamic mixture of the two phases. The parameter on the x-axis r indicates a nonthermal tuning parameter and r_c is the position of the QCP.
A second-order transition is depicted in Fig. 2.1b. The system exhibits an unstable fixed point at the QCP $r = r_c$ which separates the two phases. The so-called quantum critical region above the QCP is controlled by this unstable fixed point. In this region both thermodynamic as well as quantum fluctuations are important and its boundaries are determined by $T^* \propto |t|^\nu = |(r - r_c)/r_c|^\nu$, where ν is the correlation length exponent[1]. The physics inside the quantum critical region is governed by thermal excitations of the quantum critical ground state which may lead to unusual finite-temperature behavior of the system such as unconventional power laws or non-Fermi liquid behavior.
Figure 2.1c shows a QPT of Kosterlitz-Thouless type. In contrast to Fig. 2.1b, a renormalization group (RG) analysis shows that this kind of transitions are not related to a unstable fixed point separating the two stable phases. Therefore, a quantum critical region does not emerge in the vicinity of the QCP and the leading thermodynamic behavior shows only one crossover line. At the transition point T^* vanishes exponentially. Since the Kosterlitz-Thouless transition does not show a discontinuity in any derivative of the free energy at the transition point, it is also sometimes called an infinite-order transition.

2.2 Kondo model

W. J. de Haas, J.H. de Boer and G.J. van den Berg observed in 1934 that the electric resistivity of a gold sample, which was contaminated with a small percentage of iron, shows a minimum at low temperatures and increases again for even smaller temperatures [16]. Since both the electron-phonon scattering as well as the electron-electron scattering contribution to the resistivity are expected to decreases upon lowering the temperature, the total resistivity should also only decreases until for $T \to 0$ a constant residual resistance originating from impurities remains [52]. This counter-intuitive behavior indicates that a completely different mechanism must cause the increase of the resistivity.
It took more than 30 years until Jun Kondo could give an explanation for the observed increase of the electric resistivity in 1964 [17]. The reason are magnetic exchange interactions between the magnetic moments of the impurities and the electron spins of the

[1] In the present (0+1)-dimensional models there is no independent dynamical exponent which means $z = 1$.

conduction band. The simplest Hamiltonian describing such a system is the so-called Kondo Hamiltonian

$$H_{\mathrm{K}} = \sum_{\vec{k},\sigma} \epsilon_{\vec{k},\sigma} c^{\dagger}_{\vec{k}\sigma} c_{\vec{k}\sigma} + J \vec{S}_{\mathrm{imp}} \vec{s}_c. \tag{2.1}$$

Here, a local impurity spin $\vec{S}_{\mathrm{imp}}$ couples via an effective Heisenberg interaction J to the unit-cell volume averaged conduction electron spin $\vec{s}_c$ with

$$\vec{s}_c = \frac{1}{2N} \sum_{\vec{k},\vec{k}'} \sum_{\alpha,\beta} c^{\dagger}_{\vec{k}\alpha} \vec{\sigma}_{\alpha\beta} c_{\vec{k}'\beta} \tag{2.2}$$

where $c^{\dagger}_{\vec{k}\alpha}$ creates a conduction electron with momentum $\vec{k}$ and spin α, $\epsilon_{\vec{k}}$ is the conduction band dispersion, N the number of unit cells and $\vec{\sigma}$ is a vector comprising the Pauli matrices. While for a ferromagnetic interaction ($J < 0$) the conduction band electron spins align parallel to the impurity spin, for an antiferromagnetic interaction ($J > 0$) the spins align antiparallel enabling spin-flip scattering processes between two degenerated states. Employing a perturbation theory up to third order in the coupling J, Jun Kondo showed that these spin-flip scatterings generate a temperature dependent contribution to the resistivity which is proportional to $\propto -\ln(T)$. This contribution explains the minimum in the resistivity, however, since $-\ln(T)$ diverges for $T \to 0$, this perturbative approach produces unphyiscal results for small temperatures. Extensions to the perturbative approach using many-body techniques also lead to diverging contributions to the scattering rate below an exponential small temperature $T \leq T_{\mathrm{K}}$ where

$$T_{\mathrm{K}} = D\sqrt{\rho J} e^{-\frac{1}{\rho J}} \tag{2.3}$$

is the so-called Kondo temperature with ρ being the density of states (DOS) of the conduction band. In quantum-field theories such a logarithmic singularity is called an infra-red problem.

In 1970 P. W. Anderson gave an explanation for the breakdown of the perturbative approaches by employing a perturbative renormalization group (RG) procedure which is known as "poor man scaling". In this procedure an effective low-energy model is generate by perturbatively eliminating high order excitations. Applying the "poor man scaling" to the more general anisotropic Kondo model

$$\begin{aligned} H_{\mathrm{AK}} &= \sum_{\vec{k},\sigma} \epsilon_{\vec{k},\sigma} c^{\dagger}_{\vec{k}\sigma} c_{\vec{k}\sigma} + J_z S^z_{\mathrm{imp}} s^z_c + J_{\perp} (S^x_{\mathrm{imp}} s^x_c + S^y_{\mathrm{imp}} s^y_c) \\ &= \sum_{\vec{k},\sigma} \epsilon_{\vec{k},\sigma} c^{\dagger}_{\vec{k}\sigma} c_{\vec{k}\sigma} + J_z S^z_{\mathrm{imp}} s^z_c + \frac{1}{2} J_{\perp} (S^+_{\mathrm{imp}} s^-_c + S^-_{\mathrm{imp}} s^+_c), \end{aligned} \tag{2.4}$$

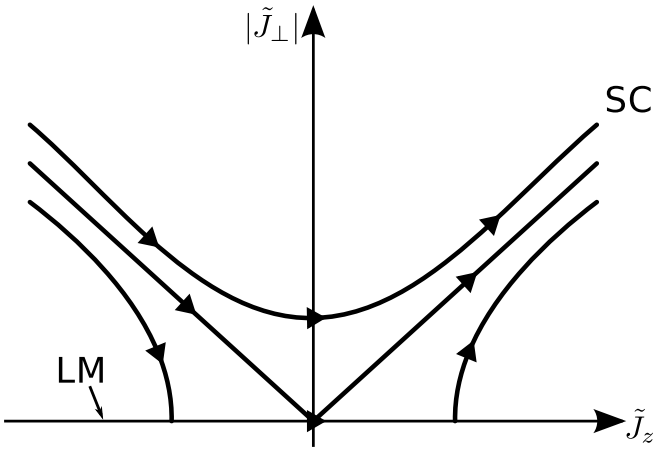

Figure 2.2: Flow of the couplings $\tilde{J}_\perp$ and $\tilde{J}_z$ for the anisotropic Kondo model. For $-\tilde{J}_z > |\tilde{J}_\perp|$ and $\tilde{J}_z < 0$ the local moment fixed point (LM) on the line $(\tilde{J}_z < 0, \tilde{J}_\perp = 0)$ is reached while for all other conditions the system flows to the strong coupling fixed point (SC) in the upper right corner.

yields differential equations for the flow of the effective couplings. These equations describe how the couplings of the effective low-energy Hamiltonian change while decreasing the bandwidth D and they are given by

$$\frac{d\tilde{J}_\perp}{d\ln D} = -\tilde{J}_\perp \tilde{J}_z \tag{2.5}$$

$$\frac{d\tilde{J}_z}{d\ln D} = -\tilde{J}_\perp^2 \tag{2.6}$$

Here we defined $\tilde{J} = \rho J$ with the DOS of the conduction band ρ. Dividing Eq. (2.5) by Eq. (2.6) and afterwards integrating the equation yields

$$\tilde{J}_z^2 - \tilde{J}_\perp^2 = \text{const.} \tag{2.7}$$

The couplings $\tilde{J}_z$ and $\tilde{J}_\perp$ are thus located on a hyperbolic curve in the parameter space $(\tilde{J}_z, \tilde{J}_\perp)$.

The flow of the couplings is depicted in Fig. 2.2. Equations (2.5) and (2.6) reveal that the flow always stops for $\tilde{J}_\perp = 0$. This is the so-called local moment (LM) fixed point and it is reached for $-\tilde{J}_z \geq |\tilde{J}_\perp|$ and $\tilde{J}_z < 0$. For all other conditions $\tilde{J}_\perp$ remains finite and leads in the case of a ferromagnetic $\tilde{J}_z$ to a sign change of the z-component of the coupling. In this case the coupling flows to the strong coupling (SC) fixed point $\tilde{J}_\perp, \tilde{J}_z \to \infty$. The line $|\tilde{J}_\perp| = -\tilde{J}_z$ represents a transition of the Kosterlitz-Thouless type. If only the isotropic Kondo model $\tilde{J} = \tilde{J}_z = \tilde{J}_\perp$ is considered, Eqs. (2.5) and (2.6) simplify to

$$\frac{d\tilde{J}}{d\ln D} = -\tilde{J}^2. \tag{2.8}$$

Integrating this differential equation yields for the coupling

$$\tilde{J} = \frac{\tilde{J}_0}{1 + \tilde{J}_0 \ln(D_0/D')} \tag{2.9}$$

which diverges at the Kondo temperature[2] $T_K = D_0 e^{-\frac{1}{J_0}}$.
For a diverging coupling $J \to \infty$, a bound singlet consisting of the impurity spin and a conduction band electron spin is formed which decouples from the rest of the conduction band. The impurity spin is hence completely screened by the conduction band electron spins and one obtains a singlet and a free conduction band with one electron removed from it.
The divergence of coupling $J \to \infty$ for temperatures $T \leq T_K$ is the reason why a perturbative approach in the coupling J can yield reliable results only for high temperatures and brakes down at small temperatures since in this case the coupling can no longer be considered to be small. The search of a solution which is also valid for $T \leq T_K$ is known as the Kondo problem.
K. G. Wilson [53] enhanced the "poor man scaling" approach and devised the nonperturbative numerical renormalization group (NRG). He was the first who was able to solve the Kondo problem in 1974/75 using the NRG. This achievement was awarded with the Nobel prize in physics in 1982 [54]. The NRG, which will be discussed in detail in Sec. 3.1, provides the tool to solve the Kondo model for arbitrary parameters and temperature including the case $T \leq T_K$.
Later in 1980 an alternative approach was developed by N. Andrei [55] and P.B. Vigman [56]. Both applied independently of each other the Bethe-ansatz technique, which was developed by H. A. Bethe in 1931 to solve the one dimensional Heisenberg model [57], to the Kondo model in order to construct a complete set of eigenstates. The analytical results obtained by Andrei and Vigman confirmed Wilson's NRG calculations.

2.3 Two impurity Kondo model

An extension of the Kondo model is given by the two impurity Kondo model (TIKM) where, for a specific type of particle-hole symmetry, the competition between magnetic exchange interactions and the Kondo effect can lead to the emergence of a new QPT.
The Hamiltonian of the TIKM is given by

$$H_{\text{TIKM}} = \sum_{\vec{k},\sigma} \epsilon_{\vec{k}} c^\dagger_{\vec{k}\sigma} c_{\vec{k}\sigma} + J \sum_{i=1}^{2} \vec{S}_i \vec{s}_c(\vec{R}_i) + H_{\text{imp}} \tag{2.10}$$

[2] The square-root pre-factor $\sqrt{\rho J}$ in Eq. (2.3) is obtained if in Eq. (2.8) also terms up to the order $\tilde{J}^3$ are considered. This pre-factor in T_K is often dropped in qualitative discussions, but it is important for more quantitative comparison.

where the impurity spin $\vec{S}_i$ at position $\vec{R}_i$ couples via a Heisenberg interaction J to the conduction electron spin expanded in plane waves

$$\vec{s}_c(\vec{r}) = \frac{1}{2}\frac{1}{N}\sum_{\sigma\sigma'}\sum_{\vec{k}\vec{k}'} c^\dagger_{\vec{k}\sigma}\vec{\sigma}_{\sigma\sigma'}c_{\vec{k}'\sigma'}e^{i(\vec{k}'-\vec{k})\vec{r}}. \tag{2.11}$$

The last term H_{imp} comprises all operators that act only on the impurity degrees of freedom such as a direct spin-spin interaction between the impurity spins $H_{\text{imp}} = K\vec{S}_1\vec{S}_2$ and will be discussed in more detail later on.
The first two terms in Eq. (2.10) generate an indirect magnetic exchange interaction K_{RKKY} between both impurity spins which is known as the RKKY interaction [58–60]. This indirect exchange interaction is mediated by the conduction electrons and can be ferro- or antiferromagnetic depending on the value $2k_{\text{F}}R$. Here, R is the distance between both impurities and k_{F} is the Fermi wave vector.
In order to formulate the model as a linear chain problem that can be solved using the NRG, which will be discussed in detail in Sec. 3.1, one needs an orthonormal basis set. However, the local conduction electron states coupling to the impurities are not orthonormal. Originally, Jones *et al.* [61, 62] extended the NRG to the TIKM by mapping the conduction electrons onto orthonormal even (e) and odd (o) parity eigenstates. This transformation is described in detail in appendix A. The Hamiltonian in this basis is given by

$$H_{\text{TIKM}} = H_0 + H_{\text{int}} + H_{\text{imp}} \tag{2.12}$$

where

$$H_0 = \sum_{\alpha=e,o}\sum_{\sigma}\int \epsilon c^\dagger_{\epsilon\sigma,\alpha}c_{\epsilon\sigma,\alpha}\, d\epsilon \tag{2.13}$$

describes the conduction band that has been divided into two bands, one with even and one with odd parity symmetry. The interaction between these conduction bands and the two impurity spins is given by

$$\begin{aligned} H_{\text{int}} = &\frac{J}{8}\int\int\sum_{\sigma\sigma'}\sqrt{\rho(\epsilon)\rho(\epsilon')}\vec{\sigma}_{\sigma\sigma'} \\ &\times\Big[(\vec{S}_1+\vec{S}_2)\left(N_e(\epsilon)N_e(\epsilon')c^\dagger_{\epsilon\sigma,e}c_{\epsilon'\sigma',e} + N_o(\epsilon)N_o(\epsilon')c^\dagger_{\epsilon\sigma,o}c_{\epsilon'\sigma',o}\right) \\ &+(\vec{S}_1-\vec{S}_2)N_e(\epsilon)N_o(\epsilon')\left(c^\dagger_{\epsilon\sigma,e}c_{\epsilon'\sigma',o} + c^\dagger_{\epsilon'\sigma,o}c_{\epsilon\sigma',e}\right)\Big]\, d\epsilon\, d\epsilon'. \end{aligned} \tag{2.14}$$

Here $\rho(\epsilon)$ is the DOS of the original conduction band and $N_{e/o}(\epsilon)$ are normalization factors that depend on the dimension and the distance between the impurities $\vec{R} = \vec{R}_1 - \vec{R}_2$. In three dimensions they are for example given by

$$N^2_{e/o}(\epsilon)\rho(\epsilon) = 2\rho_0 \left[1 \pm \frac{\sin\left(k_\mathrm{F} R(1+\frac{\epsilon}{D})\right)}{k_\mathrm{F} R(1+\frac{\epsilon}{D})}\right] \tag{2.15}$$

with D being the half bandwidth. For the derivation of Eq. (2.15) we assumed a constant DOS $\rho(\epsilon) = \rho_0$ and a linear dispersion $\epsilon(\vec{k}) = v_\mathrm{F}(|\vec{k}| - k_\mathrm{F})$, where v_F is the Fermi velocity. The normalization factors also enter the definition of the effective parity DOSs

$$\rho_{e(o)}(\epsilon) = \frac{1}{\bar{N}^2_{e(o)}} N^2_{e(o)}(\epsilon)\rho(\epsilon). \tag{2.16}$$

where the normalization constant is given by $N_{e(o)} = \sqrt{\int d\epsilon\ N^2_{e(o)}(\epsilon)\rho(\epsilon)}$.
Due to the energy-dependent parity DOSs, the Hamiltonian in Eq. (2.14) is particle-hole asymmetric. Since the energy dependence of the DOS is known to be generally irrelevant in the Kondo model, Jones *et al.* [61–63] neglected the energy dependence $N^2_{e/o}(\epsilon)\rho(\epsilon) = N^2_{e/o}(0)\rho(0) = N^2_{e/o}\rho_0$ and hence obtained a particle-hole symmetric model. However, this simplification leads to a RKKY interaction that is always ferromagnetic $\frac{K_\mathrm{RKKY}}{D} = -\frac{J^2\rho_0^2}{16} 2\ln(2)(N_e^2 - N_o^2)^2$. For a detailed derivation of the RKKY interaction for constant as well as energy-dependent DOSs we refer the reader to appendix B. In order to achieve also antiferromagnetic interactions, they included an additional direct exchange interaction $H_\mathrm{imp} = K\vec{S}_1\vec{S}_2$ between the impurity spins so that the total effective magnetic interaction is given by $K_\mathrm{eff} = K + K_\mathrm{RKKY}$.
Investigating this simplified model, Jones *et al.* observed two different phases depending on the ratio between the effective magnetic interaction and the Kondo temperature $K_\mathrm{eff}/T_\mathrm{K}$. For $K_\mathrm{eff}/T_\mathrm{K} \to -\infty$ the two impurities form a $S = 1$ spin which interacts antiferromagnetically with two conduction bands. In the case of asymmetric couplings to the conduction bands $N_e \neq N_o$, this results in a two-stage Kondo effect where at higher temperatures the $S = 1$ spin is partially screened by the stronger coupled conduction band and afterwards the residual spin $1/2$ is screened by the other conduction band at lower temperatures. This leads to a Fermi liquid ground state with a $\delta_{e/o} = \pi/2$ scattering phase shift for electrons in the even and odd channel. In this thesis we denote this phase as the Kondo phase.
In contrast, for $K_\mathrm{eff}/T_\mathrm{K} \to \infty$ the impurity spins form a singlet $S = 0$ which decouples from the conduction bands. Consequently, no Kondo effect occurs and the phase shift in both channels is zero $\delta_{e/o} = 0$. In the following, this phase called the decoupled singlet phase.
Jones *et al.* found that both phases are separated by a continuous QPT [64] with an unstable fixed point at the QCP $K_\mathrm{eff}/T_\mathrm{K} \approx 2.2$ [62, 63]. Right at the QCP the phase shifts

$\delta_{e/o}$ change discontinuously and the staggered susceptibility, which is the response to $\vec{h}(\vec{S}_1 - \vec{S}_2)$, as well as the linear coefficient of the specific-heat diverge [62, 64] indicating non-Fermi liquid behavior.
The spin-spin correlation function between both impurity spins $\langle \vec{S}_1 \vec{S}_2 \rangle$ changes continuously through the unstable fixed point. For $|K_{\text{eff}}| \ll T_{\text{K}}$ the spin correlation function is given by $\langle \vec{S}_1 \vec{S}_2 \rangle \approx 0$ and the impurities are independently screened. In contrast, for larger spin-spin interactions the impurities develop magnetic correlations as the temperature is lowered up to T_{K} where both impurities are collectively screened with a finite residual spin-spin correlation for $T \to 0$. Note that the Kondo correlations also persist in the decoupled singlet phase [63] because otherwise one would always obtain $\langle \vec{S}_1 \vec{S}_2 \rangle = -0.75$ at low temperatures. At the QCP the spin-spin correlation function is approximately given by $\langle \vec{S}_1 \vec{S}_2 \rangle \approx -0.25$ for small Kondo couplings J [65]. This is the midpoint between the values $\langle \vec{S}_1 \vec{S}_2 \rangle = 0.25$ for $K_{\text{eff}}/T_{\text{K}} \to -\infty$ and $\langle \vec{S}_1 \vec{S}_2 \rangle = -0.75$ for $K_{\text{eff}}/T_{\text{K}} \to \infty$.
In contrast to Jones observations, quantum Monte Carlo (QMC) [66–68] and later on NRG [69] calculations including the full energy-dependent DOSs have not seen such a QPT. Taking into account the proper energy dependence of the even and odd DOSs makes the model particle-hole asymmetric, destroys the QCP and leads to a continuously crossover between the two phases.
Affleck *et al.* [64] found that the emergence of the QPT is related to a specific type of particle-hole symmetry. If the model is particle-hole symmetric under the transition

$$\begin{aligned} c_{\epsilon\sigma,e} &\to c^{\dagger}_{-\epsilon\sigma,e} \\ c_{\epsilon\sigma,o} &\to c^{\dagger}_{-\epsilon\sigma,o} \,, \end{aligned} \tag{2.17}$$

the scattering phase shift can only take the values $\delta_{e/o} = \{0, \frac{\pi}{2}\}$ which can be seen if the boundary conditions of the incoming and outgoing operators

$$\begin{aligned} c^{\text{out}}_{\epsilon\sigma,e} &= e^{2i\delta_e} c^{\text{in}}_{\epsilon\sigma,e} \\ c^{\text{out}}_{\epsilon\sigma,o} &= e^{2i\delta_o} c^{\text{in}}_{\epsilon\sigma,o} \end{aligned} \tag{2.18}$$

are inserted into Eq. (2.17). This implies that there must be a QCP where the phase shifts change discontinuously.
However, if the model is particle-hole symmetric under the transition

$$\begin{aligned} c_{\epsilon\sigma,e} &\to c^{\dagger}_{-\epsilon\sigma,o} \\ c_{\epsilon\sigma,o} &\to c^{\dagger}_{-\epsilon\sigma,e} \,, \end{aligned} \tag{2.19}$$

the phase shifts must only fulfill the condition $\delta_e = -\delta_o$ which means that they may take arbitrary values. Consequently, the phase shift changes continuously between the phases, leading to a crossover rather than a QPT.

Therefore, if the energy dependence of the DOSs are taken into account, the TIKM generally does not exhibit a QPT.

2.4 Single impurity Anderson model

A more general quantum impurity system that also includes charge fluctuations is given by the single impurity Anderson model (SIAM). In the SIAM the impurity is represented by a spin degenerated energy level with an on-site Coulomb repulsion which hybridizes with a fermionic conduction band. The SIAM was introduced and first investigated by Anderson in 1964 [25]. His investigation was a first attempt to describe localized magnetic states in metals. Although his mean field approach provides a mechanism for the formation of local magnetic moments, his solution leads to an unphysical spin-polarized ground state which contradicts the Mermin Wagner theorem [70].
The Hamiltonian of the SIAM is given by

$$H_{\mathrm{SIAM}} = \sum_{\vec{k},\sigma} \epsilon_{\vec{k}} c^\dagger_{\vec{k},\sigma} c_{\vec{k},\sigma} + \sum_\sigma \epsilon_d d^\dagger_\sigma d_\sigma + U d^\dagger_\uparrow d_\uparrow d^\dagger_\downarrow d_\downarrow + \sum_{\vec{k},\sigma} V_{\vec{k}} (c^\dagger_{\vec{k},\sigma} d_\sigma + d^\dagger_\sigma c_{\vec{k},\sigma}) \tag{2.20}$$

with the dispersion of the conduction band $\epsilon_{\vec{k}}$, the level energy ϵ_d, a Coulomb repulsion U and the hybridization strength $V_{\vec{k}}$. Here, $c^\dagger_{\vec{k},\sigma}$ creates a conduction band electron with momentum $\vec{k}$ and spin σ and $d^\dagger_\sigma$ creates an electron on the impurity with spin σ. The dispersion $\epsilon_{\vec{k}}$ as well as ϵ_d are measured from the Fermi energy.
The effect of the conduction band on the impurity is completely determined by the hybridization function

$$\Gamma(\omega) = \pi \sum_{\vec{k}} \delta(\epsilon_{\vec{k}} - \omega) V^2_{\vec{k}} = \pi \rho(\omega) V^2(\omega). \tag{2.21}$$

where $\rho(\omega)$ is the DOS of the conduction band. For simplicity we consider only the case of a constant hybridization function $\Gamma(\omega) = \Gamma = \pi \rho V^2$ in the following.
If the impurity is decoupled $\Gamma = 0$, the energy level is unoccupied for $\epsilon_d > 0$, occupied with one electron for $\epsilon_d < 0$, $U + \epsilon_d > 0$ and doubly occupied in the case $U + \epsilon_d < 0$. Switching on Γ causes these states to be mixed up. However, if the coupling to the conduction band is weak, the above picture helps understanding the properties of the system for different temperature regimes. In the most interesting case for $\epsilon_d < 0$, $U + \epsilon_d > 0$ and a small hybridization $\Gamma \ll U, |\epsilon_d|$ the system shows a variety of different properties depending on the temperature regime. Under a RG transformation these temperature regimes can be related to different unstable and stable fixed points. For each fixed point the system exhibits a characteristic value of the effective local magnetic moment of the impurity μ^2_{eff}. In the following, we will briefly discuss the different fixed points the system passes through upon lowering the temperature [26, 27].

For large temperatures all impurity configurations are equally populated and the effective local magnetic moment is $\mu_{\text{eff}}^2 = 1/8$. Under a RG transformation this regime is associated with the unstable free-orbital fixed point.
If the temperature is lowered, the unstable valence fluctuation fixed point is reached. This fixed point is only present in the particle-hole asymmetric case $\epsilon_d \neq -U/2$. Here, the situation corresponds to the case where either the singly occupied $n_d = 0$ or the doubly occupied $n_d = 2$ state can be removed from consideration because in the effective low energy Hamiltonian its excitation energy is shifted to infinity. The remaining states are equally populated so that the effective local magnetic moment in this regime is given by $\mu_{\text{eff}}^2 = 1/6$.
Upon further decreasing the temperature, the system passes over to the LM fixed point in which only the $n_d = 1$ configuration of the impurity is present. In this regime the SIAM can be mapped to a Kondo model with an additional potential scattering term via a Schrieffer-Wolf transformation [71]

$$H_{\text{LM,eff}} = \sum_{\vec{k},\sigma} \epsilon_{\vec{k},\sigma} c_{\vec{k}\sigma}^\dagger c_{\vec{k}\sigma} + J \vec{S}_{\text{imp}} \vec{s}_c + \sum_{\vec{k},\vec{k}',\sigma} K c_{\vec{k}\sigma}^\dagger c_{\vec{k}'\sigma} \tag{2.22}$$

where the Heisenberg coupling and the potential scattering are given by

$$\rho J = \frac{1}{\pi} \left(\frac{2\Gamma}{|\epsilon_d|} + \frac{2\Gamma}{U + \epsilon_d} \right) \tag{2.23}$$

$$\rho K = \frac{1}{\pi} \left(\frac{\Gamma}{2|\epsilon_d|} - \frac{\Gamma}{2(U + \epsilon_d)} \right). \tag{2.24}$$

Note that if the model is particle-hole symmetric $\epsilon_d = -U/2$, the scattering term vanishes and the simple Kondo model with $\rho J = \frac{8\Gamma}{\pi U}$ is obtained. The magnetic moment in this regime is $\mu_{\text{eff}}^2 = 1/4$.
If the temperature is further lowered, the behavior of the SIAM is similar to the one of the Kondo model. In particular, for $T \to 0$ the stable SC fixed point is reached where the coupling to the conduction band diverges $\rho J \to \infty$. This corresponds to the situation where the impurity is strongly coupled to the conduction band electron state at the impurity site so that both degrees of freedom are frozen out. Consequently, the effective local magnetic moment in this regime vanishes $\mu_{\text{eff}}^2 = 0$.
In contrast to the case discussed above, for $\Gamma \gg U$ there is always a direct transition from the free orbital fixed point to SC fixed point without passing through the valence fluctuation or LM fixed point. Therefore, only for $\Gamma \ll U$ and $\Gamma \ll |\epsilon_d|$ a local magnetic moment is formed on the impurity.
The formation of local moments has also a crucial effect on the conductance through a quantum impurity when it is placed between two leads. In experiments the energy level can be changed by applying a small gate voltage V_g and it is then possible to pass a small current through the impurity. At low temperatures the differential

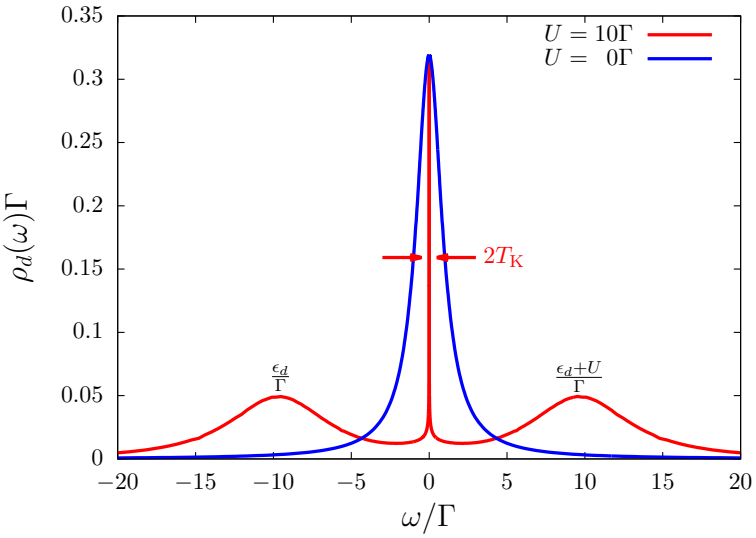

Figure 2.3: Impurity spectral function of the SIAM in the particle-hole symmetric case $\epsilon_d = -U/2$ for $\Gamma \ll U$ (red curve) and $\Gamma \gg U$ (blue curve). For $\Gamma \gg U$ only one broad peak at the Fermi energy with half width Γ is observed. In contrast, for $\Gamma \ll U$ a three peak structure typical for a Kondo effect with a very narrow Kondo resonance at $\omega = 0$ is observed. NRG parameters are $\Lambda = 1.8$, $N_s = 1200$ and a broadening $b = 0.5$.

conductance is directly proportional to the spectral function of the quantum impurity $\frac{dI}{dV}(V_g) \propto \rho_d(\omega = eV_g)$ [72]. A measurement of the differential conductance as a function of the gate voltage V_g generally yields two peaks where the differential conductance is amplified. These peaks correspond to the cases in which either the unoccupied state $n_d = 0$ or the doubly occupied state $n_d = 2$ is shifted to the Fermi energy $\epsilon_F = 0$. Between these two values the differential conductance is suppressed. This phenomena is known as the Coulomb blockade [73–75].

However, the Kondo effect opens a new channel for transport due to the strong entanglement with the conduction electrons. Figure 2.3 shows the spectral function of the impurity $\rho_d(\omega)$ in the particle-hole symmetric case $\epsilon_d = -U/2$ for $\Gamma \ll U$ and for comparison also for $\Gamma \gg U$. In the latter case only one broad peak at the Fermi energy with width Γ is observed. The spectral function in this regime is given by

$$\rho_d(\omega) = -\frac{1}{\pi} \lim_{\delta \to 0^+} \mathrm{Im} G_d(\omega + i\delta) = \frac{1}{\pi} \frac{\Gamma}{\omega^2 + \Gamma^2} \tag{2.25}$$

with the Green's function of the impurity $G_d(\omega + i\delta)$.

For $\Gamma \ll U$ the spectral function looks completely different. The formerly broad peak splits into three peaks, two broad peaks at the energies $\omega = \epsilon_d$ and $\omega = \epsilon_d + U$, which correspond to charge excitations, and a very narrow "Kondo resonance" at the Fermi energy which can be related to spin fluctuations of the local moment. The half width of the Kondo resonance is approximately given by the Kondo temperature

T_K. Interestingly, the height of the Kondo resonance is independent of the Coulomb repulsion U and is determined by the phase shift of the conduction band electrons δ [76–79]

$$\rho_d(\omega = 0) = \frac{\sin^2(\delta)}{\pi\Gamma}. \tag{2.26}$$

This three peak structure is typical for the Kondo effect and the Kondo resonance at $\omega = 0$ leads to a strong enhancement of the differential conductance $\frac{dI}{dV}(V_g = 0)$.

Chapter 3

Methods

In the last decades the interest in quantum impurity systems (QISs) has risen significantly, among other reasons because they may be used as qubits for quantum computers. However, a theoretical treatment of these systems is difficult. One major problem is the coupling to a continuum of excitations with arbitrary small energies which possibly results in infrared divergences in perturbative treatments. A classic example of this difficulty is the Kondo problem which has been presented in Sec. 2.2. The numerical renormalization group (NRG) was originally developed by Wilson [53] to solve the Kondo problem in a systematic and non perturbative way. However, the NRG proved to be suitable to solve other problems as well, e.g. the symmetric [26] and asymmetric [27] single impurity Anderson model (SIAM). Nowadays, the NRG is a commonly used method to solve many different QISs [80] and numerous extension were implemented, e.g. the coupling to a bosonic bath [81, 82] or even a mixture of fermionic and bosonic baths [83].
In the following Sec. 3.1 we will introduce the basic concepts of the NRG. Since it is beyond the scope of this thesis to consider all the extensions of the NRG, we restrict our discussion to the variants used in this work: the time-dependent numerical renormalization group (TD-NRG) is described in detail in Sec. 3.2 and the calculation of dynamic correlation functions is presented in Sec. 3.3. At the end, we will give a brief overview about the calculation of potential scattering terms of an effective low energy Hamiltonian in Sec. 3.4. We will also discuss some benchmark calculations since this method has been developed to calculate the renormalized parameters of an effective Anderson model and we adapt it to fulfill our purposes.

3.1 Numerical renormalization group

In this section we will introduce the NRG. At first, the general structure of a Hamiltonian which can be solved by the NRG is discussed. Afterwards, the three major steps of the NRG are presented: (i) logarithmic discretization of the bath, (ii) mapping the

model onto a semi-infinite chain, and (iii) solving this chain iteratively. The discussion below primarily follows the presentation of Ref. [80].

3.1.1 Structure of the Hamiltonian

The general structure of a QIS consists of three parts that are given by

$$H = H_{\text{bath}} + H_{\text{int}} + H_{\text{imp}} \,, \tag{3.1}$$

where H_{bath} describes the bath/conduction band, H_{imp} the quantum impurity and H_{int} the interaction between the bath and the impurity. The contribution of the bath is given by

$$H_{\text{bath}} = \sum_{i,k,\sigma} \epsilon_{i,k} c^\dagger_{i,k,\sigma} c_{i,k,\sigma} \,, \tag{3.2a}$$

where the index i denotes different conduction bands. The fermionic operator $c^\dagger_{i,k,\sigma}$ creates an electron with spin σ and momentum k in the conduction band i and $\epsilon_{i,k}$ is the dispersion of the corresponding conduction band.
The impurity is described by different energy levels which couple to the baths. The interaction between the baths and the impurity described by H_{int} is thus given by

$$H_{\text{int}} = \sum_{i,j} \sum_{k,\sigma} V_{i,j,k} \left(c^\dagger_{i,k,\sigma} d_{j,\sigma} + d^\dagger_{j,\sigma} c_{i,k,\sigma} \right) \,. \tag{3.2b}$$

Here $d^\dagger_{j,\sigma}$ denotes a creation operator of the energy level j and $V_{i,j,k}$ describes the k-dependent hybridization between bath i and energy level j.
The specific form of H_{imp} which describes the impurity remains arbitrary at this point. The only requirement is that the Hilbert space is small enough so that H_{imp} can be diagonalized exactly.
For simplicity we will drop the indices i for the baths and j for the energy levels in the following discussion. This means that we consider a model with only one bath and one energy level. However, a generalization to a model with more than one bath or energy level is straightforward.
The effect of the bath on the impurity is completely determined by the hybridization function $\Gamma(\omega)$:

$$\Gamma(\omega) = \pi \sum_k V_k^2 \delta(\epsilon_k - \omega) \,. \tag{3.3}$$

For the simple case of a constant hybridization $V_k = V$ Eq. (3.3) can be written as

$$\Gamma(\omega) = \pi V^2 \rho(\omega) \,, \tag{3.4}$$

where $\rho(\omega)$ is the density of states of the conduction band.
We assume that $\rho(\omega)$ lies completely in the interval $[-D, D]$ so that we have a band width of $2D$. It was shown in [84] that if we are only interested in the impurity contribution to the physics, the Hamiltonian can be rewritten in energy space as

$$H = H_{\text{imp}} + \sum_{\sigma} \int_{-D}^{D} d\epsilon \; g(\epsilon) a^{\dagger}_{\epsilon,\sigma} a_{\epsilon,\sigma} + \sum_{\sigma} \int_{-D}^{D} d\epsilon \; h(\epsilon) \left(d^{\dagger}_{\sigma} a_{\epsilon,\sigma} + d_{\sigma} a^{\dagger}_{\epsilon,\sigma} \right) , \tag{3.5}$$

with the dispersion $g(\epsilon)$ and hybridization $h(\epsilon)$. The fermionic operator $a^{(\dagger)}_{\epsilon,\sigma}$ fulfills the standard anticommutation relation $\left\{ a_{\epsilon\,,\sigma} \, , a^{\dagger}_{\epsilon',\sigma'} \right\} = \delta(\epsilon - \epsilon')\delta_{\sigma,\sigma'}$ and annihilates (creates) a conduction band electron with energy ϵ and spin σ. The two Hamiltonians (3.2) and (3.5) have the same action on the impurity if [84]

$$\Gamma(\omega) = \pi \frac{\mathrm{d}\epsilon(\omega)}{\mathrm{d}\omega} h[\epsilon(\omega)]^2 \, , \tag{3.6}$$

where $\epsilon(\omega)$ is the inverse function to $g(\epsilon)$ ($g[\epsilon(\omega)] = \omega$). Eq. (3.6) connects the new dispersion $g(\epsilon)$ and hybridization $h(\epsilon)$ with ϵ_k and V_k. For a given hybridization function $\Gamma(\omega)$ there are many possibilities to divide the energy dependence between $g(\epsilon)$ and $h(\epsilon)$. This feature is used in [84] to handle energy dependent hybridizations within the NRG. For a constant hybridization function $\Gamma(\omega) = \Gamma_0$ within the interval $[-D, D]$ Eq. (3.6) can be satisfied by $\epsilon(\omega) = \omega$ (corresponding to $g(\epsilon) = \epsilon$) and $h^2(\epsilon) = \Gamma_0/\pi$. This leads to the solution which Krishna-Murty *et al.* already derived in [26]. In this approach the one dimensional energy representation of Eq. (3.5) was arrived by expressing the conduction band states in spherical waves around the impurity.
In the following discussion the energy cutoff of the conduction band D is used as the energy unit and thus set to $D = 1$.

3.1.2 Logarithmic discretization

Following Wilson's proposal [53] the conduction band is now discretized on a logarithmic mesh. As shown in Fig. 3.1 this defines a set of discretization points

$$x_n = \pm \Lambda^{-n}, \qquad n = 0, 1, 2, \ldots \tag{3.7}$$

with the so-called discretization parameter $\Lambda > 1$. The width of the interval between two points is given by

$$d_n = \Lambda^{-n} \left(1 - \Lambda^{-1} \right) \, . \tag{3.8}$$

Due to the logarithmic discretization the width of an interval shrinks logarithmically with the interval index n. Within each interval now a complete set of orthonormal

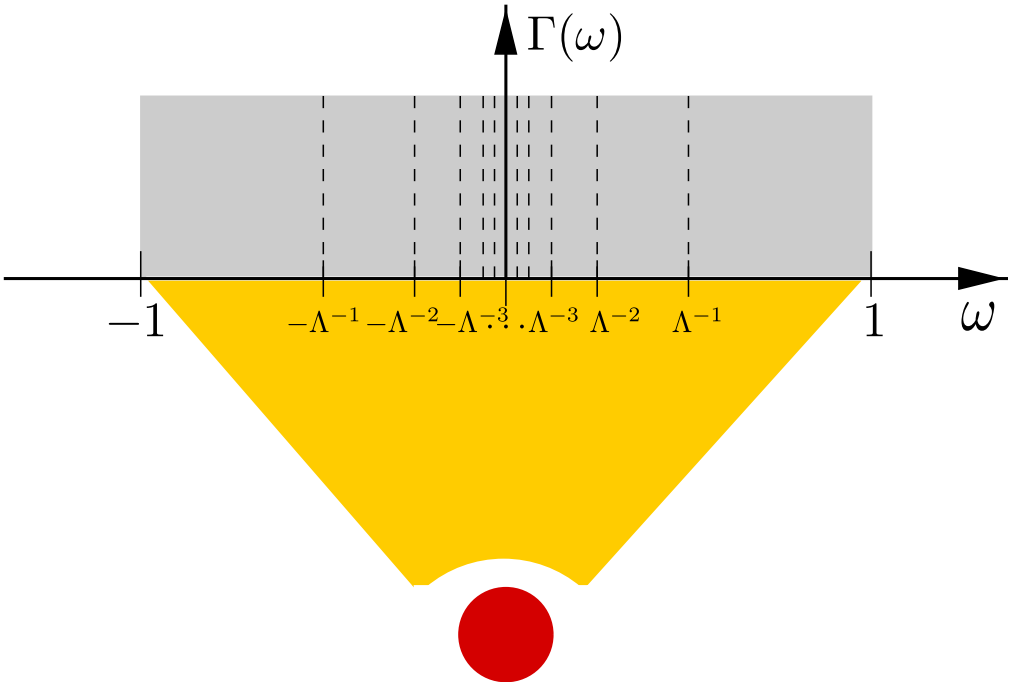

Figure 3.1: The discretization parameter Λ introduces a logarithmic set of intervals. The impurity couples to all energies of the continuous conduction band which is described by the hybridization function $\Gamma(\omega)$. Adapted from Ref. [80].

functions is introduced and the conduction band electron operators $a_{\epsilon,\sigma}$ are expanded in this orthonormal basis. Here it is necessary to distinguish between positive and negative energies. Therefore, the expansion of the band electron operators contains two new fermionic operators a and b. Because the impurity directly couples to only one energy mode in each interval, all other energy modes which appear in the bath Hamiltonian are neglected. This is the major approximation of the NRG. Since each interval now consists of only one energy mode, we have transformed the continuous band into a discretized one which is shown in Fig. 3.2. As can be seen, the number of representative energy modes of each interval becomes more dense around the Fermi energy and contains only a few high-energy states. This is justified by the fact that we are more interested in the low temperature behaviour of the system and thus energies around the Fermi energy play the dominant role.

After the expansion of $a_{\epsilon,\sigma}$ and only keeping one energy mode in each interval, the Hamiltonian is given by

$$\begin{aligned} H =& H_{\text{imp}} + \sum_{n,\sigma} \left(\xi_n^+ a_{n,\sigma}^\dagger a_{n,\sigma} + \xi_n^- b_{n,\sigma}^\dagger b_{n,\sigma} \right) \\ &+ \frac{1}{\sqrt{\pi}} \sum_{n,\sigma} \left(d_\sigma^\dagger \left(\gamma_n^+ a_{n,\sigma} + \gamma_n^- b_{n,\sigma} \right) + \left(\gamma_n^+ a_{n,\sigma}^\dagger + \gamma_n^- b_{n,\sigma}^\dagger \right) d_\sigma \right) \end{aligned} \tag{3.9}$$

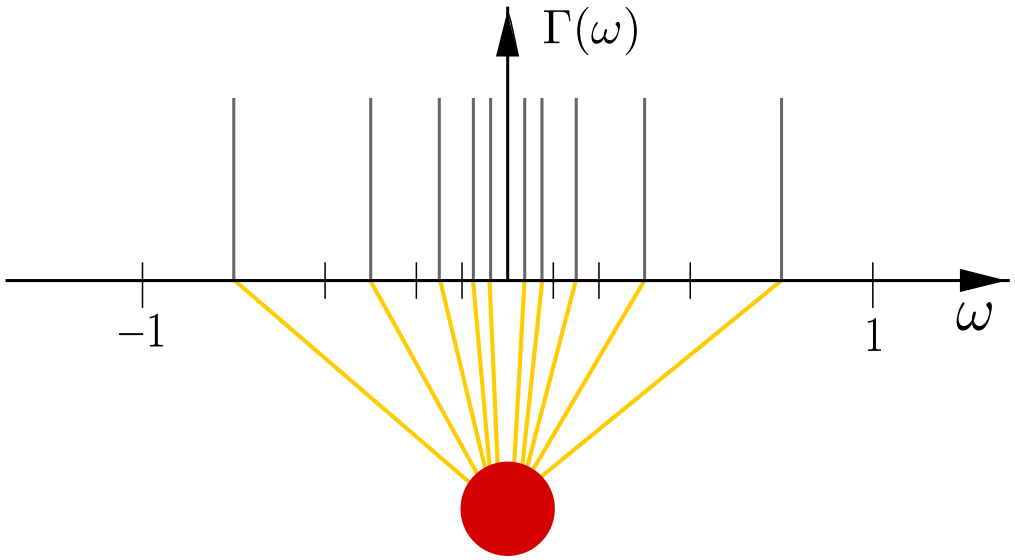

Figure 3.2: From each continuous energy interval only one energy mode is kept. The impurity couples to the discrete energy levels of the conduction band. Adapted from Ref. [80].

with

$$\gamma_n^{\pm 2} = \int^{\pm,n} d\epsilon\, \Gamma(\epsilon) \tag{3.10}$$

$$\xi_n^{\pm} = \frac{\int^{\pm,n} d\epsilon\, \Gamma(\epsilon)\epsilon}{\int^{\pm,n} d\epsilon\, \Gamma(\epsilon)} \tag{3.11}$$

and the convention

$$\int^{+,n} d\epsilon \equiv \int_{x_{n+1}}^{x_n} d\epsilon, \qquad \int^{-,n} d\epsilon \equiv \int_{-x_n}^{-x_{n+1}} d\epsilon\,. \tag{3.12}$$

A complete derivation of Eq. (3.9) can be found in [80] and a detailed discussion of an energy dependent hybridization function $\Gamma(\omega)$ and the importance of Eq. (3.6) is given in [84].

3.1.3 Mapping on a semi-infinite chain

In the next step of NRG algorithm the Hamiltonian of Eq. (3.9) is mapped on a semi-infinite chain where the impurity only couples to the first site of the chain, cf. Fig. 3.3.

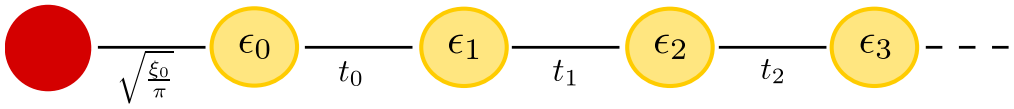

Figure 3.3: The model is mapped onto a semi-infinite chain which is often referred as the Wilson Chain. The impurity couples only to the first site of the chain with the strength $\sqrt{\frac{\xi_0}{\pi}}$. The on-sites energies ϵ_i, hopping parameters t_i and the coupling to the impurity $\sqrt{\frac{\xi_0}{\pi}}$ are defined by $\Gamma(\omega)$. Adapted from Ref. [80].

After a Householder transformation which transforms the operators a_n and b_n to a new fermionic operator c_n, the Hamiltonian takes the form

$$\begin{aligned} H =& H_{\text{imp}} + \sqrt{\frac{\xi_0}{\pi}} \sum_{\sigma} \left(d_\sigma^\dagger c_{0,\sigma} + c_{0,\sigma}^\dagger d_\sigma \right) \\ &+ \sum_{\sigma,n=0}^{\infty} \left[\epsilon_n c_{n,\sigma}^\dagger c_{n,\sigma} + t_n \left(c_{n,\sigma}^\dagger c_{n+1,\sigma} + c_{n+1,\sigma}^\dagger c_{n,\sigma} \right) \right] \end{aligned} \tag{3.13}$$

$$\text{with } \xi_0 = \int_{-1}^{1} d\epsilon \, \Gamma(\epsilon) \, . \tag{3.14}$$

The operator $c_{n,\sigma}^{(\dagger)}$ annihilates (creates) an electron on the n-th site of the so-called Wilson chain. The on-site energies ϵ_n and the hopping parameters t_n are defined by $\Gamma(\omega)$ and have to be in general calculated numerically [80]. For the simple case of a constant hybridization function $\Gamma(\omega) = \Gamma_0$ these parameters can be calculated analytically and the hopping parameters are given by

$$t_n = \frac{(1+\Lambda^{-1})(1-\Lambda^{-n-1})}{2\sqrt{1-\Lambda^{-2n-1}}\sqrt{1-\Lambda^{-2n-3}}} \Lambda^{-n/2} \, . \tag{3.15}$$

Since for a constant hybridization function Γ_0 the model is particle-hole symmetric, all on-sites energies must vanish $\epsilon_n = 0$. In the limit of large n the expression for the hopping parameters reduces to

$$t_n \to \frac{1}{2} \left(1 + \Lambda^{-1} \right) \Lambda^{-n/2} \tag{3.16}$$

and we can see that t_n exponentially decreases with the distance from the impurity. This originates from the logarithmic discretization and is vital for the NRG because this guarantees the separation of the energy scales.

Furthermore, the coupling between the impurity and the first Wilson site is sometimes multiplied by the factor [85]

$$A_\Lambda = \frac{1}{2}\frac{\Lambda+1}{\Lambda-1}\ln\Lambda \tag{3.17}$$

in order to compensate the shortcoming of the NRG to underestimate the coupling. In this thesis it will be marked if the A_Λ factor is used.

3.1.4 Iterative diagonalization

In the previous section the Hamiltonian was mapped onto the form of the semi-infinite chain of Eq. (3.13). In the following we will define an iterative renormalization procedure for this semi-infinite chain. At this step finally the renormalization group (RG) character of the NRG enters.
The chain Hamiltonian Eq. (3.13) is written as a series of Hamiltonians H_N in which H is reached in the limit $N \to \infty$:

$$H = \lim_{N\to\infty} \Lambda^{-(N-1)/2} H_N \,, \tag{3.18}$$

with

$$\begin{aligned} H_N =& \Lambda^{(N-1)/2}\left(H_{\text{imp}} + \sqrt{\frac{\xi_0}{\pi}}\sum_\sigma (d_\sigma^\dagger c_{0,\sigma} + c_{0,\sigma}^\dagger d_\sigma) \right. \\ &\left. + \sum_{\sigma,n=0}^{N} \epsilon_n c_{n,\sigma}^\dagger c_{n,\sigma} + \sum_{\sigma,n=0}^{N-1} t_n (c_{n,\sigma}^\dagger c_{n+1,\sigma} + c_{n+1,\sigma}^\dagger c_{n,\sigma}) \right) . \end{aligned} \tag{3.19}$$

The scaling factor $\Lambda^{(N-1)/2}$ has been introduced to cancel the N dependence of the last hopping parameter t_{N-1}. This yields a hopping parameter of the order $O(1)$ which is useful for the discussion of fixed points.
It is straight forward to derive the RG transformation of the NRG

$$H_{N+1} = \sqrt{\Lambda} H_N + \Lambda^{N/2} \sum_\sigma \left(\epsilon_{N+1} c_{N+1,\sigma}^\dagger c_{N+1,\sigma} + t_N (c_{N,\sigma}^\dagger c_{N+1,\sigma} + c_{N+1,\sigma}^\dagger c_{N,\sigma}) \right) \tag{3.20}$$

with the starting Hamiltonian

$$H_0 = \Lambda^{-1/2}\left(H_{\text{imp}} + \sum_\sigma \epsilon_0 c_{0,\sigma}^\dagger c_{0,\sigma} + \sqrt{\frac{\xi_0}{\pi}}\sum_\sigma (d_\sigma^\dagger c_{0,\sigma} + c_{0,\sigma}^\dagger d_\sigma) \right) . \tag{3.21}$$

Equation (3.21) describes a two-site cluster which is formed by the impurity and the first site of the Wilson chain.
The next step is to set up an iterative scheme for the diagonalization of H_N using the

recursion relation of Eq. (3.20). Therefore, we assume that the problem for a given N has already been diagonalized

$$H_N|r\rangle_N = E_N(r)|r\rangle_N, \qquad r = 1, \ldots, N_s \,, \tag{3.22}$$

with the eigenstates $|r\rangle_N$, eigenenergies $E_N(r)$ and the dimension of the Hamiltonian N_s. The basis of H_{N+1} is then given by the product states

$$|r;s\rangle_{N+1} = |r\rangle_N \otimes |s(N+1)\rangle \tag{3.23}$$

consisting of the eigenbasis of H_N and a suitable base $|s(N+1)\rangle$ of the added Wilson site, e.g. $|0\rangle, |\uparrow\rangle, |\downarrow\rangle, |\uparrow\downarrow\rangle$ for a fermionic bath. In this basis H_{N+1} can be written as

$$\begin{aligned} H_{N+1}(rs, r's') =& \langle r;s|H_{N+1}|r';s'\rangle \\ =& \sqrt{\Lambda} E_N(r)\delta_{r,r'}\delta_{s,s'} + \Lambda^{N/2}\sum_\sigma \epsilon_{N+1}\langle s|c^\dagger_{N+1,\sigma}c_{N+1,\sigma}|s'\rangle\delta_{r,r'} \\ &+ \Lambda^{N/2}\sum_\sigma t_N\left(\langle r;s|c^\dagger_{N,\sigma}c_{N+1,\sigma} + c^\dagger_{N+1,\sigma}c_{N,\sigma}|r';s'\rangle\right). \end{aligned} \tag{3.24}$$

A further diagonalization of $H_{N+1}(rs, r's')$ in Eq. (3.24) yields new eigenvalues $E_{N+1}(w)$ and new eigenstates $|w\rangle_{N+1}$ which are related to the basis $|r;s\rangle_{N+1}$ via the unitary matrix U:

$$|w\rangle_{N+1} = \sum_{rs} U_{w,rs}|r;s\rangle_{N+1} \,. \tag{3.25}$$

For simplicity the ground-state energy is set to zero after each diagonalization.
With this method, however, long Wilson chains cannot be diagonalized. Since the number of states increases by a factor (in general this factor is given by the dimension of the basis $|s(N+1)\rangle$) when a new site is added, the Hilbert space grows exponentially with the chain length N. Therefore, the dimension of the matrices becomes very large after a few iterations and the matrices cannot be diagonalized any longer.
To avoid this problem a simple truncation scheme is introduced: after each diagonalization only the N_s eigenstates with the lowest many-particle energies are kept. This leads to a fixed dimension of the Hilbert space and a linear increase of the computation time with the chain length. A justification of this truncation scheme is given in the next section 3.1.5. Suitable values for N_s highly depend on the model, therefore, different calculations with increasing N_s should be done till the results are converged.
Furthermore one usually wants that the results also converge with the number of iterations [86] which means that the RG transformation has reached a stable fixed point[1]. We can write Eq. (3.20) symbolically as $H_{N+1} = \mathcal{T}[H_N]$ and a fixed point is a Hamil-

[1] This corresponds to a zero temperature $T = 0$ calculation. For a finite temperature one has to stop at a certain iteration. For more details see sec. 3.1.5.

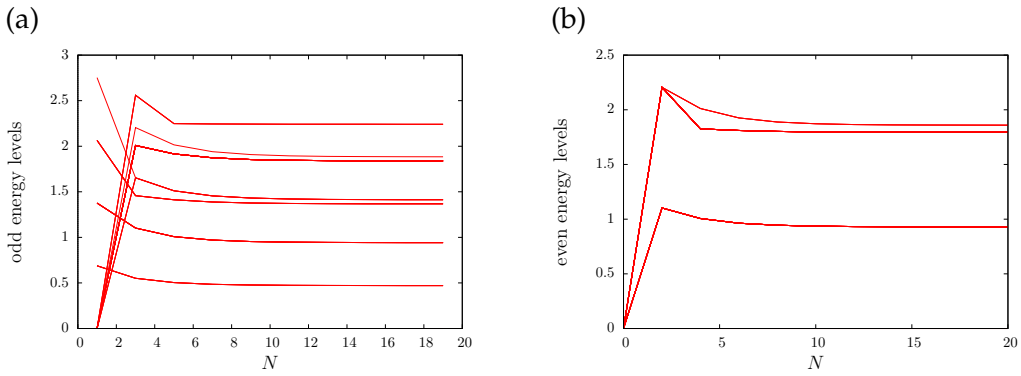

Figure 3.4: Energy-flow of the lowest eigenenergies of a free electron gas with $\Lambda = 1.5$ and $N_s = 1000$ kept states, (a) shows only the odd and (b) only the even iterations. The fixed point is reached for $N > 10$ iterations.

tonian H^* that remains invariant under that transformations: $\mathcal{T}[H^*] = H^*$. In fact $\mathcal{T}$ has no fixed point but $H_{N+2} = \mathcal{T}^2[H_N] = \mathcal{T}[\mathcal{T}[H_N]]$ has one. The reason for this lies in the even-odd asymmetry, e.g. if the model has for even iterations in average an even number of electrons, they can form a singlet ground state while for odd iterations one electron spin will be left over. In the numerics a fixed point is characterized by a set of many-particle energy levels that repeat themselves when the iterative diagonalization is performed twice. Figure 3.4a shows the so-called level- or energy-flow of the free electron gas which means the lowest many-particle energies in dependence of the iterations N for odd iterations while Fig. 3.4b shows the level-flow for even iterations. For $\Lambda = 1.5$ the level-flow of the free electron gas shows a stable fixed point for $N > 10$, therefore, the chain length in this case should be chosen larger than 10.

3.1.5 Calculation of impurity properties

Beside the low many-particle energies the NRG is also able to calculate thermodynamic expectation values of an operator O. In general the expectation value is given by

$$\langle O \rangle = \frac{1}{Z} \mathrm{Tr} \left[\mathrm{e}^{-\beta H} O \right], \tag{3.26}$$

where β is the inverse temperature and Z is the partition function. In the NRG the Hamiltonian H is approximated with the discretized and truncated version H_N

$$\langle O \rangle \approx \frac{1}{Z_N} \mathrm{Tr} \left[\mathrm{e}^{-\beta \Lambda^{-\frac{N-1}{2}} H_N} O \right] \tag{3.27}$$

$$= \frac{1}{Z_N} \sum_r \mathrm{e}^{-\beta_N E_N(r)} \, {}_N\langle r|O|r\rangle_N \tag{3.28}$$

with the eigenstates $H_N|r\rangle_N = E_N(r)|r\rangle_N$ and the partition function $Z_N = \sum_r \mathrm{e}^{-\beta_N E_N(r)}$. Here we have introduced the iteration dependent inverse temperature

$$\beta_N = \beta\Lambda^{-\frac{N-1}{2}} . \tag{3.29}$$

In the NRG the expectation value of an operator is calculated in the following way: We choose a constant value $\overline{\beta}$ of the order $O(1)$ and set $\beta_N = \overline{\beta} \approx 1$. This effectively means that we introduce an iteration dependent temperature[2] T_N which decreases exponentially with N

$$T_N = \Lambda^{-\frac{N-1}{2}} \frac{1}{\overline{\beta}} . \tag{3.30}$$

Finally, we evaluate Eq. (3.28) and get a series of expectation values $O(T_N)$ at different temperatures T_N for each iteration N.
As mentioned above the lowest eigenenergies are of the order $O(1)$ due to the rescaling of the energies. Together with a fixed $\overline{\beta}$ this leads to less and less contributing high energy states because they are exponentially reduced by the Boltzmann factor $\mathrm{e}^{-\overline{\beta}E_N(r)}$. Since these high energy states do not contribute significantly to Eq. (3.28) they can be neglected. This provides the justification why the truncation of these high energy states is a good approximation.
If we want to evaluate Eq. (3.28) for a finite temperature $T > 0$ the number of iterations N, the discretization parameter Λ and the inverse temperature $\overline{\beta}$ have to be chosen such that $T = T_N$ is fulfilled.

3.2 Time-dependent numerical renormalization group

The TD-NRG is an expansion of the NRG and was developed by F. B. Anders and A. Schiller [87, 88] to track the real time dynamics of a QIS after a sudden quench at time $t = 0$. Recently, Nghiem and Costi presented an improvement for the TD-NRG that also allows multiple quenches [89]. However, in the following we will restrict ourself to the case of only one quench.
This quench perturbs an initial Hamiltonian H^i and the system is henceforth described by a final Hamiltonian $H^f = H^i + \Delta H$. Both Hamiltonians H^i and H^f are of the form of Eq. (3.1). The basic strategy of the TD-NRG is to calculate the equilibrium density matrix with H^i and compute the time-evolution of this density matrix with the perturbed Hamiltonian H^f. Therefore, one has to diagonalize both Hamiltonians using the NRG and calculate the transformation matrix that rotates the initial eigenbasis into

[2] Note that in the employed program the definition of the series in Eq. (3.18) is slightly modified to $H = \lim_{N\to\infty} \frac{1}{2}(1+\Lambda^{-1})\Lambda^{-(N-1)/2} H_N$ and all equations adapted accordingly. Therefore, in the used program the iteration dependent temperature is given by $T_N = \frac{1}{2}(1+\Lambda^{-1})\Lambda^{-\frac{N-1}{2}}\frac{1}{\overline{\beta}}$.

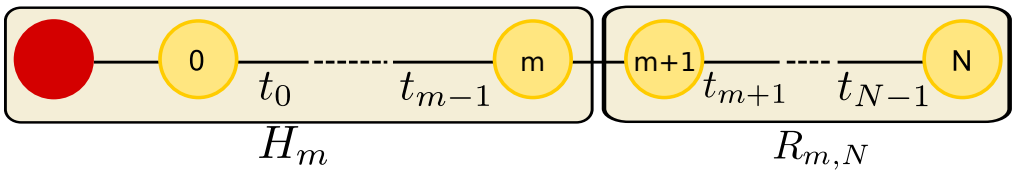

Figure 3.5: The Wilson chain of length N is divided into a subchain of length m and the "environment" $R_{m,N}$. In the TD-NRG the Hamiltonian H_m is viewed as acting on the full chain of length N, but with the hopping elements $t_m, \ldots, t_{N-1}$ all set to zero. Adapted from Ref. [88].

the final eigenbasis.
However, for an accurate description of the time-evolution all energy scales are relevant and one needs a complete basis set. This is problematic in the NRG since high energy states are truncated at each iteration. To circumvent this problem in the TD-NRG these truncated states are stored on a hard disk drive (HDD) and a complete basis set is constructed out of the NRG eigenstates. Therefore, all states that contribute to the time-evolution are considered.
The discussion below primarily follows the presentation of Ref. [88].

3.2.1 Complete basis set

In the previous Sec. 3.1 an iterative NRG solution was presented in which in each iteration step the Wilson chain is enlarged by one additional site. An alternative interpretation that is used in the TD-NRG is to start with the full chain of length N where at first all hopping matrix elements t_n are set to zero. At each successive step another hopping matrix element is switched on, until the complete Hamiltonian H_N is recovered. The Hamiltonian H_m with $m \leq N$ and $t_n = 0$ for all $n \geq m$ always acts on the Fock space of the whole chain of length N

$$H_m|r, \alpha_{m+1}, \ldots, \alpha_N\rangle = E_r^m|r, \alpha_{m+1}, \ldots, \alpha_N\rangle. \tag{3.31}$$

Here, the product state $|r, \alpha_{m+1}, \ldots, \alpha_N\rangle$ is the eigenstate of H_m belonging to the eigenenergy E_r^m and $\{\alpha_i\}$ denotes the configuration of the i-th site that does not couple to rest of the Wilson chain. Each eigenenergy has a degeneracy of d^{N-m}, where d is the number of distinct configurations of each site. The degeneracy stems from the $N-m$ decoupled "environment sites", denoted by $R_{m,N}$ in Fig. 3.5. In the following, we will use the shorthand notation $|r, e; m\rangle$ for the eigenstates where the "environment" variable $e = \{\alpha_{m+1}, \ldots, \alpha_N\}$ encodes the $N-m$ site labels.
When the hopping matrix element t_{m+1} is switched on, the new eigenstates of H_{m+1} are obtained from the unitary transformation

$$|r', e'; m+1\rangle = \sum_{r, \alpha_{m+1}} U_{r', r\alpha_{m+1}}|r, \alpha_{m+1}, e'; m\rangle. \tag{3.32}$$

An alternative notation is given by

$$|r', e'; m+1\rangle = \sum_{r,\alpha_{m+1}} P_{r',r}[\alpha_{m+1}]|r, \alpha_{m+1}, e'; m\rangle, \tag{3.33}$$

with $P_{r',r}[\alpha_{m+1}] = U_{r',r\alpha_{m+1}}$ and e' encoding the $N-m-1$ site labels $\{\alpha_{m+2}, \ldots, \alpha_n\}$. Since in the NRG high energy states are discarded at each iteration in order to keep a manageable number of basis states, we divide the states at each iteration in two distinct classes: the discarded high energy states $|l, e; m\rangle_{\text{dis}}$ and the kept low energy states $|k, e; m\rangle_{\text{kp}}$. If all eigenstates of the final iteration N are also regarded as discarded, all discarded states form a complete basis set and the following completeness relation holds:

$$\sum_{m=m_{\text{min}}}^{N} \sum_{l,e} |l, e; m\rangle_{\text{dis}}\ {}_{\text{dis}}\langle l, e; m| = 1. \tag{3.34}$$

The summation over m starts from the first iteration m_{min} at which states are discarded. Equation (3.34) can obviously be divided into two complementary parts:

$$1_m^- = \sum_{m'=m_{\text{min}}}^{m} \sum_{l',e'} |l', e'; m\rangle_{\text{dis}}\ {}_{\text{dis}}\langle l', e'; m|, \tag{3.35}$$

$$1_m^+ = \sum_{m'=m+1}^{N} \sum_{l',e'} |l', e'; m\rangle_{\text{dis}}\ {}_{\text{dis}}\langle l', e'; m|. \tag{3.36}$$

The completeness relation can therefore be rewritten as

$$1 = 1_m^- + 1_m^+. \tag{3.37}$$

Since the Operator 1_m^+ projects onto the states which are retained at iteration m, it can be expressed by the kept states

$$1_m^+ = \sum_{k,e} |k, e; m\rangle_{\text{kp}}\ {}_{\text{kp}}\langle k, e; m|. \tag{3.38}$$

3.2.2 Time-evolution of a local Operator

The time-evolution of an expectation value of a local operator is given by

$$O(t) = \text{Tr}\,[\rho(t)O] \tag{3.39}$$

$$= \sum_{m=m_{\text{min}}}^{N} \sum_{l,e} {}_{\text{dis}}\langle l, e; m|\rho(t)O|l, e; m\rangle_{\text{dis}}, \tag{3.40}$$

where we used the basis set $\{|l,e;m\rangle_{\text{dis}}\}$ that was introduced in the previous section. Inserting the completeness relation (3.37) between $\rho(t)$ and O yields

$$O(t) = \sum_{m=m_{\min}}^{N} \sum_{l,e} {}_{\text{dis}}\langle l,e;m|\rho(t)\left(1_m^- + 1_m^+\right)O|l,e;m\rangle_{\text{dis}}. \tag{3.41}$$

After further transformations, which are discussed in detail in [88], we obtain

$$O(t) = \sum_{m=m_{\min}}^{N} \sum_{r,s}^{\text{trun}} \sum_{e,e'} \langle s,e;m|\rho(t)|r,e';m\rangle\langle r,e';m|O|s,e;m\rangle. \tag{3.42}$$

Here, the resticted sum $\sum_{r,s}^{\text{trun}}$ requieres that at least one of the states r and s is discarded at iteration m. In the following we make the assumption that the operator O acts on the degrees of freedom of the impurity or on close by sites $\bar{m}$ such that all states are still available (i.e. $\bar{m} \leq m_{\min}$). Such a local operator O is independent of and, therefore, diagonal in the environmental degrees of freedom,

$$\langle r,e';m|O|s,e;m\rangle = \delta_{e,e'} O^m_{r,s}. \tag{3.43}$$

If we use the NRG basis set generated for the perturbed Hamiltonian H^f, which is motivated by the time-dependence of the density operator $\rho(t) = \mathrm{e}^{-itH^f}\rho_0\mathrm{e}^{itH^f}$, we obtain

$$O(t) = \sum_{m=m_{\min}}^{N} \sum_{r,s}^{\text{trun}} \mathrm{e}^{it(E_r^m - E_s^m)} O^m_{r,s}\rho^{\text{red}}_{s,r}(m), \tag{3.44}$$

where we used the standard NRG approximation $H^f|k,e;m\rangle \approx E_k^m|k,e;m\rangle$. The reduced density matrix $\rho^{\text{red}}_{s,r}(m)$ is given by

$$\rho^{\text{red}}_{s,r}(m) = \sum_e \langle s,e;m|\rho_0|r,e;m\rangle. \tag{3.45}$$

Since Eq. (3.44) is the centerpiece of the TD-NRG approach several comments should be made about it. At first, we want to emphasize that no restrictive assumptions were made about ρ_0, it can be an arbitrary density of states. Second, all states of the finite Fock space are retained and therefore all energy scales are taken into account.
Nevertheless two approximations were made in Eq. (3.44). The first one is the conventional NRG approximation $H^f|k,e;m\rangle \approx E_k^m|k,e;m\rangle$. However, Wilson [53] showed that the associated error in thermodynamic quantities is perturbative and small because of the separation of energy scales due to the logarithmic discretization. The second more significant error originates from the discretized finite-size representation of the continuous bath. Because of the limited energy resolution at low energy scales, Eq.

(3.44) may become inaccurate for times $t \geq 1/D_N$, where D_N is the energy scale of the N-th site. However, the NRG can reach arbitrary low energy scales and thus the TD-NRG arbitrary long times. Furthermore, a continuous spectrum is necessary for a complete relaxation in the system and the discretization may lead to unphysical oscillations [90, 91]. One way to minimize these discretization errors is discussed in Sec. 3.2.5.

3.2.3 Reduced density matrix

In order to calculate the time-dependence of a local operator, we still need to compute the reduced density matrix $\rho^{\text{red}}_{s,r}(m)$ in Eq. (3.44). In the basis set of the initial Hamiltonian H^i the density matrix ρ_0 has a simple representation. If we start from thermal equilibrium, ρ_0 is given by $\mathrm{e}^{-\beta H^i}/Z_i$ where Z_i is the initial partition function. However, in Eq. (3.44) the reduced density matrix was constructed for the NRG eigenstates of the final Hamiltonian H^f, therefore, we have to transform between the two basis sets.
To simplify the notation we distinguish the two sets by the labels. In the following the NRG states of the initial Hamiltonian H^i will be marked by an index i, for example $|l_i, e_i; m\rangle$. The NRG states belonging to H^f will be labeled as before without any indices, as in $|l, e; m\rangle$. In the basis of the initial Hamiltonian H^i the reduced density matrix is given by

$$\rho^{\text{red},0}_{s_i,r_i}(m) = \sum_{e_i} \langle s_i, e_i; m|\rho_0|r_i, e_i; m\rangle. \tag{3.46}$$

Similar to Eq. (3.37) we can write a completeness relation using the NRG states of H^i

$$1 = I^-_m + I^+_m, \tag{3.47}$$

with

$$I^-_m = \sum_{m'=m_{\text{min}}}^{m-1} \sum_{l'_i,e'_i} |l'_i, e'_i; m'\rangle_{\text{dis}\ \ \text{dis}}\langle l'_i, e'_i; m'| \tag{3.48}$$

and

$$I^+_m = \sum_{q_i,e_i} |q_i, e_i; m\rangle\langle q_i, e_i; m|. \tag{3.49}$$

Here we changed the notation from 1_m to I_m as we shifted the iteration $m' = m$ from Eq. (3.35) to Eq. (3.38). This allows us to sum over all states q_i of a given iteration m. Inserting Eq. (3.47) two times into Eq. (3.45) yields four contributions

$$\rho^{\text{red}}_{s,r} = \rho^{++}_{s,r}(m) + \rho^{+-}_{s,r}(m) + \rho^{-+}_{s,r}(m) + \rho^{--}_{s,r}(m) \tag{3.50}$$

with

$$\rho_{s,r}^{pp'}(m) = \sum_e \langle s,e;m|I_m^p \rho_0 I_m^{p'}|r,e;m\rangle, \qquad (p,p' = \pm). \tag{3.51}$$

In the following we restrict our attention to the case where ρ_0 corresponds to thermal equilibrium. In this case the only relevant combination is given by

$$\begin{aligned}\rho_{s,r}^{++}(m) &= \sum_e \langle s,e;m|I_m^+ \rho_0 I_m^+|r,e;m\rangle \\ &= \sum_e \sum_{q_i,q_i'} \sum_{e_i,e_i'} \langle s,e;m|q_i',e_i';m\rangle \langle q_i',e_i';m|\rho_0|q_i,e_i;m\rangle \langle q_i,e_i;m|r,e;m\rangle.\end{aligned} \tag{3.52}$$

The terms $\rho_{s,r}^{+-}(m)$, $\rho_{s,r}^{-+}(m)$ and $\rho_{s,r}^{--}(m)$ describe how high- and low-energy states of H^i are coupled and are only important if ρ_0 contains significant contributions from high-energy states. If we start from a state well removed from thermal equilibrium, we have to take all combinations of Eq. (3.50) into account as it is discussed by Nghiem and Costi in Ref. [89].
For the simple case that we only consider $\rho_{s,r}^{++}(m)$, the overlap matrix elements $\langle q_i,e_i;m|r,e;m\rangle$ are independent of and diagonal in the environment degrees of freedom

$$\langle q_i,e_i;m|r,e;m\rangle = \delta_{e_i,e} S_{q_i,r}(m). \tag{3.53}$$

Here we have introduced the reduced matrix $S(m)$ which records the overlap matrix elements between the NRG eigenstates of H^i and H^f. A systematic way to compute the matrix $S(m)$ is detailed in the appendix of Ref. [88]. With $S(m)$ we obtain $\rho_{s,r}^{++}(m)$ by a simple rotation of $\rho_{q_i',q_i}^{\mathrm{red},0}(m)$ into a new basis

$$\rho_{s,r}^{++}(m) = \sum_{q_i',q_i} S_{q_i',s}^*(m) \rho_{q_i',q_i}^{\mathrm{red},0}(m) S_{q_i,r}(m). \tag{3.54}$$

We now elaborate a recursion equation which allows us to compute $\rho^{\mathrm{red},0}(m)$ recursively from $\rho^{\mathrm{red},0}(m+1)$. For the last iteration N the reduced density matrix is given by

$$\rho_{s_i,r_i}^{\mathrm{red},0} = \delta_{s_i,r_i} \frac{1}{Z_i} \mathrm{e}^{-\beta E_{s_i}^N} \tag{3.55}$$

with $Z_i = \sum_{s_i} \mathrm{e}^{-\beta E^N_{s_i}}$. To execute the sum over e_i in Eq. (3.46) we set $e_i = \{\alpha_i, e_i'\}$, where e_i' is the state variable for the environment $R_{m+1,N}$. Substituting $I^+_{m+1}\rho_0 I^+_{m+1}$ for ρ_0 in Eq. (3.46) and using the overlap matrix elements

$$\langle s_i, e_i; m | k_i', e_i'; m+1\rangle = P_{k_i', s_i}[\alpha_{m+1}] \tag{3.56}$$

yields

$$\rho^{\mathrm{red},0}_{s_i,r_i}(m) = \sum_{\alpha_{m+1}} \sum_{k_i,k_i'}^{\mathrm{retain}} P_{k_i',s_i}[\alpha_{m+1}]\, P^*_{k_i,r_i}[\alpha_{m+1}]\, \rho^{\mathrm{red},0}_{k_i',k_i}(m+1). \tag{3.57}$$

The sum $\sum_{k_i,k_i'}^{\mathrm{retain}}$ is restricted to the states retained at iteration $m+1$. For the case $m = N-1$ the sum runs over all states of the final NRG iteration. If at least one of the states s_i or r_i is discarded at iteration m, the reduced density matrix $\rho^{\mathrm{red},0}_{s_i,r_i}(m)$ vanishes because of the orthogonality of the basis set.

3.2.4 TD-NRG algorithm

In the following we will present the different steps of the TD-NRG algorithm. To evaluate the time-dependence of an operator O at a desired temperature T, one first has to select the discretization parameter Λ and the chain length N such that $T \approx T_N$, cf. Sec. 3.1.5. Afterwards two simultaneous NRG runs are performed, one for the Hamiltonian H^i and another for H^f. All eigenenergies of these two Hamiltonians are stored up to the final iteration N and at each iteration m the overlap matrices $S(m)$ of Eq. (3.53) are computed. This information, as well as the matrices $P_{l',l}[\alpha_m]$ are stored on a HDD. After both NRG runs finished, the equilibrium density matrix of Eq. (3.55) is calculated using the eigenenergies of the initial Hamiltonian H^i. At this point the TD-NRG starts backward iterations beginning from iteration $m = N$. For each backward iteration the following three steps are performed:

(1) The matrices $P_{l',l}[\alpha_m]$ are used to calculate $\rho^{\mathrm{red},0}(m-1)$ from $\rho^{\mathrm{red},0}(m)$ using Eq. (3.57).

(2) With the help of the overlap matrices $S(m-1)$ and Eq. (3.54) $\rho^{\mathrm{red},0}(m-1)$ is rotated into the basis of the final Hamiltonian H^f.

(3) Using Eq. (3.44) the contribution of iteration m to $O(t_j)$ is calculated simultaneously for all times of interest t_j. Subsequently $\rho^{\mathrm{red}}(m)$ can be deleted from the memory.

These steps are repeated until iteration $m = m_{\min}$ is reached, below which no states have been discarded.

3.2.5 Restoring the continuous bath: the z-trick

It was already mentioned in Sec. 3.2.2 that the discretization of the continuous bath may lead to errors like unphysical oscillations [90, 91]. Oliveira and co-workers [92] already presented in the context of the equilibrium NRG a way how to reduce discretization errors. In the so-called z-trick a z dependent logarithmic discretization according to $\left[1, \Lambda^{-z}, \Lambda^{-z-1}, \ldots, \Lambda^{-z-n-1}, \ldots\right]$ is introduced. Unphysical oscillations can be removed by integrating the expectation values with respect to $0 < z \leq 1$ which mimics a continuous bath.
We use the same method for the TD-NRG by computing the time-evolution of Eq. (3.44) for each value of $z_i = i/N_z$, with $i = 1, \ldots, N_z$, and average over all the different realizations. Here N_z is the number of all the different z-values and should be chosen in multiples of 4 which produces the best results [92].

3.3 NRG Green's functions

The NRG is not only suitable for the calculation static properties, but also local dynamical quantities can be calculated with it. In the following, a method for the calculation of dynamical correlation functions of QISs in equilibrium with the NRG is presented. Like the TD-NRG it is based on a complete basis set of the Wilson chain. In contrast to all previous methods [93–96] this approach has no issues with the correct mixing of different energy shells. Due to the complete basis set, phenomenological patching algorithms that merge contributions of different energy shells and often suffer from overcounting of contributions become obsolete. Furthermore, the complete basis set ensures the fulfillment of spectral sum rules independently of the number of kept states. Hence, the spectral functions become more robust to truncation errors.
Below, we will first discuss the derivation of a discrete spectrum of an impurity Green's function. This discussion primarily follows the presentation in [97]. Afterwards, we will describe how to get a smooth spectrum by replacing the delta functions with some smooth distributions. At the end, an improvement for the calculation of impurity Green's functions of the SIAM is presented. In this approach the impurity Green's function is not calculated directly with the NRG but the correlation part of the self-energy by expressing it as a ratio of two impurity correlation functions.

3.3.1 Derivation of the NRG Green's function

In general the retarded Green's function is given by

$$G_{A,B}(t) = -i\theta(t)\mathrm{Tr}\left[\rho\left[A(t), B\right]_{-s}\right], \tag{3.58}$$

with $\left[A(t), B\right]_{-s} = A(t)B - sBA(t)$ and $s = +1/-1$ for bosonic/fermionic operators A and B. As it was already mentioned in Sec. 3.2.3 for the TD-NRG, the thermodynamic

density operator ρ is in thermal equilibrium only given by the states of the last iteration N. The reason for this is that the states for all iterations $m < N$ are exponentially reduced by the Boltzmann factor $\mathrm{e}^{-\beta E_l^m}$ and can therefore be neglected. The density operator is thus given by

$$\rho = \frac{1}{Z}\mathrm{e}^{-\beta H} \approx \sum_l \rho_l |l;N\rangle\langle l;N| \tag{3.59}$$

with $\rho_l = \mathrm{e}^{-\beta E_l^N}/Z_N$ and $Z_N = \sum_l \mathrm{e}^{-\beta E_l^N}$.
Inserting the completeness relation Eq. (3.37) into the first term of the commutator of Eq. (3.58) yields

$$\begin{aligned}
\mathrm{Tr}\left[\rho \mathrm{e}^{iHt} A \mathrm{e}^{-iHt} B\right] &= \sum_{l,e,m}\sum_{l',e',m'} \langle l,e;m|A\mathrm{e}^{-iHt}|l',e';m'\rangle\langle l'e';m|B\rho\mathrm{e}^{iHt}|l,e;m\rangle \\
&= \sum_{l,e,m}\sum_{l',e'} {}_{\mathrm{dis}}\langle l,e;m|A\mathrm{e}^{-iHt}|l',e';m\rangle_{\mathrm{dis}}\ {}_{\mathrm{dis}}\langle l',e';m|B\rho\mathrm{e}^{iHt}|l,e;m\rangle_{\mathrm{dis}} \\
&+ \sum_{l,e,m}\sum_{k,e'} {}_{\mathrm{dis}}\langle l,e;m|A\mathrm{e}^{-iHt}|k,e';m\rangle_{\mathrm{kp}}\ {}_{\mathrm{kp}}\langle k,e';m|B\rho\mathrm{e}^{iHt}|l,e;m\rangle_{\mathrm{dis}} \\
&+ \sum_{k,e,m}\sum_{l,e'} {}_{\mathrm{dis}}\langle l,e';m|B\rho\mathrm{e}^{iHt}|k,e;m\rangle_{\mathrm{kp}}\ {}_{\mathrm{kp}}\langle k,e;m|A\mathrm{e}^{-iHt}|l,e';m\rangle_{\mathrm{dis}}.
\end{aligned} \tag{3.60}$$

For the second term of the commutator of Eq. (3.58) one can easily derive a similar expression. The first line of Eq. (3.60) represents the case where $m' = m$, the second $m' > m$ and the third $m' < m$. Here we made use of Eq. (3.38) which connects the kept states of iteration m to the discarded states of all later iterations $m' > m$. This allows us to sum over equal shell contributions only. In the following we will drop the indications "kp" and "dis" and use the index l for a discarded state while the index k represents a kept state at a certain iteration m.
Since the states $|l,e;m\rangle$ and $|k,e;m\rangle$ are both eigenstates of H_m, we will use the standard NRG approximation $H|s,e;m\rangle \approx E_s^m|s,e;m\rangle$ which is justified by the energy hierarchy due to the logarithmic discretization. After a Laplace transformation, we obtain for the first term of Eq. (3.60) and the corresponding second term from the commutator

$$G^i_{A,B}(z) = \frac{1}{Z}\sum_{l,l'}\langle l;N|A|l';N\rangle\langle l';N|B|l;N\rangle\frac{\mathrm{e}^{-\beta E_l^N} - s\mathrm{e}^{-\beta E_{l'}^N}}{z + E_l^N - E_{l'}^N}, \tag{3.61}$$

where we used the orthogonality of the states and the form of the density operator ρ in Eq. (3.59), so that $\rho|l,e;m\rangle = 0$ for $m < N$. Therefore, only the last iteration $m = N$ contributes in the sum over all iterations m.
However, since the kept states $|k,e;m\rangle$ are not orthogonal to $|l;N\rangle$, the summation over all energy shells has to be evaluated for the last two terms in Eq. (3.60). Inserting the

completeness relation $(1_m^- + 1_m^+)$ into these two terms and their corresponding second terms from the commutator, we finally obtain

$$G^{ii}_{A,B}(z) = \sum_{m=m_{\min}}^{N-1} \sum_{l} \sum_{k,k'} A_{l,k'}(m) \rho^{\mathrm{red}}_{k',k}(m) B_{k,l}(m) \frac{-s}{z + E_l - E_k} \tag{3.62}$$

and

$$G^{iii}_{A,B}(z) = \sum_{m=m_{\min}}^{N-1} \sum_{l} \sum_{k,k'} B_{l,k'}(m) \rho^{\mathrm{red}}_{k',k}(m) A_{k,l}(m) \frac{1}{z + E_k - E_l}, \tag{3.63}$$

where we used

$$\langle k, e; m | A | l, e'; m \rangle = s^{n_{e'}} \delta_{e,e'} A_{k,l}(m). \tag{3.64}$$

Here $n_{e'}$ denotes the number of fermions in the environment times the total number of fermions created by A. The total phase factor for both operators A and B is given by $[s^{n_{e'}}]^2 = 1$ assuming that the operators A and $B^\dagger$ cause the same change of the particle number. The contribution $G^{ii}(z)$ describes negative and $G^{iii}(z)$ positive frequency excitations because $E_l - E_k > 0$ applies for all iterations. The reduced density matrix is given by

$$\rho^{\mathrm{red}}_{k,k'}(m) = \sum_{e} \langle k, e; m | \rho | k', e; m \rangle, \tag{3.65}$$

and has already been introduced in Eq. (3.45).
The full Green's function $G_{A,B}(z)$ is then given by

$$G_{A,B}(z) = G^{i}_{A,B}(z) + G^{ii}_{A,B}(z) + G^{iii}_{A,B}(z) \tag{3.66}$$

and computed in two steps. First, the contribution of $G^{i}_{A,B}(z)$ is calculated at the end of the final NRG iteration N. Afterwards, the NRG proceeds, similarly to the TD-NRG, with backward iterations starting from $m = N - 1$ and ending at iteration $m = m_{min}$ below which no state has been discarded. For each backward iteration the density matrix $\rho^{\mathrm{red}}_{k',k}(m)$ is computed from $\rho^{\mathrm{red}}_{k',k}(m+1)$ using the recursion relation of Eq. (3.57) and the contribution of $G^{ii}_{A,B}(z)$ and $G^{iii}_{A,B}(z)$ to the full Green's function $G_{A,B}(z)$ is calculated.

3.3.2 Broadening

With the procedure described above we only obtain a discrete spectrum that consists of delta functions $\delta(\omega \pm f_{r,s})$ at frequencies $f_{r,s} = E_r - E_s > 0$. For a comparison with the experiment we have to smooth the spectrum and replace the delta functions by a smooth distribution $P(\omega \pm f_{r,s})$. There are many option how to choose such a smooth

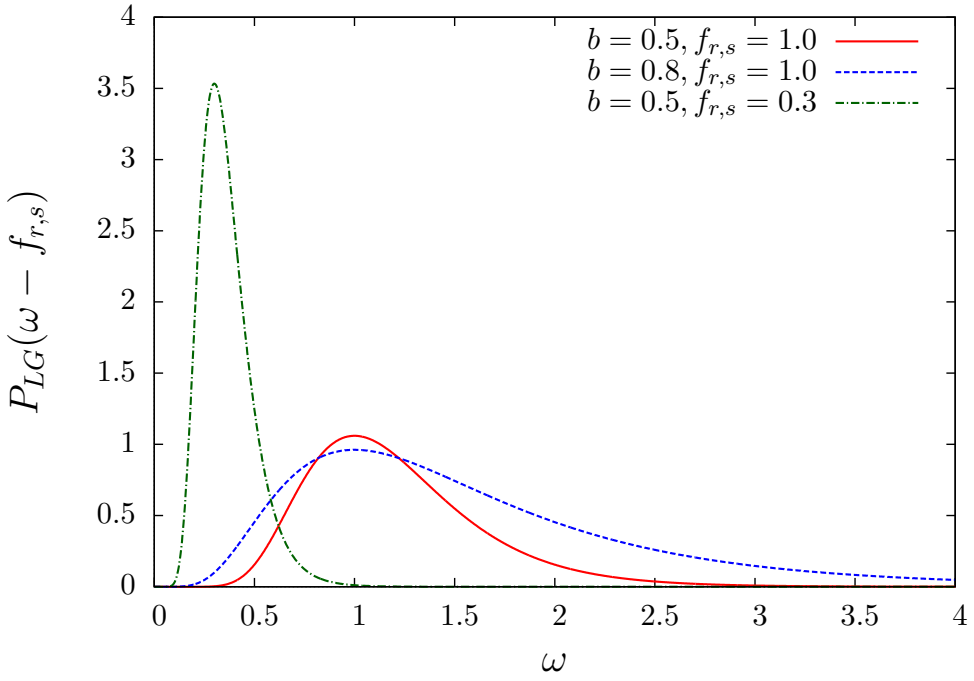

Figure 3.6: Logarithmic Gaussian $P_{LG}(\omega - f_{r,s})$ for different values of the broadening b and frequencies $f_{r,s}$.

distribution but the most frequently used [93, 96, 98] and the one we are using in the following is the logarithmic Gaussian

$$P_{LG}(\omega \pm f_{r,s}) = \frac{e^{-b^2/4}}{b f_{r,s}\sqrt{\pi}} e^{-\ln(|\omega|/f_{r,s})^2/b^2} \tag{3.67}$$

with the broadening parameter b that determines the width of the logarithmic Gaussian peak. Typical values for the broadening are $b = 0.3 - 0.8$. The logarithmic Gaussian is shown for different broadenings b and frequencies $f_{r,s}$ in Fig. 3.6. In contrast to a normal Gaussian, the logarithmic Gaussian gives little weight to low energy excitations and more weight to higher excitations. Furthermore, the broadening of P_{LG} is proportional to the energy which seems to be a better choice for a logarithmic discretization. However, the difference in using a normal Gaussian is small [80].
Due to the proportionality of the broadening to the energy, a peak of width Γ at frequency Ω is well resolved provided that $\Omega \ll \Gamma$. However, a peak at higher frequencies may be insufficiently resolved due to the low logarithmic resolution at such high frequencies. Therefore, the width and height of such a high energy peak may be captured incorrectly. An example of such high energy peaks are the resonant level peaks of a SIAM. A method how to handle this problem for a SIAM is given in the next section.

3.3.3 Self-energy of the single impurity Anderson model

In the following we will present an improvement to the calculation of the SIAM Green's function. In this approach, which was developed by Bulla *et al.* [99], the correlation part of the one-particle self-energy is calculated directly by writing this quantity as a ratio of two correlation functions. The advantages of this method are the explicitly included single-particle broadening and the accurate calculation of the self-energy. An accurate self-energy of the SIAM is particularly important for applications to dynamical mean field theory (DMFT), where the self-energy of a lattice in infinite dimensions is mapped onto an impurity self-energy [100, 101].
As described in Sec. 2.4, the Hamiltonian of the SIAM is given by

$$H = \sum_{k,\sigma} \epsilon_k c^\dagger_{k,\sigma} c_{k,\sigma} + \sum_{k,\sigma} V_k \left(d^\dagger_\sigma c_{k,\sigma} + c^\dagger_{k,\sigma} d_\sigma \right) + \sum_\sigma \epsilon_d d^\dagger_\sigma d_\sigma + U d^\dagger_\uparrow d_\uparrow d^\dagger_\downarrow d_\downarrow. \tag{3.68}$$

The final goal is to calculate the impurity Green's function $G_{d_\sigma, d^\dagger_\sigma}(z)$ which can be written in general as

$$G_{d_\sigma, d^\dagger_\sigma}(z) = \ll d_\sigma | d^\dagger_\sigma \gg (z) = \frac{1}{z - \epsilon_d - \Sigma_\sigma(z)}. \tag{3.69}$$

Here, we introduced the one-particle self-energy $\Sigma_\sigma(z)$ that includes all effects of the bath on the impurity. We now express the self-energy in terms of standard impurity correlation functions, using the equation of motion

$$z \ll A|B \gg (z) + \ll [H, A]\,|B \gg (z) = \langle [A, B]_{-s} \rangle, \tag{3.70}$$

with $[A(t), B]_{-s} = A(t)B - sBA(t)$ and $s = 1$ if both A and B are bosonic operators, while $s = -1$ for fermionic operators. The correlation functions are defined as

$$\ll A|B \gg (z) = -i \int_0^\infty \mathrm{e}^{izt} \langle [A(t), B]_{-s} \rangle \, dt. \tag{3.71}$$

Inserting $A = d_\sigma$ and $B = d^\dagger_\sigma$ into the equation of motion Eq. (3.70) yields

$$(z - \epsilon_d) G_{d_\sigma, d^\dagger_\sigma}(z) - U \ll d_\sigma d^\dagger_{\bar\sigma} d_{\bar\sigma} | d^\dagger_\sigma \gg (z) - \sum_k V_k \ll c_{k,\sigma} | d^\dagger_\sigma \gg (z) = 1, \tag{3.72}$$

with the new two-particle correlation function $\ll d_\sigma d^\dagger_{\bar\sigma} d_{\bar\sigma} | d^\dagger_\sigma \gg (z)$ and the one-particle correlation function $\ll c_{k,\sigma} | d^\dagger_\sigma \gg (z)$. The letter one can be associated with $G_{d_\sigma, d^\dagger_\sigma}(z)$ via the equation of motion Eq. (3.70) using $A = c_{k,\sigma}$ and $B = d^\dagger_\sigma$

$$(z - \epsilon_k) \ll c_{k,\sigma} | d^\dagger_\sigma \gg (z) - V_k G_{d_\sigma, d^\dagger_\sigma}(z) = 0. \tag{3.73}$$

Inserting the result of Eq. (3.73) into Eq. (3.72), we finally obtain

$$\left((z-\epsilon_d) - U\frac{F_\sigma(z)}{G_{d_\sigma,d_\sigma^\dagger}(z)} - \Delta(z)\right) G_{d_\sigma,d_\sigma^\dagger}(z) = 1, \tag{3.74}$$

where we have defined

$$F_\sigma(z) = \ll d_\sigma d_{\bar\sigma}^\dagger d_{\bar\sigma} | d_\sigma^\dagger \gg (z) \quad \text{and} \quad \Delta(z) = \sum_k \frac{V_k^2}{z-\epsilon_k}. \tag{3.75}$$

$\Delta(z)$ is a given quantity and can be calculated exactly. Its imaginary part is related to the hybridization function $\Gamma(\omega)$ of Eq. (3.3) via the equation

$$\Gamma(\omega) = -\operatorname{Im}\Delta(\omega + i0^+) = \pi \sum_k V_k^2 \delta(\omega - \epsilon_k). \tag{3.76}$$

By a comparison of Eq. (3.74) with Eq. (3.69) we obtain for the total self-energy

$$\Sigma_\sigma(z) = \Delta(z) + \Sigma_\sigma^U(z), \tag{3.77}$$

where the contribution of the Coulomb correlations to the self-energy $\Sigma_\sigma^U(z)$ is given by

$$\Sigma_\sigma^U(z) = U\frac{F_\sigma(z)}{G_{d_\sigma,d_\sigma^\dagger}(z)}. \tag{3.78}$$

The impurity Green's function is calculated in the following way: The spectral density of both correlation functions $G_{d_\sigma,d_\sigma^\dagger}(z)$ and $F_\sigma(z)$ is calculated using NRG as described above in Sec. 3.3.1. Via a Kramers-Kronig transformation the corresponding real parts of the correlation functions are obtained and the self-energy $\Sigma_\sigma(z)$ is computed using Eq. (3.77). Inserting $\Sigma_\sigma(z)$ into Eq. (3.69) finally yields the impurity Green's function and its spectral density is given by

$$\rho_{d_\sigma,d_\sigma^\dagger}(\omega) = -\frac{1}{\pi}\operatorname{Im} G_{d_\sigma,d_\sigma^\dagger}(\omega + i0^+). \tag{3.79}$$

The main advantage of using Eq. (3.69) instead of the impurity Green's function which has been directly calculated with the NRG is that the single-particle broadening $\Delta(z)$ is included exactly and thus the resolution of the high energy peaks is improved. Furthermore, Eq. (3.78) provides an accurate way for the calculation of the correlation part

of the self-energy $\Sigma_\sigma^U(z)$ which is needed in a DMFT application. An alternative and more naive approach for the calculation of $\Sigma_\sigma^U(z)$ is given by

$$\Sigma_\sigma^U(z) = z - \epsilon_d - \Delta(z) - G^{-1}_{d_\sigma, d_\sigma^\dagger}(z). \tag{3.80}$$

However, Eq. (3.78) is numerically more stable due to the division instead of the subtraction of correlation functions. Therefore, one should always use Eq. (3.78) for the calculation of the impurity self-energy.

3.4 Parameters of an effective low energy Hamiltonian

In this section we will show how to determine the parameters of an effective low energy Hamiltonian by assuming that the fixed point spectrum describes a Fermi liquid. This method was originally developed by Hewson *et al.* [102] to calculate the renormalized parameters of an effective Anderson model. However, we will modify this method and use it to calculate the effective potential scattering terms of a particle-hole asymmetric two impurity Kondo model (TIKM), where the effective low energy Hamiltonian is given by the Hamiltonian of the free-electron gas plus potential scatterings.
The main idea of this method is to calculate the Green's function of the effective Hamiltonian expressed in the form of a semi-infinite Wilson chain and treating the lowest particle and hole excitations E_p and E_h of a NRG calculation as if they were excitations of this effective low energy Hamiltonian.

3.4.1 Effective low energy Hamiltonian

As described in Sec. 2.3, the TIKM exhibits two different low temperature phases depending on the ratio between the Kondo temperature T_K and the effective spin-spin interaction between the impurity spins K_eff. For $k_\mathrm{B}T_\mathrm{K} \gg K_\mathrm{eff}$ the model is in the Kondo phase where the impurities are magnetically screened by the conduction electrons. In the case of large antiferromagnetic interactions $K_\mathrm{eff} \gg k_\mathrm{B}T_\mathrm{K}$ the model is in the decoupled singlet phase where the two impurities are locked in a singlet and decouple from the conduction band.
In both cases the effective low energy Hamiltonian of the TIKM can be related to the free-electron Hamiltonian which consists of two free Wilson chains if the conduction band is separated in conduction bands with even and odd parity. In a particle-hole asymmetric case the effective low energy Hamiltonian also exhibits potential scatter-

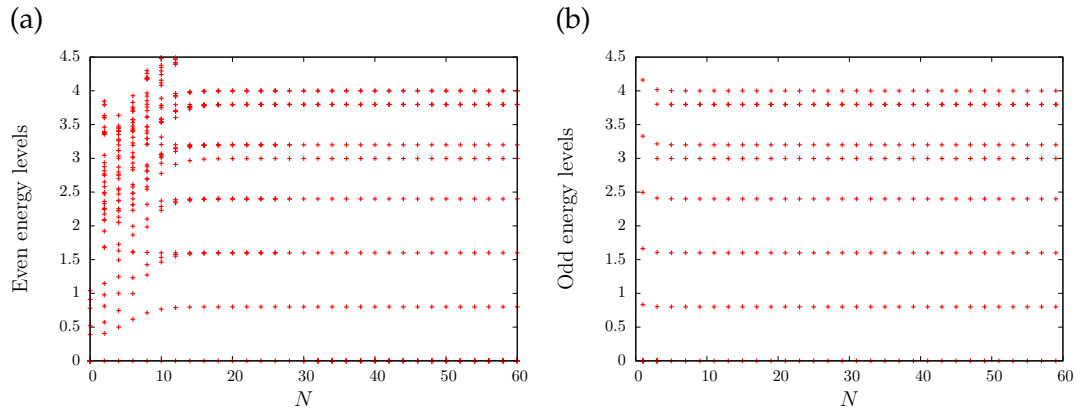

Figure 3.7: (a) The fixed point energy levels of the particle-hole symmetric TIKM in the Kondo phase at even iterations correspond to the (b) fixed point energy levels of the free-electron gas at odd iterations. The same is true for the odd iterations of the TIKM and the even iterations of the free-electron gas.
TIKM parameters: constant even and odd densities of states (DOSs), $\rho J = 0.3$, $N_o/N_e = 1$ and $K = 0D$. NRG parameters: $\Lambda = 3$ and $N_s = 2000$.

ings and thus two potential scattering terms must be added to the two free Wilson chains. The total effective low energy Hamiltonian is then given by

$$H_{0,N} = \Lambda^{(N-1)/2} \left[\sum_{\alpha=\{e,o\},\sigma} \sum_{n=0}^{N-1} t_{n,\alpha} \left(c^\dagger_{\alpha,n+1,\sigma} c_{\alpha,n,\sigma} + c^\dagger_{\alpha,n,\sigma} c_{\alpha,n+1,\sigma} \right) \right.$$
$$\left. \sum_{\alpha=\{e,o\},\sigma} \sum_{n=0}^{N} \epsilon_{n,\alpha} c^\dagger_{\alpha,n,\sigma} c_{\alpha,n,\sigma} + \sum_{\alpha=\{e,o\},\sigma} \tilde{V}_\alpha c^\dagger_{\alpha,0,\sigma} c_{\alpha,0,\sigma} \right]. \tag{3.81}$$

with the hopping elements $t_{n,\alpha}$ and onsite energies $\epsilon_{n,\alpha}$ introduced in Sec. 3.1.3.
The potential scatterings $\sum_{\alpha=\{e,o\},\sigma} \tilde{V}_\alpha c^\dagger_{\alpha,0,\sigma} c_{\alpha,0,\sigma}$ are the only terms that might additionally appear in the effective Hamiltonian. Since the TIKM is invariant under the exchange of the impurity spins $\vec{S}_1 \leftrightarrow \vec{S}_2$, all combinations that mix even and odd sites like $c^\dagger_{e/o,i,\sigma} c_{o/e,i,\sigma}$ are excluded because they break the parity symmetry. Furthermore, the combinations $c^\dagger_{\alpha,0,\sigma} c_{\alpha,0,\sigma}$ with $\alpha = \{e,o\}$ are the only that yield marginal contributions since $c_{\alpha,0,\sigma} \propto \Lambda^{-(N-1)/4}$ [26, 27, 53]. All other combinations that include operators of Wilson sites $i > 0$ only lead to irrelevant contributions because with increasing N they are decreasing even faster than $c_{\alpha,0,\sigma}$, e.g. $c_{\alpha,1,\sigma} \propto \Lambda^{-3(N-1)4}$.
For the decoupled singlet phase, where no Kondo effect occurs, the impurity spins form a singlet, the Kondo coupling is renormalized to zero $J \to 0$ and hence the impurity spins decouple from the conduction band. The fixed point spectrum in this phase is, therefore, given by the spectrum of the free-electron Hamiltonian plus potential scatterings which is described by the Hamiltonian $H_{0,N}$.
In the Kondo phase the coupling is renormalized to $J \to \infty$ and the impurity spins are screened by conduction electrons. As shown in figure Fig. 3.7a and b in this phase the

fixed point spectrum of the even iterations of the particle-hole symmetric TIKM corresponds exactly to the fixed point spectrum of the free-electron Hamiltonian at odd iterations. The same applies for the odd iterations of the TIKM and the even iterations of the free-electron Hamiltonian. This can be explained by the fact that the electrons that screen the two impurity spins are locked into a singlet with these impurity spins and therefore each chain has one free electron less. Hence, the fixed point spectrum at iteration N can be described by the free-electron Hamiltonian at iteration $N-1$. As before, in the particle-hole asymmetric case potential scatterings have to be added to the free-electron Hamiltonian. Therefore, the fixed point spectrum of the particle-hole asymmetric TIKM in the Kondo phase at iteration N can be described by $H_{0,N-1}$.

3.4.2 Algorithm

With the equation of motion technique of Eq. (3.70) one can calculate the Green's function of the zeroth Wilson site $i = 0$ which is given by

$$G_{00,\alpha}(\omega) = \frac{1}{\omega - \tilde{V}_\alpha \Lambda^{(N-1)/2} - \epsilon_{0,\alpha}\Lambda^{(N-1)/2} - \Lambda^{(N-1)} t_{0,\alpha}^2 g_{11,\alpha}(\omega)}, \tag{3.82}$$

where $g_{11,\alpha}(\omega)$ is the Green's function of site $i = 1$ described by the Hamiltonian $H_{1,N}$. Here $H_{i,N}$ is the part of the effective low energy Hamiltonian of Eq. (3.81) without the potential scatterings and the Wilson chains are starting at sites i rather than at the sites 0. The Green's function $g_{11,\alpha}(\omega)$ is given by

$$g_{11,\alpha}(\omega) = \frac{1}{\omega - \epsilon_{1,\alpha}\Lambda^{(N-1)/2} - \Lambda^{(N-1)} t_{1,\alpha}^2 g_{22,\alpha}(\omega)}, \tag{3.83}$$

with $g_{22,\alpha}(\omega)$ the Green's function of site $i = 2$ described by the Hamiltonian $H_{2,N}$. An extension of this procedure can be used to calculate $g_{11,\alpha}(\omega)$ in the form of a continued fraction. The one-particle excitations E_α of chain α are given by the poles of the Green's function in (3.82)

$$E_\alpha - \tilde{V}_\alpha \Lambda^{(N-1)/2} - \epsilon_{0,\alpha}\Lambda^{(N-1)/2} - \Lambda^{(N-1)} t_{0,\alpha}^2 g_{11,\alpha}(E_\alpha) = 0. \tag{3.84}$$

If $E^0_{p,\alpha}(N)$ and $E^0_{h,\alpha}(N)$ are the lowest particle and hole excitations of the corresponding chain α from the ground state of the Hamiltonian $H_{0,N}$, then the effective potential scattering $\tilde{V}_\alpha$ is given by

$$\tilde{V}_\alpha = \lim_{N\to\infty} \Lambda^{-(N-1)/2} E^0_{p,\alpha}(N) - \epsilon_{0,\alpha} - \Lambda^{(N-1)/2} t_{0,\alpha}^2 g_{11,\alpha}(E^0_{p,\alpha}(N)) \tag{3.85}$$

$$= \lim_{N\to\infty} -\Lambda^{-(N-1)/2} E^0_{h,\alpha}(N) - \epsilon_{0,\alpha} - \Lambda^{(N-1)/2} t_{0,\alpha}^2 g_{11,\alpha}(-E^0_{h,\alpha}(N)). \tag{3.86}$$

In the limit of $N \to \infty$, which means at low temperatures, when the model can be described by the effective Hamiltonian of Eq. (3.81), the obtained effective potential scattering $\tilde{V}_\alpha$ should not only be converged and hence be independent of N but also both excitations, particle and hole, should yield the same effective $\tilde{V}_\alpha$.
The Green's function $g_{11,\alpha}(E^0_{p,\alpha}(N))$ is calculated iteratively using the form of a continued fraction of Eq. (3.83). The iteration starts with the calculation of Green's function of the last site $g_{NN,\alpha}(E^0_{p,\alpha}(N)) = 1/(E^0_{p,\alpha}(N) - \epsilon_{N,\alpha}\Lambda^{(N-1)/2})$ and inserts this result into the corresponding form of Eq. (3.83) for $g_{N-1N-1,\alpha}(E^0_{p,\alpha}(N))$. Afterwards this result is inserted in $g_{N-2N-2,\alpha}(E^0_{p,\alpha}(N))$. This procedure can be continued until $g_{11,\alpha}(E^0_{p,\alpha}(N))$ is reached.
To measure the potential scattering in the Kondo phase the same algorithm as described above is used. However, since in this case the Wilson chains in the effective low energy Hamiltonian have one chain site less, the calculation of the Green's function $g_{11,\alpha}(E^0_{p,\alpha}(N))$ slightly changes. This time the iteration to compute the Green's function $g_{11,\alpha}(E^0_{p,\alpha}(N))$ starts with $g_{N-1N-1,\alpha}(E^0_{p,\alpha}(N)) = 1/(\sqrt{\Lambda}E^0_{p,\alpha}(N) - \epsilon_{N-1,\alpha}\Lambda^{(N-1)/2})$ rather than with $g_{NN,\alpha}(E^0_{p,\alpha}(N))$. The factor $\sqrt{\Lambda}$ needs to be added so that the energies of the last iteration N are on the energy scales of the Wilson sites $N-1$. The effective potential scatterings obtained from this method will be marked with an index K, e.g. $\tilde{V}_{\alpha,K}$, to distinguish them from the potential scatterings obtained from the full chain.

3.4.3 Benchmark calculations

In Fig. 3.8a a benchmark calculation of a free electron gas for constant even and odd DOSs and with initial potential scatterings $V_e = 0.2D$ and $V_o = -0.1D$ is shown. The measured effective potential scatterings $\tilde{V}_e$ and $\tilde{V}_o$ coincide with the input parameters V_e and V_o for every iteration which must be the case since this model is exactly described by the Hamiltonian of Eq. (3.81) for every iteration N.
In the following $\tilde{V}_{e,(K)}$ and $\tilde{V}_{o,(K)}$ always denote the measured effective potential scatterings of the last iteration where they have already been converged and are independent of the iteration N.
Figure 3.8b shows the measured effective potential scatterings of a TIKM for constant DOSs, $N_o/N_e = 1$ and with initial potential scatterings $V_e = 0.2D$ and $V_o = -0.1D$. The Hamiltonian of such a system is given by

$$H_{\text{TIKM+pot}} = H_{\text{TIKM}} + \sum_\sigma \left[V_e c^\dagger_{e,0,\sigma} c_{e,0,\sigma} + V_o c^\dagger_{o,0,\sigma} c_{o,0,\sigma} \right] \tag{3.87}$$

where H_{TIKM} is the Hamiltonian (2.12) of the TIKM and $c_{e/o,0,\sigma}$ the operator that creates an electron on the zeroth site of the even/odd Wilson chain. The measured scattering terms $\tilde{V}_e$ and $\tilde{V}_o$ are plotted against the coupling ρJ for different antiferromagnetic direct impurity spin-spin interactions K. These large antiferromagnetic K ensure that the

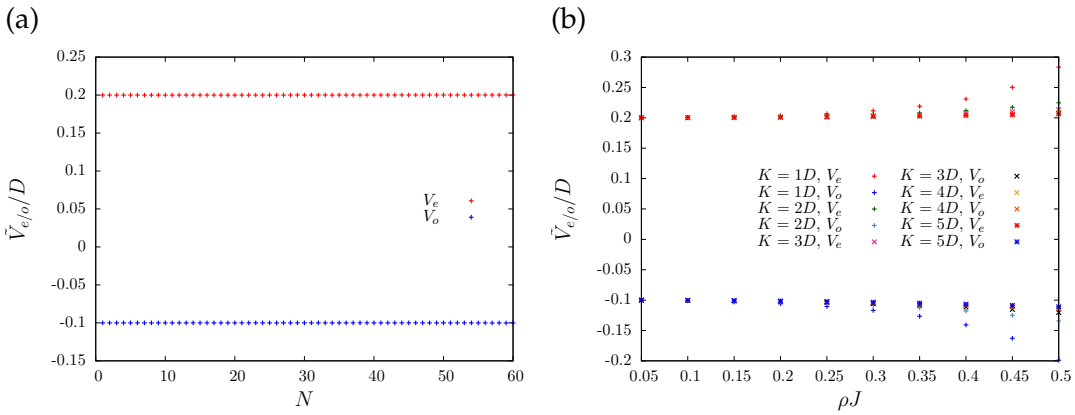

Figure 3.8: Benchmark calculations: (a) A free electron gas for constant even and odd DOSs and with potential scatterings $V_e = 0.2D$ and $V_o = -0.1D$. The measured effective potential scatterings $\tilde{V}_e$ and $\tilde{V}_o$ coincide with input parameters for every iteration. (b) The measured potential scatterings of a TIKM for constant DOSs, $N_o/N_e = 1$ and with potential scatterings $V_e = 0.2D$ and $V_o = -0.1D$ plotted against the coupling ρJ for different large antiferromagnetic direct impurity spin-spin interactions K. For small couplings ρJ the measured scatterings coincide with the input parameters but with increasing ρJ they are renormalized to larger values. This effect of renormalization is stronger for smaller K.
NRG parameters: $\Lambda = 3$, $N_s = 2000$ and $N = 60$.

decoupled singlet is the ground state and, therefore, the effective low energy Hamiltonian at iteration N is given by $H_{0,N}$ where both chains have the full length of N sites. For small couplings ρJ the measured scatterings coincide with the input potential scatterings V_e and V_o. With increasing ρJ the absolute values of the effective potential scatterings grow since the input potential scatterings are renormalized to larger values. However, the effect of renormalization becomes weaker for larger K. The reason for this is that with increasing K the impurity spins form a singlet at higher temperatures and hence decouple earlier from the chain which leads to a cutoff of the renormalization. Therefore, for a large K the potential scatterings are almost not renormalized even for large ρJ.

Figure 3.9a shows the measured effective potential scatterings $\tilde{V}_{e,K}$ and $\tilde{V}_{o,K}$ of a TIKM in the Kondo phase for constant DOSs, $N_o/N_e = 1$ and with potential scatterings $V_e = 0.2D$ and $V_o = -0.1D$ plotted against the coupling ρJ for different large ferromagnetic interactions K. The ferromagnetic interactions ensure that the model is in the Kondo phase at low temperatures. As before, for small couplings ρJ the measured potential scatterings coincide with the input parameters. This time, however, with increasing ρJ the potential scatterings are renormalized to smaller values. As in the decoupled singlet phase the effect of renormalization becomes weaker for larger ferromagnetic interactions K. This is caused by the fact that for larger ferromagnetic interactions between the impurity spins the effective coupling J_{eff} to the conduction band decreases [103] since the second part of the interaction between the impurity

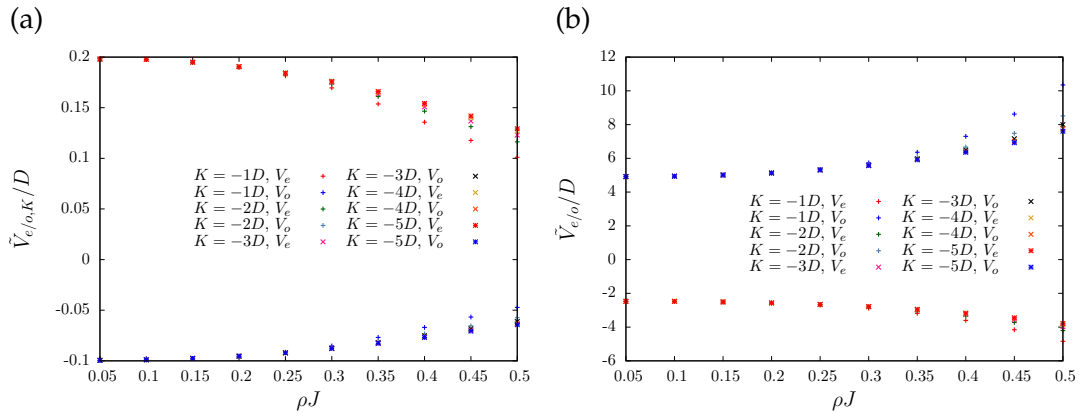

Figure 3.9: Benchmark calculation: a) The measured potential scatterings $\tilde{V}_{e,K}$ and $\tilde{V}_{o,K}$ of a TIKM in the Kondo phase for constant DOSs, $N_o/N_e = 1$ and with potential scatterings $V_e = 0.2D$ and $V_o = -0.1D$ plotted against the coupling ρJ for different large ferromagnetic direct impurity spin-spin interactions K. With increasing ρJ the potential scatterings are renormalized to smaller values. This effect is stronger for smaller K. b) The measured potential scatterings $\tilde{V}_e$ and $\tilde{V}_o$ for the same model. Using $\tilde{V}_e$ and $\tilde{V}_o$ in the Kondo phase yields potential scatterings that do not agree with the input parameters $V_e = 0.2D$ and $V_o = -0.1D$. NRG parameters: $\Lambda = 3$, $N_s = 2000$ and $N = 100$.

spins and the conduction bands in Eq. (2.14), which is proportional to $\propto (\vec{S}_1 - \vec{S}_2)$, is suppressed leading to the weaker renormalization.

For comparison Fig. 3.9b shows the measured effective potential scatterings for the Wilson chains of the full length $\tilde{V}_e$ and $\tilde{V}_o$ for the same TIKM. The absolute values of the measured scatterings are much larger than the input parameters $V_e = 0.2D$ and $V_o = -0.1D$ and even start growing with increasing coupling ρJ. This demonstrates that one really needs to distinguish the two phases and take the different chain lengths in the effective low energy Hamiltonians seriously. Therefore, one has to use $\tilde{V}_{e/o}$ in the decoupled singlet phase and $\tilde{V}_{e/o,K}$ in the Kondo phase in order to get reliable estimates for the potential scatterings.

The appendix A of Ref. [27] derives a connection between $\tilde{V}_\alpha$ and $\tilde{V}_{\alpha,K}$ for constant DOSs which is given by[3]

$$\tilde{V}_{\alpha,K}(\tilde{V}_\alpha) = -\frac{1}{\pi}\frac{\ln(\Lambda)}{1-\Lambda^{-1}}\frac{1}{\tilde{V}_\alpha}. \tag{3.88}$$

Note that the potential scatterings occurring in (3.88) are measured in units of the band width D and are, hence, dimensionless. Figure 3.10a shows a comparison between the

[3] In the appendix A of Ref. [27] an additional factor 2 occurs in the formula. However, different benchmark calculations for the free-electron gas with various discretization parameters Λ have shown that this factor 2 yields results in which the measured scatterings are twice as large as the input scatterings. The reason for the difference is not clear since all relevant definitions in this work and in [27] seem to be equal.

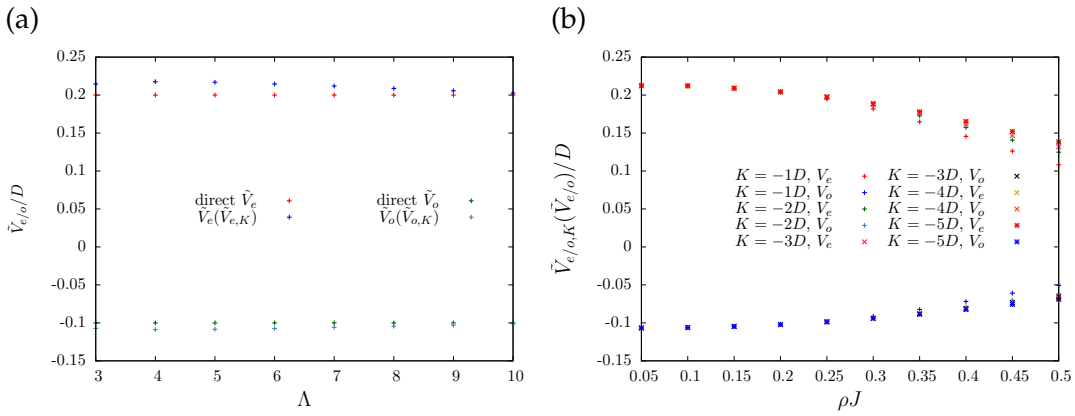

Figure 3.10: Benchmark calculation: a) A comparison between the directly measured $\tilde{V}_{e/o}$ and the calculated $\tilde{V}_{e/o}(\tilde{V}_{e/o,K})$ for the free-electron gas with potential scatterings $V_e = 0.2$ and $V_o = -0.1$ plotted against the discretization parameter Λ. The absolute value of the calculated $\tilde{V}_{e/o}(\tilde{V}_{e/o,K})$ is slightly larger than the directly measured $\tilde{V}_{e/o}$. b) The measured scatterings $\tilde{V}_\alpha$ of Fig. 3.9b are used to calculate the effective potential scatterings of the TIKM in the Kondo phase. NRG parameters: $\Lambda = 3$ and $N_s = 2000$.

directly measured $\tilde{V}_{e/o}$ and the calculated $\tilde{V}_{e/o}(\tilde{V}_{e/o,K})$ for the free-electron gas with initial potential scatterings $V_e = 0.2$ and $V_o = -0.1$ for different discretization parameters Λ. $\tilde{V}_{e/o}(\tilde{V}_{e/o,K})$ denotes the potential scattering calculated with Eq. (3.88) for the decoupled singlet phase where the measured $\tilde{V}_{e/o,K}$ was used as an input parameter. The absolute values of the calculated $\tilde{V}_{e/o}(\tilde{V}_{e/o,K})$ are slightly larger than the directly measured $\tilde{V}_{e/o}$ and the input parameters. The difference between $\tilde{V}_{e/o}$ and $\tilde{V}_{e/o}(\tilde{V}_{e/o,K})$, however, is always smaller than 7%. In Fig. 3.10b the measured scatterings $\tilde{V}_{e/o}$ of Fig. 3.9b are used to calculate the effective potential scatterings of the TIKM in the Kondo phase. A comparison with Fig. 3.9a shows that the absolute value of the calculated $\tilde{V}_{\alpha,K}(\tilde{V}_\alpha)$ are only slightly larger than the directly measured $\tilde{V}_{\alpha,K}$.

Therefore, for constant DOSs we can in principle either use the directly measured $\tilde{V}_{\alpha,K}$ or the calculated $\tilde{V}_{\alpha,K}(\tilde{V}_\alpha)$ to determine the effective scattering of the TIKM in the Kondo phase. However, we will always use the directly measured potential scatterings, namely $\tilde{V}_{\alpha,K}$ in the Kondo phase and $\tilde{V}_\alpha$ in the decoupled singlet phase.

The method outlined above will be used to determine the automatically generated effective potential scattering terms of an energy dependent particle-hole asymmetric TIKM in order to find corresponding counter potential scatterings which make the model particle-hole symmetric again. However, as can already been seen in the benchmark calculation above, even if one uses $\tilde{V}_{e/o}$ in the decoupled singlet and $\tilde{V}_{e/o,K}$ in the Kondo phase, the renormalization may lead to completely different potential scatterings than the original input parameters V_e and V_o. Therefore, in general it will not be possible to simply set $V_e = -\tilde{V}_{e(,K)}$ and $V_o = -\tilde{V}_{o(,K)}$ to make the model particle-hole symmetric again.

Chapter 4

Spatial and temporal propagation of Kondo correlations

While the equilibrium properties of the Kondo problem were studied over the last decades and are now theoretically well understood by virtue of Wilson's numerical renormalization group (NRG), cf. Sec. 3.1, and the exact Bethe-ansatz solution [104], its nonequilibrium properties are subject to recent and active research [87, 88, 105–115]. In this chapter we investigate the fundamental question how spatial Kondo correlations are building up in time when the impurity spin $\vec{S}_{\mathrm{imp}}$ is initially decoupled from the conduction band using the time-dependent numerical renormalization group (TD-NRG) which has been introduced in Sec. 3.2. For this purpose we examine the time-dependent spin correlation function $\chi(\vec{r},t) = \langle \vec{S}_{\mathrm{imp}} \vec{s}(\vec{r}) \rangle(t)$ in the Kondo model. The correlation function $\chi(\vec{r},t)$ vanishes for times $t < 0$ since the impurity spin and the conduction electron spin density are initially uncorrelated. Therefore, we can use it to measure the buildup of entanglement between the impurity spin and the spin density at distance $R = |\vec{r}|$.

The equilibrium spatial correlation function $\chi_\infty(\vec{r}) = \lim_{t\to\infty} \chi(\vec{r},t)$ of the Kondo model must be recovered for infinitely long times. This correlation function has been investigated by Affleck and co-workers [116–119] using field theoretical methods. However, the field theory yields results that are only valid for distances $R \ll \xi_{\mathrm{K}}$ or $R \gg \xi_{\mathrm{K}}$ and lacks the possibility to determine the correlation function for intermediate values $R \approx \xi_{\mathrm{K}}$. Here $\xi_{\mathrm{K}} = v_{\mathrm{F}}/T_{\mathrm{K}}$ is the characteristic length scale at which the crossover between different power-law decays in $\chi_\infty(\vec{r})$ occurs [47, 120–122], where v_{F} denotes the Fermi velocity and T_{K} the Kondo temperature. A standard interpretation of the so-called Kondo length scale ξ_{K} is that the impurity spin is screened by a surrounding cloud of conduction electrons with a spatial extent of ξ_{K} [116–119, 123]. Furthermore, the equilibrium correlation function $\chi_\infty(\vec{r})$ has also been recently investigated using a real-space density matrix renormalization group (DMRG) [120]. Therefore, the two reference points $t = 0$ and $t = \infty$ are known and can be compared with our calculations.

Borda was the first who calculated the equilibrium spatial correlation function for the Kondo model using the NRG [47]. He has realized that the mapping that was used to

calculate the two-impurity Kondo model with the NRG [61, 62, 64] can also be used to calculate $\chi_\infty(\vec{r})$, where the second impurity spin has to be removed and the spin density $s(\vec{r})$ at distance R is introduced to probe the spatial correlations. In this approach the calculation of spatial correlations becomes accessible by mapping the problem onto two $\vec{r}$-dependent linear combinations of conduction electrons, one with even and one with odd symmetry under spatial inversion around the midpoint $\vec{r}/2$. For each distance R a single two-band NRG run is required and, therefore, the numerical effort to calculate the R-dependent correlation function is high.

In the following, we will present an improved mapping compared to the one of Borda. With our modifications we are able to (i) accurately reproduce the analytically known sum rules [47, 116, 123] for the spin-correlation function at least in one dimension, (ii) reproduce the analytical spin-spin correlation function of the decoupled Fermi sea, and (iii) obtain sign changes in $\chi_\infty(\vec{r})$ at short and intermediate distances which are expected for RKKY mediated correlations and have also been observed recently in DMRG calculations [115]. In contrast, Borda reports [47] that the correlation function $\chi_\infty(\vec{r})$ is negative for all distances R and couplings J. We observe oscillating and power-law decaying $\chi_\infty(\vec{r}) < 0$ only for distances $R \gg \xi_\mathrm{K}$ which is in accordance with previous analytical 1D field theory predictions [47, 116]. Since for distances $R \ll \xi_\mathrm{K}$ the Kondo screening is incomplete, alternating signs can be found in $\chi_\infty(\vec{r})$. However, we are not able to tell the exact differences of our mapping to the one in [47] because Borda does not provide a detailed derivation of his mapping.

For the nonequilibrium correlation function $\chi(\vec{r}, t)$ we find for an antiferromagnetic coupling $J > 0$ that, as a consequence of spin conservation, a ferromagnetic correlation propagates with the Fermi velocity v_F away from the impurity. In addition to the correlations inside the light cone, also finite and nonexponential correlations outside of the light cone are observed. We are able to trace the origin of these correlations outside of the light cone back to the intrinsic entanglement of the Fermi sea by using a second-order expansion in the coupling J and comparing the perturbative results with TD-NRG results. Since $\chi(\vec{r}, t)$ is not a response function, nonexponential contributions outside the light cone are allowed.

The TD-NRG and perturbation theory results agree remarkably well for short and intermediate time and length scales. However, for large distances $R \geq \xi_\mathrm{K}$ the perturbation theory fails to capture the Kondo effect and, therefore, yields incorrect power-law decays for the long-time limit of $\chi(\vec{r}, t)$.

Our data confirm the recent findings by Medvedyeva *et al.* [114] and their suggestion that the correlations outside the light cone originate from the intrinsic entanglement of the Fermi sea. However, we considerably extend their work: we include the full spatial dependence that allows us to access the full $2k_\mathrm{F}$ oscillations inherent to the RKKY mediated correlations. Furthermore, with the NRG we are able to capture the crossover between short and long distance behaviour, including the Kondo physics at low tem-

peratures.
We also discuss the spectral functions of the retarded spin-spin susceptibility as a function of R and use these results to calculate the linear response of the host spin density at a distance R to a local magnetic field applied to the impurity. Any real response must vanish outside of the light cone in accordance with relativity if the momentum cutoff is sent to infinity [114]. However, for a finite momentum cutoff, as we use in the NRG, this statement is weakened to a fast decay on the length of the inverse momentum cutoff. Therefore, we find an algebraic decay and a suppression of the response outside of the light cone. The calculations of the NRG spectral functions are benchmarked with the retarded spin susceptibility of the host without impurity for which the susceptibility can be calculated analytically. We find that the analytically calculated susceptibility agrees only for short distances with the NRG susceptibility since the NRG cannot capture high energy oscillations that occur for larger distances. Therefore, the results for the real response are restricted to small distances where the NRG yields reliable results.
This chapter is organized as follows: At first, we derive the mapping to the two-impurity model and discuss the sum rules for the spatial correlation function in Sec. 4.1. In Sec. 4.2 we present the results of our equilibrium NRG calculations for different dimensions and compare them to the data of Borda [47]. The nonequilibrium data obtained from the TD-NRG and the results of the second-order perturbative calculations are presented in Sec. 4.3. Afterwards, the results for the retarded spin-spin susceptibility and the response function are discussed in Sec. 4.4. At the end we conclude with a summary in Sec. 4.5.
Most of the following results and figures in this chapter have already been published in [124]. In the following, we recapitulate these results and augment them.

4.1 Theory

4.1.1 The Hamiltonian and the spin density

If the spin density $\vec{s}(\vec{r})$ is expanded in plane waves [15], it is given by

$$\vec{s}(\vec{r}) = \frac{1}{2}\frac{1}{NV_u}\sum_{\sigma\sigma'}\sum_{\vec{k}\vec{k}'} c^\dagger_{\vec{k}\sigma}\vec{\sigma}_{\sigma\sigma'}c_{\vec{k}'\sigma'}e^{i(\vec{k}'-\vec{k})\vec{r}}, \tag{4.1}$$

where N is the number of unit cells in the volume V, $V_u = V/N$ is the volume of such a unit cell, $\vec{k}$ a momentum vector and $\vec{\sigma}$ a vector of the Pauli matrices. The Kondo Hamiltonian in energy representation can be written as

$$\begin{aligned} H =& H_0 + H_K, \\ H_0 =& \sum_\sigma \int_{-D}^{D} d\epsilon\, \epsilon\, c^\dagger_{\epsilon\sigma} c_{\epsilon\sigma}, \\ H_K =& J \vec{S}_{\text{imp}} \vec{s}_c(0). \end{aligned} \tag{4.2}$$

H_K describes how a local impurity spin located at the origin couples via an effective Heisenberg coupling J to the unit-cell volume averaged conduction electron spin $\vec{s}_c(\vec{r}) = V_u \vec{s}(\vec{r})$ and H_0 accounts for the energy of the free conduction electrons. For a more detailed discussion of the Kondo model see Sec. 2.2.

While Wilson's original approach of the NRG was intended to calculate only the properties of the impurity and those of the conduction band close to the impurity, we are explicitly interested in the spatial correlation function $\langle \vec{S}_{\text{imp}} \vec{s}(\vec{r}) \rangle$ which only depends on the distance $R = |\vec{r}|$ if the system is rotationally invariant.

Borda [47] was the first who realized that the calculation of the spatial correlations is related to a simplified two impurity Kondo model (TIKM). He has used the same mapping originally Jones *et al.* [61, 62] have used to extend the NRG to the TIKM with one impurity spin at the position $\vec{R}_+ = +\vec{r}/2$ and the other at $\vec{R}_- = -\vec{r}/2$. In the following we will give a brief overview of this mapping, a more detailed derivation can be found in appendix A.

In this approach the spatial dependence is included into two nonothogonal energy dependent field operators

$$c_{\epsilon\sigma,\pm} = \frac{1}{\sqrt{N\rho(\epsilon)}} \sum_{\vec{k}} \delta(\epsilon - \epsilon_{\vec{k}}) c_{\vec{k}\sigma} e^{\pm i\vec{k}\vec{r}/2}, \tag{4.3}$$

which are combined to even (e) and odd (o) parity eigenstates

$$\begin{aligned} c_{\epsilon\sigma,e} =& \frac{1}{N_e(\epsilon)} \left(c_{\epsilon\sigma,+} + c_{\epsilon\sigma,-} \right), \\ c_{\epsilon\sigma,o} =& \frac{1}{N_o(\epsilon)} \left(c_{\epsilon\sigma,+} - c_{\epsilon\sigma,-} \right), \end{aligned} \tag{4.4}$$

with the dimensionless normalization functions

$$\begin{aligned} N_e^2(\epsilon) =& \frac{4}{N\rho(\epsilon)} \sum_{\vec{k}} \delta(\epsilon - \epsilon_{\vec{k}}) \cos^2\left(\frac{\vec{k}\vec{r}}{2}\right), \\ N_o^2(\epsilon) =& \frac{4}{N\rho(\epsilon)} \sum_{\vec{k}} \delta(\epsilon - \epsilon_{\vec{k}}) \sin^2\left(\frac{\vec{k}\vec{r}}{2}\right). \end{aligned} \tag{4.5}$$

Here $\rho(\epsilon)$ denotes the density of states (DOS) of the original conduction band. The normalization functions $N_{e/o}(\epsilon)$ are chosen such that the anti-commutator relation $\{c_{\epsilon\sigma,\alpha}, c^\dagger_{\epsilon'\sigma',\alpha'}\} = \delta(\epsilon-\epsilon')\delta_{\alpha\alpha'}\delta_{\sigma\sigma'}$ is fulfilled. Note that both functions $N_e(\epsilon)$ and $N_o(\epsilon)$ depend on the distance $R = |\vec{r}|$ and are not normalized.
The TIKM can be written in terms of these even and odd fields and solved using the NRG. If we omit the impurity spin at postion $\vec{R}_-$, the original Kondo model Hamiltonian of Eq. (4.2) with the impurity spin the position $\vec{R}_+$ is recovered. We can then use $\vec{s}(\vec{R}_-)$ to probe the spin density at a distance R from the impurity.
The local even or odd parity conduction electron operator coupling to the impurity spin takes the form

$$f_{0\sigma,e(o)} = \frac{1}{\bar{N}_{e(o)}} \int d\epsilon \, \sqrt{\rho(\epsilon)} N_{e(o)}(\epsilon) c_{\epsilon\sigma,e(o)}. \tag{4.6}$$

The normalization constants

$$\bar{N}_{e(o)} = \sqrt{\int d\epsilon \, N^2_{e(o)}(\epsilon)\rho(\epsilon)} \tag{4.7}$$

are determined by the anticommutator $\{f_{0\sigma,e(o)}, f^\dagger_{0\sigma',e(o)}\} = \delta_{\sigma,\sigma'}$ and depend on the distance R. These constants also enter the definition of the effective parity DOS

$$\rho_{e(o)}(\epsilon) = \frac{1}{\bar{N}^2_{e(o)}} N^2_{e(o)}(\epsilon)\rho(\epsilon). \tag{4.8}$$

These DOSs contain the spatial information and are used to construct the NRG tight-binding chains, cf. Eq. (3.4).
Positioning the impurity spin at $\vec{R}_+$ and expanding the original Kondo Hamiltonian of Eq. (4.2) in these orthogonal even and odd fields yields

$$\begin{aligned} H = &\sum_\sigma \sum_{\alpha=e,o} \int_D^D d\epsilon \, \epsilon c^\dagger_{\epsilon\sigma,\alpha} c_{\epsilon\sigma,\alpha} \\ &+ \frac{J}{8} \sum_{\sigma\sigma'} \left(\bar{N}_e f^\dagger_{0\sigma,e} + \bar{N}_o f^\dagger_{0\sigma,o}\right) \vec{\sigma}_{\sigma\sigma'} \left(\bar{N}_e f_{0\sigma,e} + \bar{N}_o f_{0\sigma,o}\right). \end{aligned} \tag{4.9}$$

The spin density $\vec{s}(\vec{R}_-)$ at position $\vec{R}_-$ entering the spatial spin-spin correlation function is then given by

$$\vec{s}(\vec{R}_-) = \frac{1}{8V_u} \sum_{\sigma\sigma'} \left(\bar{N}_e f^\dagger_{0\sigma,e} - \bar{N}_o f^\dagger_{0\sigma,o}\right) \vec{\sigma}_{\sigma\sigma'} \left(\bar{N}_e f_{0\sigma,e} - \bar{N}_o f_{0\sigma,o}\right), \tag{4.10}$$

where V_u accounts for its dimensions.
Note that the inclusion of the proper R-dependent normalization constants $\bar{N}_e$ and $\bar{N}_o$

into the Hamiltonian (4.9) and the spin density operator of Eq. (4.10) is crucial for recovering the exact sum rules that are discussed in the following section.

4.1.2 Sum rules of the spatial correlation function

The quality of our calculated spartial correlation function can be verified by exact sum rules at zero temperature $T = 0$. For an antiferromagnetic coupling $J > 0$, the Hamiltonian approaches the strong coupling (SC) fixed point at low temperatures and the ground state $|0\rangle$ is a singlet. Therefore, the application of the total spin operator $\vec{S}_{\text{tot}}$ comprising the impurity spin and the total conduction electron spin

$$\vec{S}_{\text{tot}}|0\rangle = \left(\vec{S}_{\text{imp}} + \int \vec{s}(\vec{r})\, d^D r\right)|0\rangle = 0 \tag{4.11}$$

must vanish. Consequently, the correlator $\langle 0|\vec{S}_{\text{imp}}\vec{S}_{\text{tot}}|0\rangle$ also vanishes

$$\langle 0|\vec{S}_{\text{imp}}\vec{S}_{\text{tot}}|0\rangle = \frac{3}{4} + \int \langle 0|\vec{S}_{\text{imp}}\vec{s}(\vec{r})|0\rangle\, d^D r = 0, \tag{4.12}$$

where we have used $\langle 0|\vec{S}_{\text{imp}}\vec{S}_{\text{imp}}|0\rangle = \frac{3}{4}$. Hence, $\chi_\infty(\vec{r})$ must obey the sum rule

$$\int \chi_\infty(\vec{r})\, d^D r = \int \langle \vec{S}_{\text{imp}}\vec{s}(\vec{r})\rangle\, d^D r = -\frac{3}{4} \tag{4.13}$$

at $T = 0$. For a generic system the spin-spin correlation function is isotropic and the angular integration can be performed analytically. Substituting the dimensionless variable $x = k_{\text{F}}R/\pi$ and integrating over the angles yields

$$\frac{C_D \pi^D}{k_{\text{F}}^D} \int_0^\infty x^{D-1}\chi_\infty(x)\, dx = -\frac{3}{4}, \tag{4.14}$$

where D is the dimension, $C_1 = 2$, $C_2 = 2\pi$ and $C_3 = 4\pi$.
In the case of a linear dispersion $\epsilon(|\vec{k}|) = v_{\text{F}}(|\vec{k}| - k_{\text{F}})$ the Fermi wave vector in different dimensions is given by $k_{\text{F}} = \pi/(2V_u)$ in 1D, $k_{\text{F}} = \sqrt{\pi/V_u}$ in 2D and $k_{\text{F}} = (\pi^2/V_u)^{1/3}$ in 3D. Note that the volume of a unit cell V_u in the Fermi wave vector cancels the factor $1/V_u$ in the spin density $\vec{s}(x)$ of Eq. (4.10).
Using the NRG to evaluate the sum rule (4.14), we are able to confirm the theoretical value of $-\frac{3}{4}$ with an error of less than 2% in 1D. In higher dimensions it is more complicated to confirm the sum rule. Since $\chi_\infty(R) \propto R^{-(D+1)}$ for $R \to \infty$, the integral kernel $R^{D-1}\chi_\infty(R)$ is very susceptible to numerical errors in higher dimensions, which leads to a decreasing of the accuracy with increasing dimension. Therefore, to prevent the integral $\int_0^\infty R^{D-1}\chi_\infty(R)\, dR$ from diverging, a very high number of kept states in the NRG is needed.
In the case of a ferromagnetic coupling $J < 0$, the Hamiltonian approaches the local

moment (LM) fixed point with a decoupled impurity spin. For the local moment fixed point the effective magnetic moment of the impurity is given by $\vec{\mu}^2_{\text{eff}} = \frac{3}{4}$ [26, 27], cf. Sec. 2.4. In the NRG the effective magnetic moment $\vec{\mu}^2_{\text{eff}}$ is defined by the difference of the total magnetic moment of the system with and without the impurity [26, 27, 53]:

$$\vec{\mu}^2_{\text{eff}} = \langle \vec{S}_{\text{tot}} \vec{S}_{\text{tot}} \rangle - \langle \vec{S}_{\text{bath}} \vec{S}_{\text{bath}} \rangle \stackrel{!}{=} \frac{3}{4}, \tag{4.15}$$

with $\vec{S}_{\text{bath}} = \int \vec{s}(\vec{r})\, d^D r$. If we insert the definition of $\vec{S}_{\text{tot}}$ from Eq. (4.11), the correlator of the bath $\langle \vec{S}_{\text{bath}} \vec{S}_{\text{bath}} \rangle$ is canceled and we obtain the sum rule

$$\int \langle \vec{S}_{\text{imp}} \vec{s}(\vec{r}) \rangle \, d^D r = 0 \tag{4.16}$$

which is valid for $T = 0$ and $J < 0$. Consequently, we expect an oscillatory solution for $\chi_\infty(R)$ with sign changes at all length scales and a decay $R^{-\alpha}$ with $\alpha \geq D$. Therefore, the spin correlation function will be significantly different in the ferromagnetic $J < 0$ and in the antiferromangetic $J > 0$ regime.

4.1.3 Effective densities of states in 1D, 2D and 3D

The spatial correlations depend on the dimensionality of the host. At a constant distance R, the dimensionality primarily enters via the dimension of the wave vector $\vec{k}$ which occurs in Eqs. (4.5) and the energy dispersion $\epsilon_{\vec{k}}$ of the host.
In the following, we assume an isotropic linear dispersion $\epsilon_{\vec{k}} = v_{\text{F}} \left(|\vec{k}| - k_{\text{F}} \right)$ in order to obtain information on generic spectral densities $N^2_{e(o)}(\epsilon)\rho(\epsilon)$ appearing in Eqs. (4.7) and (4.8). Here v_{F} is the Fermi velocity and k_{F} denotes the Fermi wave vector. Inserting the dispersion in Eqs. (4.5) yields in 1D

$$N^2_{e(o)}(\epsilon)\rho(\epsilon) = 2\rho_0 \left[1 \pm \cos\left(x\pi \left(1 + \frac{\epsilon}{D} \right) \right) \right] \tag{4.17}$$

where $\rho_0 = 1/2D$ is the constant DOS of the original conduction band and $x = k_{\text{F}} R/\pi$. In higher dimensions we can perform the angular integration analytically and obtain for 2D

$$N^2_{e(o)}(\epsilon)\rho(\epsilon) = 2\rho_0 \left[1 \pm J_0\left(x\pi \left(1 + \frac{\epsilon}{D} \right) \right) \right] \tag{4.18}$$

with the zeroth Bessel function $J_0(x)$. In 3D, the effective DOSs [61, 62] is given by

$$N^2_{e(o)}(\epsilon)\rho(\epsilon) = 2\rho_0 \left[1 \pm \frac{\sin\left(x\pi \left(1 + \frac{\epsilon}{D} \right) \right)}{x\pi \left(1 + \frac{\epsilon}{D} \right)} \right]. \tag{4.19}$$

Note that in 2D and 3D $\rho(\epsilon)$ is not constant for a linear dispersion, and hence $\rho(\epsilon) = \rho_0 = 1/2D$ is a simplification.

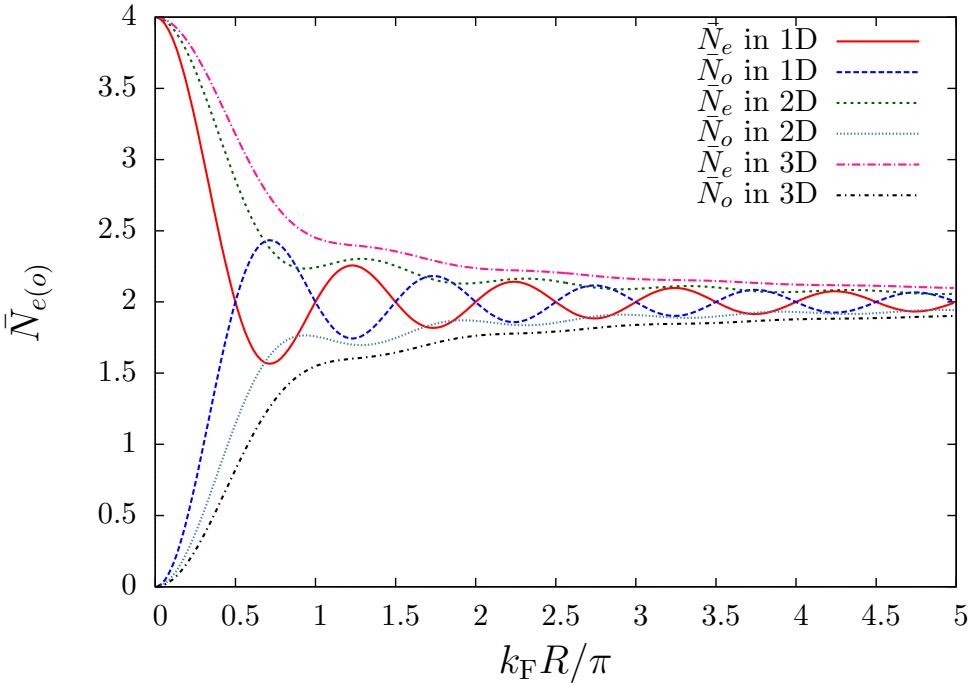

Figure 4.1: Normalization constants $\bar{N}_{e(o)}$ for different dimensions D vs. the dimensionless distance $x = k_F R/\pi$. For $R \to 0$ the odd band decouples and for $R \to \infty$ the normalization constant $\bar{N}_e$ is equal to $\bar{N}_o$.
Figure taken from [124].

The distance R dependent normalization constants $\bar{N}_{e(o)}$ that occur in the Hamiltonian (4.9) and the spin density (4.10) reveal important information on the admixture of even and odd bands. These normalization constants are shown as a function of the dimensionless distance $x = k_F R/\pi$ for different dimensions D in Fig. 4.1. Clearly, for $\bar{N}_o(x = 0) = 0$ the odd band decouples from the problem in any dimension, and the standard Kondo model is recovered which allows to calculate local ($R = 0$) expectation values within a standard single band NRG [1].
As can be seen from Eqs. (4.17)-(4.19), the oscillations of the even and odd DOS $\rho_{e(o)}$ decay as $\propto R^{(1-D)/2}$ with increasing distance R. For large distances $R \to \infty$ the even and odd bands become equal and as shown in Fig. 4.1 the normalization constants approach the same value. In the case of 1D, strong oscillations are observed for $\bar{N}_{e(o)}$ for short distances that are suppressed in higher dimensions. Apparently, the R dependence will be more pronounced in lower dimensions and the correlation function will decay with a different power law than in higher dimensions.

[1] In order to avoid different numerical accuracy for $R = 0$ and $R > 0$ calculations, we have used $k_F R/\pi = 0.01$ in the NRG calculations for $R \to 0$.

$\rho_0 J$	T_K/D	$k_F\xi_K$
0.05	$1 \cdot 10^{-10}$	$1 \cdot 10^{10}$
0.075	$1.7 \cdot 10^{-7}$	$5.88 \cdot 10^{6}$
0.1	$7.5 \cdot 10^{-6}$	$1.33 \cdot 10^{5}$
0.15	$3.9 \cdot 10^{-4}$	2564.10
0.2	$2.4 \cdot 10^{-3}$	421.59
0.25	0.0077	129.87
0.3	0.0178	56.31
0.35	0.0290	34.53
0.4	0.0418	23.90
0.45	0.0578	17.30
0.5	0.0749	13.35
0.6	0.115	8.69
0.7	0.2103	4.76

Table 4.1: The Kondo temperature T_K and Kondo length scale ξ_K for different Kondo couplings $\rho_0 J$. The Kondo temperatures have been obtained from the NRG level flow and is defined as the energy scale at which the first excitation reaches 80% of its fixed point value.

4.2 Equilibrium

4.2.1 Kondo regime (J>0): short distance versus large distance behavior

The problem has two characteristic length scales: $\frac{1}{k_F}$ defined by the metallic host which governs the power-law decay of $\chi_\infty(R)$ and its Ruderman-Kittel-Kasuya-Yosida (RKKY) oscillations, and the Kondo length scale $\chi_K = \frac{v_F}{T_K}$, sometimes referred to as the size of the Kondo screening cloud [116–119, 123, 125]. The Kondo length scale ξ_K depends exponentially on the coupling $\rho_0 J$, therefore, we use different $\rho_0 J$ to present results for the two different regimes $R \gg \xi_K$ and $R \ll \xi_K$.

Since the Kondo temperature is a crossover scale, it is only defined up to an arbitrary constant of the order one. We define the Kondo temperature T_K from the NRG level flow as the energy scale at which the first excitation reaches 80% of its fixed point value. Table 4.1 shows the Kondo temperature as well as the Kondo length scale ξ_K for different couplings $\rho_0 J$.

In Fig. 4.2a the spin correlation function is shown for $R \ll \xi_K$ and $\frac{T}{T_K} \to 0$. We rescaled the correlation function $\chi_\infty(R)$ with the distance R to reveal the $\frac{1}{R}$ decay at short distances in 1D which originates from the analytical form of the RKKY interaction. In contrast to Bordas original work [47], we observe ferromagnetic as well as antiferromagnetic correlations for short distances in accordance with predictions [116–119, 123, 125] made by Affleck and his co-workers. For short distances $R \ll \xi_K$ the

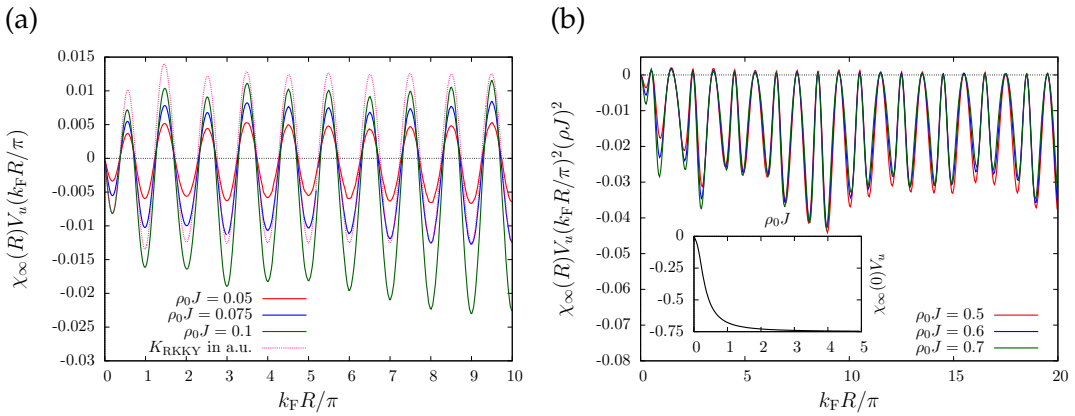

Figure 4.2: (a) The rescaled spin correlation function $R\chi_\infty(R)$ plotted against the dimensionless distance $x = k_FR/\pi$ in 1D for different couplings $\rho_0 J$, $\frac{T}{T_K} \to 0$ and $\frac{R}{\xi_K} \ll 1$. A RKKY interaction between the impurity spin and a fictitious probe spin in distance R is added for comparison. (b) $R^2\chi_\infty(R)$ plotted against the dimensionless distance x in 1D for different large couplings $\rho_0 J$. The rescaling with R^2 reveals the $\frac{1}{R^2}$ decay at large distances $R \gg \xi_K$. The inset shows the values of the correlation function at the origin $\chi_\infty(0)V_u$ versus $\rho_0 J$. For large couplings $\rho_0 J$ the correlation function reaches the value $-\frac{3}{4}$.

Kondo effect has no influence, the impurity is still unscreened and behaves more like a free spin.

Along with the correlation function Fig. 4.2a also show the RKKY interaction K_{RKKY} between the impurity spin and a fictitious probe spin at distance R from the impurity for comparison. K_{RKKY} is obtained from second-order perturbation theory in J and details of the calculation of the RKKY interaction can be found in appendix B. As can be seen, the oscillating part of $\chi_\infty(R)$, and the position of the minima and maxima nicely agree with the RKKY interaction $\propto \cos(2k_FR)$. For multiples of the integer $x = k_FR/\pi = n$ the correlation function and K_{RKKY} exhibit minima and for odd multiple $x = n + \frac{1}{2}$ they have maxima.

Figure 4.2b shows the correlation function for larger couplings $\rho_0 J$ so that we can access distances $R \gg \xi_K$. This time the correlation function is rescaled with R^2 in order to reveal the $\frac{1}{R^2}$ decay at large distances. In contrast to the short distance behavior we only find antiferromagnetic correlations for $R \gg \xi_K$, and $\chi_\infty(R)$ remains negative at all distances. In this regime, the maxima have the value $\chi_\infty(R) = 0$ which is in accordance with field theory predictions [116–119, 125, 126]. For such large distances the impurity spin is screened by the conduction band electrons and, therefore, the envelope of $\chi_\infty(R)$ has to decrease faster.

Since we have plotted $R\chi_\infty(R)$ and $R^2\chi_\infty(R)$ which vanish for $R = 0$, the information of $\chi_\infty(0)$ is not included in Fig. 4.2. Therefore, the inset of Fig. 4.2b shows the local spin correlation function $\chi_\infty(0)$ plotted against the coupling $\rho_0 J$. As expected for an antiferromagnetic coupling, the correlation function is always negative $\chi_\infty(0) < 0$, and

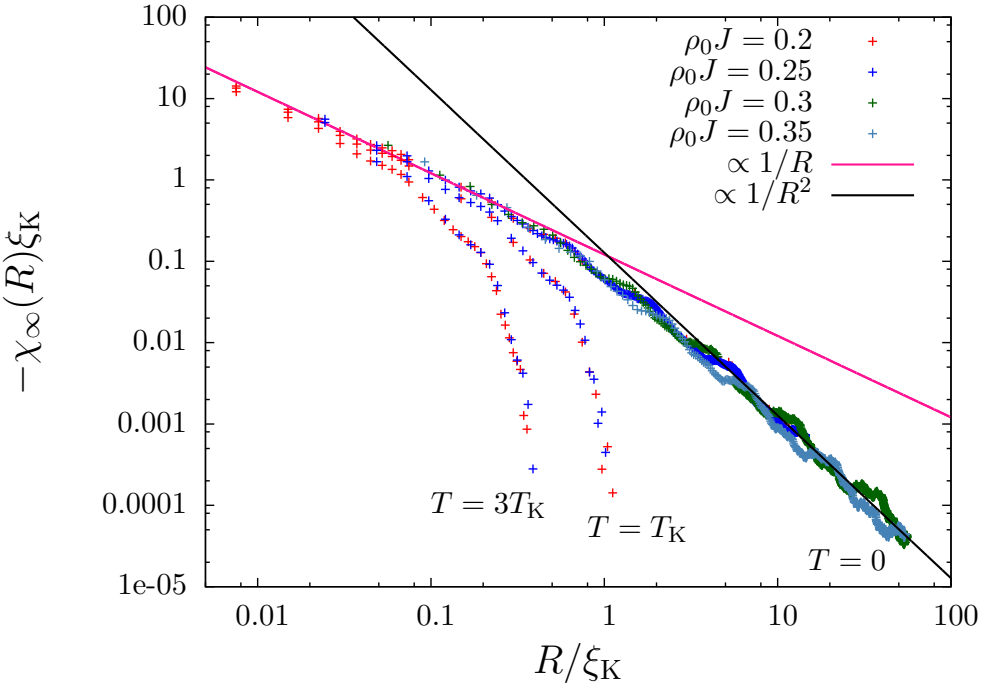

Figure 4.3: The envelope of the correlation function $\chi_\infty(R)$ rescaled with the Kondo length scale ξ_K plotted against the rescaled distance $\frac{R}{\xi_K}$ for different couplings $\rho_0 J$ and temperatures. The rescaling leads to universal behavior. The crossover from the $\frac{1}{R}$ (pink line) to the $\frac{1}{R^2}$ (black line) decay is around the Kondo length scale $R \approx \xi_K$. Finite temperature introduces a new length scale $\xi_T = \frac{v_F}{T}$ beyond which the correlations are exponentially suppressed. NRG parameters are $\Lambda = 3$ and $N_s = 2000$.

for very large couplings $\rho_0 J$ the strong coupling value of $-\frac{3}{4}$ is approached. For such large couplings almost the whole contribution to the sum rule (4.14) lies in the first antiferromagnetic minimum at $R = 0$, and consequently $\chi_\infty(R)$ has to decay very rapidly with increasing distance R.

Figure 4.3 shows the envelope of the correlation functions $\chi_\infty(R)$ rescaled with the Kondo length scale ξ_K plotted against the rescaled distance $\frac{R}{\xi_K}$ for different couplings $\rho_0 J$ and temperatures. The envelope is defined by $\chi_\infty(k_F R = n\pi)$, where n is an integer. Due to the rescaling, the envelope functions for different couplings $\rho_0 J$ nicely collapse onto one universal curve. Like in Ref. [47] the envelope functions decay as $\frac{1}{R^2}$ for large distances, indicated by the black line, while for short distances the envelope functions show a $\frac{1}{R}$ decay which is indicated by the pink line. The crossover between these different decays occurs at around the Kondo length scale ξ_K. This supports the interpretation that the impurity spin is screened by a cloud of surrounding electron spins with a size of ξ_K.

For finite temperature a new length scale $\xi_T = \frac{v_F}{T}$ is introduced. While for $R \ll \xi_T$ the correlation function $\chi_\infty(R)$ is almost unaffected, for $R \gg \xi_T$ correlations are exponentially suppressed. When the temperature is much smaller than the Kondo temperature

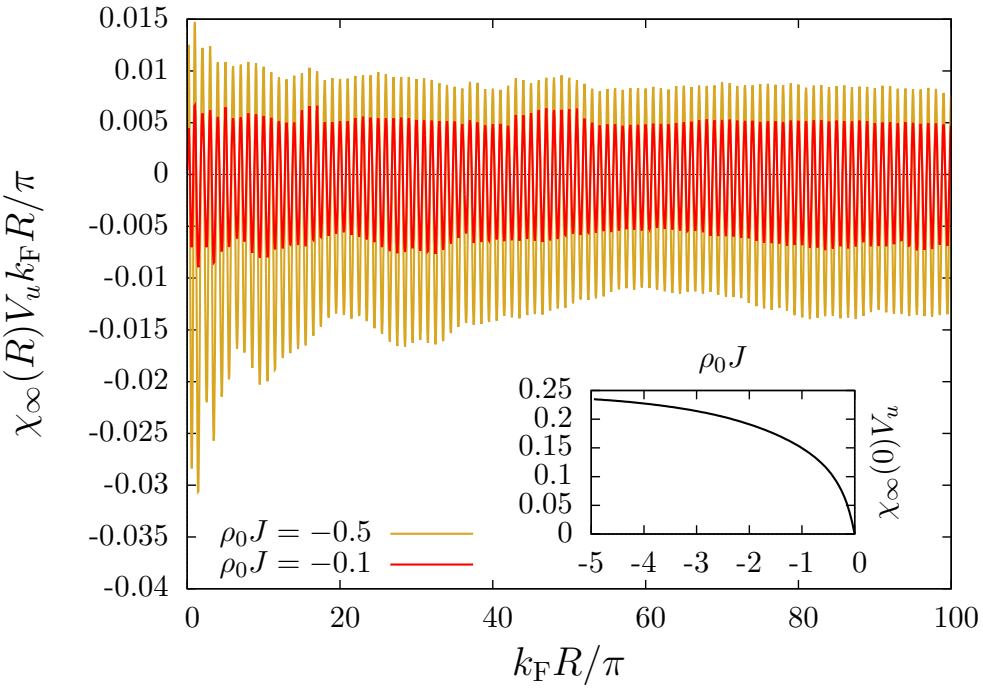

Figure 4.4: The spin correlation function $R\chi_\infty(R)$ as a function of the dimensionless distance $x = k_F R/\pi$ in 1D for two different ferromagnetic Kondo couplings $\rho_0 J = -0.1$, $\rho_0 J = -0.5$ and $T \to 0$. For ferromagnetic couplings $\chi_\infty(R)$ decays with $\frac{1}{R}$ at every distance. The inset shows $\chi_\infty(0)V_u$ vs. $\rho_0 J$. For large ferromagnetic couplings the value 0.25 is reached. NRG parameters are $\Lambda = 3$ and $N_s = 1400$. Figure taken from Ref. [124].

$T \ll T_K$, the corresponding thermal length scale is much larger than the Kondo length scale $\xi_T \gg \xi_K$. Therefore, the effect of a small finite temperature is just a small correction to the perfectly screened impurity at $T = 0$. On the other hand, for $T > T_K$ the thermal length scale is shorter than the Kondo length scale $\xi_T < \xi_K$ and the impurity spin is no longer fully screened.

4.2.2 Ferromagnetic couplings $J < 0$

So far we have only investigated the model for antiferromagnetic couplings which leads to a Kondo singlet for $T \to 0$ and the Hamiltonian approaches the strong coupling fixed point. We now extend our discussion to ferromagnetic couplings. The ferromagnetic regime is characterized by the local moment fixed point and a twofold degenerated ground state. As mentioned above in Sec. 4.1.2, the sum rule for $\chi_\infty(R)$ with ferromagnetic couplings $J < 0$ predicts that the spatial integral of the correlation function vanishes. We numerically checked the sum rule for different couplings and found almost no deviations from zero in 1D.

Figure 4.4 shows the rescaled spin correlation function $R\chi_\infty(R)$ plotted against the dimensionless distance $x = k_F R/\pi$ for two different ferromagnetic couplings $\rho_0 J = -0.1$

and $\rho_0 J = -0.5$. For ferromagnetic couplings, the Kondo length scale diverges $\xi_K \to \infty$, and, therefore, we observe a $\cos(2k_F R)$ oscillation and a $\frac{1}{R}$ decay for all distances in 1D. The RKKY oscillations and the $\frac{1}{R}$ decay of the envelope function are clearly visible even up to very large distances $k_F R = 100\pi$.
In the ferromagnetic regime, the local spin correlation function $\chi_\infty(0)$ must be positive and approaches its upper limit of $\chi_\infty(0) = \frac{1}{4}$ for $\rho_0 J \to -\infty$ as shown in the inset of Fig. 4.4. Note that $\chi_\infty(R)$ does not oscillate symmetrically around the x-axis since in order to fulfill the sum rule, $\chi_\infty(R)$ must be slightly shifted to antiferromagnetic correlations to compensate the ferromagnetic peak at $R = 0$.

4.2.3 Spin correlation function in 2D and 3D

We now investigate the equilibrium spin correlation function for 2D and 3D dispersions. Figure 4.5a shows the short distance behavior of the rescaled spin correlation function $R^2\chi_\infty(R)$ in 2D. As for 1D, the oscillating part and the positions of the minima and maxima of $\chi_\infty(R)$ and the 2D RKKY interaction nicely agree. Both the RKKY interaction and the correlation function decay as $\frac{1}{R^2}$ for short distances in 2D. In contrast to 1D, the RKKY interaction acquires a more complex mathematical structure even for a simple linear dispersion replacing the simple $\cos(2k_F R)$ oscillations in 1D. In Fig. 4.5b, the short distance behavior of $R^3\chi_\infty(R)$ for a 3D dispersion is shown. As before, the oscillating part of the 3D RKKY interaction and $\chi_\infty(R)$ nicely agree and like in 2D, the RKKY interaction and $\chi_\infty(R)$ have a more complicated structure than the simple oscillations in 1D. Furthermore, in 3D the expected $\frac{1}{R^3}$ decay of the RKKY interaction and $\chi_\infty(R)$ is observed for short distances.
In Fig. 4.5c the envelope of the correlation function $\chi_\infty(R)$ for a 2D dispersion is shown. In 2D the correlation function $\chi_\infty(R)$ has to be rescaled with ξ_K^2 in order to make it dimensionless and consequently to observe universal behavior. Note that the positions of the minima and maxima of the correlation function change in higher dimensions, therefore, in 2D the envelope is defined by $\chi_\infty(k_F R = n\pi + \frac{1}{4})$, with the integer n. The observed oscillations of the envelope function originate from the more complicated structure of the envelope in 2D where every second maximum has a lower amplitude. For short distances $R \ll \xi_K$ a $\frac{1}{R^2}$ decay is observed, which is marked by the blue line. For larger distances $R > \xi_K$ the envelope function decays faster and approaches the expected $\frac{1}{R^3}$ decay [125, 126] that is indicated by the black line.
In order to observe the real $\frac{1}{R^3}$ decay of the correlation function, we would need to go to even larger distances $R \gg \xi_K$. This is, however, a challenging task since due to the fast decay of the correlation function in higher dimensions, the numerical noise of the NRG rapidly exceeds the value of $\chi_\infty(R)$. Although larger distances R can be reached with an increase of the discretization parameter Λ and the number of kept states N_s, an unsuitable high number of kept states N_s would be needed in order to actually observe

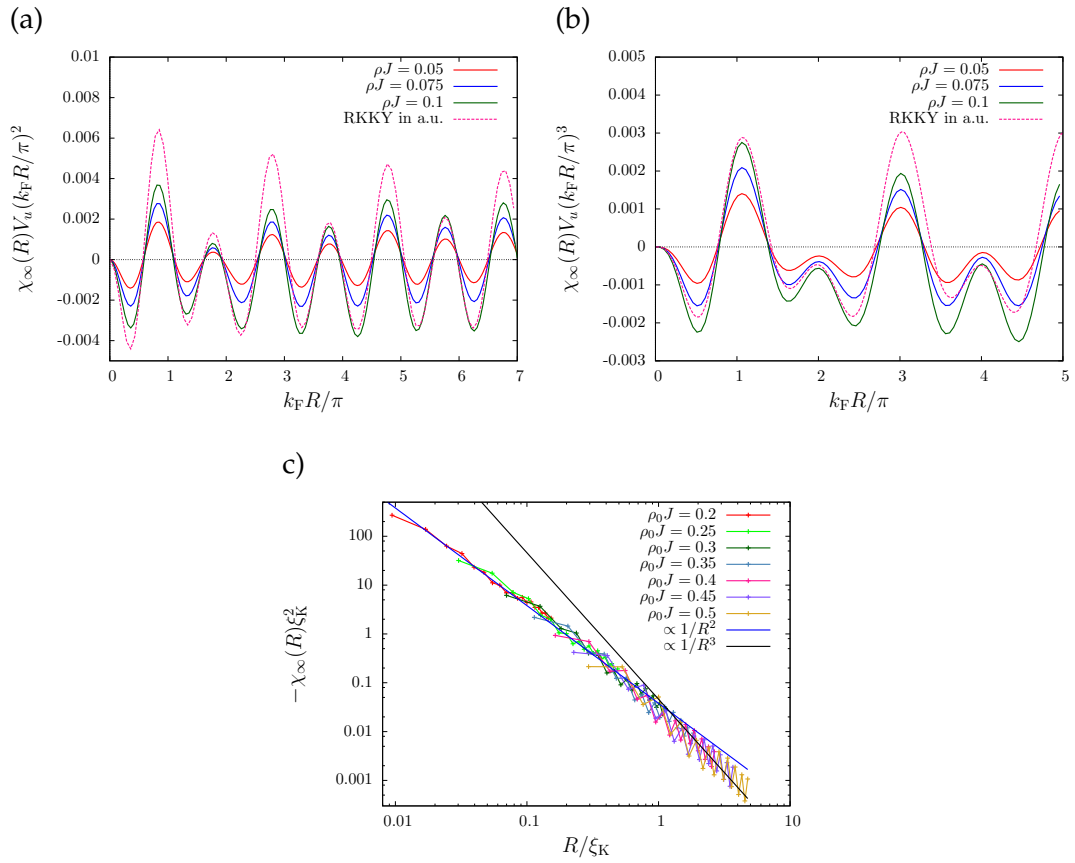

Figure 4.5: The rescaled spin correlation functions (a) $R^2\chi_\infty(R)$ in 2D and (b) $R^3\chi_\infty(R)$ in 3D as a function of the dimensionless distance $x = k_F R/\pi$. Both in 2D and 3D, the envelope of the RKKY interaction and $\chi_\infty(R)$ has a more complicated structure than in 1D. NRG parameters are (a) $\Lambda = 5$ and $N_s = 3000$ and (b) $\Lambda = 10$ and $N_s = 4000$. (c) The envelope of the correlation function $\chi_\infty(R)$ rescaled with the Kondo length scale ξ_K^2 plotted against the rescaled distance $\frac{R}{\xi_K}$ in 2D. As in 1D, universal behavior is observed. For short distances the envelope decays with $1/R^2$ (blue line) and for larger distances it approaches the $1/R^3$ (black line) decay. NRG parameters are $\Lambda = 5$ and $N_s = 3500$.

the $\frac{1}{R^3}$ decay. Therefore, it is even more desperate to observe the $\frac{1}{R^4}$ decay for a 3D dispersion.

4.3 Nonequilibrium

After discussing the equilibrium properties of the correlation function, we now turn to the results of the full time-dependent correlation function $\chi(\vec{r}, t)$. In the TD-NRG calculations the Kondo coupling $\rho_0 J$ between the prior decoupled impurity spin and conduction band is switched on at time $t = 0$. As described in Sec. 2.2, the NRG fixed point differs for different signs of the Kondo coupling. For an antiferromagnetic coupling $J > 0$ the system approaches the strong coupling fixed point while for $J < 0$

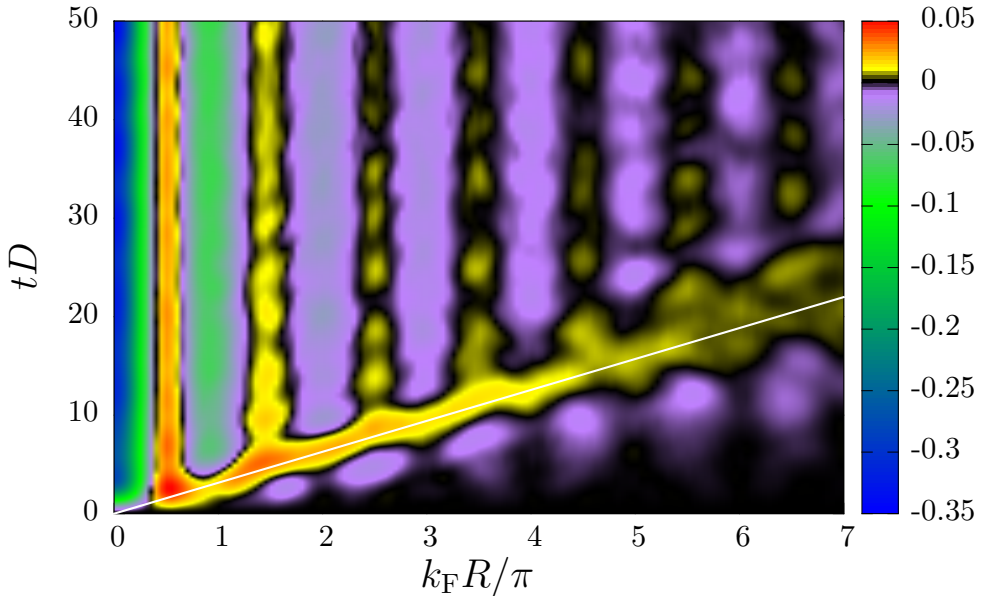

Figure 4.6: The time- and spatial-dependent spin-spin correlation function $\chi(R,t)$ vs. the dimensionless distance $k_F R/\pi$ and dimensionless time tD for the Kondo coupling $\rho_0 J = 0.3$ as a color contour plot. The correlation propagates with the Fermi velocity v_F, which is added as a white line as a guide to the eye. NRG parameters are $\Lambda = 3$, $N_s = 1400$ and $N_z = 4$. Figure taken from Ref. [124].

the local moment fixed point is reached. Therefore, we present data for both regimes and begin with the investigation of antiferromagnetic Kondo couplings and compare the results with our perturbation theory. Afterwards we turn to the ferromagnetic $J < 0$ case.

4.3.1 Time-dependent spatial correlation function in the Kondo regime

The full time-dependent spin-spin correlation function $\chi(\vec{r},t)$ is shown as a function of the dimensionless distance $k_F R/\pi$ and the dimensionless time tD for a moderate antiferromagnetic Kondo coupling $\rho_0 J = 0.3$ as a color contour plot for 1D in Fig. 4.6. Since each distance R requires a single TD-NRG run, we have restricted ourselves to $N_z = 4$ values for the z-averaging and only use a moderate number of $N_s = 1400$ kept NRG states.

The development of the ferromagnetic correlation maximum at $k_F R/\pi = \frac{1}{2}$ is clearly visible already after very short times, cf. Fig. 4.2a. For large times $t \to \infty$ the equilibrium correlation function $\chi_\infty(R)$ with the RKKY oscillations is recovered. The correlation function has maxima for $k_F R/\pi = n + \frac{1}{2}$ and minima for $k_F R/\pi = n$, with n being an integer. For large times and distances the ferromagnetic correlations are suppressed so that the maxima have the value $\chi(R,t) = 0$ and purely antiferromagnetic correlations are observed, as expected from the equilibrium correlation function.

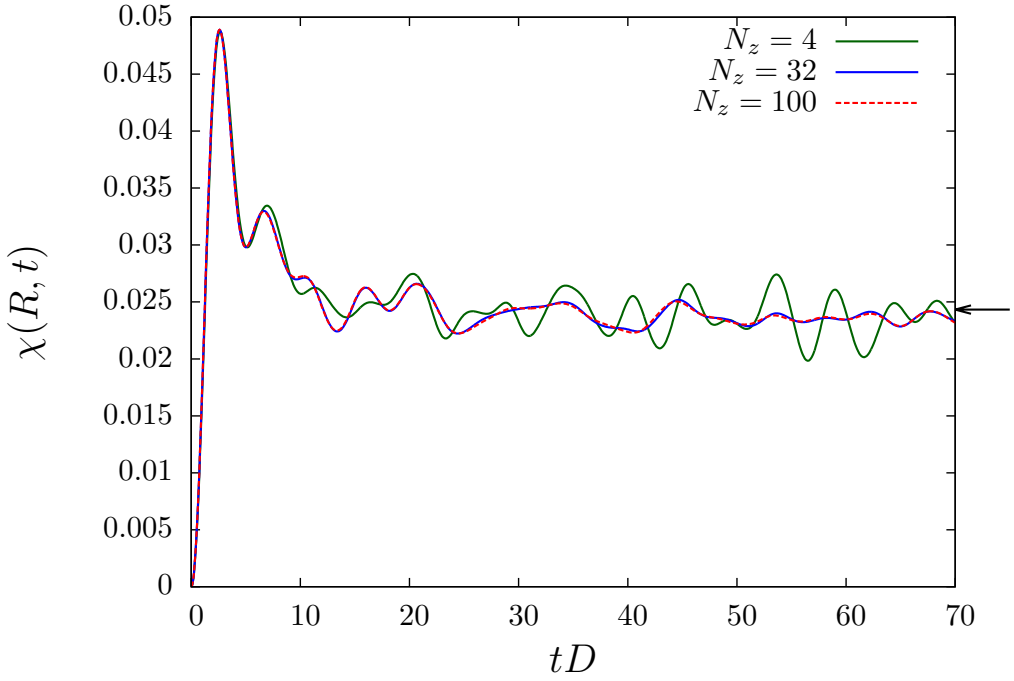

Figure 4.7: The time-dependent spin correlation function $\chi(R,t)$ for a fixed distance $k_\mathrm{F}R/\pi = 0.51$ vs. the dimensionless time tD for different numbers of z-averages N_z and $\rho_0 J = 0.3$. The black arrow indicates the value of the equilibrium correlation function $\chi_\infty(R = 0.51\pi/k_\mathrm{F})$. NRG parameters are $\Lambda = 3$ and $N_s = 1600$.

After the ferromagnetic maximum has passed, we observe for $\chi(R = \text{const}, t)$ some weak oscillations in time. Figure 4.7 shows the correlation function $\chi(k_\mathrm{F}R/\pi = 0.51, t)$ for a constant distance and different numbers of z-averages N_z in order to distinguish between the in Sec. 3.2 described finite size oscillations originating from the bath discretization and the real nonequilibrium dynamics of the continuum. As can be seen, the short-time oscillations clearly converge with increasing N_z so that the curves for $N_z = 32$ and $N_z = 100$ are almost identical. Therefore, we can conclude that the short-time oscillations contain relevant real-time dynamics and will be analysed in more detail below.

In the long-time limit, the TD-NRG oscillates around a time average, which is independent of N_z and is very close to the equilibrium value of the correlation function $\chi_\infty(R = 0.51\pi/k_\mathrm{F})$ indicated by the black arrow in Fig. 4.7. The difference between the long-time average and the equilibrium value is smaller than 3%. These oscillations around the time average are partially related to the bath discretization and are suppressed for increasing number of z values N_z, decreasing discretization parameter Λ and increasing number of kept NRG states N_s, cf. Sec. 3.2. Therefore, we can conclude that the thermodynamic equilibrium is reached up to the well understood small discretization errors.

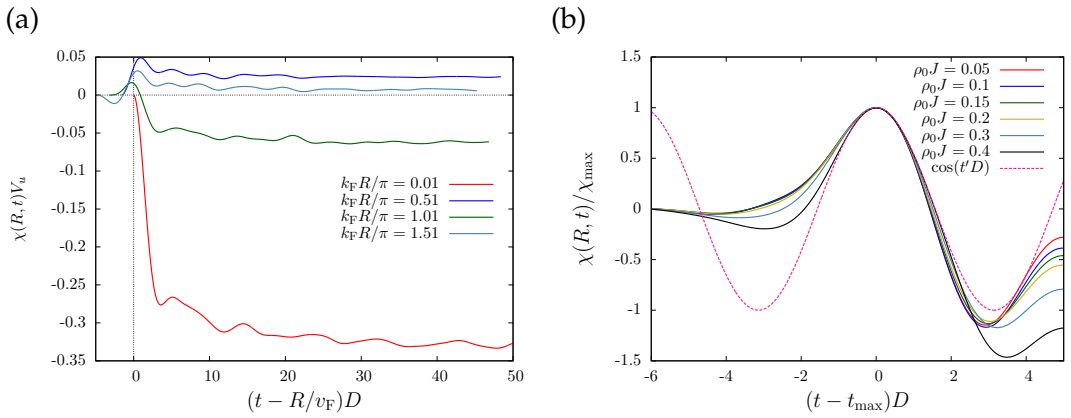

Figure 4.8: (a) Time-dependent correlation function $\chi(R,t)$ vs. $t' = t - R/v_F$ for four different distances $k_F R/\pi = 0.01, 0.51, 1.01, 1.51$ and the Kondo coupling $\rho_0 J = 0.3$. (b) Rescaled time-dependent correlation function $\chi(R,t)/\chi_{max}$ plotted against the shifted time $t - t_{max}$ for $k_F R/\pi = 2.01$ and for different couplings $\rho_0 J$. Here t_{max} denotes the position and χ_{max} the amplitude of the ferromagnetic peak. NRG parameters are $\Lambda = 3$, $N_s = 1200$ and $N_z = 32$.

$\rho_0 J$	0.05	0.1	0.15	0.2	0.3	0.4
t_{max}/π	1.91	1.95	1.97	1.99	2.02	2.00
χ_{max}	0.0052	0.0101	0.0147	0.0183	0.0201	0.0151

Table 4.2: The coupling dependent positions t_{max} and maximum amplitude of the ferromagnetic peaks for the fixed distance $k_F R/\pi = 2.01$. Until the medium coupling strength $\rho_0 J = 0.3$ the position t_{max} is shifted to larger times with increasing coupling. For small couplings the maximum amplitude χ_{max} is proportional to the coupling $\rho_0 J$.

How are the Kondo correlations building up at different distances with time?

The propagation of the ferromagnetic correlation away from the impurity with the Fermi velocity v_F is clearly visible in Fig. 4.6. For an antiferromagnetic coupling $\rho_0 J$ we observe an antiferromagnetic spin-spin correlation at the impurity site that develops rather rapidly. Since the total spin in the system is conserved, a ferromagnetic correlation at $R = 0.5\pi/k_F$ is built up the same time as the antiferromagnetic correlation at $R = 0$. This ferromagnetic correlation propagates spherically away from the impurity through the system. The added white line $R = v_F t$ in Fig. 4.6 serves as a guide to the eye to exemplify this point. This line represents the analog to a light cone in the electrodynamics.

Inside the light cone, after the ferromagnetic correlation wave has passed, the equilibrium value of the correlation function is reached rather fast. In Fig. 4.8a the correlation function $\chi(R,t)$ is plotted against the relative time $t' = t - \frac{R}{v_F}$ for four different distances R to illustrate this. Negative times $t' < 0$ correspond to correlations outside of

the light cone, while for $t' > 0$ the spin correlation function $\chi(R,t)$ inside the light cone is depicted.

At the origin of the impurity[2] ($R = 0.01$) , an antiferromagnetic correlation develops on the time scale $\frac{1}{\sqrt{J}}$: the short time dynamics is linear in the Kondo coupling and proportional to t^2. This will be discussed in greater detail below in Sec. 4.3.2.

At $t' = 0$ and finite distance $R > 0$, a significant ferromagnetic correlation peak is observed which decays rather rapidly. The position of this ferromagnetic peak corresponds to the ferromagnetic correlation wave that defines the yellow light cone in Fig. 4.6. In order to investigate this rapid decay in more detail, in Fig. 4.8b the ratio $\chi(R,t)/\chi_{\max}$ is plotted against $(t - t_{\max})D$ for the constant distance $\frac{k_F R}{\pi} = 2.01$ and different couplings $\rho_0 J$. $\chi_{\max}$ is defined as the maximum of the ferromagnetic peak $\chi_{\max} = \chi(R, t_{\max})$, and $t_{\max}$ is the position of this ferromagnetic peak. The different values of $t_{\max}$ and $\chi_{\max}$ are shown in Tab. 4.2.

Note that $t_{\max}$ slightly differs from the bare time scale of the light cone $\frac{R}{v_F}$. Up until medium couplings $\rho_0 J$, the position $t_{\max}$ is slightly shifted to larger times with increasing coupling $\rho_0 J$. The increasing shift for small and medium couplings can be understood analytically with second-order perturbation theory in the coupling J and is discussed in more detail in Sec. 4.3.2 below.

After dividing the correlation function by the amplitude $\chi_{\max}$ we find universal behavior for small couplings $\rho_0 J$. Once again, this can be explained by perturbation theory. For small couplings, the correlation function is essentially described by first-order perturbation theory which is proportional to the coupling strength $\propto \rho_0 J$. Therefore, as can be seen in Tab. 4.2, for small couplings $\rho_0 J$ the maximum amplitude $\chi_{\max}$ is also proportional to $\propto \rho_0 J$. Hence, the division of $\chi(R,t)$ by $\chi_{\max}$ cancels the coupling dependence of the time-dependent correlation function and the curves fall onto one universal curve.

For comparison we also plotted $\cos(t'D)$ (pink dashed line) and find a remarkable agreement with the oscillations of the correlation function for times $0 < t'D < 1$ for all coupling strengths. This indicates that for a fixed distances the functional form of the correlation function $\chi(R,t)$ consists of a damped oscillating $\cos(t'D)$ term whose maximum is reached when the ferromagnetic correlation wave reaches the distance R at time $t_{\max}$. Since $\chi(k_F R/\pi = 2.01, t)$ has to approach a finite antiferromagnetic value for larger times t', the oscillations in the TD-NRG are not centered around the origin $\chi(R,t) = 0$ but shifted to negative values as can be seen in Fig. 4.8b by comparing with the undamped $\cos(t'D)$ curve.

However, most striking is the built up of correlations for $t' < 0$ outside of the light cone. These correlations seem to be purely antiferromagnetic and show a nonexpo-

[2] A two-channel NRG calculation requires a finite $\bar{N}_o$. For zero distance $R = 0$ the normalization $\bar{N}_o$ would also be zero and the numerics break down. Therefore, we use a small but finite distance to mimic $R \to 0$.

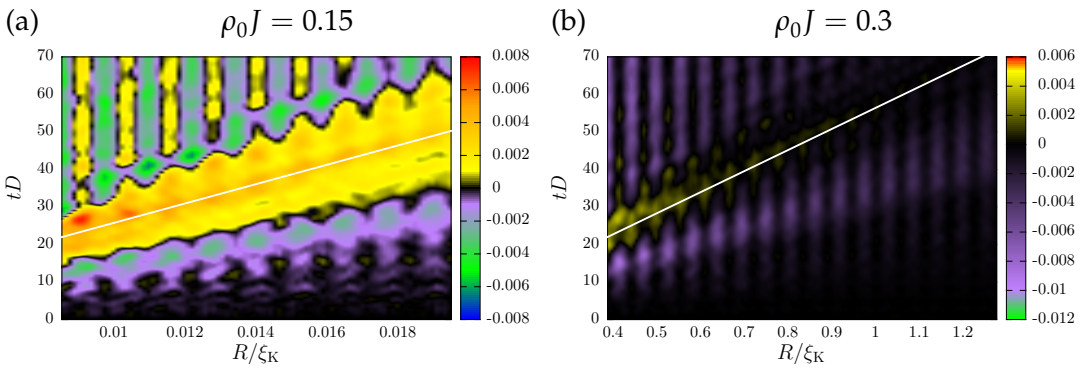

Figure 4.9: The time-dependent correlation function $\chi(R,t)$ for different ratios R/ξ_K as a color contour plot. (a) The oscillation between ferromagnetic and antiferromagnetic correlations is only observed for small distances $R \ll \xi_K$. (b) For larger distances and long times, only oscillations between zero and antiferromagnetic correlations are observed. The ferromagnetic propagation vanishes at around $R \approx \xi_K$. Both long time behaviors are in good agreement with the NRG equilibrium results. NRG parameters are $\Lambda = 3$, $N_s = 1400$ and $N_z = 32$.

nential decay in time. They appear shortly in front of the light cone, have their largest absolute value for odd numbers of $k_F R = n + \frac{1}{2}$ and decay with a power law as tD goes to zero.

As we will show below in Sec. 4.3.2, these correlations also appear in the results obtained from perturbation theory. Such a build up of correlations outside of the light cone has also recently be reported in a perturbative calculation at the Toulouse point of the anisotropic Kondo model [114] neglecting, however, the $2k_F$ oscillations. In contrast to Ref. [114] we present here results for a full nonperturbative calculation which includes the Friedel oscillations containing the RKKY mediated effective spin-spin interaction. These results have recently been confirmed by DMRG calculations [115]. We will provide a detailed analysis of the origin of these correlation outside the light cone and present an analytical calculation in J that agrees remarkably well with the observed TD-NRG results below in Sec. 4.3.3.

The different behavior of the correlation function for short and long distances plotted against $\frac{R}{\xi_K}$ is shown in Fig. 4.9a and b respectively. For short distances $R \ll \xi_K$ we find the distinctive ferromagnetic correlation waves that propagates with Fermi velocity v_F through the system. Inside the light cone we observe the RKKY like $2k_F$ oscillations between ferromagnetic and antiferromagnetic correlations. In Fig. 4.9b the behavior of the correlation function for larger distances is depicted. We find that the ferromagnetic propagation vanishes at around the Kondo length scale $R \approx \xi_K$. At these distances we only observe oscillations between zero and antiferromagnetic correlations inside the light cone. Therefore, we can conclude that for short as well as for long distances the long-time behavior agrees remarkably well with the NRG equilibrium results.

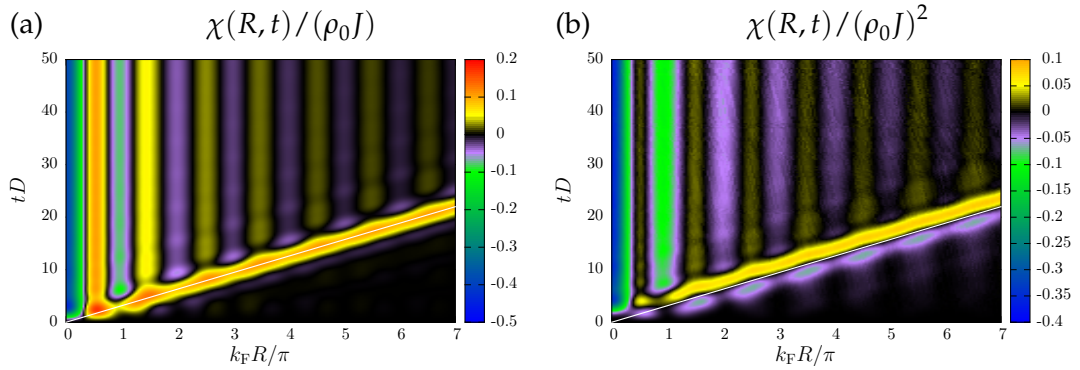

Figure 4.10: The perturbatively calculated (a) first-order contribution $\chi(R,t)/(\rho_0 J)$ and (b) second-order contribution $\chi(R,t)/(\rho_0 J)^2$ evaluated numerically as color contour plots. The light cone $R = v_F t$ has been added as a white line.

4.3.2 Perturbation theory

The most surprising result of the TD-NRG results is the build up of spin correlations outside of the light cone which do not decay exponentially. In order to exclude TD-NRG artefacts and investigate the origin of these correlations, we perturbatively calculate $\chi(\vec{r},t) = \langle \vec{S}_{\text{imp}} \vec{s}(\vec{r}) \rangle (t)$ up to second order in the coupling J. For this purpose we transform all operators into the interaction picture since only the part of the free conduction electrons H_0 enters the initial density operator. After integrating the von Neumann equation, we obtain for the density operator in the interaction picture

$$\begin{aligned} \rho^I(t) \approx & \rho_0 + i \int_0^t \left[\rho_0, H_K^I(t_1)\right] \, dt_1 \\ & - \int_0^t \int_0^{t_1} \left[\left[\rho_0, H_K^I(t_2)\right], H_K^I(t_1)\right] \, dt_2 \, dt_1, \end{aligned} \tag{4.20}$$

which is exact in second order in the Kondo coupling J. Here the index I labels the operators in the interaction picture $A^I(t) = \mathrm{e}^{iH_0 t} A \mathrm{e}^{-iH_0 t}$. The initial condition is given by $\rho^I(t=0) = \rho_0$. Using this density operator $\rho^I(t)$, we calculate the spin-spin correlation function

$$\chi(\vec{r},t) = \mathrm{Tr}\left[\rho^I(t) \vec{S}_{\text{imp}} \vec{s}^I(\vec{r},t)\right], \tag{4.21}$$

where only expectation values with respect to the initial density operator ρ_0 enter. The occuring tedious commutators can be calculated analytically and details about the perturbative calculation of $\chi(\vec{r},t)$ can be found in appendix C. The time integrals can simply be performed analytically, however, the multiple momenta integrations of the free conduction electron states have to be performed numerically.

The first- and second-order contribution of the perturbatively calculated correlation function $\chi(R,t)$ are shown in Fig. 4.10a and Fig. 4.10b. For the leading order in

the Kondo coupling $\rho_0 J$, the ferromagnetic wave propagates exactly on the light cone $R = v_F t$. Furthermore, some small antiferromagnetic correlations outside of the light cone are already visible. In contrast to the first-order, the second-order contribution of the correlation function is zero exactly on light cone. Directly in front of the light cone a strong antiferromagnetic correlation is observed and immediately after the light cone follows a strong ferromagnetic correlation. For the first-order as well as for the second-order contribution we observe the distance dependent $2k_F$ oscillations between ferromagnetic and antiferromagnetic correlations for long times.

In Sec. 4.3.1 we found that the positions of the ferromagnetic peaks t_{max}, which are listed in Tab. 4.2, are coupling dependent. For up to medium coupling strengths $\rho_0 J$, the positions t_{max} are slightly shifted to larger times with increasing coupling. Our analytical analysis can provide a detailed understanding of this effect. While the first-order contribution Eq. (C.6) yields a peak of the ferromagnetic correlations positioned exactly on the light cone, the maximum of the second-order contribution Eq. (C.7) is shifted to slightly larger times. If we add both contributions, a J-dependent line for the ferromagnetic peak position away from the light cone is generated. The larger the coupling J, the later the ferromagnetic maximum occurs due to the increasing importance of the second-order contribution.

Furthermore, the rising influence of the second-order contribution also explains the increasing antiferromagnetic correlations with increasing coupling $\rho_0 J$ for short times in Fig. 4.8b. The antiferromagnetic correlations for $t - t_{max} < 0$ originate from the large antiferromagnetic correlations directly in front of the light cone in the second-order contribution and, therefore, they are only observed for larger couplings $\rho_0 J$ where the second-order contribution has a significant influence.

However, our second-order perturbation theory cannot explain the effect that t_{max} once again decreases with increasing $\rho_0 J$ for very large couplings, cf. Tab. 4.2. Since the second-order perturbation theory is not valid anymore for such large couplings, we would need to calculate higher-order contributions to get an insight in this effect.

The sum of the first- and second-order contributions to $\chi(R,t)$ for the medium coupling $\rho_0 J = 0.3$ is shown in Fig. 4.11. Clearly, the Kondo physics is not included in such a perturbative approach and the result remains only valid for $R \ll \xi_K$ and $t \ll 1/T_K$. Therefore, we expect deviations at large distances and times from the NRG results.

Nevertheless, the results of the perturbation theory qualitatively agree very well with the NRG results depicted in Fig. 4.6. As in the TD-NRG, a ferromagnetic wave propagates away from the impurity with the Fermi velocity v_F which is added as a white line in Fig. 4.11. Since such a perturbative approach is only expected to work well for short times, it is surprising that even the distance dependent $2k_F$ oscillations between ferro- and antiferromagnetic correlations are recovered for long times. Furthermore, we also find the same antiferromagnetic correlations outside of the light cone as in the TD-NRG results. Again, the maxima of these correlations are located at odd multiples

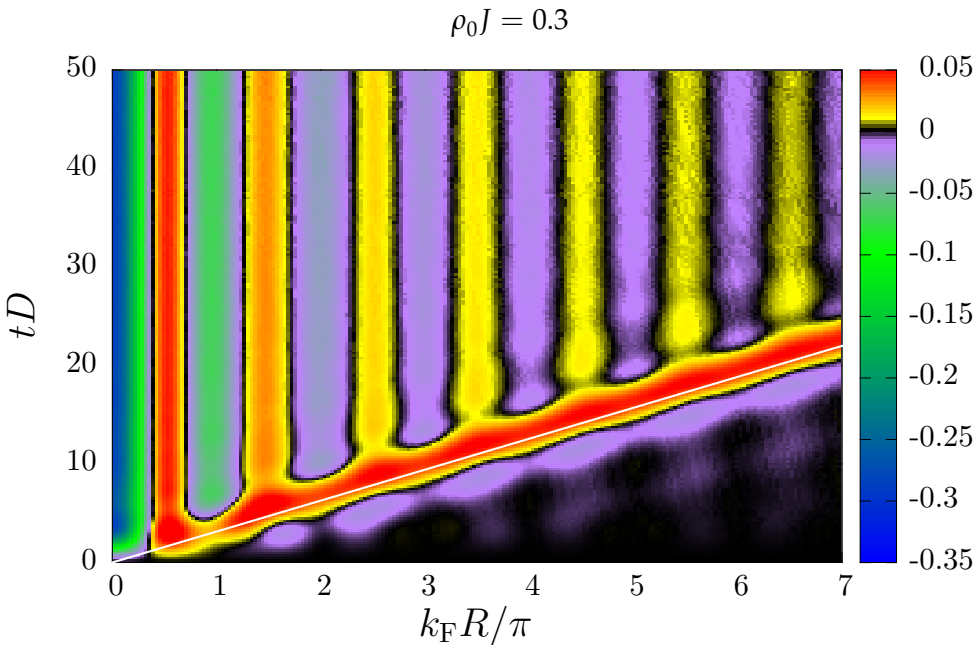

Figure 4.11: The sum of the first- and second-order contributions of the perturbatively calculated correlation function $\chi(R,t)$ for the medium coupling $\rho_0 J = 0.3$ as a color contour plot. The light cone $R = v_F t$ has been added as a white line.

of $k_F R/\pi = n + \frac{1}{2}$.

While these spatial oscillations are implicitly encoded in the effective even and odd DOS in the NRG calculations, they are explicitly generated by the momenta integrations in the perturbative calculation. This confirms our TD-NRG results and provides a better understanding of the numerical data.

However, a comparison between Fig. 4.6 and Fig. 4.11 shows the shortcomings of the perturbative approach which remains only valid for $R \ll \xi_K$. As discussed for the equilibrium correlation function in Sec. 4.2 above, in 1D the decay of the envelope function crosses over from a $\frac{1}{R}$ to a $\frac{1}{R^2}$ behavior at around $R \approx \xi_K$ due to the Kondo screening of the local moment. Since the perturbative approach is unable to reproduce the Kondo singlet formation, the long-time behavior of the perturbative solution depicted in Fig. 4.11 always shows a $\frac{1}{R}$ decay for all distances. Furthermore, for $tD \to \infty$ the perturbatively calculated correlation function $\chi(R,t)$ remains oscillating between ferro- and antiferromagnetic correlations for all distances, while the TD-NRG correctly predicts oscillations only between zero and antiferromagnetic correlations once R exceeds the Kondo length scale ξ_K.

4.3.3 Intrinsic correlations of the Fermi sea

Since our perturbative results agree remarkably well with our TD-NRG results, we can use our analytical approach to gain some insight into the correlations outside of the light cone. Medvedyeva proposed [114] that these correlations originate from the

intrinsic spin-spin correlations in the Fermi sea $\langle \vec{s}(0)\vec{s}(\vec{r})\rangle$ which are already present prior to the coupling of the impurity. These intrinsic entanglements of the Fermi sea between the local spin density and the spin density at a distance R are instantaneously probed once the impurity is coupled to the local spin density $\vec{s}(0)$ at time $t = 0$.
For a decoupled impurity $J = 0$, $\langle \vec{s}(0)\vec{s}(R)\rangle$ can be calculated analytically and in 1D it is given by

$$\langle \vec{s}(0)\vec{s}(R)\rangle = \frac{3\sin(k_F R)\sin(\frac{k_F R}{2})\cos(\frac{3}{2}k_F R)}{4V_u^2(k_F R)^2}. \tag{4.22}$$

A detailed derivation of Eq. (4.22) can be found in appendix D. As shown in Fig. 4.12a, the exact result of Eq. (4.22) coincides with the NRG data obtained by setting $J = 0$ in an equilibrium NRG calculation. This excellent agreement between the analytical and NRG results serves as a further evidence for the numerical accuracy of our mapping of Eqs. (4.6)-(4.8) to the two discretized and properly normalized Wilson chains for even and odd parity conduction bands.
In order to connect the intrinsic spin entanglement of the decoupled Fermi sea with the observed antiferromagnetic correlations outside of the light cone, we expand the perturbatively calculated $\chi(R,t)$ up to second order for small times $0 \leq tD \ll 1$ and perform the momentum integrations for the first- and second-order contributions analytically. Since the first-order term in the time tD vanishes, the leading order term is proportional to $\propto (tD)^2$ and decays as $\frac{1}{R^2}$ with the distance in 1D. Note the difference between the $\frac{1}{R^2}$ decay outside of the light cone for short times and the well understood $\frac{1}{R}$ decay inside the light cone when the equilibrium is reached. Therefore, we have plotted the perturbative results in 1D as $\chi(R,t)V_u\left(\frac{k_F R}{tD\pi}\right)^2$ in Fig. 4.12b to eliminate the time-dependence and compensate the spatial decay of the envelope function. For the coupling $\rho_0 J = 0.3$ the first-order contribution is shown as a red line, the second-order as a blue, and the sum of both is depicted as a green line in Fig. 4.12b.
Since the second-order in J contribution to $\chi(0,t)$ remains always zero in a short-time expansion, the time evolution of the antiferromagnetic correlation at the origin $R = 0$ is dominated by the first-order term which is proportional to $\propto Jt^2$. This leads to a time scale for the initial fast buildup of the antiferromagnetic correlation that is given by $\frac{1}{\sqrt{J}}$ which confirms the short-time results of the TD-NRG for $k_F R/\pi = 0.01$ as depicted in Fig. 4.8a.
The largest contribution for short times stems from the ferromagnetic correlation peak at around $k_F R/\pi = 0.65$. However, correlations are visible at all length scales which develop quadratically in time and decay with $\frac{1}{R^2}$ in distance. A comparison with Fig. 4.12a shows that the position of the maxima and minima agree remarkably well with those of the intrinsic correlation function $\langle \vec{s}(0)\vec{s}(R)\rangle$ of the Fermi sea and, furthermore, both envelope functions decay with $\frac{1}{R^2}$.

(a)

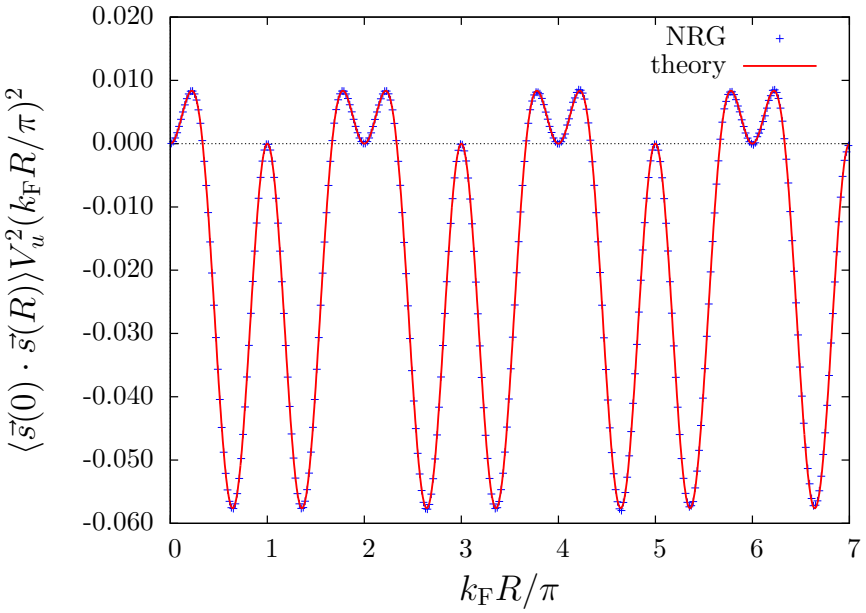

(b)

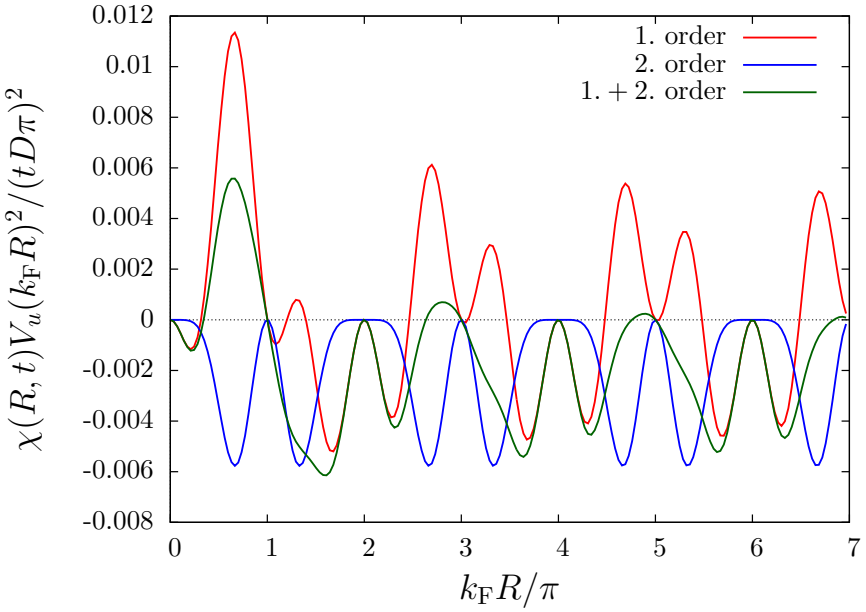

Figure 4.12: (a) The intrinsic spin-spin correlations of the Fermi sea between the spin densities $\vec{s}(0)$ and $\vec{s}(R)$ in 1D. Via the mapping to the even and odd conduction bands, we are able to measure bath properties at distance R with the NRG and get a perfect agreement between theory and NRG results. NRG parameters are $\lambda = 3$ and $N_s = 1200$. Figure taken from Ref. [124].
(b) For small times $tD \ll 1$ expanded first- and second-order contributions of $\chi(R,t)$ for $\rho_0 J = 0.3$ in 1D. Even for short times, we observe correlations for large distances. A comparison with (a) shows that the positions of these correlations coincide with the positions of the intrinsic correlations of the Fermi sea. So the correlations outside the light cone originate from these intrinsic correlations.

Since the first-order contribution is sensitive to the sign of J, its maxima contribute with equal sign as $\langle \vec{s}(0)\vec{s}(R)\rangle$ for ferromagnetic J and with opposite sign for an antiferromagnetic coupling. The second-order terms are independent of the sign of the coupling and only add antiferromagnetic contributions to $\chi(R,t)$. The positions of the antiferromagnetic peaks of the second-order contribution coincide with the antiferromagnetic peak positions of the spin-spin correlation function $\langle \vec{s}(0)\vec{s}(R)\rangle$ of the decoupled Fermi sea shown in Fig. 4.12a. However, the second-order contribution has no peaks and remains zero at the locations of the ferromagnetic peaks of $\langle \vec{s}(0)\vec{s}(R)\rangle$. In contrast, the first-order contribution shows peaks at every position where the intrinsic correlation function of the Fermi sea has a peak. If we add both contributions for antiferromagnetic couplings, the ferromagnetic peaks of the first-order contribution are attenuated by the antiferromagnetic peaks of the second-order contribution. Therefore, the sum of both orders contains only small ferromagnetic correlations for larger distances $k_\mathrm{F}R/\pi > 1$ and $\rho_0 J = 0.3$. The larger the coupling J the smaller these ferromagnetic correlations are due to the increasing influence of the second-order term.
We can conclude from this detailed analysis that the antiferromagnetic correlations directly on front of the light cone originate from the antiferromagnetic correlation peak at $k_\mathrm{F}R/\pi \approx 1.6$. This antiferromagnetic correlation also propagates with the Fermi velocity through the conduction band. The propagation of antiferromagnetic correlation for larger distances are not or only barely visible because of the $\frac{1}{R^2}$ decay of the intrinsic correlations.

4.3.4 Local moment regime: ferromagnetic coupling $J < 0$

We now extend our investigation of the full time-dependent correlation function $\chi(R,t)$ to ferromagnetic Kondo couplings. For ferromagnetic couplings the Hamiltonian approaches the local moment fixed point and the ground state is twofold degenerate in the absence of an external magnetic field. In the renormalization group (RG) process, the Kondo coupling is renormalized to zero. Nevertheless, the equilibrium spatial correlation function $\chi_\infty(R)$ remains finite for $T \to 0$ as discussed in Sec. 4.2.2. The reason for this is that the renormalization of the coupling to zero occurs on a lower energy scale than the formation of the correlations.
Figure 4.13 shows the time-dependent spin correlation function $\chi(R,t)$ for the ferromagnetic coupling $\rho_0 J = -0.1$. While panel (a) shows the TD-NRG calculation, the analytical result for the same parameters obtained in second-order perturbation theory is shown in panel (b). The analytical result differs significantly from the antiferromagnetic regime depicted in Fig. 4.11 since the first-order term is sign sensitive.
As in the Kondo regime, the perturbation theory and the TD-NRG results agree qualitatively remarkably well. The $2k_\mathrm{F}$ oscillations known from the RKKY interaction are clearly visible inside the light cone. Note that due to the sign change there is a phase shift compared to the Kondo regime: now the ferromagnetic correlations

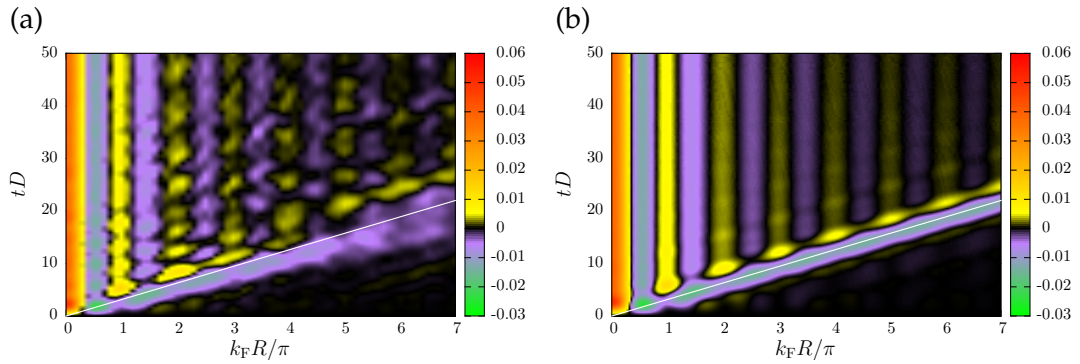

Figure 4.13: (a) Time-dependent spin correlation function $\chi(R,t)$ for a ferromagnetic coupling $\rho_0 J = -0.1$ in 1D as a color contour plot. NRG parameters are $\Lambda = 3$, $N_s = 1400$ and $N_z = 32$. (b) The correlation function $\chi(R,t)$ for the same parameters calculated perturbatively in second-order perturbation theory in J. Figures taken from [124].

occur at $k_F R/\pi = n$ and the antiferromagnetic correlations at half integer values $k_F R/\pi = n + \frac{1}{2}$.

Since a ferromagnetic correlation is built up at the impurity spin position $R = 0$ on a very short time scale $\propto \frac{1}{\sqrt{J}}$, and the total spin must be conserved, this time an antiferromagnetic correlation wave propagates spherically away from the impurity through the system with the Fermi velocity, which again has been added as a white line in both panels. Due to the sign change of the first-order contribution, the peak position of the propagation $t_{\max}$ is slightly shifted to earlier times with increasing $\rho_0 J$ for ferromagnetic couplings. Compared to the Kondo regime, the correlations outside of the light cone are stronger suppressed. Again, we can trace the origin of these correlations outside the light cone to the intrinsic entanglement of the Fermi sea which has already been discussed in the previous section 4.3.3.

4.3.5 Finite temperature: cutoff of the Kondo correlations

So far we have only investigated the time-dependent correlation function $\chi(R,t)$ for zero temperature. Now we extend the discussion to the propagation of the correlations at finite temperature. In Fig. 4.14 the difference between the time-dependent correlations functions for the two different temperatures (a) $T = 0$ and (b) $T = 2T_K$ is shown. Note that for Fig. 4.14a we have used the same data as for Fig. 4.6, however, this time the distance R is measured in units of the Kondo length scale ξ_K.

For both temperatures we observe the $2k_F$ oscillations for long times, the correlations outside of the light cone and the propagation of a ferromagnetic correlation wave with the Fermi velocity v_F as already discussed in Sec. 4.3.1. While for $\frac{R}{\xi_K} < 0.15$ the correlation functions for both temperatures agree well, for larger distances the correlations in and outside of the light cone are strongly suppressed for the finite temperature

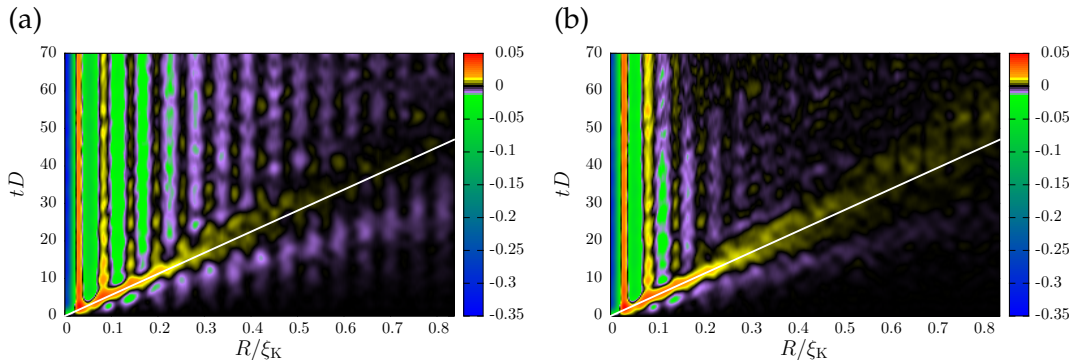

Figure 4.14: The correlation function $\chi(R,t)$ computed with the TD-NRG plotted as a color contour plot for the medium coupling $\rho_0 J = 0.3$ and a 1D dispersion for different temperatures. A comparison between the different correlation functions for (a) zero temperature and (b) the finite temperature $T = 2T_K$ reveals that the correlations inside and outside of the light cone vanish at around $R \approx 0.5\xi_K$ for $T = 2T_K$. NRG parameters are $\Lambda = 3$, $N_s = 1400$ and $N_z = 4$.

$T = 2T_K$. Once R exceeds the thermal length scale $\xi_T = \frac{v_F}{2T_K} = 0.5\xi_K$, these correlations are cut off. However, the ferromagnetic wave that propagates through the conduction band is amplified. An explanation for this effect is that due to the spin conservation and the strong suppression of the correlations inside and outside the light cone, the total spin has to be distributed over a larger area.

The approach to the equilibrium correlation function at large times is shown in Fig. 4.15. Here the spatial dependence of the correlation function $\chi(R, tD = 70)$ at the largest time $tD = 70$ is plotted for both temperatures using the data of Fig. 4.14. In the $T = 0$ case, the $2k_F$ oscillations between ferromagnetic and antiferromagnetic correlations are observed for small distances while for larger distances only antiferromagnetic correlations appear. For the finite temperature $T = 2T_K$, however, the correlations are cut off and due to the fast decay, only the first few oscillations are visible.

The inset of Fig. 4.15 shows the envelope of the correlation function $\chi(R, tD = 70)$ for the two different temperatures. To increase the numerical accuracy and reduce the unphysical oscillations, we used a higher number of kept NRG states N_s and higher number of z-averages N_z compared to Fig. 4.14. As expected from the equilibrium calculations, the envelope of the correlation function for $T = 0$ shows a power-law decay with the distance. For the finite temperature $T = 2T_K$ the envelope exhibits the expected exponential decay at short distances. At larger distances, although we have used higher values for N_s and N_z, the numerical noise of the TD-NRG exceeds the rapid suppression of the correlation function. Therefore, the inset shows only the beginning of the exponential decay of the correlation function for $T = 2T_K$. In order to observe the exponential decay at larger distances, one needs to resort the equilibrium NRG, cf. Fig. 4.3.

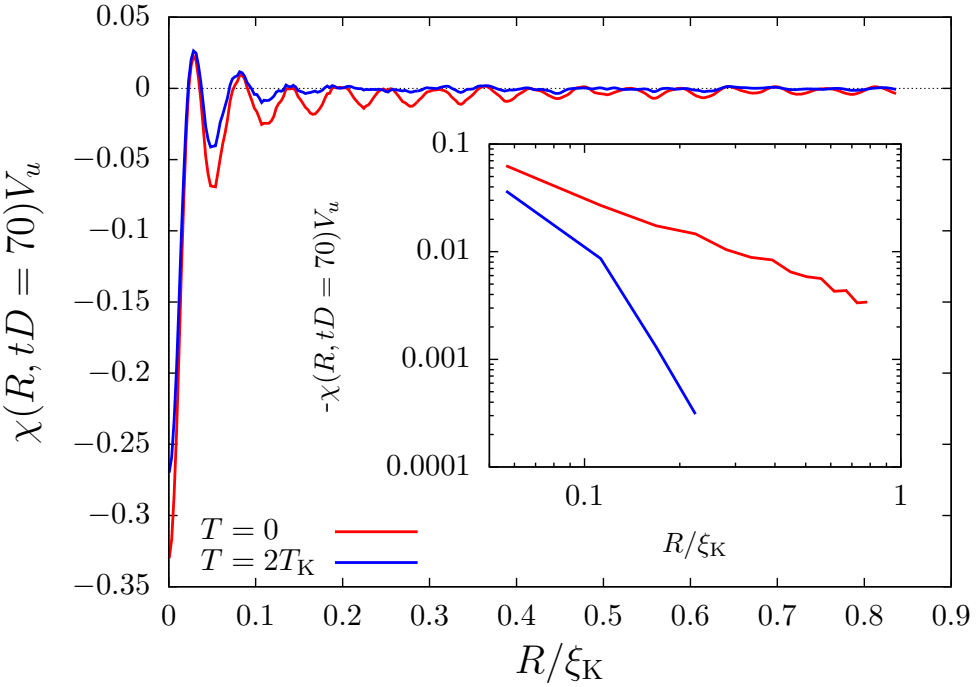

Figure 4.15: The correlation function $\chi(R, tD = 70)$ for the two different temperatures $T = 0$ and $T = 2T_K$ for the medium coupling $\rho_0 J = 0.3$ and the constant time $tD = 70$ in 1D. For $T = 0$, the RKKY-like $2k_F$ oscillations are observed while for $T = 2T_K$ the correlations are cut off. We used the same data as for Fig. 4.14. The inset shows the envelope function of $\chi(R, tD = 70)$. To increase the numerical accuracy we used $\Lambda = 3$, $N_s = 2400$ and $N_z = 16$ as NRG parameters for the inset.

4.4 Response

Now we extend the discussion to a real response function. We investigate the conduction electron spin-density polarization $\langle \vec{s}(R,t) \rangle$ as a function of an externally applied local field $\vec{B}(t)$ within linear response theory. The retarded spin-spin susceptibility tensor must be diagonal and proportional to the unit matrix because the Kondo Hamiltonian is rotationally invariant in the spin space. Therefore, we only investigate the conduction electron spin-density polarization in z direction $\langle s^z(R,t) \rangle$ at a distance R caused by applying a local magnetic field $\vec{B}(t) = B\vec{e}_z$ acting on the impurity spin $\vec{S}_{\text{imp}}$ with $\vec{e}_z$ being the unit vector in z direction.
Within the linear-response theory we can write the spin-density polarization $\langle s^z(R,t) \rangle$

$$\langle s^z(R,t) \rangle = \langle s^z(R, t = -\infty) \rangle + \int_{-\infty}^{\infty} \chi^r_{\text{imp}-c}(R, t - t') \Delta(t')\, dt' \tag{4.23}$$

where the retarded spin susceptibility

$$\chi^r_{\text{imp}-c}(R,t) = -i \langle \left[s^z(R,t), S^z_{\text{imp}} \right] \rangle \theta(t) \tag{4.24}$$

is a true response function and $\Delta(t) = g\mu_B B(t)$ is the locally applied time-dependent Zeeman splitting. At $t = -\infty$ the system is unpolarized and, therefore, the term $\langle s^z(R, t = -\infty)\rangle = 0$ can be neglected. Since the spin-density $s^z(R,t)$ and the impurity spin S^z_{imp} are both Hermitian operators, the spectrum

$$\rho^r_{\text{imp}-c}(\omega) = \lim_{\delta\to 0^+} -\frac{1}{\pi}\text{Im}\chi^r_{\text{imp}-c}(R, \omega + i\delta) \tag{4.25}$$

has to be an odd function $\rho^r_{\text{imp}-c}(\omega) = -\rho^r_{\text{imp}-c}(-\omega)$ [127]. Here $\chi^r_{\text{imp}-c}(R, \omega + i\delta)$ is the Laplace transformation of $\chi^r_{\text{imp}-c}(R,t)$. Therefore, we can write the inverse Laplace transformation as a purely real integral

$$\chi^r_{\text{imp}-c}(R,t) = -2\int_0^\infty \rho^r_{\text{imp}-c}(R,\omega)\sin(\omega t)\theta(t)\, d\omega. \tag{4.26}$$

To calculate the response function using the NRG, we first compute the spectral function $\rho^r_{\text{imp}-c}(\omega)$ as described in Sec. 3.3 and insert this result into Eq. (4.26). Finally, the spin-density polarization $\langle s^z(R,t)\rangle$ can be calculated using the convolution Eq. (4.23).

4.4.1 Retarded host susceptibility $\chi^r_{c-c}(R,t)$

Before we discuss the susceptibility $\chi^r_{\text{imp}-c}(R,t)$, we investigate the retarded equilibrium host spin-density susceptibility

$$\chi^r_{c-c}(R,t) = -i\langle\left[s^z(R,t), s^z(0,0)\right]\rangle\theta(t) \tag{4.27}$$

which can be calculated analytically for $J = 0$. A detailed discussion about the analytical derivation of $\chi^r_{c-c}(R,t)$ and its spectral function $\rho^r_{c-c}(r,\omega)$ can be found in appendix E. For a 1D dispersion, we obtain for the spectral function

$$\begin{aligned}\rho^r_{c-c}(R,\omega) =& \frac{1}{2\pi V_u^2 N^2}\sum_{k_1,k_2}\left[f(\epsilon_{k_2}) - f(\epsilon_{k_1})\right] \\ &\times\left(\pi\cos\left[(k_2-k_1)R\right]\delta(\omega - (\epsilon_{k_1} - \epsilon_{k_2})) + \frac{\sin\left[(k_2-k_1)R\right]}{\omega - (\epsilon_{k_1} - \epsilon_{k_2})}\right).\end{aligned} \tag{4.28}$$

This analytical expression of the spin-spin susceptibility contains the dimensionless frequency $k_F R$ that causes increasing frequency oscillations with increasing distance R. Since the high energy spectrum of the NRG is much less accurate than the low energy part, the numerical effort for a calculation of these retarded spin-spin susceptibilities and their spectral functions using the NRG grows exponentially at large distances. While the analytical calculation makes full use of the bath continuum, the conduction band is discretized on a logarithmic energy scale and consist of only a few bath sites representing the high energy spectrum. Note that the NRG is geared towards the

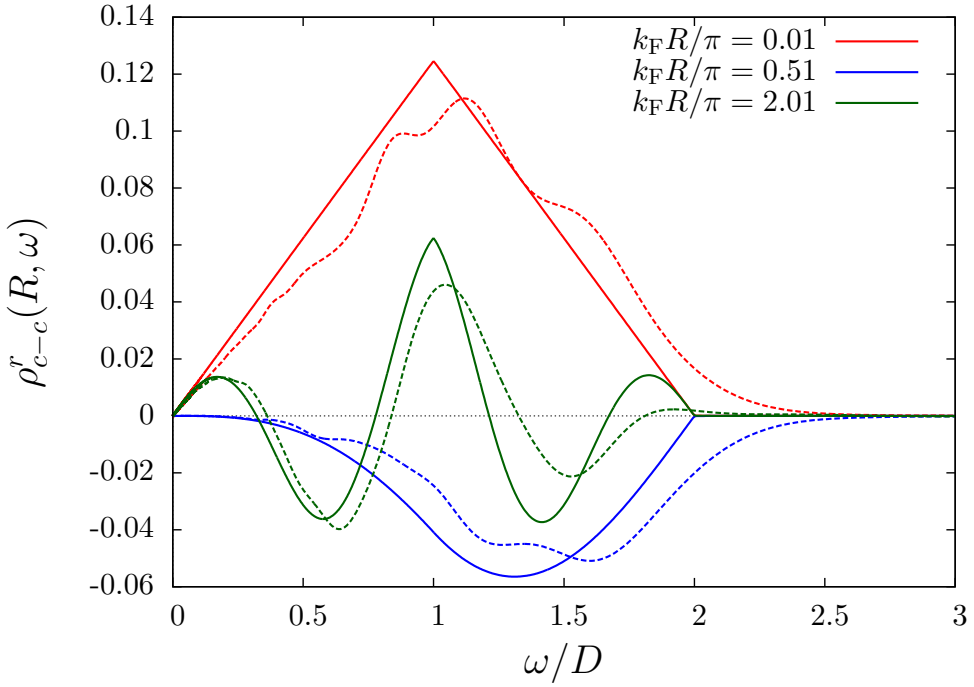

Figure 4.16: The spectral function $\rho^r_{c-c}(R,\omega)$ of the retarded host spin-density susceptibility $\chi^r_{c-c}(R,t)$ for a decoupled impurity ($J = 0$) and different distances R. The solid lines show the exact analytical result and the dashed lines the results obtained from a NRG calculation. NRG parameters are $\Lambda = 3$, $N_s = 3000$ and $N_z = 16$. Figure taken from [124]

calculation of the impurity properties, while in this case we are using it to compute a bath correlation function. Therefore, we are limited to short distances in the NRG calculation because for larger distances the NRG cannot capture the high frequency oscillations at high energies.

To illustrate this point, Fig. 4.16 shows a comparison between the analytical and the NRG spectral function as a benchmark. Apart from the fact that the NRG spectrum is slightly shifted to higher energies due to the NRG spectral broadening, the agreement between the analytical and NRG results is very good at short distances. However, significant deviations are observed for $k_F R = 2.01\pi$. While for these distances also the low energy parts of the spectra agree very well, the NRG completely fails to capture the high energy maximum at $\frac{\omega}{D} \approx 1.7$ due to the limitation of the NRG to accurately resolve the high energy parts of the oscillations in the spectrum. The frequency scale of these oscillations is of the order of the bandwidth D as can be seen from Eq. (4.28). For large distances R, these high energy oscillations cannot be properly resolved by the NRG because for a finite $\Lambda > 1$ the NRG provides only a very low resolution of excitations energies in this frequency range. However, the low energy spectrum is excellently recovered by the NRG as expected.

After benchmarking the accuracy of the spectral functions at small distances, we have

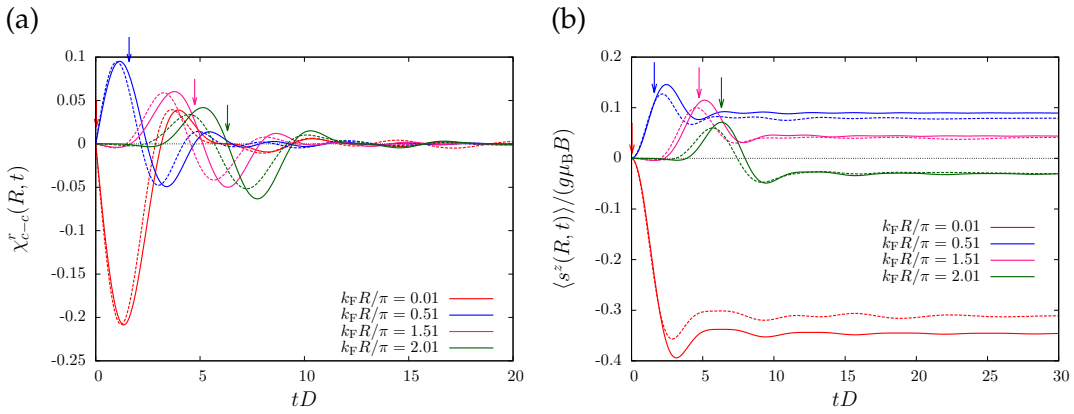

Figure 4.17: (a) The retarded host spin-density susceptibility $\chi^r_{c-c}(R,t)$ plotted vs. the time for different distances R. The solid lines show the exact analytical result while the dashed lines depict the results obtained from a NRG calculation. The arrows in the top indicate the time $\tau = R/v_F$. (b) The conduction electron spin-density polarization $\langle s^z(R,t)\rangle$ vs. time as a response to a Zeeman splitting $\Delta(t) = g\mu_B B\theta(t)$ locally applied to the spin-density $s^z(0)$ at the origin. $\langle s^z(R,t)\rangle$ has been normalized to the Zeeman energy $\Delta_0 = g\mu_B B$. For the calculation of $\langle s^z(R,t)\rangle$ the convolution Eq. (4.23) and the susceptibility $\chi^r_{c-c}(R,t)$ shown in (a) have been used. As before, the arrows indicate the time $\tau = R/v_F$. NRG parameters are $\Lambda = 3$, $N_s = 3000$ and $N_z = 16$.

used the corresponding version of Eq. (4.26) for $\chi^r_{c-c}(R,t)$ to calculate the retarded host spin-density susceptibilities in time domain. The $\chi^r_{c-c}(R,t)$ obtained from the NRG are shown in Fig. 4.17a as dashed lines while the analytical susceptibilities are depicted as solid lines. We observe a maximum that is followed by a minimum and both propagate with the Fermi velocity v_F through the system. The agreement between the analytical and NRG results is quite good, however, the NRG results are slightly shifted to earlier times which originates from the shift of spectral weight to higher energies due to the spectral broadening in the NRG as illustrated in Fig. 4.16. The center of the propagation is expected to be at the time $\tau = \frac{R}{v_F}$ which is marked by arrows in the top of Fig. 4.17a. The analytical susceptibility can be calculated for arbitrary distances R. Indeed, we find that for the distance $k_F R/\pi = 2$ and larger distances[3] the zero-crossing between the maximum and the minimum of the analytical result is exactly located at the time $\tau = \frac{R}{v_F}$. Furthermore, the RKKY-like $2k_F$ oscillations can already be observed in $\chi^r_{c-c}(R,t)$ since for odd distances $k_F R/\pi = n + \frac{1}{2}$ the maximum is larger while for multiples of the distance $k_F R/\pi = n$ the minimum is larger.

To clearly see the RKKY-like oscillations and how a response propagates through the system, we calculate the time- and spatially-dependent conduction electron spin-density polarization $\langle s^z(R,t)\rangle$. For this purpose we apply a local fictitious Zeeman splitting $\Delta(t) = g\mu_B B\theta(t)$ locally to $s^z(0)$ at the origin that induces a spin-density polarization. A comparison between the analytical results (solid lines) and the NRG

[3] For clarity, distances larger than $k_F R/\pi = 2$ are not shown in Fig. 4.17a and b.

results (dashed lines) is shown in Fig. 4.17b. Here we have normalized $\langle s^z(R,t)\rangle$ to the Zeeman energy $\Delta_0 = g\mu_B B$ to eliminate the trivial proportionality to the applied field strength. For the calculation of both spin-density polarizations we have used the convolution of Eq. (4.23), where $\chi^r_{\mathrm{imp}-c}(R,t)$ has been replaced by $\chi^r_{c-c}(R,t)$.
The induced time-dependent spin-density polarization can be understood as a response to a spin wave propagating with the Fermi velocity v_F through the system and a consecutive fast equalization. In the time-dependent spin-density polarization the RKKY-like $2k_F$ oscillations are clearly visible. For multiples of the distance $k_F R/\pi = n$ the long-time value of $\langle s^z(R,t)\rangle$ aligns parallel, and for odd multiples of the distance $k_F R/\pi = n + \frac{1}{2}$ antiparallel to the spin-density at the origin $s^z(0)$. In the analytical results the maximum of the spin wave is located at the expected time $\tau = \frac{R}{v_F}$ for distances $k_F R/\pi \geq 2$ while for shorter distances we observe a slight shift. In Fig. 4.17b the time τ is also indicated by arrows. As for $\chi^r_{c-c}(R,t)$ the slight shift of the NRG results to earlier times can be traced back to the NRG spectral broadening. Some response is found outside of the light cone related to the finite width of the spin wave. This response originates from the maximum directly in front of $\tau = \frac{R}{v_F}$ in the susceptibility $\chi^r_{c-c}(R,t)$. The reason for the finite width of the spin wave is the finite spatial resolution which is directly linked to the momentum cutoff in the analytical formula defined by the restriction of the k values to the first Brillouin zone. A sharp suppression of the signal outside of the light cone would require to send the momentum cutoff to infinity as done in the analytical calculation of Ref. [114].
By comparing the numerical results with the analytical ones, it becomes clear that the small oscillations after the spin wave around the long-time limit of the spin-density are not a numerical artifact due to the NRG discretization errors but related to the finite bandwidth and the linear conduction band dispersion.
Note that we observe for the distance $k_F R/\pi = 0.01$ a significant deviation between the long-time limit of the analytically calculated spin-polarization and the one calculated with the NRG. In appendix F we show that the stationary value is determined by the integral over $\frac{\rho^r_{c-c}(R,\omega)}{\omega}$. As discussed above and shown in Fig. 4.16, the finite resolution and the NRG broadening shifts some spectral weight to higher energies compared to the exact solution and, therefore, we find a reduced value for $|\langle s^z(0, t\to\infty)\rangle|$ since $\frac{\rho^r_{c-c}(0,\omega)}{\omega}$ does not change sign. The accuracy of the long-time limit $\langle s^z(R, t\to\infty)\rangle$ increases once the spectral function exhibits sign changes because in this case the broadening errors partially cancel out.

4.4.2 Retarded susceptibility $\chi^r_{\mathrm{imp}-c}(R,t)$

Now we turn to the retarded spin susceptibility $\chi^r_{\mathrm{imp}-c}(R,t)$ for finite couplings J describing the response of the conduction band spin-density at a distance R to a perturbative magnetic field in z direction applied locally to the impurity spin. The spectral function of $\chi^r_{\mathrm{imp}-c}(R,t)$ is shown in Fig. 4.18 for different distances R to illustrate the

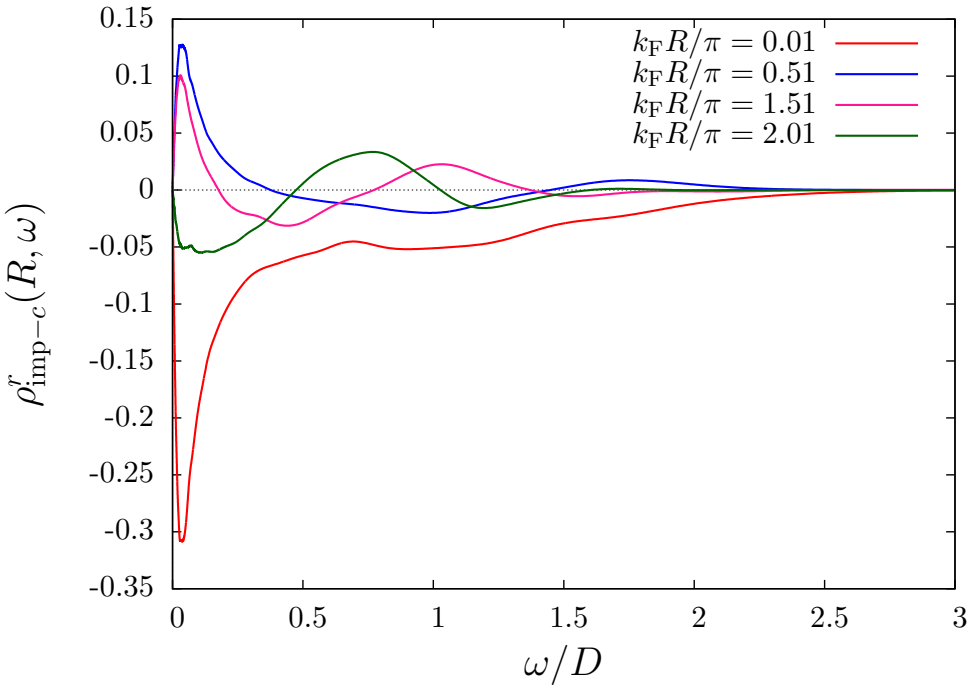

Figure 4.18: The spectral function of the retarded spin susceptibility $\rho^r_{\mathrm{imp}-c}(R,\omega)$ plotted vs. ω/D for different distances and $\rho_0 J = 0.3$. Compared to $\rho^r_{c-c}(R,\omega)$ spectral weight is shifted to lower energies. The distinctive peak at $\omega \approx T_\mathrm{K}$ reflects the Kondo physics. NRG parameters are $\Lambda = 2.25$, $N_s = 3000$ and $N_z = 16$.

changes due to the presence of the Kondo spin. We restrict ourselves to distances $k_\mathrm{F}R/\pi \leq 2$ because we expect that, as before for $\chi^r_{c-c}(R,t)$, the NRG cannot capture the high frequency oscillations at high energies for large distances.

The increasing number of oscillations in the frequency spectra with increasing distance R are clearly visible. We observe a change of sign in $\rho^r_{\mathrm{imp}-c}(R,\omega)$ compared to $\rho^r_{c-c}(R,\omega)$ due to the antiferromagnetic coupling J. Furthermore, significant spectral weight is now located at low energies. The Kondo physics is reflected in a distinctive peak at $\omega \approx T_\mathrm{K}$ which appears for all distances R.

Figure 4.19a shows the time-dependent susceptibility $\chi^r_{\mathrm{imp}-c}(R,t)$ vs. the rescaled time tT_K for different distances. The inset of Fig. 4.19a shows $\chi^r_{\mathrm{imp}-c}(R,t)$ vs. tD for short times and the arrows indicate the time $\tau = \frac{R}{v_\mathrm{F}}$. We observe a maximum that propagates with the Fermi velocity v_F through the conduction band and for larger distance the center of the maximum is around τ. However, we expect that the real susceptibility is slightly shifted to larger times because, as for $\chi^r_{c-c}(R,t)$, the spectrum shown in Fig. 4.18 should be slightly shifted to higher energies due to the broadening in the NRG. Compared to the retarded host susceptibility $\chi^r_{c-c}(R,t)$ it takes much longer until the susceptibility is zero once again after the maximum has passed: the time scale is given by the slow Kondo time scale $\frac{1}{T_\mathrm{K}}$.

In Fig. 4.19b, the time-dependent spin-polarization $\langle s^z(R,t)\rangle$ is shown vs. the rescaled

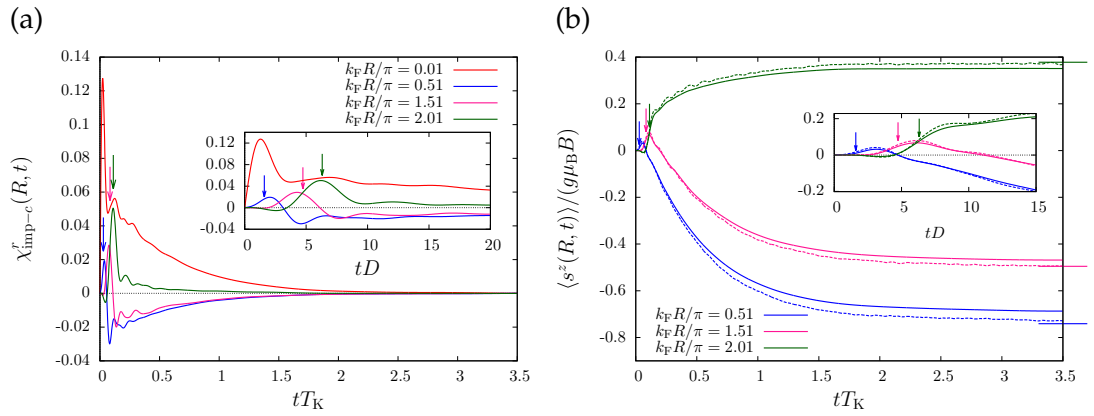

Figure 4.19: (a) The time-dependent retarded spin susceptibility $\chi^r_{\mathrm{imp}-c}(R,t)$ plotted against the rescaled time tT_K for different distances and $\rho_0 J = 0.3$. (b) The time-dependent spin-polarization $\langle s^z(R,t)\rangle$ vs. the rescaled time tT_K after switching on the Zeeman splitting $\Delta(t) = g\mu_\mathrm{B}B\theta(t)$ on the impurity spin. Dashed lines indicate $\langle s^z(R,t)\rangle$ calculated with the TD-NRG for a very weak magnetic field $g\mu_\mathrm{B}B/D = 10^{-6}$ applied to the impurity. In the insets the respective short-time behaviors are shown and the arrows indicate the time $\tau = R/v_\mathrm{F}$. The horizontal lines on the right of (b) mark the equilibrium value $\langle s^z(R,\infty)\rangle/(g\mu_\mathrm{B}B)$ obtained from an equilibrium NRG calculation with $N_z = 1$ and a small applied magnetic field $g\mu_\mathrm{B}B/D = 10^{-6}$. NRG parameters are $\Lambda = 2.25$, $N_s = 3000$ and $N_z = 16$.

time tT_K for a Zeeman splitting $\Delta(t) = g\mu_\mathrm{B}B\theta(t)$ applied to the impurity spin. Due to the antiferromagnetic coupling J, we observe a sign change in the response compared to the response obtained from $\chi^r_{c-c}(R,t)$. Now for multiples of $k_\mathrm{F}R/\pi = n$ the conduction electron spin-density aligns antiparallel, and for odd multiples of $k_\mathrm{F}R/\pi = n + \frac{1}{2}$ the spin-density aligns parallel to the impurity spin for long times. These $2k_\mathrm{F}$ oscillations for the long-time limit of the spin-polarization reflect the RKKY mediated spin response.

As for the susceptibility $\chi^r_{\mathrm{imp}-c}(R,t)$ we can identify two relevant time scales in the induced spin-density: the fast light cone time scale $\tau = \frac{R}{v_\mathrm{F}}$ and the slow Kondo time scale $\frac{1}{T_\mathrm{K}}$. The inset of Fig. 4.19b shows the spin-density polarization for short times and the arrows once again indicate the time τ. Until the spin-wave has propagated from the impurity to the distance R, the spin-density polarization remains almost zero and afterwards $\langle s^z(R,t)\rangle$ starts to build up. Again, we can trace back the finite width of the spin-wave to the finite momentum cutoff of our single symmetric conduction band used in the NRG calculations as already discussed in Sec. 4.4.1. In contrast to the fast response of the decoupled Fermi sea, where the equilibrium value of the spin-polarization is reached rather fast on the time scale $\frac{1}{D}$, the steady state value of the response for a finite coupling J is reached very slowly. The long-time approach is governed by the Kondo time scale $\frac{1}{T_\mathrm{K}}$ and independent of the distance R as shown in Fig. 4.19b.

To gauge the quality of the long-time value of the spin-polarization $\langle s^z(R,t)\rangle$ obtained

from the linear response theory, we have used a NRG equilibrium calculation to compute the equilibrium value $\frac{\langle s^z(R,\infty)\rangle}{g\mu_B B}$ for a very small magnetic field $\frac{g\mu_B B}{D} = 10^{-6}$ applied to the impurity spin. These values are shown as horizontal lines on the right of Fig. 4.19b. For a vanishing magnetic field, the linear response theory becomes exact and the steady state value must coincide with the equilibrium expectation value. Similar to the case for the decoupled Fermi sea, the absolute value of the steady state $|\langle s^z(R, t \to \infty)\rangle|$ calculated from the spectral function is slightly smaller than the equilibrium value due to the shift of spectral weight to higher energies caused by the NRG broadening.
As a second verification of the quality, we measure $\langle s^z(R,t)\rangle$ after switching on a very weak magnetic field $\frac{g\mu_B B}{D} = 10^{-6}$ applied to the impurity spin using the TD-NRG. These results are depicted as dashed lines in Fig. 4.19b. The agreement between $\langle s^z(R,t)\rangle$ calculated from $\chi^r_{\mathrm{imp}-c}(R,t)$ and the one obtained from the TD-NRG is remarkably good especially for short times which are shown in the inset of Fig. 4.19b. Only for longer times both curves start to deviate and the spin polarization of the TD-NRG reaches, as expected, the equilibrium long-time value $\langle s^z(R,\infty)\rangle$ marked by the horizontal lines. This demonstrates that the NRG provides reliable results for the spectral function $\rho^r_{\mathrm{imp}-c}(R,\omega)$ at short distances.

4.5 Summary

We have presented a detailed study of the temporal and spatial propagation of Kondo correlations for ferro- and antiferromagnetic Kondo couplings J using the TD-NRG. In our NRG approach we have divided the conduction band into two distance dependent even and odd parity bands and have used these parity bands to construct two Wilson chains. Furthermore, we have considered the full energy-dependence and the correct normalization of the bands to obtain accurate results. The quality of our mapping has been benchmarked by: (i) calculating the intrinsic spatial dependence of the spin-spin correlation of the decoupled ($J = 0$) Fermi sea with the equilibrium NRG which perfectly coincides with the exact analytical calculation for the full continuum, and (ii) checking the fulfillment of the analytically known sum rules of the equilibrium correlation function for ferro- and antiferromagnetic couplings. The deviation of our numerical data from the sum rule is only 2% for a 1D dispersion. This provides a second independent check of our distance dependent NRG mapping.
The results obtained from our equilibrium NRG calculations significantly differ from previous NRG results [47] where only antiferromagnetic correlation for all distances R were found. While for large distances $R \gg \xi_K = \frac{v_F}{T_K}$ our results agree with the previous ones [47] in the way that we also only observe antiferromagnetic correlations, we find oscillations between ferro- and antiferromagnetic correlations for short distances $R \ll \xi_K$ which is, however, in accordance with predictions made by Affleck and his co-workers [125]. In agreement with Ref. [47], a $\frac{1}{R^D}$ decay at short distances $R \ll \xi_K$

and a $\frac{1}{R^{D+1}}$ decay at large distances $R \gg \xi_K$ is observed for the envelope function of $\chi_\infty(R)$ for a D-dimensional dispersion. The crossover between these two decays occurs at around the Kondo length scale $R \approx \xi_K$ which supports the common interpretation of ξ_K as being the size of the Kondo screening cloud.
In the ferromagnetic regime, the Kondo length scale ξ_K diverges and, therefore, a $\frac{1}{R^D}$ decay and oscillations between ferromagnetic and antiferromagnetic correlations is observed for all distances. Additionally, the positions of the minima and maxima are interchanged due to the sign change of the Kondo coupling J.
For the full time-dependent correlation function $\chi(R,t)$ we find a light cone defined by the Fermi velocity v_F that divides the parameter space of $\chi(R,t)$ into two parts. As a consequence of a build up of local antiferromagnetic correlations, a ferromagnetic wave propagates on the light cone away from the impurity location. Inside the light cone, the correlation function develops rather rapidly and approaches towards the equilibrium correlation function. In accordance with this equilibrium correlation function, for long times the typical decaying RKKY-like $2k_F$ oscillations in spatial dependence are observed. Additionally, the long-time behavior exhibits only antiferromagnetic correlations for large distances $R \gg \xi_K$. For ferromagnetic couplings, the long-time limit of the time-dependent correlation function also agrees with the equilibrium correlation function so that $\chi(R, t \to \infty)$ remains oscillating between ferro- and antiferromagnetic correlations and always decays as $\frac{1}{R}$.
Surprisingly, we have found in our TD-NRG data for ferro- as well as antiferromagnetic Kondo couplings a build up of correlations outside of the light cone that do not decay exponentially. Using a second-order perturbative expansion in the Kondo coupling J, we have been able to trace back these correlations to the intrinsic entanglement of the Fermi sea. Furthermore, the sum of the first- and second-order contribution provides an explanation for the observed difference between ferro- and antiferromagnetic Kondo couplings which originate from the fact that the first order is sensitive to the sign of the coupling J.
The extension of our NRG and TD-NRG calculations to finite temperatures have shown the emergence of a new length scale $\xi_T = \frac{v_F}{T}$. Once the distance R exceeds ξ_T both correlations, in- and outside of the light cone, are exponetially cut off.
Moreover, we have presented data for the retarded susceptibility $\chi^r_{\mathrm{imp}-c}$ and its spectra for different distances R. We have used this susceptibility to calculate the response of the spin-density polarization $\langle s^z(R,t)\rangle$ induced by a very weak magnetic field applied locally on the impurity spin. For the real-time response of $\langle s^z(R,t)\rangle$ we have found almost no correlations outside of the light cone. The finite width of the spin wave that propagates through the system could be traced back to the finite momentum cutoff. However, benchmark calculations with the retarded host spin-density susceptibility $\chi^r_{c-c}(R,t)$, which can be calculated analytically, have shown that this method yields reliable results only for short distances $k_F R/\pi \leq 2$.

Chapter 5

Metal-molecule complexes on an Au(111) surface

A comparison between STS and NRG spectra

In the last few years the interest in magnetic properties of nanoscale structures has been growing rapidly. The reason for this is the demand to design miniaturized spin-based devices, e.g. for spintronics or quantum computation [30, 128]. The idea of combining the molecular pathway with magnetism is now attracting more attention [129, 130] because molecular compounds demonstrate a remarkable tendency to self-assemble. For this reason it is essential to obtain a better understanding of spin and charge transfer processes between molecules, surfaces and even single atoms. In this context, dimers of two molecules constitute important model systems, since they are simple and yet embody the crucial physics: the competition of interactions within the nanostructure with those between the nanostructure and its environment.

This chapter is divided into two parts: At first, in Sec. 5.1 the formation of a radical and the existence of a local moment after adsorption of a single Au atom onto a PTCDA molecule deposited on an Au(111) surface is demonstrated by observing a zero-bias differential conductance peak in the scanning tunneling spectroscopy (STS) spectrum that originates from the Kondo effect. For the theoretical description of the properties of the Au-PTCDA complex a hierarchy of methods is used, ranging from density functional theory (DFT) including a van der Waals correction to many-body perturbation theory (MBPT) and the numerical renormalization group (NRG) approach. The combined DFT/MBPT+NRG approach provides an accurate description of the low-energy excitation spectrum of the spin degree of freedom, predicting a Kondo temperature very close to the experimental value. Furthermore, we provide a guideline how to extract the Kondo temperature reliably from the experiment in a particle-hole asymmetric case by analyzing the universality of various definitions of the Kondo temperature T_K in detail.

In the second part in Sec. 5.2 the interaction between two adjacent Au-PTCDA complexes is investigated. We propose a novel approach to tailor the magnetic properties

of a nanostructure which is not based on a magnetic exchange interaction. Instead, it relies on the systematic use of the ubiquitous non-magnetic chemical interaction between the components of the nanostructure. The approach is based on spin-moment carrying orbitals of the Au-PTCDA that are extended in space and allow, therefore, the direct coupling of magnetic properties to wave function overlap. If the wave function overlap between the two monomers is changed, the dimer is tuned through a quantum phase transition from a triplet to a singlet ground state.
Since we compare the results of the NRG with experimental data, we use the A_Λ factor of Eq. (3.17) in this chapter in order to achieve more accurate results.

5.1 Monomer

We start with the investigation of the monomer where a metal-molecule complex is constructed that is a paramagnetic radical. Unlike common molecule magnets where the spin is usually located in a d or f orbital, the spin is transferred into a π-orbital that extends over the whole molecule. The advantage of such an extended radical is its increased probability to interact with its neighbors, offering the potential to utilize this coupling. In the experiment, chemically bonded metal-molecule complexes are formed by reacting perylene-tetracarboxylic dianhydride (PTCDA) molecules, which are adsorbed on an Au(111) surface, with a single Au atoms. These Au-PTCDA complexes are investigated by means of scanning tunneling microscopy (STM).
The observation of the Kondo effect in the experiment is an unambiguous proof that the Au-PTCDA complex has indeed an unpaired electron. This electron generates a local moment in the π-orbital due to the large Coulomb interaction compared to the electron substrate coupling.
On the theory side, a DFT calculation including van der Waals corrections is used to describe the geometrical structure of the Au-PTCDA complex. The results are in perfect agreement with the experimental observations.
However, a correct physical description of the local moment formation and the Kondo effect is not possible with such a mean field approach. Therefore, we use the DFT plus MBPT results as input parameters for NRG calculations and obtain the excitation spectrum of the complex at high and low energies.
For this purpose the full energy dependent hybridization function between the Au-PTCDA complex and the substrate is employed which is extracted from the DFT/MBPT approach. This enables us to achieve a quantitative description of the electronic properties of the Au-PTCDA/Au(111) complex, predicting a Kondo temperature which is within 1 K of the experimentally measured one.
The results of this section have already been published in [131].

5.1.1 Experiment and DFT: setup and theory

In the following, we briefly discuss the experimental setup and the theory for the DFT calculations. The experiments were done at the Peter Grünberg Institute in the Forschungszentrum Jülich by Taner Esat, Christian Wagner, Ruslan Temirov and F. Stefan Tautz while the DFT calculations were carried out at the Institut für Festkörpertheorie at the Westfälische Wilhelms-Universität Münster by Thorsten Deilmann, Peter Krüger and Michael Rohlfing.

Experimental setup

For the experimental setup an atomically clean Au(111) surface was prepared. Afterwards a submonolayer film of PTCDA molecules was deposited onto the Au(111) surface using a Knudsen cell. The whole sample was then transferred into a low-temperature STM with a base-temperature of $T = 9.5$ K. By heating a thin gold wire, gold atoms were evaporated onto the PTCDA submonolayer. The clean gold surface was then scanned with the STM until the spectroscopic signature of the adsorbed Au atoms appeared and differential conductance $dI/dV(V)$ spectra were recorded.
For the investigation of the Kondo effect the differential conductance spectrum was measured at different temperatures. Since broadening effects due to temperature have a crucial effect on the linewidths of narrow peaks in STS, it is essential to take these effects into account. Therefore, the measured spectra were deconvoluted [132].

DFT: theory

In addition to the experimental measurements, the system is also investigated theoretically by computing its geometrical and electronic structures. The geometrical structure is calculated with DFT using a generalized gradient approximation (GGA) [133] which also considers the van der Waals interaction [134] while for the mean field electronic structures a hierarchy of DFT calculations with local density approximation (LDA) or local spin density approximation (LSDA) combined with MBPT is employed.
This combined approach is required since the electronic properties of organic molecules in LDA often suffer from a distinct underestimation of the gap between the highest occupied molecular orbital (HOMO) and lowest unoccupied molecular orbital (LUMO). Therefore, the MBPT replaces the exchange potential of the DFT by the self-energy operator, for which the GW approximation [135] is used resulting in more realistic quasiparticle (QP) energies. However, including the metal substrate in a GW calculation is a difficult task and, hence, a perturbative L(S)DA+GdW approach [136] as a further approximation is introduced which yields reliable QP energies by employing a model for the dielectric screening due to the substrate. In this approach the substrate is only included in terms of its dielectric polarization. Previous investigations using this method have shown good agreement with experiment [137].

The spectrum of a state $|\phi_i\rangle$ in the full system is then given by its projected density of states (PDOS)

$$\rho_i(E-\Delta_i) = \sum_n |\langle \Psi_n | \phi_i \rangle|^2 \, \delta(E - E_n - \Delta_i). \tag{5.1}$$

Here, E_n is the energy of the full Au-PTCDA/Au(111) system corresponding to the wave function $|\Psi_n\rangle$, $|\phi_i\rangle$ denotes the wave functions of a few relevant states of the Au-PTCDA system where the Au(111) surface has been excluded and Δ_i is the QP correction obtained from the L(S)DA+GdW.
The occupation of the orbital i is determined by the PDOS according to

$$n_i = \int_{-\infty}^{E_F} \rho_i(E-\Delta_i)\, dE \tag{5.2}$$

while the intraorbital Coulomb repulsion U_i in orbital i is given by

$$U_i = \int\int |\phi_i(\vec{r})|^2 W(\vec{r},\vec{r}') |\phi_i(\vec{r}')|^2 \, d^3r d^3r', \tag{5.3}$$

where W is the screened Coulomb interaction. For further details about the calculations of the PDOS, the QP shift and the intraorbital Coulomb repulsion we refer the reader to Ref. [138].
Note, that such a mean field approach is incapable to describe the local moment formation or the Kondo effect correctly and, therefore, NRG calculations are required to incorporate dynamical correlation effects. However, the LDA-GdW results can be used as a starting point for the NRG.

5.1.2 Experiment and DFT: results

The Au-PTCDA complex and its structure

Figure 5.1 shows the PTCDA layer after the Au atoms have been deposited. In the inset the area around the adsorbed Au atoms is depicted in more detail. The PTCDA molecules arranged into the so-called herringbone structure on the Au(111) surface are clearly visible. The adsorbed Au adatoms appear as circles with a diameter of about 10 Å in the STM images.
The precise adsorption positions of the Au atoms relative to the PTCDA layer are shown in more detail in Fig. 5.2a. The centers of the adsorbed Au atoms (blue spots) are close to one of the two carbon atoms (gray circles) that are located midway along the edges of the PTCDA molecule. Due to the symmetry of the unit cell of the freestanding PTCDA layer, all data points can be displayed within one of its quadrants. This allows four equivalent adsorption positions on one PTCDA molecule.
The agreement between the experimentally observed adsorption positions of the Au atoms and the positions predicted by DFT calculations is very good. The potential

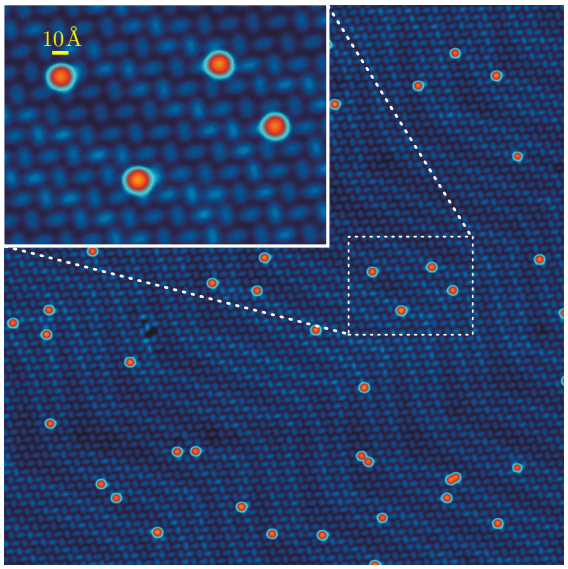

Figure 5.1: Constant current STM image after deposition of single Au atoms on a PTCDA submonolayer on Au(111) (710 Å $\times$ 710 Å). The inset shows the area around the adsorbed Au atoms in more detail. The adsorbed Au atoms appear as circles with a diameter of about $\approx$ 10 Å. Figure taken from Ref. [131].

energy surface calculated with the DFT for the Au atoms on the PTCDA monolayer is shown in Fig. 5.2b. Two nearly equivalent minima A and B with binding energies of 0.69 eV and 0.66 eV are found. Near the oxygen atoms (red circles) the interaction with the Au atoms almost vanishes. Due to the symmetry, four such minima are found labeled by A, B, A′ and B′. The Au atoms are adsorbed in a height of 2.1 Å above the monolayer with a distance of 2.2 Å to the nearest carbon atom. This bonding distance indicates a formation of a covalent bond between the PTCDA and the Au atom which is in agreement with the observations in Ref. [139]. Consequently, what at first sight appeared to be an Au atom in Fig. 5.1 is in fact a covalently bonded Au-PTCDA complex. The image is predominantly formed by the Au atom which sticks out of the surface layer.

A second set of calculations have been carried out including the topmost three layers of the Au(111) surface to determine the influence of the metal substrate on the Au atom bonding. The adsorption sites relative to the PTCDA molecule stay the same as in the freestanding case, however, the binding energy in the minima becomes larger due to the interaction with the surface. Essentially, the whole potential energy landscape is shifted by 0.15 eV to larger binding energies compared to the freestanding layer. The distance to the nearest carbon is again 2.2 Å and the adsorbed atom is located 5.4 Å above the topmost Au(111) surface layer.

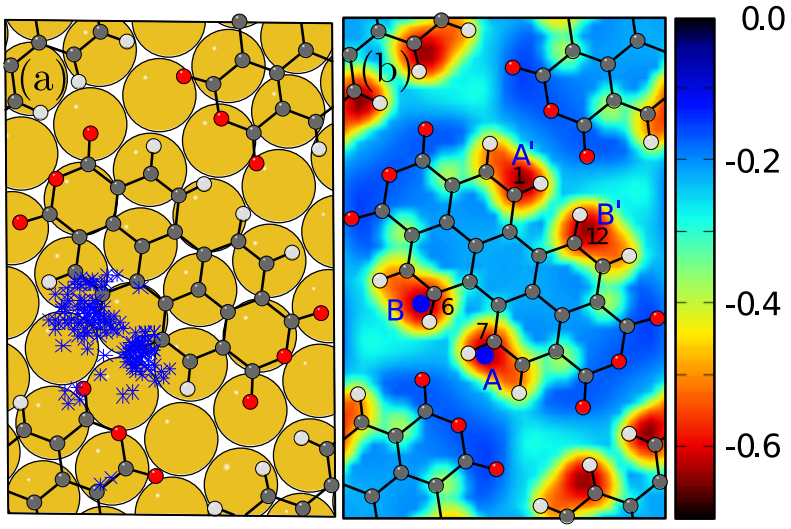

Figure 5.2: (a) Experimentally determined centers of the adsorbed Au atoms (blue spots) in the PTCDA unit cell on Au(111). The white, gray and red circles indicate hydrogen, carbon and oxygen atoms of the PTCDA molecule. The golden spheres denote the positions of the Au atoms in the topmost layer of the Au surface. (b) Potential energy surface in eV for an Au atom adsorbed on a PTCDA freestanding monolayer. Adapted from Ref. [131].

Scanning tunneling spectra of the Au-PTCDA complex: Kondo effect

Having established the existence of covalent bonded Au-PTCDA complexes, in the following the electronic properties of this complex on the Au(111) surface are studied by using STS.

Figure 5.3 shows the differential conductance spectrum of an Au-PTCDA complex. A peak at zero-bias voltage and three peaks at -800, 500 and 1200 mV are observed. A comparison of the peak at zero-bias with the other peaks in the spectrum reveals that the former is much sharper and has a Lorentzian lineshape. This suggests that the zero-bias peak does not correspond to an electronic eigenstate of the Au-PTCDA complex.

It is known from earlier work that charge transfer to the PTCDA molecule may cause a Kondo effect [140]. Since the formation of a chemically bonded complex may lead to such a charge transfer and a formation of a radical, it seems reasonable to suppose that the zero-bias peak is in fact a Kondo resonance. This assumption is confirmed by the analysis of its full width at half maximum (FWHM) and the peak height ($dI/dV(V = 0)$) as a function of the temperature.

The extracted FWHMs of the zero-bias peaks are depicted in Fig. 5.4a. The data shows the expected temperature dependence of a Kondo resonance. The Kondo temperature is extracted by fitting the expression [141]

$$\mathrm{FWHM} = \sqrt{(\alpha k_\mathrm{B} T)^2 + (2k_\mathrm{B} T_\mathrm{K}^{\mathrm{exp,FWHM}})^2} \tag{5.4}$$

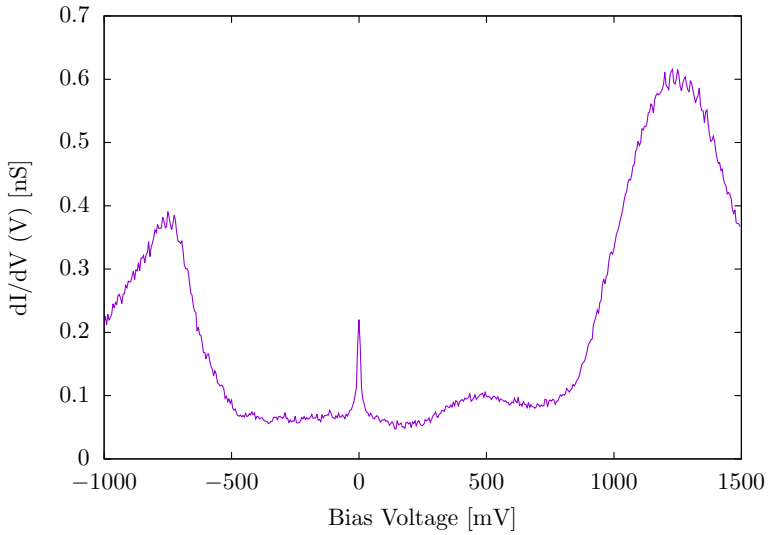

Figure 5.3: $dI/dV(V)$ spectrum of an Au-PTCDA complex. Three broad peaks at -800 mV, 500 mV and 1200 mV are visible. Additionally, a very sharp peak at 0 mV appears.

to the data. Here α and the Kondo temperature $T_K^{\text{exp,FWHM}}$ are fitting parameters. This procedure yields a Kondo temperature of $T_K^{\text{exp,FWHM}} = (30.7 \pm 1.0)$ K and a value of $\alpha = (5.3 \pm 0.2)$ where α is in a good agreement with the theoretical value [142] of $\alpha = 5.4$.

Figure 5.4c shows the height of the zero-bias peak plotted against the temperature. To extract the zero-bias peak, the data points for all temperatures have been measured on the same Au atom with the same tip. The tip has always been stabilized at a constant height above the Au-PTCDA complex. Some spectra acquired with this method are shown on Fig. 5.4d for different temperatures.

By fitting the data shown in Fig. 5.4c to the empirical formula [143]

$$\frac{dI}{dV}(V=0) = \frac{G_0}{\left[1 + \left(2^{1/s} - 1\right)\left(\frac{T}{T_K^{\text{zbc}}}\right)\right]^s} \tag{5.5}$$

with $s = 0.22$ for a spin 1/2 system, a Kondo temperature of $T_K^{\text{zbc}} = (38 \pm 8)$ K (zbc=zero-bias conductance) and a value of $G_0 = (4.1 \pm 0.3)$ nS is obtained. Note that changing the distance between the tip and the Au-PTCDA complex does not change the measured Kondo temperature.

Both Kondo temperatures $T_K^{\text{exp,FWHM}}$ and T_K^{zbc} agree within the error ranges. However, there is no unique definition of the Kondo temperature and, therefore, different approaches to determine T_K may lead to slightly different values. This will be discussed later on in Sec. 5.1.3 below. We can conclude that the Au-PTCDA complex is indeed a spin 1/2 radical which gives, together with the itinerant electrons of metal substrate, rise to a Kondo effect.

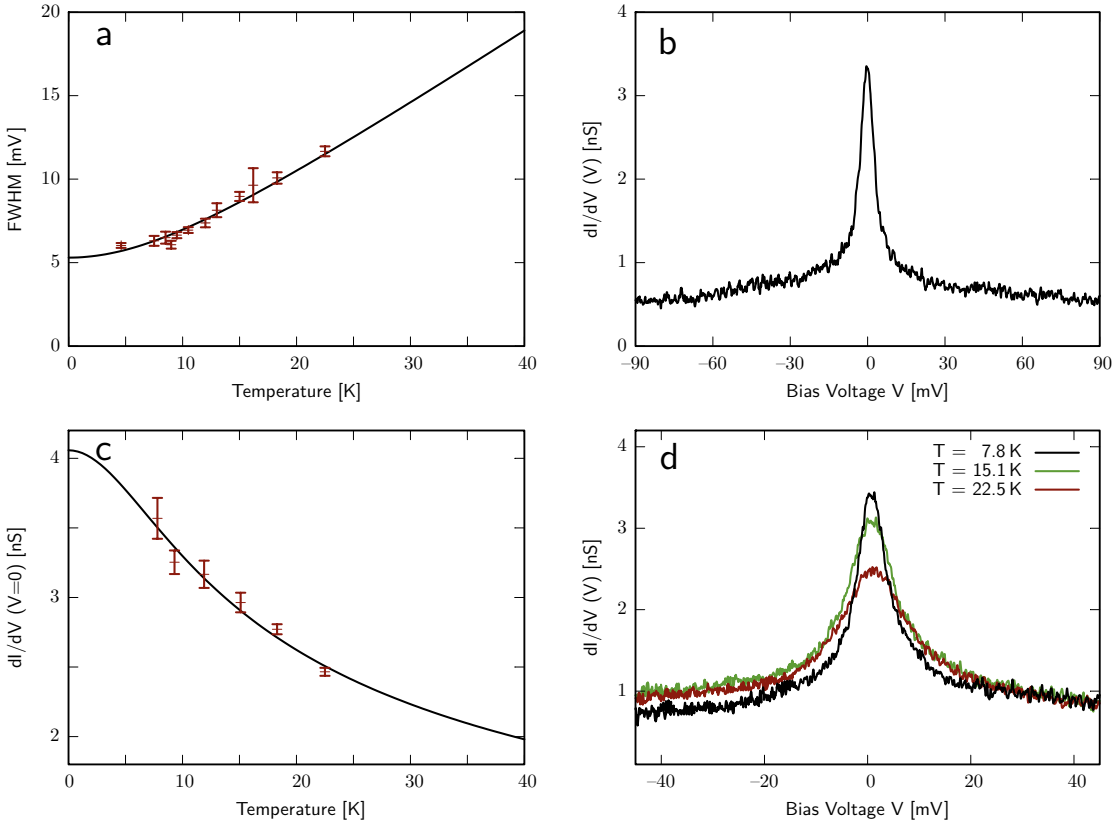

Figure 5.4: (a) FWHM of the differential conductance peak at zero-bias for different temperatures. The data has been deconvoluted to take the broadening due to finite temperature into account. (b) $dI/dV(V)$ conductance (not deconvoluted) of an Au-PTCDA complex at $T \approx 5$ K. (c) Peak heights of the differential conductance peak at zero-bias for different temperatures. (d) $dI/dV(V)$ conductance of an Au-PTCDA complex measured at different temperatures. Figure taken from Ref. [131].

Electronic properties of the Au-PTCDA: DFT results

Having proven that the Au-PTCDA complex on the Au(111) surface undergoes a Kondo effect, the DFT results of the electronic properties of the Au-PTCDA complex in the gas-phase are briefly discussed in the following.

The isosurfaces of some Au-PTCDA frontier wave functions are shown in Fig. 5.5 in comparison with those of the bare PTCDA and Tab. 5.1 lists some contributions to the most important states of the gas-phase Au-PTCDA complex. Note that the numbers in each line of Tab. 5.1 do not sum up to one since many other states which contribute to a smaller extent are neglected. It turns out that the LUMO of the bare PTCDA molecule hybridizes strongly with the Au 6s level of the adsorbed atom, forming a bonding LUMO+Au and an antibonding LUMO-Au combination.

Since the Au-PTCDA complex has an odd number of electrons (Au $6s^1$), its highest occupied level is half filled and it turns out that this is the LUMO+Au state. Therefore, we can conclude that it is the LUMO+Au level which contributes the most to the Kondo ef-

	Au_{6s}	Au_{6p}	HOMO	LUMO	LUMO+3
HOMO+Au	0.14	0.00	0.74	0.01	0.00
LUMO+Au	0.29	0.07	0.16	0.31	0.03
LUMO−Au	0.12	0.07	0.01	0.64	0.07

Table 5.1: The orbital composition of the three most important states of the gas-phase Au-PTCDA complex in terms of projection amplitudes onto states of the Au atom $(6s, 6p)$ and the PTCDA molecule (HOMO, LUMO, LUMO+3). The states of the Au-PTCDA complex are labeled according to their dominant character as HOMO+Au, LUMO+Au and LUMO−Au. Only the most significant contributions are listed. Table taken from Ref. [131].

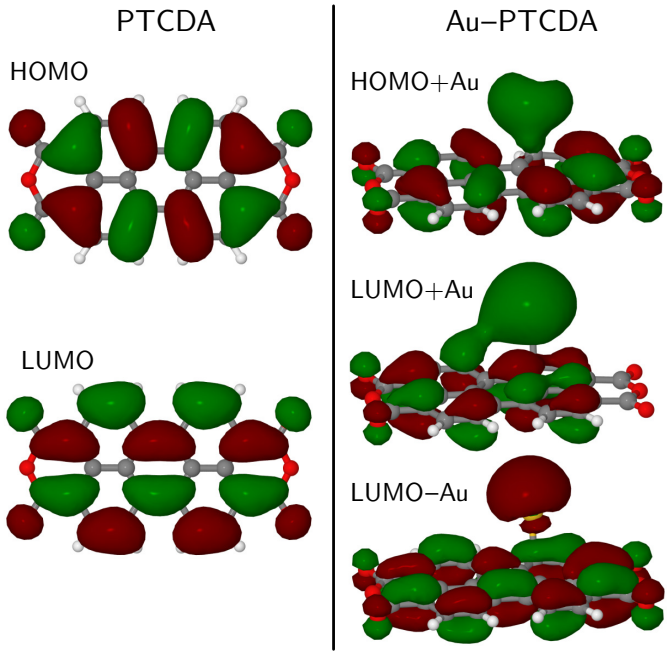

Figure 5.5: Wave functions of the PTCDA (left side) and the Au-PTCDA (right side) for orbitals around the Fermi energy E_F calculated within LDA. Green indicates positive and red negative isosurfaces. Figure taken from Ref. [131].

fect. A comparison between the experimental spectrum of Fig. 5.3 with spin-polarized electronic structure LSDA+GdW calculations for the Au-PTCDA complex adsorbed on the Au(111) surface suggests that the measured peaks at −800 mV and 500 mV can be assigned to charge excitations of the LUMO+Au while the large peak at 1200 mV can be ascribed to the LUMO-Au.

Before turning to the NRG calculations, we make a few comments on the accuracy of the input parameters for the NRG. At first, there is a small difference in the adsorption height of the PTCDA calculated with the GGA compared to the experiment which is of the order of 0.1 Å. This may influence the level positions with respect to the Fermi energy of the substrate. Furthermore, there is an uncertainty in the QP correction calculated with the LDA+GdW which cannot be reduced to less than 0.1 eV. As a

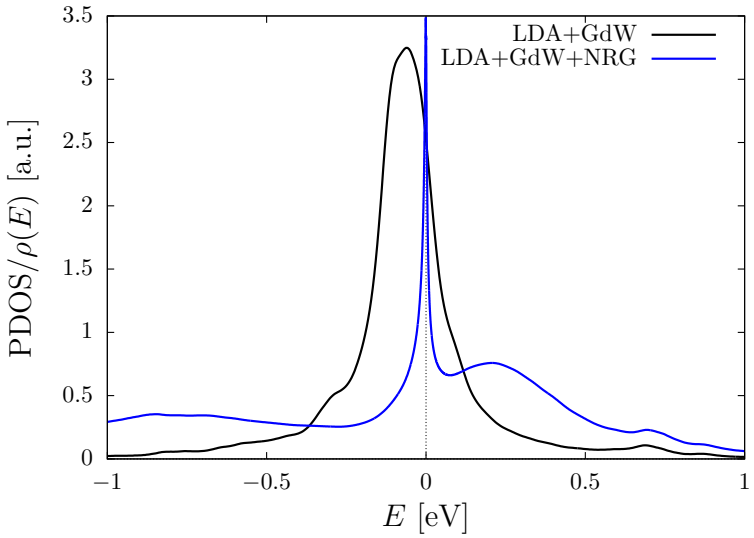

Figure 5.6: Comparison between the projected density of states of the LUMO+Au orbital from a LDA+GdW calculation (black line) and the spectrum obtained from a LDA+GdW+NRG calculation for $T = 0$ K and $U = 1.2$ eV.

consequence of these inaccuracies, and additionally because a finite $\vec{k}$ point mesh and a finite broadening for the calculation of the PDOS have been employed, an uncertainty of $\Delta n = 0.05$ in the occupation of LUMO+Au state cannot be excluded. This will affect the level position ϵ_0 and the hybridization in the same order. Finally, the Coulomb repulsion U slightly differs for different Au atom positions in the unit cell (positions A, A', B, B' in Fig. 5.2) in the range of 0.1 eV.

5.1.3 NRG studies of the electronic properties

Combining the LDA+GdW and the NRG

We now discuss the NRG calculations to incorporate dynamical correlation effects into the spectrum of the Au-PTCDA on the Au(111) surface. This procedure has already been employed in Ref. [138]. In this approach the LDA+GdW result is mapped onto a single impurity Anderson model (SIAM) which is then solved using the NRG in order to properly incorporate the Kondo effect that is experimentally observed in the dI/dV spectrum in Fig. 5.3. It is sufficient to use only a single-orbital Anderson model to model the dynamical coupling of the LUMO+Au orbital to the substrate since only the LUMO+Au state shows a significant contribution to the spectral function around the Fermi energy E_{F}.

The basic idea of this combined approach is to treat the PDOS, which is obtained by

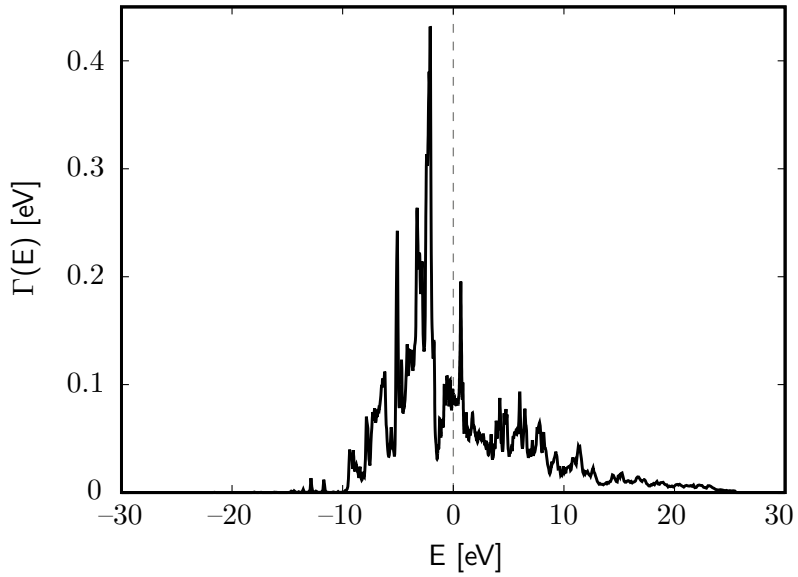

Figure 5.7: The full energy-dependent hybridization function $\Gamma(E)$ which is obtained from the LDA+GdW PDOS. Since $\Gamma(E)$ is independent of the Coulomb interaction U, for every NRG calculation with an energy-dependent hybridization this $\Gamma(E)$ is used. Figure taken from [131].

the LDA+GdW and shown in Fig. 5.6 (black line), as an effective mean field spectrum $\rho_{\mathrm{GdW}}(E)$. By equating

$$\rho_{\mathrm{GdW}}(E) \equiv \lim_{\delta\to 0^+} \mathrm{Im}\frac{1}{\pi}\frac{1}{E - i\delta - \epsilon_0 - nU - \Delta(E - i\delta)}, \tag{5.6}$$

we are able to extract the bare level position ϵ_0 and the complex coupling function $\Delta(E)$ between Au-PTCDA complex and the substrate. Here, U labels the estimated intraorbital Coulomb interaction obtained from Eq. (5.3), and n the occupation number of the energy level given by Eq. (5.2). Details about the calculations of the NRG parameters can be found in appendix G.

Since the LDA+GdW and LSDA+GdW predict slightly different Coulomb interactions (see also the discussion at the end of Sec. 5.1.2), we take U as a model parameter and vary the interaction within the predicted bounds. While the LDA+GdW yields $U = 1.1$ eV with an occupation $n = 0.71$, the LSDA+GdW predicts $U = 1.3$ eV and an occupation of $n = 0.5$. The parameters U, ϵ_0 and $\Delta(z)$ enter a NRG calculation. Here $\Gamma(E) = -\lim_{\delta\to 0^+} \mathrm{Im}\Delta(E + i\delta)$ (c.f. Eq. (3.3)) is the hybridization strength between the Au-PTCDA complex and the substrate. It will turn out that it is crucial to retain the full energy-dependence of the hybridization function $\Gamma(E)$ to obtain the correct Kondo temperature from the NRG calculations. The extracted $\Gamma(E)$, which is used in all following NRG calculations with an energy-dependent hybridization, is plotted in Fig. 5.7. Using Eq. (5.6) we find that the energy level ranges from $\epsilon_0 = -0.88$ eV for $U = 1.1$ eV, over $\epsilon_0 = -0.95$ eV for $U = 1.2$ eV to $\epsilon_0 = -1.02$ eV for $U = 1.3$ eV.

A resulting NRG spectrum for $U = 1.2$ eV is depicted in Fig. 5.6 (blue line). Indeed, the spectrum now shows a sharp Kondo peak at the Fermi energy $E = 0$ and two charge excitation peaks at -0.9 eV and 0.25 eV. The charge excitation peaks are found reasonably close to the experimental positions (-0.8 eV and 0.5 eV) depicted in Fig. 5.3. Given the uncertainties of the LDA+GdW input parameters into the NRG, the agreement with the experimental measured charge excitations to within 0.25 eV is pretty good which shows that our modeling describes the system at a quantitative level. Note that we observe in the NRG a slight reduction of the "effective U" which is defined as the difference between the two charge excitation peaks. For the spectrum shown in Fig. 5.6 this reduction is given from $U = 1.2$ eV to $U_{\text{eff}} = 1.15$ eV.
To illustrate the effect of the above mentioned uncertainties of the Coulomb interaction U, the NRG spectrum is plotted in Fig. 5.8a for different interactions U and a temperature of $T = 5$ K. With increasing interaction U we observe a narrowing of the Kondo resonance and, consequently, a reduction of the Kondo temperature. This effect can be explained by the analytical formula of the Kondo temperature which is stated in Eq. (5.9) below.

Results for the Kondo temperature

We now turn to the investigation of the Kondo temperatures resulting from the NRG calculations. Since the Kondo temperature depends extremely sensitively on the physical parameters such as the metal-molecule coupling, the energy level and the Coulomb interaction, a comparison of the LDA+GdW+NRG predicted Kondo temperatures with those obtained by the experiment is a very sensitive measurement of the accuracy of the first-principle DFT/MBPT analysis.
However, since the Kondo temperature is a crossover scale rather than a transition scale, there is a no unique definition. Therefore, we employ three different approaches to obtain the Kondo temperature: At first, we make a fit to the temperature dependent zero-bias conductance which should be a universal function of T/T_{K}. This leads to a Kondo temperature which we denote $T_{\text{k}}^{\text{zbc}}$ (zbc =zero-bias conductance). Afterwards, we evaluate the analytic formula for the Kondo temperature of the particle-hole asymmetric SIAM in which the same orbital parameters from our DFT/MBPT calculations enter but where we replace the full energy-dependent hybridization strength $\Gamma(E)$ by its value at the Fermi energy $\Gamma = \Gamma(0)$. This leads to an analytic estimate of the Kondo temperature which is denoted by $T_{\text{K}}(\Gamma, \epsilon_0, U)$ in the following. At the end, we analyze the FWHM of the zero-temperature spectral function around the chemical potential which provides the Kondo temperature $T_{\text{K}}^{\text{FWHM}}$.
We start with the discussion of the Kondo temperature $T_{\text{k}}^{\text{zbc}}$ obtained from the zero-bias conductance. Figure 5.8b shows the spectral function $\rho_{\text{NRG}}(E)$ of the combined LDA+GdW+NRG approach for the LUMO+Au orbital at fixed $U = 1.2$ eV for three different temperatures. The spectra are in a good agreement with the corresponding

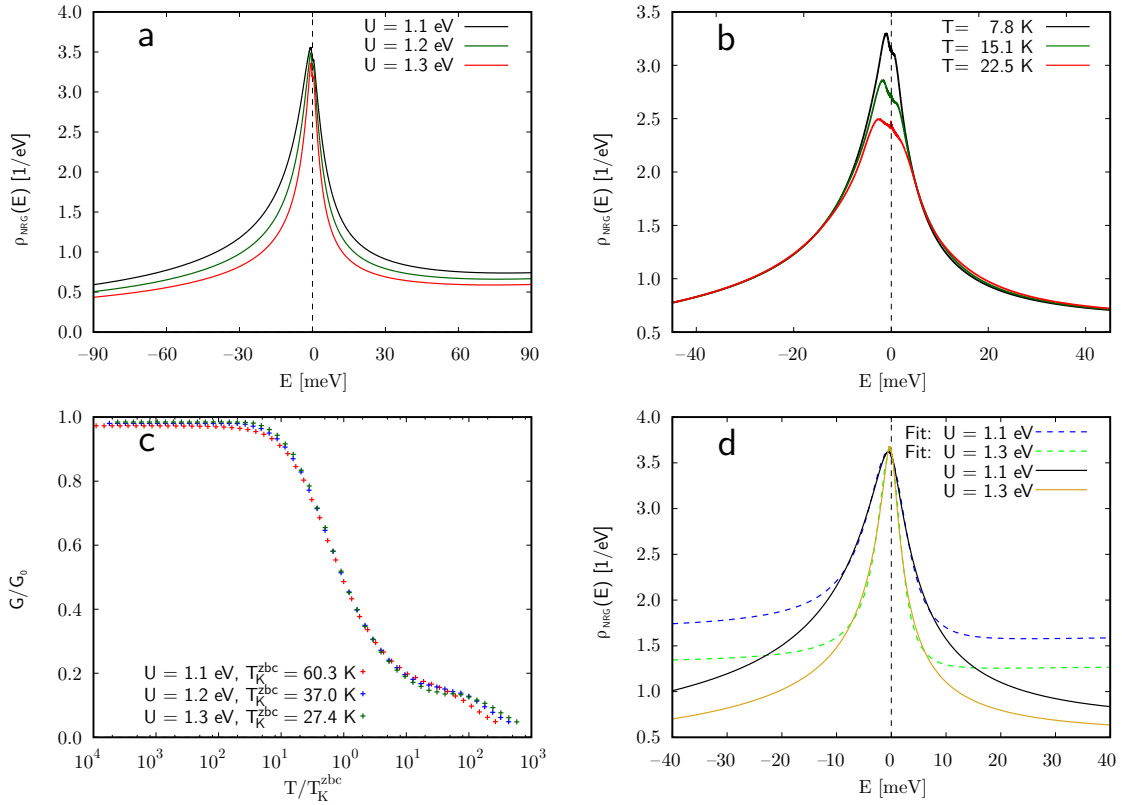

Figure 5.8: Results of the combined LDA+GdW+NRG approach for the Au-PTCDA complex on an Au(111) surface. (a) Spectral function for three different values of the Coulomb interaction $U = 1.1, 1.2, 1.3$ eV and $T = 5$ K. The width of the Kondo resonance and consequently the Kondo temperature is increasing with decreasing U. (b) The Kondo resonance for $U = 1.2$ eV and the three different temperatures $T = 7.8, 15.1, 22.5$ K. (c) The temperature dependent zero-bias differential conductance for different interactions U as a universal function of T/T_K^{zbc}. (d) Zero-temperature spectra for the interactions $U = 1.1$ eV and $U = 1.3$ eV and their Fano fits to extract the FWHM. Figure taken from [131].

experimental results of the differential conductance $dI/dV(V)$ which are shown in Fig. 5.4. However, the NRG spectrum is slightly more asymmetric which will be discussed later on.

The temperature dependent spectral function $\rho_{\mathrm{NRG}}(E)$ enters the calculation of the differential conductance [144, 145] in the tunneling regime,

$$\frac{dI}{dV}(V) = G_0 \int dE\, \pi\Gamma(E)\rho_{\mathrm{NRG}}(E)(-f'_{\mathrm{tip}}(E,V)), \tag{5.7}$$

where the reference conductance G_0 is given by [144]

$$G_0 = \frac{2e^2}{h}\frac{4\Gamma_{\mathrm{tip}}(0)\Gamma(0)}{(\Gamma_{\mathrm{tip}}(0)+\Gamma(0))^2}. \tag{5.8}$$

		U		
	Exp.	1.1 eV	1.2 eV	1.3 eV
T_K^{zbc}	38 ± 8	60.3	37.0	27.4
$T_K(\Gamma, \epsilon_0, U)$	n/a	41.7	28.4	19.5
T_K^{FWHM}	30.7 ± 1	51.0	42.9	30.2

Table 5.2: Experimental and calculated Kondo temperatures in K. For the calculated T_K^{zbc} and T_K^{FWHM} we have used the full energy-dependent $\Gamma(E)$, while for $T_K(\Gamma, \epsilon_0, U)$ Eq. (5.9) has been evaluated for $\Gamma = \Gamma(0) = 86$ meV. Table taken from [131]

G_0 depends only on $\Gamma(0)$ and $\Gamma_{tip}(0)$ which are the charge fluctuation scales at the chemical potential induced by the coupling to the substrate and the tip, respectively. $f_{tip}(E, V)$ denotes the Fermi distribution of the STM tip also including the bias voltage V. Note that for a STM tunneling $\Gamma_{tip}(E) \to 0$, the reference conductance is given by $G_0 \to (2e^2/h)(4\Gamma_{tip}(0)/\Gamma(0))$ and hence the tunnel current is strongly suppressed. For zero temperature the derivative of the Fermi distribution is $-f'_{tip}(E, V) = \delta(E - eV)$ and the formula for the differential conductance simplifies to $dI/dV(V) = \pi G_0 \Gamma(eV)\rho_{NRG}(eV)$.

Fitting the zero-bias conductance of Eq. (5.7) using the $\rho_{NRG}(E)$ obtained from the LDA+GdW+NRG approach to the empirical formula Eq. (5.5) yields Kondo temperatures that range from $T_K^{zbc} = 27.4$ K for $U = 1.3$ eV to $T_K^{zbc} = 60.3$ K for $U = 1.1$ eV. These values are perfectly bracketing the experimentally estimated Kondo temperature of $T_K^{exp,zbc} = (38 \pm 8)$ K. The best agreement is given for $U = 1.2$ eV for which we obtain $T_K^{zbc} = 37.0$ K. The values of the Kondo temperature for all Coulomb interactions U are listed in Tab. 5.2.

The calculated zero-bias differential conductance, normalized to G_0 is depicted in Fig. 5.8c as a universal function of T/T_K^{zbc}.

We now turn to the investigation of the analytic Kondo temperature. In general the Kondo temperature is defined as the universal energy scale governing the excitation and the thermodynamic response at low temperatures. However, physical properties may also depend on the degree of particle-hole asymmetry. This degree is not only responsible for the asymmetric shapes of the spectral function and dI/dV curves but also enters the analytic expression of the Kondo temperature T_K.

Krishna-murthy *et al.* [27] have shown that for a particle-hole asymmetric SIAM with constant hybridization function $\Gamma(E) = \Gamma = \text{const.}$ the Kondo temperature is given by

$$T_K(\Gamma, \epsilon_0, U) = 0.182 |E_0^*| \sqrt{\rho J_{eff}} \exp\left(-\frac{1}{\rho J_{eff}}\right) \tag{5.9}$$

for the regime where double occupancy of the level is energetically suppressed and the orbital remains close to integer valence. Here, E_0^* is the solution of the self-consistent equation $E_0^* = \epsilon_0 + (\Gamma/\pi)\ln(-U/E_0^*)$ [146] and describes the renormalization of the

bare level due to high-energy charge fluctuations. $\rho J_{\text{eff}} = \rho J[1 + (\pi\rho K)^2]^{-1}$ is an effective Kondo coupling that not only contains the bare Kondo coupling

$$\rho J = \frac{2\Gamma}{\pi}\left(\frac{1}{|E_0^*|} + \frac{1}{\epsilon_0 + U}\right) \tag{5.10}$$

but also a modification by the degree of particle-hole asymmetry

$$\rho K = \frac{\Gamma}{2\pi}\left(\frac{1}{|E_0^*|} - \frac{1}{\epsilon_0 + U}\right), \tag{5.11}$$

which are both obtained from a Schrieffer-Wolff transformation [71]. Note that for particle-hole symmetry, the particle-hole symmetry breaking term ρK vanishes and that for weak coupling $E_0^* \approx \epsilon_0$.

Because the Kondo effect is dominated by the low-energy excitations, we use in Eq. (5.9) the constant value $\Gamma(E = 0) \approx 86$ meV which is the value of the energy-dependent hybridization function at the Fermi energy (cf. Fig. 5.7). For $\epsilon_0 = -0.95$ eV and $U = 1.2$ eV we obtain $T_{\text{K}} = 28.4$ K which agrees well with the numerical fit to the differential conductance $T_{\text{K}}^{\text{zbc}} = 37$ K. The Kondo temperatures for the other values of the Coulomb interaction U can be found in Tab. 5.2.

As already mentioned above, we found an increase of the Kondo temperature for a decreasing Coulomb interaction U. This behavior can be explained by the exponential dependence of the Kondo temperature on the Kondo coupling ρJ given by Eq. (5.10). $T_{\text{K}}(\Gamma, \epsilon_0, U)$ has a minimum for the particle-hole symmetric case $\epsilon_0 = -U/2$ and two maxima, one at $\epsilon_0 = 0$ and the second for $\epsilon_0 = -U$. In the case discussed above, we move with decreasing U further away from particle-hole symmetry towards the mixed valence regime where $\epsilon_0 \approx -U$ and, hence, the Kondo temperature is rising.

However, we stress that this analytical Kondo temperature neglects effects stemming from an energy-dependent hybridization $\Gamma(E)$. Therefore, we can use $T_{\text{K}}(\Gamma, \epsilon_0, U)$ only as a preliminary estimate that needs modifications by the full LDA+GdW+NRG approach to describe the experiment properly.

Finally, we discuss the Kondo temperature $T_{\text{K}}^{\text{FWHM}}$ obtained from the width of the Kondo resonance at zero temperature. In the experiment the FWHM of the $dI/dV(V)$ spectrum has been fitted to Eq. (5.4) to calculate the Kondo temperature. We now apply the same technique to the data of the combined LDA+GdW+NRG approach shown in Fig. 5.8a. The results are depicted in Fig. 5.8d.

For the results of the NRG a temperature dependent fit is not needed since the NRG is able to reach arbitrarily small temperatures, therefore, Eq. (5.4) simplifies to

$$\text{FWHM}(T = 0) = 2k_{\text{B}}T_{\text{K}}^{\text{FWHM}}. \tag{5.12}$$

Furthermore, in the tunneling regime the differential conductance is proportional to the spectral function $dI/dV(V) \propto \rho(E = eV)$ for $T \to 0$ and hence the Kondo temperature T_K^{FWHM} can be estimated directly from the spectral function. However, in a particle-hole asymmetric case, the spectra and the dI/dV curves have an asymmetric shape. Given this asymmetry, three questions arise, namely (i) how to extract T_K^{FWHM}, (ii) do the different fit procedures yield comparable values and (iii) how do the various T_K^{FWHM} compare with the other estimates of the Kondo temperature, namely T_K^{zbc} and $T_K(\Gamma, \epsilon_0, U)$?

The simplest approach would be to take the definition full width at half maximum (FWHM) literally. In addition to the Kondo peak, however, the spectra also contain broad charge excitations peaks at high energy (c.f. blue curve of Fig. 5.6) that invalidate such a procedure. The estimated T_K^{FWHM} are typically double the value of those obtained by the fit procedure Eq. (5.5) due to this background.

The experimental FWHM shown in Fig. 5.4 were extracted from a Lorentzian fit but since the NRG spectrum is slightly more asymmetric, we allow an asymmetry [147, 148] in the fitting process and employ a Fano resonance line shape for the Kondo peak of the form $\rho(E) = \rho_0 + A\frac{(q+\epsilon)^2}{1+\epsilon^2}$ with $\epsilon = (E - E_0)/\Gamma$ to extract its FWHM. Here, E_0 determines the location of the resonance which is shifted slightly away from the chemical potential in accordance with the Friedel sum rule [76, 79, 149]. While q parameterizes the asymmetry of the spectrum, Γ denotes the width of the peak and defines, therefore, the fit for T_K^{FWHM}. The zero-temperature spectra for the two different interaction values $U = 1.1$ eV and $U = 1.3$ eV and their corresponding Fano fits are depicted in Fig. 5.8d. Extracting the Kondo temperature from the NRG spectra, we find Kondo temperatures ranging from $T_K^{FWHM} = 30.2$ K for $U = 1.3$ to $T_K^{FWHM} = 51.0$ K for $U = 1.1$ which again brackets the experimentally measured $T_K^{exp,FWHM} = (30.7 \pm 1.0)$ K.

Note that when using Eq. (5.4) or Eq. (5.12) in a high particle-hole asymmetric case, the extracted Kondo temperature T_K^{FWHM} slightly depends on the fitted function which requires a significant modification from a symmetrical Lorentzian. We will show in the following that T_K^{FWHM} can only yield the correct order of magnitude of the Kondo temperature since its value is definition dependent and does not need to coincide with the Kondo temperature defined in Eq. (5.9) that has been derived from the screening of the local spin moment. Again, we have listed all obtained Kondo temperatures T_K^{FWHM} together with the experimental ones in Tab. 5.2.

Comparison of the Kondo temperatures

In the following, we will compare the various calculated Kondo temperatures among each other to provide a guideline for a reliable extraction of the Kondo temperature T_K from the experiment.

The Kondo temperature is only defined up to an arbitrary constant of the order of one since it is only a crossover scale. Therefore, the question arises whether $T_K^{(exp,)FWHM}$ ex-

		U		
	Exp.	1.1 eV	1.2 eV	1.3 eV
T_K^{zbc}	38 ± 8	98.0	63.0	42.8
$T_K(\Gamma, \epsilon_0, U)$	n/a	41.7	28.4	19.5
T_K^{FWHM}	30.7 ± 1.0	74.8	57.0	42.9
T_K^{μ}	n/a	49.9	34.2	23.9
$T_K(\Gamma, \epsilon_0, U)/T_K^{\mu}$	-	0.836	0.830	0.810
$T_K(\Gamma, \epsilon_0, U)/T_K^{zbc}$	-	0.426	0.450	0.456
$T_K(\Gamma, \epsilon_0, U)/T_K^{FWHM}$	-	0.577	0.498	0.455

Table 5.3: Experimental and calculated Kondo temperatures in K. Note that for the calculated Kondo temperatures a constant $\Gamma = 86$ meV has been used. Table taken from [131].

tracted from the FWHM and $T_K^{(exp,)zbc}$ obtained from the zero-bias conductance should indeed be expected to be universal *up to a universal scaling constant*.

With the NRG we have an optimal tool at disposal to investigate the differences between the various definitions of the Kondo scale systematically. Since we have neglected the energy-dependence of the hybridization function $\Gamma(E)$ for the calculation of the analytical Kondo temperature $T_K(\Gamma, \epsilon_0, U)$, we have repeated the NRG calculations with a constant hybridization $\Gamma = 86$ meV and extracted the new values of T_K^{FWHM} and T_K^{zbc} from these calculations in order to exclude an influence of the energy-dependent hybridization on the comparison. The new values can now be compared directly with the analytic estimate $T_K(\Gamma, \epsilon_0, U)$. The obtained new Kondo temperatures are listed in the upper part of Tab. 5.3. The table contains also the value of the new Kondo scale T_K^{μ} which is again determined for a constant hybridization $\Gamma = 86$ meV. Originally, Wilson [27] has defined the Kondo temperature as the temperature T_K^{μ} at which the local moment is reduced to approximately 26% of its original value. This reduction is caused by screening through conduction electrons. At zero temperature $T = 0$ the system is in a Kondo singlet ground state and the effective local moment is zero. T_K^{μ} follows then from the implicit equation

$$\mu_{eff}^2 = T_K^{\mu} \chi(T_K^{\mu}) = 0.07, \tag{5.13}$$

where μ_{eff}^2 is the effective local magnetic moment and $\chi(T)$ its isothermal magnetic susceptibility. Note that this screening has also entered the analytical Kondo temperature $T_K(\Gamma, \epsilon_0, U)$ in Eq. (5.9).

Calculating the ratios $T_K(\Gamma, \epsilon_0, U)/T_K^{\mu}$ and $T_K(\Gamma, \epsilon_0, U)/T_K^{zbc}$ for the three different Coulomb interactions $U = 1.1, 1.2, 1.3$ eV, corresponding to $\epsilon_0 = -0.88, -0.95, -1.02$ eV, we observe almost constant ratios of $T_K(\Gamma, \epsilon_0, U)/T_K^{\mu} \approx 0.83$ and $T_K(\Gamma, \epsilon_0, U)/T_K^{zbc} \approx 0.45$. Consequently, all three definitions $T_K(\Gamma, \epsilon_0, U)$, T_K^{μ} and T_K^{zbc} are connected by universal scaling factors and hence fully equivalent.

In contrast, Tab. 5.3 shows that the ratios $T_K(\Gamma, \epsilon_0, U)/T_K^{FWHM}$ are not constant and dependent on the Coulomb interaction U, varying over a range from ≈ 0.58 to ≈ 0.46. This situation does not change if we use different fitting procedures of the zero-bias conductance peak to extract the FWHM. In particular, we have tested three different methods: (i) a Lorentz-fit to the symmetrized spectrum $\rho_{sym}(E) = 0.5(\rho(E) + \rho(-E))$, (ii) a Lorentz-fit to the low-energy part of the spectrum, and (iii) the above mentioned and in Fig. 5.8d shown Fano line shape fit. With all three procedures we obtain roughly the same Kondo temperatures T_K^{FWHM}. Therefore, we can conclude that the Kondo temperature T_K^{FWHM} is nonuniversal and depends on the degree of particle-hole asymmetry. In particular, for small Coulomb interactions U we find a T_K^{FWHM} that is much smaller than T_K^{zbc}, while it approaches the fit of the zero-bias conductance for $U = 1.3$ where the spectrum is narrower and much more symmetric. Note that in fact particle-hole symmetry was explicitly assumed in the derivation of Eq. (5.4) [141].
The discussion above shows that the difference between T_K^{FWHM} and T_K^{zbc} originate from a nonuniversal scaling factor. We can, therefore, summarize that the fit to the zero-bias conductance T_K^{zbc} is the most reliable way to extract the Kondo temperature from experiments since in this case at temperature T only excitations of the order of T enter. In contrast, for T_K^{FWHM} measured at temperature $T/T_K \ll 1$ always contains high-energy excitations in addition to errors stemming from nonequilibrium effects due to a finite current through the molecule for larger bias voltages. However, as Tab. 5.3 shows, T_K^{FWHM} can still serve as a reasonable estimate for the Kondo temperature which provides the correct order of magnitude of T_K.
Note that the Kondo temperatures calculated with a constant hybridization Γ are significantly different from those obtained with the full energy-dependent $\Gamma(E)$ which agree with the experimental T_K very well. The Kondo temperatures for constant Γ are up to a factor of two larger than the T_K for nonconstant hybridization $\Gamma(E)$. Therefore, we can conclude that the combined full LDA+GdW+NRG approach is needed to explain the experimental data on a quantitative level. In particular, a perfect match between the experimental Kondo temperature $T_K^{exp,zbc} \approx 38$ K and the Kondo temperature $T_K^{zbc} \approx 37$ K obtained from the NRG for $U = 1.2$ eV is achieved.

Occupancy of the LUMO+Au orbital

At the end, we discuss the occupancy of the LUMO-Au orbital. The LDA+GdW predicts an occupancy per spin of about $n = 0.71$ while the inclusion of correlation effects in the NRG reduces this value to $n \approx 0.55$. Since the Coulomb interaction strongly suppresses double occupancy and hence constrains the filling closer to half-integer values, such a reduction is expected. However, both methods the LDA+GdW and the LDA+GdW+NRG agree in predicting the binding of an extra fraction of an electron that is drawn from the substrate (LDA+GdW+NRG: 0.1 electrons, LDA+GdW: 0.4 electrons), in addition to the one electron from the Au atom.

5.1.4 Monomer: Summary

It has been demonstrated that when doping a PTCDA/Au(111) monolayer with a single Au atom, an Au-PTCDA complex is formed by a chemical reaction. Due to an unpaired electron drawn of the Au 6s orbital, this complex is a radical with spin $S = 1/2$. Remarkably, the orbital in which the unpaired spins resides extends almost over the whole molecule. In particular, this orbital is given by the bonding combination of the Au 6s and the LUMO of the free PTCDA.
On the Au(111) surface an additional small fraction of electrons (about 0.1) is drawn from the surface into the LUMO+Au orbital of the complex. This additional charge transfer is, however, limited by the strong Coulomb repulsion which prevents double occupation. In fact, the LUMO+Au orbital remains close to single occupation. One can think of the Au-PTCDA complex as an intermediate between the PTCDA on Au(111) where no charge transfer occurs [150] and PTCDA on Ag(111) where almost two electrons are transfered from the surface to the molecule [151]. For the case of Au-PTCDA/Au(111) discussed here, the coupling to the substrate is much weaker than for PTCDA/Ag(111), so that for similar intraorbital Coulomb repulsion the double occupancy is only suppressed for Au-PTCDA/Au(111). In contrast, if we compare Au-PTCDA/Au(111) to PTCDA/Au(111), where the LUMO remains unfilled, the charge transfer from the adsorbed Au atom to the π-system bypasses the charging barrier for PTCDA on Au(111) that is caused by the large work function of Au(111).
As a consequence of the single occupation, a local moment is formed. The spin of the complex interacts with the conduction electrons and, therefore, a Kondo effect emerges in this system. In the experimental STS spectra, the Kondo effect is revealed by a sharp resonance at the chemical potential. An analysis of the temperature dependent FWHM and the zero-bias conductance yields Kondo temperature of about $T_{\mathrm{K}}^{\mathrm{exp,zbc}} \approx 38$ K for the zero-bias conductance and $T_{\mathrm{K}}^{\mathrm{exp,FWHM}} \approx 31$ K for the FWHM. The observation of the Kondo effect is an unambiguous proof that the Au-PTCDA complex is indeed a paramagnetic radical.
On the theory side, a fully quantitative description of the Au-PTCDA complex was achieved by employing a DFT with generalized gradient approximation (GGA), including van der Waals corrections, as well as a combined LDA+GdW+NRG approach. The DFT predicted adsorption positions of the Au atom relative to the PTCDA are in perfect agreement with the experimental observed positions of the Au atom.
To describe the electronic properties of the Au-PTCDA complex, including the low-energy region, we have mapped the DFT/MBPT results on the $S = 1/2$ SIAM. We have considered the full energy-dependent hybridization function, which turns out to be crucial for the quantitatively correct description of the system.
The NRG spectrum consists of two broad charge excitation peaks which are both within 0.25 eV of the experimental values, and a sharp Kondo resonance at the Fermi energy E_{F}. Due to the strong particle-hole asymmetry of the system, we observe an asymmet-

ric lineshape of the Kondo resonance. In the experiments the asymmetry of the Kondo peaks is less obvious, although the charge excitation peaks clearly show the particle-hole asymmetry in the measured spectra.
We have carried out a careful analysis of the scaling behavior of various definition of the Kondo temperature in order to provide a guideline how the Kondo temperature can be extracted reliably from the experiment for particle-hole asymmetric systems. Since the Kondo temperature is a crossover scale, Kondo temperatures extracted from a NRG calculation or an experiment my vary up to a scaling factor. However, this scaling factor has to be universal for a valid extraction scheme.
In the present case, we find that the Kondo temperatures obtained from the zero-bias conductance and the screening of the effective local moment scale universally with the analytic formula for the particle-hole asymmetric SIAM. In contrast, the Kondo temperature derived from the FWHM of the zero-bias peak scales nonuniversally, no matter which fitting function is used to extract the FWHM. This means for the experiment that one should use the zero-bias conductance to obtain the Kondo temperature since it is not affected by nonuniversal aspects of the lineshape. If we apply this method to experiment and NRG, we obtain a NRG Kondo temperature of $T_K \approx 37$ K for $U = 1.2$ which is in perfect agreement with the experimental Kondo temperature of $T_K = 38$ K. Furthermore, we stress that it is not sufficient to replace the full energy-dependent hybridization $\Gamma(E)$ by its value $\Gamma(0)$ at the Fermi energy to obtain a correct T_K, in spite of the fact that the Kondo effect is determined by low-energy excitations.
Since the Kondo temperature depends very sensitively on the coupling to the substrate, the energy level and the Coulomb interaction, the good agreement between theory and experiment observed here shows that the structural and electronic properties of the Au-PTCDA complex are accurately described by the DFT/MBPT and NRG.
Note that the delocalized character of the spin-carrying π-orbital makes the Au-PTCDA complex to an ideal candidate for the quantitative study of interactions between extended molecular magnets. Such an interacting system will be investigated and discussed in detail in the next section 5.2.

5.2 Dimer

We now discuss the case when two Au atoms adsorb on adjacent PTCDA molecules and thus interact with each other.
Usually, when two local moments on a metal surface interact, this is discussed in terms of a competition between the Kondo effect and the Ruderman-Kittel-Kasuya-Yosida (RKKY) interaction [152–156]. The RKKY interaction is an indirect exchange interaction which is mediated by the conduction electrons [58–60] and has already been introduced in Secs. 2.3 and 4.2. Depending on distance, it favors ferromagnetic or antiferromagnetic alignments of local moments, whereas the Kondo effect tends to

quench the moments locally with the help of the conduction electrons [62–64, 66, 156]. Here, however, we describe a different scenario. In this case the driving force of a quantum phase transition (QPT) in a system of two local moments on a metal surface is the competition between the kinetic energy gain due to the entanglement with the substrate and the binding energy gain due to the chemical interaction between the moment-carrying orbitals. Interestingly, in this scenario the Kondo effect favors a ferromagnetic alignment of the two local moments while the chemical interaction promotes the formation of a local singlet. The mechanism is expected to be generic and widespread, because it relies only on very general features of chemical interactions and Kondo physics. Moreover, since it is straightforward to engineer the chemistry, the mechanism will allow for an easy tuning of the magnetic interaction between local moments.
To demonstrate the novel scenario, we use dimers formed by two Au-PTCDA complexes that each consists of a perylene-tetracarboxylic dianhydride (PTCDA) molecule, adsorbed on the inert Au(111) surface, and a single Au atom. The interaction between those Au-PTCDA complexes is investigated by means of scanning tunneling spectroscopy (STS). Specifically, we show that the dimers are indeed located very close to a quantum critical point (QCP) [157, 158], so that depending on the precise configuration of the dimer distinct ground states (singlet or triplet) are realized.
The results of this section have been submitted to *Nature Physics* [159].

5.2.1 Dimer: Experiment and DFT

The experimental setup and the theory of the combined DFT/MBPT approach is the same as for the monomer, therefore, we refer the reader to Sec. 5.1.1 for a more detailed discussion. Here, we only briefly present the differences compared to the case of a single noninteracting Au-PTCDA complex.
As for the monomer, the experiments have been done at the Peter Grünberg Institute in the Forschungszentrum Jülich by Taner Esat, Christian Wagner, Ruslan Temirov and F. Stefan Tautz while the density functional theory (DFT) calculations have been carried out at the Institut für Festkörpertheorie at the Westfälische Wilhelms-Universität Münster by Thorsten Deilmann, Peter Krüger and Michael Rohlfing.

Setup and theory

The investigated dimers are formed by two adjacent metal-molecules that each consists of a PTCDA molecule, adsorbed on the inert Au(111) surface, and a single Au atom. As discussed above in Sec. 5.1, in each monomer the 6s electron of the Au atom is transferred into an empty π-orbital of the PTCDA that is only weakly coupled to the substrate and, consequently, forms a well-defined spin moment delocalised over the entire PTCDA molecule. A large scale image of a PTCDA layer on which Au atoms have

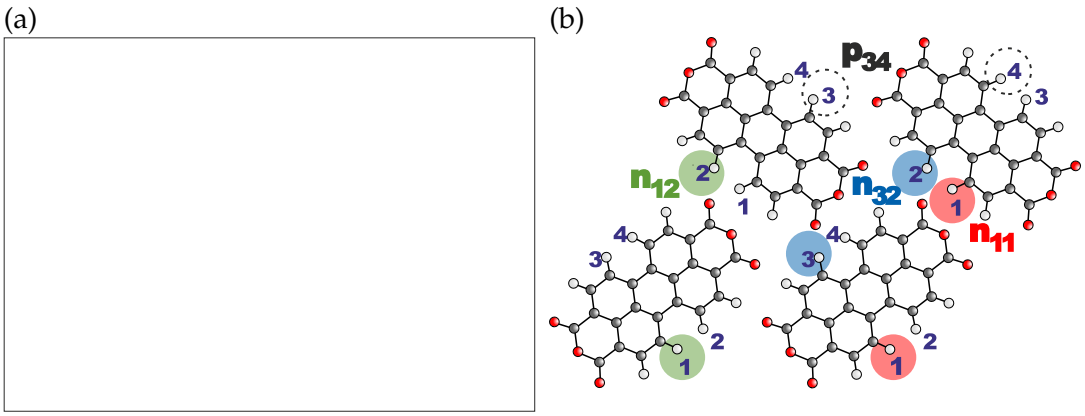

Figure 5.9: (a) Constant current STM image after the deposition of Au atoms on a PTCDA submonolayer on Au(111). The white circle indicates the formation of a dimer. (b) Herringbone structure of the PTCDA on Au(111). Numbers indicate possible Au sites in Au-PTCDA monomers. Dimer configurations can be classified as n_{ij} (normal) or p_{ij} (parallel), with the index i(j) specifying the position in the molecule. The white, gray and red circles indicate hydrogen, carbon and oxygen atoms of PTCDA. Figures taken from [159].

been deposited is shown in Fig. 5.9a, each bright spot indicates an Au-PTCDA complex. The white circle in Fig. 5.9a reveals a dimer that has formed spontaneously upon Au deposition. The interaction between the two spin moments on both monomers are investigated by STS to detect the ground state of the dimer.

Within the DFT the dimer structures are optimized in a cell including eight PTCDA molecules. Only the situation where two Au atoms adsorb on neighbouring PTCDA molecules is analyzed since in the experiment the binding of two Au atoms to the same PTCDA molecule was never observed. As for the monomer case, the Au atom can bind to a PTCDA on one of four positions so that together with the herringbone structure of the PTCDA, with two inequivalent molecules in the unit cell, there are 32 structurally distinct dimers. The different configurations are shown in Fig. 5.9b, where p_{ij} (n_{ij}) labels a dimer consisting of two complexes whose PTCDA backbones are parallel (normal) to each other, with the Au atom in the first (second) complex in position i(j). The binding energies of all 32 positions vary by less than 10 meV which agrees with the experiment where indeed most of the configurations are observed. Note that in contrast to the monomer in the previous Sec. 5.1, the surface atoms are fixed at the experimental molecule surface distance of 3.3 Å.

Similarly to Eq. (5.3) for the isolated monomer, the intraorbital Coulomb interactions on complex i is given by

$$U_i = \int\int |\Psi^i_{\mathrm{LUMO+Au}}(\vec{r})|^2 W(\vec{r},\vec{r}\,')|\Psi^i_{\mathrm{LUMO+Au}}(\vec{r}\,')|^2 \, d^3r d^3r' \tag{5.14}$$

where $W(\vec{r},\vec{r}')$ is the screened Coulomb interaction and $\Psi^i_{\mathrm{LUMO+Au}}(\vec{r}')$ the wave function of the LUMO+Au orbital of monomer i. For the Coulomb interaction U_j of monomer j an analogous formula holds. In contrast to the case of an isolated monomer in Sec. 5.1, slightly increased Coulomb interactions of about $U = 1.4$ eV are found. The generally larger U values calculated for the dimer are caused by the different computational set up, namely slightly different unit cells and the usage of the experimental molecule surface distance.
In analogy to Eq. (5.14), an interorbital Coulomb repulsion can be calculated according to

$$U'_{ij} = \int\int |\Psi^i_{\mathrm{LUMO+Au}}(\vec{r})|^2 W(\vec{r},\vec{r}') |\Psi^j_{\mathrm{LUMO+Au}}(\vec{r}')|^2 \, d^3r d^3r'. \tag{5.15}$$

Interestingly, the intraorbital Coulomb interaction U is reduced by a factor of 2 if the surrounding PTCDA molecules and the surface are included in the calculations while U' is reduced by a factor of 7 due to the metal screening.
In addition to the Coulomb interactions, a tunneling between the two monomers is calculated. This tunneling corresponds to the level splitting between even and odd combinations of monomer LUMO+Au orbitals and is computed by performing local density approximation (LDA) calculations of two Au-PTCDA complexes in the gas phase. The tunneling t is then given by

$$t = E_{\mathrm{Even}} - E_{\mathrm{odd}}. \tag{5.16}$$

Furthermore, a direct exchange interaction J between the monomers can be calculated. However, evaluating these interactions for different dimer configurations yields interactions that are in the range of the direct exchange term $J_{\mathrm{ex}} \approx t^2/(U - U')$ [160, 161] which is caused by the finite tunneling t between the two monomers. Therefore, we neglect an additional direct exchange interaction J in the two impurity Anderson model (TIAM) later on and set it to zero.

Results

Figure 5.10a shows the STS spectra of different dimer configurations. In most cases (black line) the Au-PTCDA complexes undergo a $S = 1/2$ Kondo effect like in the case of a single noninteracting monomer (gray line), however, for some configurations the dimers show broader (red line) or even gapped (green and blue lines) zero-bias peaks. This suggests that the local moments on the two monomers interact with each other. An analysis of the spectra reveals that broadened or gapped zero-bias peaks exclusively occur in the n_{11}, n_{12} and n_{32} configurations.
For atoms on surfaces, gapped zero-bias peaks have been associated with a competition

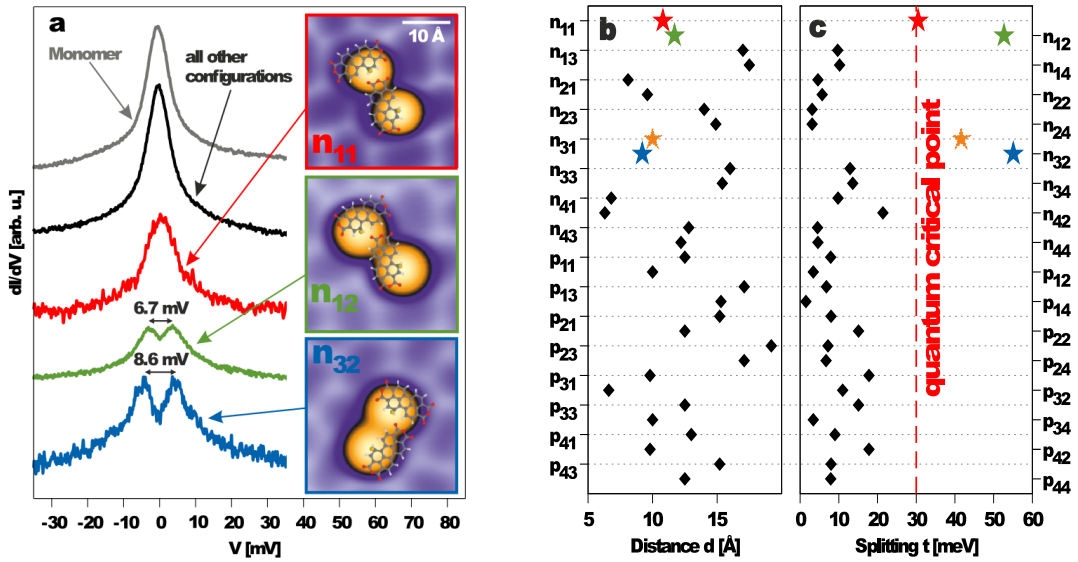

Figure 5.10: (a) dI/dV conductance spectra of Au-PTCDA monomers and several dimers measured at $T = 9.5$ K. The latter are recorded on one of the two Au atoms. The insets show STM images of the corresponding dimers with Au-PTCDA molecules overlayed. n_{ij} configurations are explained in Fig. 5.9b. (b) Au-Au distances for the various dimer configurations and (c) chemical splitting t for the various dimer configurations, both calculated in LDA. Symbols in panels (b) and (c) refer to spectral properties, black diamonds: unbroadened Kondo peaks, stars: broadened or gapped zero-bias peaks, with colors as in panel (a) (orange n_{31} not observed in the experiment). Figures taken from [159].

n_{ij}	$j=1$	$j=2$	$j=3$	$j=4$		p_{ij}	$j=1$	$j=2$	$j=3$	$j=4$
$i=1$	30.5	52.7	9.7	10.2		$i=1$	7.9	3.4	6.8	1.5
$i=2$	4.6	5.7	3.1	3.1		$i=2$	8.0	15.1	7.2	6.7
$i=3$	41.6	55.1	12.9	13.6		$i=3$	17.8	11.0	15.1	3.4
$i=4$	9.8	21.4	4.5	4.6		$i=4$	9.0	17.8	8.0	7.9

Table 5.4: Calculated splittings t in meV for all configurations. Only for the normal n_{ij} configurations large splittings are found. Table taken from [159].

between the Kondo effect and the RKKY [152–155] or exchange interaction [162]. This requires a clear correlation of the spectra to the distance between the local moments. However, Fig. 5.10c shows that in the present case such a correlation is not found. As depicted in Fig. 5.10a, a first hint is the fact that the dimer configuration has a profound influence on the spectra. The dimers of the configuration n_{11} show a single broadened zero-bias peak while the n_{12} and n_{32} exhibit gaps of 6.7 meV and 8.6 meV, respectively. In order to explain these observations, the influence of the dimer configuration on the interaction between the monomers is analyzed with the DFT. Indeed, a splitting t between the even and odd combination of the complexes is found that ranges from $t = 1.5$ meV to $t = 55.1$ meV, suggesting a weak chemical interaction. The various values of the tunneling t between the monomers are listed in Tab. 5.4 for all possible

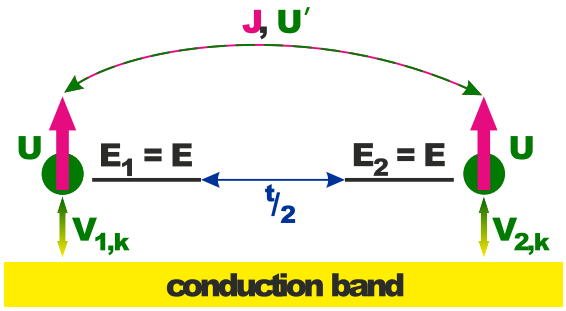

Figure 5.11: Schematic view of the two impurity Anderson model (TIAM) with the level energies $E_1 = E_2 = E$, the intraorbit Coulomb interaction U, the interorbit Coulomb interaction U', the Heisenberg interaction J and the hybridizations $V_{1/2,k}$. In the case discussed here, the Heisenberg interaction is set to zero $J = 0$.

configurations. Figure 5.10c reveals that there is a strong correlation of the formation of a gap to the orbital splitting, while Fig. 5.10b shows that the Au-Au distance seems to play no role. Only for the two largest splittings $t = 55.1$ meV and $t = 52.7$ meV a gap in the spectrum is observed, while an intermediate splitting of $t = 30.5$ meV for the n_{11} configuration leads only to a single broadened zero-bias peak. For all other configurations the orbital splitting is smaller than $t < 22$ meV and a zero-bias peak with essentially the same width as for the monomer is found. Note that the configuration n_{31} with a predicted splitting of $t = 41.6$ meV was not observed in the experimental ensemble along with the n_{41} and n_{42} configurations.

5.2.2 NRG mapping and transmission function

Mapping onto a TIAM

While we have mapped the single Au-PTCDA complex onto a single impurity Anderson model (SIAM), we map the dimer, based on the above considerations of the monomer-monomer interactions, on a two impurity Anderson model (TIAM) [163–165]. A schematic view of the model is depicted in Fig. 5.11. Its Hamiltonian consists of three parts $H_{\mathrm{TIAM}} = H_0 + H_d + H_{\mathrm{hyb}}$. The first term H_0 describes a single conduction band

$$H_0 = \sum_{\vec{k},\sigma} \epsilon_{\vec{k}\sigma} c^\dagger_{\vec{k},\sigma} c_{\vec{k},\sigma} \tag{5.17}$$

where $c^\dagger_{\vec{k},\sigma}$ creates an electron with spin σ and momentum $\vec{k}$ and the conduction band dispersion is given by $\epsilon_{\vec{k}}$. H_d labels the part of the impurities and can be written as

$$H_d = \sum_{j,\sigma} E_j d^\dagger_{j,\sigma} d_{j,\sigma} + U \sum_j n_{j,\uparrow} n_{j,\downarrow} + U' \sum_{\sigma,\sigma'} n_{1,\sigma} n_{2,\sigma'} + \frac{t}{2} \sum_\sigma \left(d^\dagger_{1,\sigma} d_{2,\sigma} + d^\dagger_{2,\sigma} d_{1,\sigma} \right). \tag{5.18}$$

Here $d^\dagger_{j,\sigma}$ creates an electron with spin σ on monomer j with the energy E_j. The tunneling between the two monomers is given by t while U and U' denote the intra- and interorbital Coulomb interaction, respectively. As already discussed above, the DFT does not predict any additional direct spin interactions and we, therefore, omit an direct Heisenberg interaction J between the monomers in Eq. (5.18). The hybridization between the conduction band and the impurities is given by

$$H_{\text{hyb}} = \sum_{j\in\{1,2\}k,\sigma} V_{j,k} c^\dagger_{\vec{k},\sigma} e^{i\vec{k}\vec{R}_j} d_{j,\sigma} + \text{h.c.}, \tag{5.19}$$

with the hybridization strength $V_{j,\vec{k}}$ and $\vec{R}_j$ being the location of the π-orbital Ψ_j.
In the following, we will use the simplification $V_{1,\vec{k}} = \alpha V_{2,\vec{k}}$, based on the assumption that the energy dependencies of the monomer coupling functions

$$\Gamma_1(\epsilon) = \pi \sum_{\vec{k}} |V_{1,\vec{k}}|^2 \delta(\epsilon - \epsilon_{\vec{k}}) = \pi\alpha^2 \sum_{\vec{k}} |V_{2,\vec{k}}|^2 \delta(\epsilon - \epsilon_{\vec{k}}) = \alpha^2 \Gamma_2(\epsilon) \tag{5.20}$$

only differ by an overall scaling factor α which becomes $\alpha = 1$ for fully identical monomers. As already discussed in Sec. 3.1.1 the effect of the bath on an impurity is completely determined by the hybridization function $\Gamma(\epsilon)$ (cf. Eq. (3.3)). Therefore, the $\vec{k}$-dependence of $V_{j,\vec{k}}$ only enters $\Gamma_j(\epsilon) = \pi \overline{V}_j \rho_c(\epsilon)$ via the energy-dependent effective density of states (DOS) $\rho_c(\epsilon)$. Here, $\overline{V}_j$ is given by

$$\pi \overline{V}_j^2 = \int \Gamma_j(\epsilon)\, d\epsilon. \tag{5.21}$$

To solve the TIAM using the numerical renormalization group (NRG), we have to transform the operators $c_{\vec{k},\sigma} e^{i\vec{k}\vec{R}_j}$ to an orthogonal even/odd basis [47, 61, 62, 64, 124, 165] (cf. also with Sec. 4.1.1 and appendix A). For this purpose, the origin of the coordinate system is placed in the middle between the two orbital positions and the vector distance $\vec{R} = \vec{R}_1 - \vec{R}_2$ between both orbitals is introduced. In the new even/odd basis, H_{hyb} reads in energy representation as

$$\begin{aligned} H_{\text{hyb}} = & \frac{1}{2} \sum_\sigma \int d\epsilon \sqrt{\rho_c(\epsilon)} \Big\{ N_{\text{e}}(\epsilon, \vec{R}) c^\dagger_{\epsilon\text{e},\sigma} (\overline{V}_1 d_{1,\sigma} + \overline{V}_2 d_{2,\sigma}) \\ & + N_{\text{o}}(\epsilon, \vec{R}) c^\dagger_{\epsilon\text{o},\sigma} (\overline{V}_1 d_{1,\sigma} - \overline{V}_2 d_{2,\sigma}) \Big\} + \text{h.c.}, \end{aligned} \tag{5.22}$$

where the energy-dependent field operators $c_{\epsilon\text{e/o},\sigma}$ are defined by Eq. (A.5) and the normalization factors $N_{\text{e/o}}(\epsilon, \vec{R})$ are given by Eq. (A.9). Note that in the definitions of $c_{\epsilon\text{e/o},\sigma}$ and $N_{\text{e/o}}(\epsilon, \vec{R})$ the DOS $\rho(\epsilon)$ has to be replaced by the effective DOS $\rho_c(\epsilon)$. As for the two impurity Kondo model (TIKM) described in Sec. 2.2 and appendix A, the two impurities couple to two effective conduction bands, one with even parity and the other with odd parity. Since the size of the LUMO+Au orbitals is similar to the

distance R between the monomers, we neglect the detailed spatial dependence and let $R \to 0$. With this approximation, the normalization factor of the odd conduction band vanishes $N_{\mathrm{o}}(\epsilon, R \to 0) \to 0$, and the odd-parity band completely decouples from the impurity, yielding

$$H_{\mathrm{hyb}} = \sum_{\sigma} \int d\epsilon \sqrt{\rho_c(\epsilon)} [c^{\dagger}_{\epsilon \mathrm{e},\sigma} (\overline{V}_1 d_{1,\sigma} + \overline{V}_2 d_{2,\sigma}) + \mathrm{h.c.}]. \tag{5.23}$$

If we assume identical orbital energies $E = E_1 = E_2$ in both monomers, the single-particle eigenbasis in the presence of the tunneling term t in the dimer is given by the even- and odd-parity orbitals

$$d_{\mathrm{e/o},\sigma} = \frac{1}{\sqrt{2}} (d_{1,\sigma} \pm d_{2,\sigma}). \tag{5.24}$$

With these new impurity operators, H_{hyb} can be written as

$$H_{\mathrm{hyb}} = \sum_{\vec{k},\sigma} [c^{\dagger}_{\vec{k},\sigma} (V_{\mathrm{e},\vec{k}} d_{\mathrm{e},\sigma} + V_{\mathrm{o},\vec{k}} d_{\mathrm{o},\sigma}) + \mathrm{h.c.}] \tag{5.25}$$

without referring to an energy representation and using the new hybridizations

$$V_{\mathrm{e/o},\vec{k}} = \frac{1}{\sqrt{2}} (V_{1,\vec{k}} \pm V_{2,\vec{k}}). \tag{5.26}$$

Note that in the limit $\vec{R} \to 0$ the even conduction electron band is identical to the original band, and the odd band vanishes. Transforming H_d into these new impurity operators yields

$$H_d = \sum_{\sigma} \left[E_{\mathrm{e}} d^{\dagger}_{\mathrm{e},\sigma} d_{\mathrm{e},\sigma} + E_{\mathrm{o}} d^{\dagger}_{\mathrm{o},\sigma} d_{\mathrm{o},\sigma} \right] + \frac{1}{2} \sum_{abcd \in \{\mathrm{e,o}\}, \sigma\sigma'} \tilde{U}_{abcd} d^{\dagger}_{a,\sigma} d^{\dagger}_{b,\sigma'} d_{c,\sigma'} d_{d,\sigma} \ , \tag{5.27}$$

with $E_{e/o} = E \pm t/2$ and the non-vanishing matrix elements of $\tilde{U}_{abcd}$ are given by

$$\tilde{U} = \tilde{U}_{aaaa} = \frac{U + U'}{2} \tag{5.28}$$

$$\tilde{U}' = \tilde{U}_{abba} = \frac{U + U'}{2} \tag{5.29}$$

$$\tilde{J} = \tilde{U}_{abab} = \tilde{U}_{aabb} = \frac{U - U'}{2}, \tag{5.30}$$

ensuring rotational invariance in spin space [166]. The general form of Eq. (5.27) is equivalent to

$$H_d = \sum_{\alpha=\{e,o\},\sigma} E_\alpha d^\dagger_{\alpha,\sigma} d_{\alpha,\sigma} + \tilde{U} \sum_\alpha n_{\alpha,\uparrow} n_{\alpha,\downarrow} + \frac{2\tilde{U}' - \tilde{J}}{2} \sum_{\sigma,\sigma'} n_{e,\sigma} n_{o,\sigma'} - 2\tilde{J} \vec{S}_e \vec{S}_o + \tilde{J} \left(d^\dagger_{e,\uparrow} d^\dagger_{e,\downarrow} d_{o,\downarrow} d_{o,\uparrow} + \text{h.c.} \right), \tag{5.31}$$

using the three parameters $\tilde{U}, \tilde{U}'$ and the effective ferromagnetic ($U > U'$) Heisenberg interaction between the even and odd orbital $\tilde{J}$.
Note that if we consider the full parity symmetric case $E_1 = E_2$ and also $V_{1,\vec{k}} = V_{2,\vec{k}}$, the odd-parity orbital decouples from the conduction band according to Eqs. (5.25) and (5.26). However, it turns out that in order to explain the experimentally observed formation of a gap in the spectra, a small parity asymmetry is needed so that the even conduction electrons weakly hybridize with the odd dimer orbital. We consider parity breaking by introducing a small scaling factor $q = V_{o,\vec{k}}/V_{e,\vec{k}} = (\alpha - 1)/(\alpha + 1)$. For $q \neq 0$ the hybridization strengths $V_{1,\vec{k}}$ and $V_{2,\vec{k}}$ of the two monomers slightly differ by an overall scaling factor $\alpha = (1+q)(1-q) \neq 1$.
The assumption of a parity breaking is justified since the local environments around the monomer orbitals are in general slightly different due to the alignments of the PTCDA molecules. Therefore, the single particle energies are slightly different, too, i.e. $E_1 \neq E_2$. Nevertheless, even for $E_1 \neq E_2$ we are still able to diagonalize the single-particle basis of the two monomer orbitals into a new basis of a bonding and an antibonding orbital, albeit with a modified unitary transformation

$$\begin{aligned} d_{e,\sigma} &= a_1 d_{1,\sigma} + a_2 d_{2,\sigma} \\ d_{o,\sigma} &= a_2 d_{1,\sigma} - a_1 d_{2,\sigma} \end{aligned} \tag{5.32}$$

which lacks even and odd symmetry for generic linear combinations $a_1^2 + a_2^2 = 1$.
Using the same unitary transformation for the hybridization matrix, Eq. (5.26) will be modified analog to Eq. (5.32). Consequently, even for $V_{1,\vec{k}} = V_{2,\vec{k}}$ a finite matrix element $V_{o,\vec{k}}$ is generated which is enhanced by the slight symmetry breaking of $V_{1,\vec{k}} \neq V_{2,\vec{k}}$. The Hamiltonian in the even/odd basis is, hence, the generic description where t parameterizes the total splitting stemming from $E_1 - E_2$ as well as the hopping term, and $q = V_{o,\vec{k}}/V_{e,\vec{k}}$ denotes the generic degree of asymmetry. It turns out that the precise value of $q \ll 1$ does not influence the gap formation, the gap width as well as the location of quantum phase transition which will be discussed later on.

Parameters of the TIAM

As for the monomer, the parameters of the model are extracted from the DFT/MBPT calculations by treating the projected DOS ρ_{GdW} as an effective mean-field spectrum

$$\rho_{\mathrm{GdW}}(\epsilon) \equiv \lim_{\delta\to 0^+} \mathrm{Im}\frac{1}{\pi}\frac{1}{\epsilon - i\delta - E_j - nU - \Delta_j(\epsilon - i\delta)} \tag{5.33}$$

with $\Delta_j(z) = \int d\epsilon \Gamma_j(\epsilon)/(z-\epsilon)$. For this purpose we use the same $\rho_{\mathrm{GdW}}(\epsilon)$ as for the monomer shown in Fig. 5.6 (black line) yielding the same hybridization strength $\Gamma(E)$ depicted in Fig. 5.7. The hybridization functions of the even and odd orbitals are then defined by

$$2\Gamma(E) = \Gamma_e(E) + \Gamma_o(E) = (1+q^2)\Gamma_e(E). \tag{5.34}$$

For the intraorbital Coulomb interaction we use a uniform $U = 1.4$ eV for both monomers. This value is slightly larger than the values obtained for the monomer (see discussion above in Sec. 5.2.1) and we, therefore, also derive a different level energy of about $E = -1.09$ eV for both Au-PTCDA complexes. The interorbital Coulomb interaction U' calculated for the n_{32} configuration is given by $U' = 0.12$ eV[1]. Note that while in the NRG the tunneling t is a continuously tunable parameter, in experiment it is determined by the dimer configuration n_{ij} and hence discrete, albeit with a rather dense spacing.

Conduction electron transmission function

We now discuss the quantity that can be directly compared to experimental STS spectra. Since only the linear combination

$$A^\dagger_\sigma = \frac{1}{\sqrt{V_1^2+V_2^2}}\left(V_1 d^\dagger_{1,\sigma} + V_2 d^\dagger_{2,\sigma}\right) = \frac{1}{\sqrt{1+q^2}}(d^\dagger_{\sigma,\mathrm{e}} + q d^\dagger_{\sigma,\mathrm{o}}) \tag{5.35}$$

of orbitals couple to the substrate according to Eq. (5.25), the spectrum of conduction electron transmission function which is accessible to the STS is given by $\rho_\sigma(\omega) = \mathrm{Im}G_\sigma(\omega - i0^+)/\pi$ with the Green's function $G_\sigma(z) = \langle A_\sigma | A^\dagger_\sigma\rangle(z)$. Any position-dependent scanning tunneling microscopy (STM) matrix elements have not been taken into account. Since we solve the TIAM in the limit $R \to 0$ and thus neglect any spatial dependence, this approximation is justified. Convoluting $\rho_\sigma(\omega)$ with the derivative of the Fermi functions yields the differential conductance $dI/dV(V)$ up to a prefactor. Note that for the parity symmetric case ($q = 0$), the odd orbital decouples and hence only the properties of the even orbital are measured.

[1] For the other configurations U' ranges from 0.06 eV to 0.14 eV.

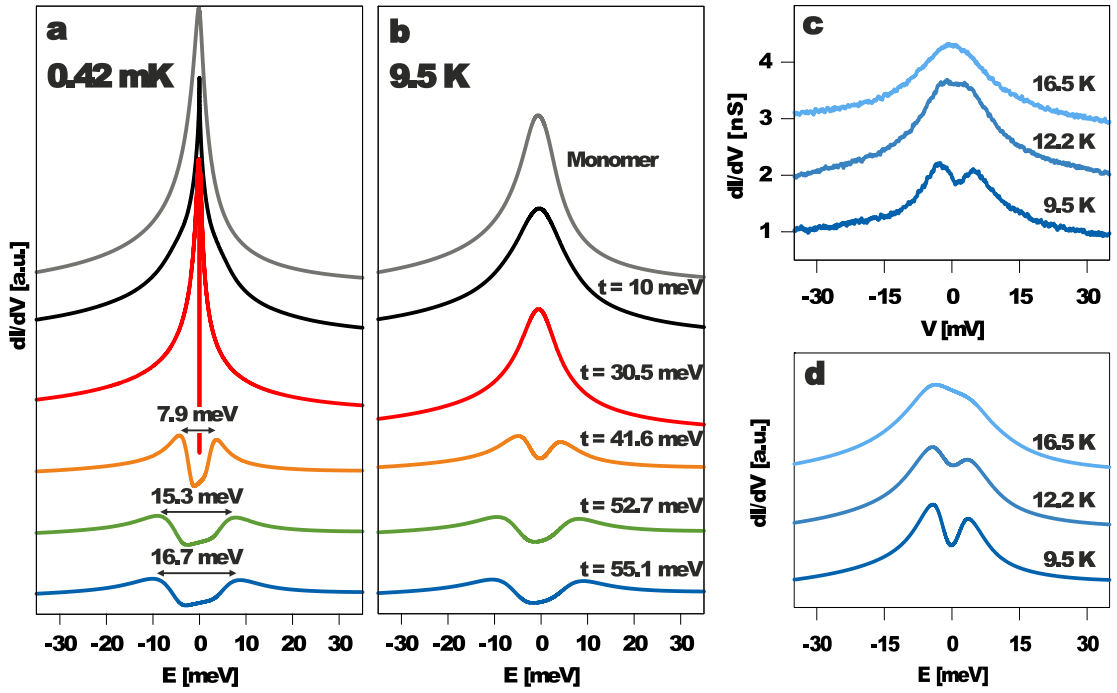

Figure 5.12: (a) dI/dV spectra from NRG for different values of t, $q = V_o/V_e = 0.1$ and $T = 0.42 \approx 0$ mK. The parameters of the TIAM $E = -1.089$ eV, $U = 1.4$ eV, $U' = 0.12$ eV and $J = 0$ are extracted from the LDA+GdW. (b) dI/dV spectra from NRG for the same temperature as in the experiment $T = 9.5$ K, all other parameters as in panel (a). (c) Experimentally measured dI/dV conductance spectra of a n_{32} dimer recorded at three different temperatures. (d) dI/dV spectra from NRG for the same temperatures as in panel (c), using parameters from panel (a), $t = 40$ meV (as best fit of the gap) and $q = 0.1$.

Furthermore, we investigate the orbital diagonal spectral functions of the even and odd orbital which are defined as

$$\rho_{\sigma,\mathrm{e}}(\omega) = \frac{1}{\pi}\mathrm{Im}\langle d_{\sigma,\mathrm{e}} | d^{\dagger}_{\sigma,\mathrm{e}}\rangle(\omega - io^{+}) \tag{5.36}$$

$$\rho_{\sigma,\mathrm{o}}(\omega) = \frac{1}{\pi}\mathrm{Im}\langle d_{\sigma,\mathrm{o}} | d^{\dagger}_{\sigma,\mathrm{o}}\rangle(\omega - io^{+}). \tag{5.37}$$

The mixed contributions $\rho_{\sigma,eo}(\omega)$ and $\rho_{\sigma,oe}(\omega)$ could in principle be calculated by the difference between $\rho_{\sigma}(\omega)$, $\rho_{\sigma,\mathrm{e}}(\omega)$ and $\rho_{\sigma,\mathrm{o}}(\omega)$ with the appropriate weight factors. However, it is not expected that these contributions contain new information, besides, the mixed contributions vanish for the parity symmetric case ($q = 0$) and, therefore, their contributions to the measured spectra for a small parity asymmetry $q \ll 1$ are expected to be weak.

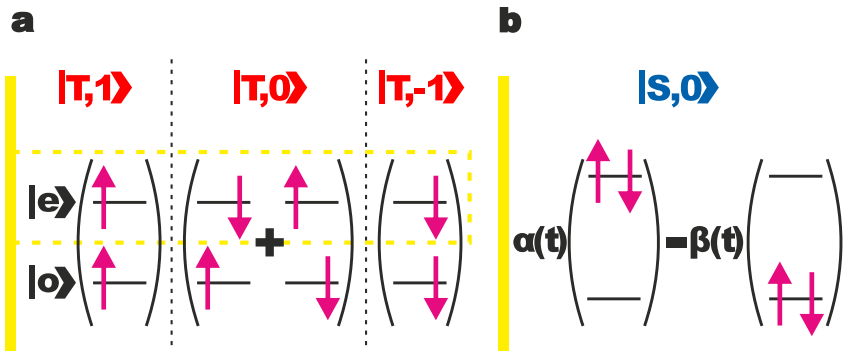

Figure 5.13: (a) For $t < t_c$ the ground state consists of the three triplet states $S_z = 1, 0, -1$. The yellow dashed line indicates that the screening of the spin in the even orbital by the conduction band electrons due to the Kondo effect. (b) The ground state for $t > t_c$ is a singlet which is a linear combination of the two doubly occupied orbitals. For $t = 0$ and a particle-hole symmetric substrate the coefficients are given by $\alpha = \beta = 1/\sqrt{2}$.

5.2.3 NRG results

Comparison with experiment

Figures 5.12a and b show the results of the combined DFT+MBPT+NRG calculation for the different temperatures $T = 0.42 \approx 0$ mK and $T = 9.5$ K, respectively. The results for $T = 9.5$ K are in excellent agreement with the experimental data depicted in Fig. 5.10a, without any fitting parameters. The agreement covers the monomer spectrum, which has been discussed in Sec. 5.1, and the configuration dependence of the dimer spectra. Using the corresponding t for the different configurations, which are obtained from the DFT, we find a single zero-bias peak for n_{11} (red curve) and gapped peaks for n_{12} (green curve) and n_{32} (blue curve). The LDA+GdW+NRG predicts also a gap for the n_{31} configuration (orange curve, $t = 41.6$ meV), however, this configuration was not observed in the experiment. For $T \approx 0$ (Fig. 5.12a) the single peak of the n_{11} configuration (red curve) turns into a very narrow gap. However, this gap cannot be seen in the experiment because of the finite temperature of about $T = 9.5$ K. Furthermore, also the temperature evolution of the experimentally measured dI/dV curves shown in Fig. 5.12c agrees very well with the one observed in the NRG spectra depicted in Fig. 5.12d. Note that the gaps for n_{12} and n_{32} are a factor of two larger in the calculation than in experiment. However, since the size of the gap depends very sensitively on t, U' and via the Kondo temperature also exponentially on the Coulomb interaction U, a reduction of t by less than 10 meV would bring the calculated gap into agreement with experiment.

Detailed analysis: Quantum critical points

After we have verified the excellent agreement between the experimental dI/dV curves and the spectra obtained from the LDA+GdW+NRG approach, we now turn to a de-

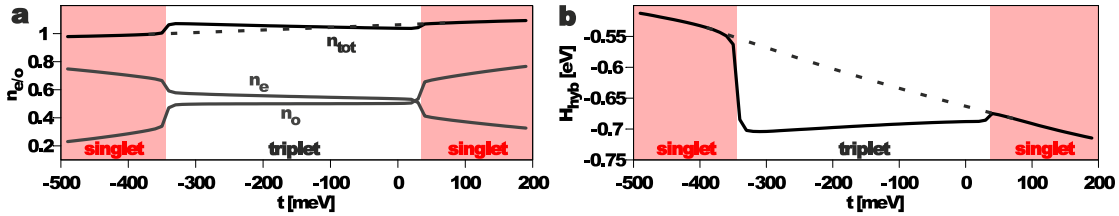

Figure 5.14: (a) Occupation numbers per spin n_e, n_o and $n_{tot} = n_e + n_o$ as a function of t for $q = 0.1$. At the QCPs $t_c^{\pm}$ steps in the occupation occur. The dotted line indicates the overall increase of n_{tot} in the singlet state. (b) Expectation value of the hybridization energy $\langle H_{Hyb} \rangle$ as a function of t for $q = 0.1$. At the QCPs $t_c^{\pm}$ the hybridization $|\langle H_{Hyb} \rangle|$ drops sharply. For $t_c^- < t < t_c^+$ the triplet ground state is stabilized by $\langle H_{Hyb} \rangle$. The dashed line indicates the overall increase of the energy gain due to hybridization in the singlet state.

tailed discussion of the NRG results. Since the isolated Au-PTCDA monomers carry a $S = 1/2$ moment in their LUMO+Au orbital, the two Au-PTCDA monomers, brought together in close vicinity, maintain a four-fold spin-degenerate ground state consisting of three triplet states $|\uparrow_1, \uparrow_2\rangle$, $|\downarrow_1, \downarrow_2\rangle$, $\frac{1}{\sqrt{2}}(|\uparrow_1, \downarrow_2\rangle + |\downarrow_1, \uparrow_2\rangle)$ and one singlet state $\frac{1}{\sqrt{2}}(|\uparrow_1, \downarrow_2\rangle - |\downarrow_1, \uparrow_2\rangle)$, if all additional interactions besides U and U' are neglected. From the ground state the two singlet states $|\uparrow\downarrow_1, 0_2\rangle$ and $|0_1, \uparrow\downarrow_2\rangle$ are separated by the energy difference $U - U'$.

The same degeneracy is also found in the even-odd basis. The ground state comprises the three triplet states $|\uparrow_e, \uparrow_o\rangle$, $|\downarrow_e, \downarrow_o\rangle$, $\frac{1}{\sqrt{2}}(|\uparrow_e, \downarrow_o\rangle + |\downarrow_e, \uparrow_o\rangle)$ which are shown in Fig. 5.13a. However, the singlet state $\frac{1}{\sqrt{2}}(|\uparrow_e, \downarrow_o\rangle - |\downarrow_e, \uparrow_o\rangle)$ is separated from the triplet by $2\tilde{J} = U - U'$. This shift is caused by the fourth term of Eq. (5.31). The large pair hopping term (last term of Eq. (5.31)) leads to an entanglement between the two doubly occupied states, while the singlet state $\frac{1}{\sqrt{2}}(|\uparrow\downarrow_e, 0_o\rangle + |0_e, \downarrow\uparrow_o\rangle)$ is shifted to an energy $U - U'$ above the ground states, the combination $\frac{1}{\sqrt{2}}(|\uparrow\downarrow_e, 0_o\rangle - |0_e, \downarrow\uparrow_o\rangle)$ is shifted to lower energies, leading to a four-fold spin-degenerate ground state which again consists of three triplet and one singlet state.

However, interactions between the monomers have to be taken into account. A finite tunneling $t/2$ between the two monomer valence orbitals generates an antiferromagnetic exchange $J_{ex} \approx t^2/(U - U')$ promoting independently of the sign of t the dimer singlet ground state $\alpha(t)|\uparrow\downarrow_e, 0_o\rangle - \beta(t)|0_e, \uparrow\downarrow_o\rangle$ which is depicted in Fig. 5.13b. Here, $\alpha(t)$ and $\beta(t)$ are coefficients depending on the splitting t which define the admixtures of the even and odd orbital to the singlet state. J_{ex}, however, is too small to explain the width and the temperature dependence of the gaps in the spectra, hence, the exchange interaction alone cannot be responsible for the observations.

Additionally, also the coupling to the conduction band has to be considered. Since the electrons in the singlet state are more localized, the system gains kinetic energy in the triplet state. Furthermore, the two monomer local moments couple antiferromagnetically to the local even conduction electron spin via an effective Kondo coupling J_K [80]

at low temperatures. Consequently, the Kondo effect yields an additional energy gain of the local triplet over the singlet ground state.

With increasing splitting t, the energy of the singlet is lowered and once $|t|$ exceeds critical values $|t_c^{\pm}|$, defining two QCPs, a QPT occurs since the singlet is favored over the kinetic energy gain which leads to a breakdown of the Kondo effect.

Because the singlet state is related to the double occupancy of the even and odd orbital, the QPT also involves a sudden change of the occupancy of the orbitals which is shown in Fig. 5.14a. For $t_c^- < t < t_c^+$ both the even and the odd orbital are almost singly occupied while for $t > t_c^+$ the occupancy of the odd orbital suddenly rises and the occupancy of the even orbital drops down. For $t < t_c^-$ the opposite is the case. This is in accordance with a single particle picture in which a positive splitting lowers the energy level of the odd orbital $E_o = E - t/2$ leading to an almost doubly occupied odd orbital ($|\alpha(t)| < |\beta(t)|$), while for negative t the energy level of the even orbital $E_e = E + t/2$ is shifted to lower energies ($|\alpha(t)| > |\beta(t)|$).

We now address the mechanism in more detail which at finite t stabilizes the triplet states with one electron each in the even and odd orbitals against the singlet and thus leads to quantum phase transitions at finite $t_c^{\pm}$. Usually the separation of a triplet and a singlet is governed by the exchange interaction [163]. Since DFT predicts a negligibly small exchange interaction $|J_{\mathrm{ex}}| \ll t_c^{\pm}$, the stabilization of the triplet state at finite t is related to the gain of additional kinetic energy due to the hybridization with the substrate. For illustration, the total hybridization energy $\langle H_{\mathrm{hyb}} \rangle$ is plotted as a function of t in Fig. 5.14b. In the local singlet regime ($t < t_c^-$ and $t_c^+ < t$), $\langle H_{\mathrm{hyb}} \rangle$ decreases nearly linearly as function of t, as indicated by the dashed line interpolating the energy in the triplet regime. The reason for this is that the more the even orbital is depleted, the more its electron becomes itinerant, resulting in larger $|\langle H_{\mathrm{hyb}} \rangle|$. In the triplet regime, however, additional hybridization energy is gained. This is observed in the interval $t_c^- < t < t_c^+$, where $\langle H_{\mathrm{hyb}} \rangle$ lies below the interpolated singlet hybridization energy. $\langle H_{\mathrm{hyb}} \rangle$ changes continuously across the QCP, and only its derivative diverges at the QCP. Moreover, the Kondo effect yields a further energy gain of the triplet over the singlet ground state at low temperatures.

Although a QPT occurs for positive and negative tunnelings t, only a positive t yields a perfect agreement with the experiment which is, however, in agreement with DFT that also predicts a positive t. The asymmetry between the two values t_c^+ and t_c^-, shown in Figs. 5.14a and b, is generated by the strongly energy-dependent coupling to the substrate. The real part of the complex coupling function $\Delta(z)$ shifts the energy levels slightly to higher energies. Since the even orbital hybridizes more strongly to the substrate, the even orbital is shifted above the odd orbital already for $t = 0$. Afterwards, only a relatively small additional positive molecular t is needed to drive the system across the QCP. This means that it is "easier" to achieve the singlet state where the odd orbital is almost doubly occupied than the almost even doubly occupied state.

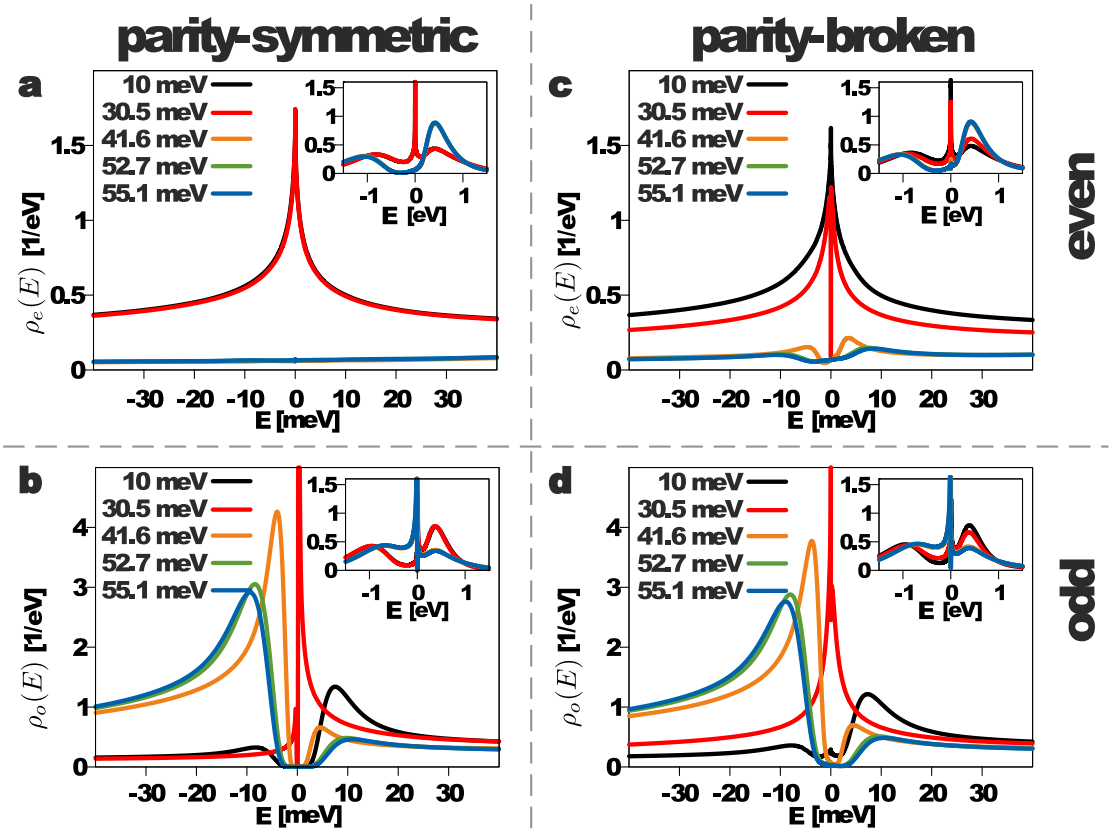

Figure 5.15: Spectral functions of the (a) even orbital and (b) odd orbital in the parity symmetric case ($q = 0$) for different splittings t. (c) Even and (d) odd orbital spectral functions for various t in the parity broken case ($q = 0.1$). Colors as in Fig. 5.10. The insets show the spectral functions for a larger energy range.

Finally, we stress that the presented microscopic mechanism based on a chemically driven QPT is generic. Including an additional finite direct J only influences the values of the critical splitting $t_c^{\pm}$, but not the quantum critical scenario. Only for a very large direct antiferromagnetic coupling J the QPT is destroyed and no Kondo effect can be detected.

Origin of the gap in the STM spectra

In order to investigate the physics of the gap in the zero-bias peak in more detail, we now examine the spectral functions of the even and odd orbital (Eqs. (5.36) and (5.37)) separately. For this purpose, we first consider the parity symmetric case ($q = 0$) and afterwards the parity broken ($q = 0.1$).

The spectral functions of the even and odd orbital for the parity symmetric case are shown in Fig. 5.15a and b, respectively. In the spectral function of the even orbital for $t < t_c^+ \approx 30.5$ meV the Kondo resonance of an underscreened $S = 1$ Kondo effect is clearly visible. If an electron is injected into the even orbital, the system responds by ejecting an electron with opposite spin into the conduction band because of the large

Coulomb interaction U. Therefore, this injection provokes a transition between the two degenerate triplet states $S_z = 1$ and $S_z = 0$. As a consequence of this spin-flip excitation, the previously mentioned Kondo resonance at $E = 0$ appears in the spectrum. The underscreened Kondo effect arises from the fact that in the parity symmetric case only the spin in the even orbital is screened by the conduction band electrons while the odd orbital completely decouples and hence remains unscreened. However, the spin of the odd orbital fluctuates as well since it is ferromagnetically coupled to the spin in the even orbital via the Heisenberg interaction $\tilde{J}$.

For $t > t_c^+ \approx 30.5$ meV the Kondo effect breaks down indicating a change of the many-body ground state. As discussed above, this breakdown of the Kondo effect is caused by the transition from the triplet (Fig. 5.13a) to the singlet state (Fig. 5.13b). The change of the ground state is also visible in the high energy peaks shown in the inset of Fig. 5.15a. After the breakdown of the Kondo effect spectral weight is shifted to the high energy peaks at $E \approx -1.0$ eV and $E \approx 0.4$ eV where the peak at positive energies is larger because for a positive tunneling $|\alpha(t)| < |\beta(t)|$ applies, cf. Fig. 5.13b.

In contrast, the spectrum for the odd orbital shows a completely different behavior. Since the odd orbital is decoupled from the conduction band, charge fluctuations from and into the orbital do not occur and thus there is no dynamical spin degree of freedom of the scatterer, except that it suddenly changes its occupation once. The potential scattering of the conduction electrons due to this structureless scatterer gives rise to the gap in the spectral function that is similar to x-ray absorption edges [167]. The side peaks of the gap are single particle signatures of an imminent change of the many-body ground state in which the odd state becomes either completely empty or filled.

For $t < t_c$ the peaks correspond to an excitation from the triplet to the singlet state. If the odd orbital is suddenly occupied (peak at positive energies), the system can only respond by transferring the electron of the even orbital into the conduction band due to the large Coulomb interactions since the odd orbital is decoupled and hence cannot be depleted. On the other hand, if an electron is removed from the odd orbital (peak at negative energies), an additional electron is transferred from the conduction band into the even orbital so that it is doubly occupied. Accordingly, the peaks correspond to excitations from the singlet to the triplet state if the splitting is increased beyond the QCP $t > t_c$.

Unlike the triplet-triplet transition in the even orbital, this is not a zero-energy transition but involves a finite transition energy. As a consequence, the spectral signature of this process occurs at finite energy. The threshold energy is related to the energy difference between the two competing ground states (triplet vs. singlet) of the dimer. At the QCP ($t = t_c$) the energy difference between the triplet and the singlet ground state diminishes and, therefore, the width of the gap vanishes. This can be seen in Fig. 5.15b for $t = 30.5$ meV which is very close to the QCP.

Since for this process the overcoming of a certain threshold, namely the energy dif-

ference between singlet and triplet states, is required, the spectral signatures appear as *sharp* adsorption edges. However, due to the broadening in the NRG spectra, these sharp edges are smoothed. In contrast to the spin-flip excitations in the even orbital, in this process the many-body ground state changes from a triplet to a singlet and, therefore, gives rise to a different potential which is felt by the conduction band electrons. By injecting an electron into or extracting an electron from the odd orbital, the dimer becomes a charged scatterer.

Note that these excitations are entirely different from the high energy charge excitations shown in the inset since the total occupation number of the dimer does not change.

As already mentioned above, the STM can only detect those parts of the local spectral function that are included in the conduction electron transmission function of Eq. (5.35). In the parity symmetric case the odd spectral function and hence the gap is not detectable.

Therefore, the experimental spectra prove that parity symmetry must be broken in the dimer, as it is also expected considering the lack of symmetry in the dimer. If parity is broken, the odd orbital also couples to the even conduction band and thus properties of the odd orbital are weakly mixed into the spectral function of the even orbital (Figs. 5.15c and d) as well as into the total transmission function (Fig. 5.12a). Below the QCP at $t < t_c^+ \approx 30$ meV the system is in the triplet state (black curve) and the picture is essentially unchanged compared to the parity symmetric case since the Kondo resonance in the even spectrum dominates over the other terms. In contrast, for $t > t_c^+ \approx 30$ meV the total spectrum is now determined by the absorption edges of the odd orbital because the Kondo peak in the even orbital has collapsed. This opens the gap in the STM spectrum. The physics of the gapped 'Kondo peak' is hence not the Kondo effect itself, but a remnant of the gap in the odd spectrum, which in turn is related to the fact that in the parity symmetric case the spin-dynamics in the odd orbital decouples from the conduction electrons.

The size of the odd admixture determines mainly the height of the spectral features but has only a small influence on the width of the gap or the positions of the QCPs. As for the parity symmetric case, the width of the gap reflects the distance to the QCP. This is illustrated by Figs. 5.15c and d for $t = 30.5$ meV (red curve) which corresponds to the experimental configuration n_{11}. Located very close to the QCP, at finite temperature the spectral properties are those of the Kondo effect. Only at an exponentially small temperature that is not accessible to the experiment, a very small gap opens. In particular, for $t = 30.5$ meV (red curve in Figs. 5.12a and b) the edges above and below the Fermi level merge to a single peak for $T = 9.5$ K which is in agreement with the experimental observations for the n_{11} configuration depicted in Fig. 5.10a.

5.2.4 Dimer: Summary

In this section we have investigated the interaction between two adjacent Au-PTCDA complexes adsorbed on an Au(111) surface. The spin carrying orbitals in the Au-PTCDA are delocalized over the complete molecules leading to a strong chemical hybridization between the molecular monomers. This ordinary chemical hybridization is strong enough to drive a QPT from a Kondo singlet with almost equally populated orbitals to a local singlet with orbital ordering, without the need for an additional exchange interaction.

In the experiment the QPT could be revealed by means of STS. While for dimer configurations with a weak hybridization between the monomers a Kondo resonance has been observed, the particularly strong interactions of specific dimer configurations lead to a formation of a gap in the STS spectrum.

As for the case of a single Au-PTCDA complex, presented in Sec. 5.1, the experimental data and the results of the combined LDA+GdW+NRG approach are in excellent agreement. In particular the LDA+GdW+NRG is able to predict the formation of a gap in the spectrum for the correct dimer configurations without any fitting parameters.

For adatoms on a metallic surface the formation of a gap in the spectrum is often associated with the competition between an indirect exchange interaction (RKKY) and the Kondo effect. However, the RKKY interaction, although present in the model, does not materialize in this system since an expected distance dependence of the spectra is not found.

It is remarkable that in the present case the entanglement with the substrate stabilizes the local triplet state against the preference of the local singlet state due to chemical hybridization. The subsequent underscreened Kondo effect yields a further energy gain and reduces the triplet moment to an effective $S = 1/2$.

In contrast to the case discussed here, in the conventional generic two-impurity Kondo physics [62–64, 66, 154, 156] no QPT and only a crossover is found, cf. Sec. 2.3. In addition, the screening of the local triplet is complete and occurs via a two-stage Kondo effect involving even as well as odd conduction electron states. These profound differences between the conventional scenario and our situation are related to the spatially extended nature of the individual monomer π-orbitals which are large compared to the lattice spacing of the underlying substrate as well as the shortest distance between the two monomers.

Finally, we stress that mere changes of the relative orientations of the monomers, and thus tiny changes in the wave function overlap, are enough to drive the system through the QCP. Thus, we have here an extremely sensitive chemical handle on the magnetic properties of a supermolecular architecture. Because it relies only on general principles of chemical interactions and Kondo physics, we expect this mechanism to be of general validity, opening up a new road to engineer magnetic interactions.

Chapter 6

Two impurity Kondo model

The particle-hole symmetric two impurity Kondo model (TIKM) with constant even and odd densities of states (DOSs) exhibits a quantum critical point (QCP) which separates the Kondo phase and the decoupled singlet phase [62, 63]. Its position depends on the ratio between the Kondo temperature T_K and the effective spin-spin interaction between the two impurity spins $\vec{S}_1$ and $\vec{S}_2$. However, the constant DOSs are an approximation which always leads to a ferromagnetic RKKY interaction for all distances [61, 62]. On the other hand, quantum Monte Carlo (QMC) calculations [64, 67, 68] with energy-dependent couplings have not seen such a QCP and, therefore, this QCP is often considered to be artificial. Taking into account the proper energy-dependence of the even and odd DOSs makes the model particle-hole asymmetric, destroys the QCP and leads to a continuous crossover between the two phases. For a more detailed description of the TIKM and its QCP we refer the reader to Sec. 2.3.
In this chapter we demonstrate how the QCP of the energy-dependent TIKM can be restored by adding potential scattering terms to the Hamiltonian of the TIKM

$$H_{\text{TIKM+pot}} = H_{\text{TIKM}} + \sum_{\sigma} \left[V_e c^{\dagger}_{e,0,\sigma} c_{e,0,\sigma} + V_o c^{\dagger}_{o,0,\sigma} c_{o,0,\sigma} \right] \tag{6.1}$$

where H_{TIKM} is the Hamiltonian (2.12) of the TIKM and $c_{e/o,0,\sigma}$ the operator that creates an electron on the zeroth site of the even/odd Wilson chain. These initial potential scatterings are intended to compensate the potential scatterings that are automatically generated by the numerical renormalization group (NRG) in a particle-hole asymmetric case [27]. Furthermore, we present some first basic nonequilibrium results of the TIKM with constant as well as with energy-dependent DOSs after a quench in the spin-spin interaction between the two impurity spins for two different kinds of initial conditions.
This chapter is organized as follows: Section 6.1 deals with the equilibrium properties of the TIKM, the method how the QCP is restored as well as the occurring problems are discussed in detail. Afterwards, we turn to the investigation of the nonequilibrium dynamics. At first, we present in section 6.2 the nonequilibrium data for different spin-spin interaction quenches within a phase as well as quenches over the QCP for

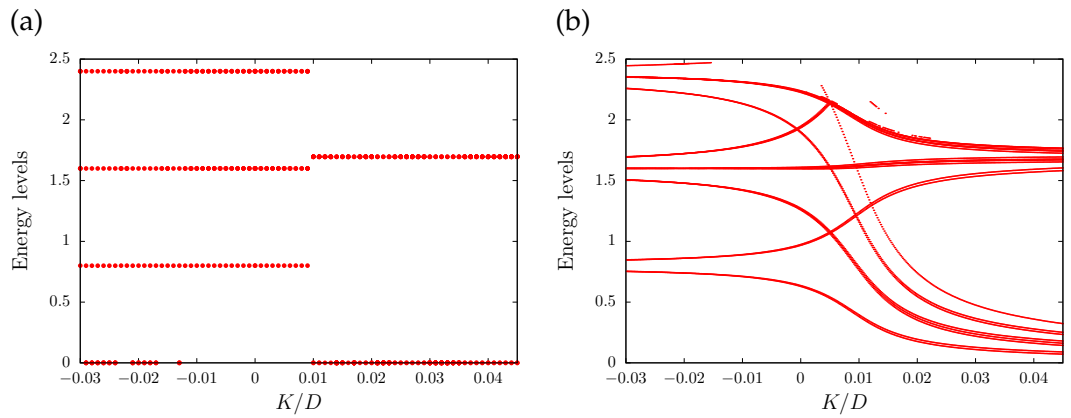

Figure 6.1: (a) Fixed point spectrum of the TIKM with constant DOSs vs. the spin-spin interaction K for even iterations, $\rho J = 0.2$ and $N_o/N_e = 1$. The two different phases and the QCP at $K_c \approx 0.01D$ which separates them are clearly visible. (b) Even iterations fixed point spectrum of the TIKM with full energy-dependent DOSs plotted against K for $k_F R/\pi = 0.6591$ and $\rho J = 0.2$. Degeneracies are lifted by the particle-hole asymmetry and the QCP is replaced by a crossover. NRG parameters are $\Lambda = 3$ and $N_s = 1500$.

constant DOSs so that the model always exhibits a QCP. This section is intended to set the stage for the next section 6.3 where we investigate the nonequilibrium data for the full energy-dependent TIKM after the QCP has been restored and compare the results with those for the constant DOSs in Sec. 6.2. At the end we give a short conclusion and outlook in Sec. 6.4.

6.1 Restoring the quantum critical point

In this section we briefly summarize how the QCP can be restored in the particle-hole asymmetric TIKM with energy dependent DOSs. This method is based on the fact that the fixed point Hamiltonian in both the Kondo phase and the decoupled singlet phase can be related to the Hamiltonian of the free electron gas. In the particle-hole asymmetric case the fixed point Hamiltonian contains additional potential scattering terms which break the particle-hole symmetry [27].

The idea to restore the QCP is to add initial potential scattering terms of the form $V_{e/o} c^\dagger_{e/o,0,\sigma} c_{e/o,0,\sigma}$ to the Hamiltonian of the TIKM. These initial scattering terms are adjusted so that they compensate the scattering terms that are generated during the NRG steps due to particle-hole asymmetry. Here the operator $c^\dagger_{e/o,0,\sigma}$ creates an electron on the zeroth site of the even/odd Wilson chain. More details about the fixed point spectra and Hamiltonians of the TIKM with and without particle-hole symmetry can be found in Sec. 3.4 where the measurement of the potential scatterings $\tilde{V}_{e/o}$ of an effective low energy Hamiltonian is described.

The fixed point spectrum of the TIKM for even iterations with constant even and odd

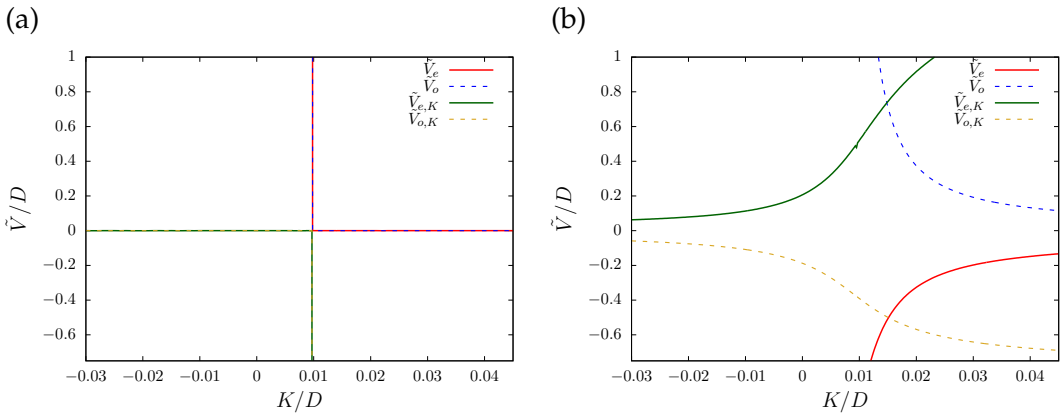

Figure 6.2: (a) The measured potential scatterings of the TIKM with constant DOSs vs. the interaction K. For $K \to \infty$ the scatterings $\tilde{V}_{e/o}$ are exactly zero while for $K \to -\infty$ the measured scatterings of the Kondo phase $\tilde{V}_{e/o,K}$ vanish. At the QCP the scatterings diverge. (b) In the particle-hole asymmetric case the potential scatterings are always finite $\tilde{V}_{e/o(,K)} \neq 0$ and continuously change between the two phases. NRG parameters are $\Lambda = 3$ and $N_s = 1500$.

DOSs is shown versus the spin-spin interaction K in Fig. 6.1a. For $K \to \infty$ the system is in the decoupled singlet phase and the fixed point spectrum coincides with the fixed point spectrum of the free electron gas for even iterations while for $K \to -\infty$ the system is in the Kondo phase and the spectrum coincides with the fixed point spectrum of the free electron gas for odd iterations, cf. Sec. 3.4.1. The QCP that separates the Kondo phase from the decoupled singlet phase is clearly visible at $K_c \approx 0.01D$.
For comparison Fig. 6.1b shows the fixed point spectrum of the TIKM with full energy-dependent DOSs plotted against the interaction K. Due to the particle-hole asymmetry, more energy levels are visible in the spectrum since degeneracies are lifted. Furthermore, the QCP is replaced by a continuous crossover between the two phases.
Figures 6.2a and 6.2b show the measured potential scatterings for the TIKM with constant and with energy-dependent DOSs, respectively. Here, $\tilde{V}_{e/o}$ denotes the measured potential scattering in the decoupled singlet phase where the fixed point spectrum is that of a free electron gas with potential scattering terms and $\tilde{V}_{e/o,k}$ denotes the measured scattering in the Kondo phase where the spectrum coincides with the one of the free electron gas with one electron less plus scattering terms. Details about the difference between $\tilde{V}_{e/o}$ and $\tilde{V}_{e/o,k}$ and the way they are measured within the NRG can be found in Sec. 3.4.2.
In the case of constant DOSs the measured potential scattering $\tilde{V}_{e/o,K}$ is exactly zero in the Kondo phase while $\tilde{V}_{e/o}$ is zero in the decoupled singlet phase since the model is particle-hole symmetric and, thus, no potential scattering terms occur. Directly at the QCP, which separates both phases, all potential scatterings diverge. In contrast, the potential scatterings of the particle-hole asymmetric model with energy-dependent DOSs are always finite and continuously change between the two phases. Since for the

phase shifts in the even and odd channel $\delta_e = -\delta_o$ must apply, we find $V_{e(,k)} \approx -V_{o(,k)}$ up to numerical errors, cf. Sec. 2.3.

In order to compensate the generated potential scatterings and, hence, restore the QCP, the naive expectation would be to adjust the initial scattering terms $V_{e/o} = -\tilde{V}_{e/o(,K)}$. However, already the benchmark calculations in Sec. 3.4.3 show that the initial scatterings $V_{e/o}$ are renormalized depending on the Kondo coupling J to a different effective potential scattering. Furthermore, the generated potential scattering depends on the value of the spin-spin correlation function $\langle \vec{S}_1 \vec{S}_2 \rangle$ [168], therefore, the generated scatterings are different in the Kondo and in the decoupled singlet phase and change continuously near the QCP. To make matters worse, generally the initial scatterings $V_{e/o}$ also influence the effective RKKY interaction. Therefore, if we change $V_{e/o}$ to compensate the generated potential scattering, we move on the K-axis of Fig. 6.2b and end at a different effective interaction K where we in general need a different $V_{e/o}$ to restore the particle-hole symmetry.

Only in the limits $K = \pm\infty$ it is relatively easy to restore the particle-hole symmetry since the change of the RKKY interaction is negligible compared to K and the spin correlation takes the constant values $\langle \vec{S}_1 \vec{S}_2 \rangle = -0.75$ for $K = \infty$ and $\langle \vec{S}_1 \vec{S}_2 \rangle = 0.25$ for $K = -\infty$. The only remaining difficulty is the renormalization of the initial scatterings $V_{e/o}$ which, however, means that particle-hole symmetry can be restored if we set $V_{e/o} = -\alpha_{e/o}(J)\tilde{V}_{e/o(,K)}$ where $\alpha_{e/o}(J)$ is a J dependent factor. Nevertheless, the model becomes particle-hole asymmetric again if we approach the crossover regime.

Therefore, it seems to be impossible to restore the QCP with the use of the potential scattering terms but there are two important restrictions which help us:

An effective generated potential scattering of the form $\tilde{V}(c^\dagger_{e,0,\sigma} c_{e,0,\sigma} + c^\dagger_{o,0,\sigma} c_{o,0,\sigma})$ only shifts both the Kondo resonance in the even and in the odd channel equally away from the Fermi energy [63, 168] and can, thus, be considered as only a shift of the chemical potential. For $\tilde{V}_e \neq \tilde{V}_o$, however, the Kondo resonances of both channels split and the QCP vanishes [64, 168]. Consequently, we do not need to restore the full particle-hole symmetry, it is sufficient to move the Kondo resonances back on top of each other such that $\tilde{V}_e - \tilde{V}_o = 0$.

Secondly, we do not need to adjust $\tilde{V}_e = \tilde{V}_o$ for every K. It follows from Ref. [64] that for $\tilde{V}_e = \tilde{V}_o$ the scattering phase shifts δ_e and δ_o can only take the two values $\delta_e = \delta_o = \pi/2 + \delta_V$, which means that the system is in the Kondo phase, or $\delta_e = \delta_o = 0 + \delta_V$, where the system is in the decoupled singlet phase, cf. Sec. 2.3. Here δ_V is the trivial phase shift originating from the scattering term $\tilde{V}_e = \tilde{V}_o = \tilde{V}$. Therefore, it is sufficient to adjust $\tilde{V}_e = \tilde{V}_o$ in the vicinity of the QCP since in this case the scattering phase shifts must suddenly jump from $0 + \delta_V$ to $\pi/2 + \delta_V$.

Even with this simplifications it is a tedious task to restore the QCP. To do this we proceed as follows: At first, we adjust the spin-spin interaction K so that the spin correlation function takes the value $\langle \vec{S}_1 \vec{S}_2 \rangle = -0.25$ which is the value the correlation

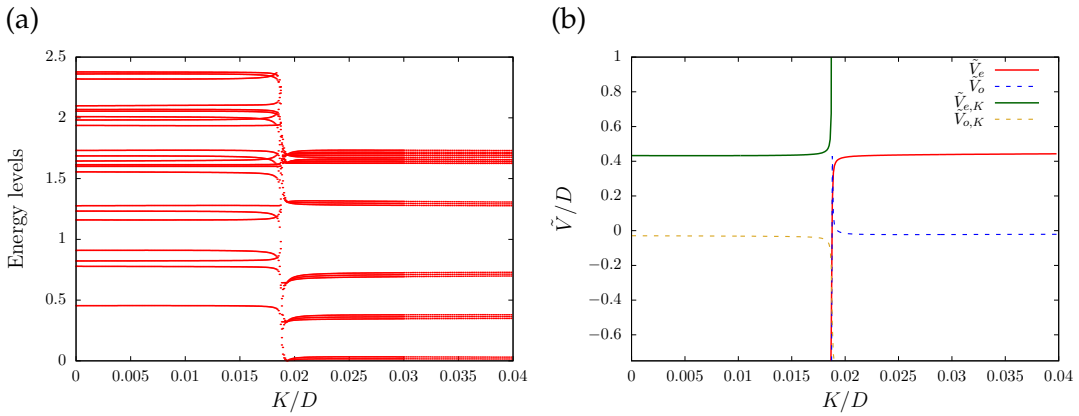

Figure 6.3: (a) Even iterations fixed point spectrum of the TIKM with full energy-dependent DOSs plotted against K after the QCP has been restored for $k_{\mathrm{F}}R/\pi = 0.6591$, $\rho J = 0.2$ and $V_e = 0.48725D$. The spectrum suddenly changes at the QCP at $K_c \approx 0.0188D$ (b) The measured potential scatterings of the TIKM with full energy-dependent DOSs plotted against K after the QCP has been restored for the same parameters as in (a). Only at the QCP the generated potential scatterings coincide $\tilde{V}_e = \tilde{V}_o$. NRG parameters are $\Lambda = 3$ and $N_s = 1500$.

function takes in the vicinity of the QCP, cf. Sec. 2.3. Afterwards, the potential scattering[1] V_e is changed in order to achieve $\tilde{V}_e - \tilde{V}_o = 0$. However, due to the change of the potential scattering, we also change the effective spin-spin interaction. Therefore, we have to re-adjust the spin-spin interaction K to tune the correlation function once again to the value $\langle \vec{S}_1 \vec{S}_2 \rangle = -0.25$ and, afterwards, adjust the potential scattering again. The whole procedure is repeated until both the spin-spin interaction K and the potential scattering V_e converge.

Figure 6.1a shows the fixed point spectrum of the TIKM with full energy-dependent DOSs plotted against K after the QCP has been restored. A comparison with Fig. 6.1b shows that due to the initial potential scattering $V_e = 0.48725D$, the QCP re-emergence at the critical spin-spin interaction $K_c \approx 0.0188D$. Like in the particle-hole symmetric case shown in Fig. 6.1a, the level flow suddenly changes from the spectrum of the Kondo phase for $K \to -\infty$ to the spectrum of the decoupled singlet phase for $K \to \infty$. However, since the model is still particle-hole asymmetric $V_e = V_o \neq 0$, the spectrum exhibits more energy levels in comparison to the particle-hole symmetric case shown in Fig. 6.1a.

The measured potential scatterings after the QCP has been restored are depicted in Fig. 6.3b. In the Kondo phase $\tilde{V}_{e,K}$ and $\tilde{V}_{o,K}$ are constant but in contrast to Fig. 6.2a not zero since the model is not particle-hole symmetric. The divergence of $\tilde{V}_e \to -\infty$ and $\tilde{V}_o \to \infty$ in this regime reflects the $\pi/2$ phase shift due to the Kondo effect. In the decoupled singlet phase the opposite is the case, here $\tilde{V}_{e,K}$ and $\tilde{V}_{o,K}$ diverge and $\tilde{V}_e$ and

[1] In principle we could either change V_e, V_o or both to achieve $\tilde{V}_e - \tilde{V}_o = 0$. However, we only change the scattering of the even conduction band V_e.

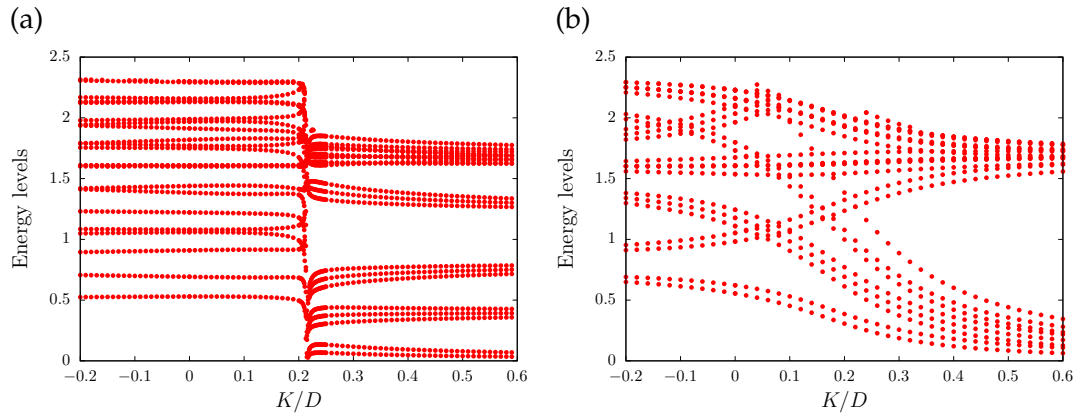

Figure 6.4: (a) Even iterations fixed point spectrum of the TIKM with full energy-dependent DOSs plotted against K after the QCP has been restored for $k_F R/\pi = 0.59$, $\rho J = 0.4$ and $V_e = 0.54D$. The QCP occurs at $K_c \approx 0.21D$ (b) For comparison, the fixed point spectrum for the same parameters but with $V_e = 0$ so that the QCP is not restored and the system instead exhibits crossover. NRG parameters are $\Lambda = 3$ and $N_s = 1500$.

$\tilde{V}_o$ take approximately the same constant values as $\tilde{V}_{e,K}$ and $\tilde{V}_{o,K}$ in the Kondo phase. Both phases are separated by the QCP where all potential scatterings change abruptly. As it has been adjusted, directly at the QCP the lines of $\tilde{V}_e$ and $\tilde{V}_o$ intersect so that $\tilde{V}_e = \tilde{V}_o$.

The fixed point spectrum for a different larger Kondo coupling $\rho J = 0.4$ and a different distance[2] $k_F R/\pi = 0.59$ is shown in Figs. 6.4. Panel (a) shows the spectrum after the QCP has been restored for $V_e = 0.54D$ while panel (b) shows the spectrum without any initial scattering terms $V_e = V_o = 0$ for comparison. As it turns out the potential scattering needed to restore the QCP is also of the order of $D/2$ and is only slightly larger in comparison to the $\rho J = 0.2$ case. Therefore, $V_e = 0.5D$ seems to be a good starting point for the restoration of the QCP and only needs to be fine-tuned depending on the Kondo coupling J and distance R.

Figure 6.5 shows the spin-spin correlation function $\langle \vec{S}_1 \vec{S}_2 \rangle$ for $\rho J = 0.4$ versus the spin interaction K before (red line) and after (blue line) the QCP has been restored. The same data as in Fig. 6.4 has been used. The blue curve is slightly shifted to antiferromagnetic interactions because due to the initial potential scattering $V_e = 0.54D$, the effective RKKY interaction becomes more ferromagnetic. Both curves change continuously from 0.25 for $K = -\infty$ to -0.75 for $K = \infty$. The inset of Fig. 6.5 shows that for the blue curve the derivative of the correlation function with respect to the interaction K diverges at the QCP. This has already been observed for the TIKM with constant DOSs [62, 169] and reflects that directly at the QCP the staggered susceptibility, which is the response to $\vec{H} \cdot (\vec{S}_1 - \vec{S}_2)$, diverges [62–64], cf. Sec. 2.3.

[2] The distance $k_F R/\pi = 0.59$ is chosen such that the correlation function $\langle \vec{S}_1 \vec{S}_2 \rangle (K = 0) = 0$ vanishes for $K = 0$.

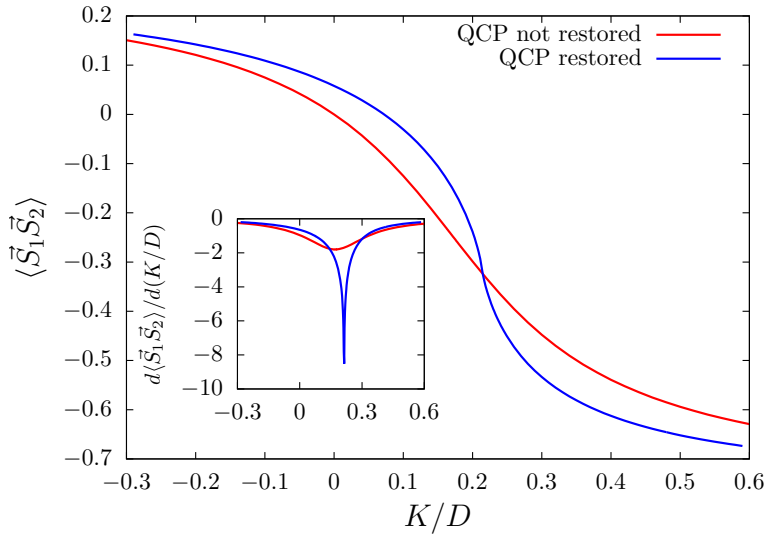

Figure 6.5: The spin-spin correlation function $\langle \vec{S}_1 \vec{S}_2 \rangle$ plotted against the interaction K for $\rho J = 0.4$ and $k_F R/\pi = 0.59$. The red line shows the correlation function before ($V_e = 0$) and the blue line after ($V_e = 0.54D$) the QCP has been restored. In the inset the derivative of $\langle \vec{S}_1 \vec{S}_2 \rangle$ with respect to K is shown. At the QCP the derivative of the blue curve diverges. The same data as in Fig. 6.4 has been used. NRG parameters are $\Lambda = 3$ and $N_s = 1500$.

Since we have shown that it is in principle possible to restore the QCP with initial potential scattering terms, we now want to say some words about an experimental realization. The restoration of the QCP in the experiment is an even more difficult task than in the NRG since one cannot directly change the potential scattering term of the even or odd conduction band. One way to influence the particle-hole symmetry in the experiment is to vary the energy levels of both impurities via a gate voltage which would generate a potential scattering term of the form $V(c^\dagger_{1,\sigma} c_{1,\sigma} + c^\dagger_{2,\sigma} c_{2,\sigma})$ provided that the change of the energy levels of both impurities is equal. Here $c_{1/2,\sigma}$ is an annihilation operator for conduction electrons in a spherical wave around impurity 1 and 2 respectively. However, potential scatterings of this form would, if mapped to even and odd conduction bands, only create a scattering $V(c^\dagger_{e,0,\sigma} c_{e,0,\sigma} + c^\dagger_{o,0,\sigma} c_{o,0,\sigma})$ which can be considered as only a shift of the chemical potential and, thus, does not shift the even and odd Kondo resonances back onto each other. Nevertheless, such a term also generates[3] a potential scattering term of the form $V_{12}(c^\dagger_{e,0,\sigma} c_{e,0,\sigma} - c^\dagger_{o,0,\sigma} c_{o,0,\sigma})$ [168] in second order in the Kondo coupling J with $V_{12} = (V_e - V_o)/2 \propto J^2 V$ which is exactly the form needed to restore the QCP.

An alternative approach would be to tune the tunneling t between the two impurities. It is known that such a tunneling term destroys the QCP of the two impurity Anderson model (TIAM) even for constant DOSs [170–175]. The reason for this is that if the

[3] A term $V_{12}(c^\dagger_{e,0,\sigma} c_{e,0,\sigma} - c^\dagger_{o,0,\sigma} c_{o,0,\sigma})$ is only generated in the case $N_e(\epsilon) \neq N_o(\epsilon)$ which effectively means in the case $R < \infty$.

impurities are mapped to an even and odd basis $d_{e/o} = d_1 \pm d_2$, the tunneling shifts the even and odd energy levels differently $\epsilon_{e/o} = \epsilon \pm t$. Here, $d_{1/2}$ annihilates an electron on the first/second impurity and $\epsilon = \epsilon_1 = \epsilon_2$ is the energy level of both impurities. The different energy levels also generate different potential scattering terms $V_e \neq V_o$ which produce a shift between the even and odd Kondo resonances. However, in the full energy-dependent model, where the resonances are separated anyway, it should be possible to shift the Kondo resonances back on top of each other using the tunneling.

6.2 Nonequilibrium TIKM: constant densities of states

In this section we present nonequilibrium results of the TIKM with constant DOSs in order to set the stage for the full energy-dependent model in Sec. 6.3. Note that we do not use any initial potential scatterings in this section since the TIKM with constant DOSs always exhibits a QCP and we, therefore, do not need to restore it. Since for constant DOSs the RKKY interaction automatically generated by the NRG is always ferromagnetic [61, 62], cf. appendix B, we use a direct spin-spin interaction K between the impurity spins to achieve antiferromagnetic interactions. For simplicity we adjust $N_o/N_e = 1$ which means that the RKKY interaction in Eq. (B.9) vanishes and, hence, K is the only remaining interaction between the impurity spins.
In the following, we investigate different quenches in the interaction K within a phase and also over the QCP. For this purpose we consider the two different initial condition of parallel and antiparallel aligned impurity spins.

6.2.1 Parallel aligned impurity spins

We start with the investigation of the initial condition where both impurity spins are parallel aligned. Considering that, we prepare the two impurity spins with two strong magnetic fields $H_1 = H_2 = -10D$ that act locally on the z-component of the impurity spins such that both impurities are fully polarized and in a spin up state. At time $tD = 0$ the magnetic fields are switched off and the direct spin-spin interaction K is switched on.
Figure 6.6a shows the time-dependent expectation value $\langle \vec{S}_{1/2} \rangle (t)$ for $\rho J = 0.4$ and different ferro- and antiferromagnetic spin-spin interactions K on a logarithmic time scale. Since the initial state is symmetrical with respect to the two impurity spins, the time evolution of both spins is identical $\langle S_1^z \rangle (t) = \langle S_2^z \rangle (t)$.
The decrease of the polarization for short times can only be caused by spin-flip processes with conduction electrons because the initial state is an eigenstate of the interaction $K\vec{S}_1\vec{S}_2$. Therefore, the short-time dynamic is completely independent of the spin-spin interaction K and only depends on the Kondo coupling J.
In order to investigate the time scales for short times, the short-time behavior of $\langle S_{1/2}^z \rangle (t)$ is plotted in Fig. 6.6b for different couplings and no spin-spin interaction

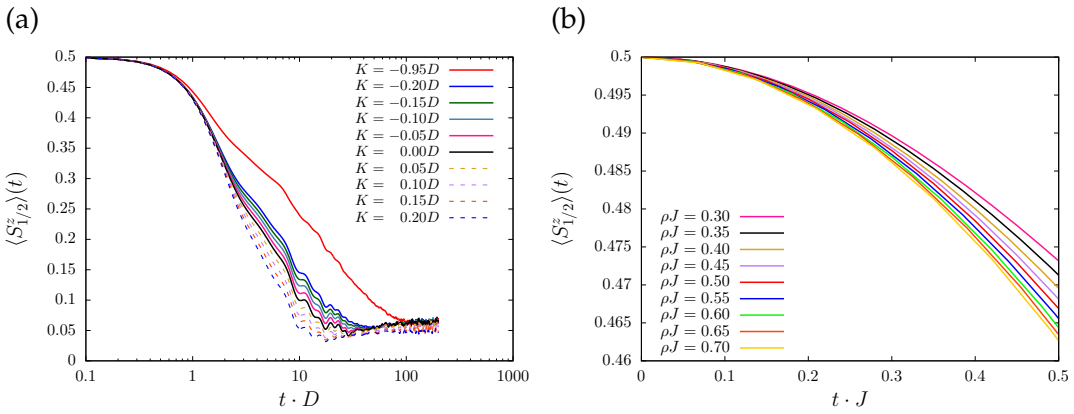

Figure 6.6: (a) The time-dependent expectation values $\langle S^z_1\rangle(t) = \langle S^z_2\rangle(t)$ for $\rho J = 0.4$ and different spin-spin interactions K. With increasing antiferromagnetic K the polarization decreases faster. The short-time behavior is independent of the spin-spin interaction K. (b) Short-time behavior of $\langle \vec{S}_{1/2}\rangle(t)$ for different Kondo couplings J and $K = 0$ vs. the rescaled time tJ. The relevant time scale is given by $1/J$. NRG parameters are $\Lambda = 3$, $N_s = 1500$ and $N_z = 16$.

$K = 0$ against the rescaled time tJ. The polarization decreases quadratically as one expects from Fermi's golden rule and the time scale is given by $1/J$.

Figure 6.6a shows that with increasing antiferromagnetic interaction the polarization decreases faster and finally reaches the value $\langle S^z_{1/2}(t \to \infty)\rangle \approx 0.05$. The finite long-time value $\langle S^z_{1/2}\rangle(t \to \infty) \neq 0$ and the small oscillations around it both originate from discretization errors of the time-dependent numerical renormalization group (TD-NRG) [88, 91]. While a larger number of z-averages leads to a reduction of the oscillations, the long-time value will remain finite for a finite discretization parameter Λ. The reason for this is that the polarization on the impurity spin cannot be completely transfered to the Wilson chain. Due to the exponential decreasing hopping parameters of the Wilson chain, a fraction of the spin polarization is reflected to the impurity at each Wilson site. A way to circumvent this shortcoming may be the recently developed hybrid NRG-DMRG approach [91].

In order to identify the relevant long-time scale, we rescale the data of Fig. 6.6a with the thermodynamic Kondo temperature T_K. T_K is defined from the equilibrium NRG level flow and is the energy scale at which the first excitation of the even iterations reaches 80% from its fixed point value. The obtained values for the Kondo temperature and corresponding time scales $t_\mathrm{K} D = D/T_\mathrm{K}$ are shown in Tab. 6.1. The table only contains Kondo temperatures up to the antiferromagnetic interaction $K = 0.20D$ since larger antiferromagnetic interactions exceed the critical value $K_c = 0.241D$, which is the position of the QCP, and, consequently, the Kondo effect breaks down for these interactions. Table 6.1 shows that the Kondo temperature is largest for the interaction $K = 0$ and decreases for ferromagnetic as well as for antiferromagnetic interactions. The reason for this is that for a ferromagnetic interaction the two impurity spins form

K/D	$T_K/D \cdot 10^2$	$t_K D = D/T_K$
-0.95	1.029	97,16
-0.20	2.200	45.45
-0.15	2.351	42.53
-0.10	2.520	39.69
-0.05	2.681	37.30
0.00	2.756	36.29
0.05	2.642	37.85
0.10	2.279	43.88
0.15	1.563	63.96
0.20	0.441	226.51

Table 6.1: The Kondo temperature T_K and the corresponding time scale $t_K D = D/T_K$ for different spin-spin interactions K. The Kondo temperatures have been obtained from the NRG level flow - see text.

K/D	0.0	0.1	0.2	0.25	0.3	0.35	0.4	0.5	0.6	0.7	0.8	0.9
$t_{\text{low}} D$	5.03	4.24	3.63	3.4	3.24	3.11	3.00	2.84	2.73	2.65	2.59	2.55

Table 6.2: The time scale t_{low} at which the polarization reaches 40% of its initial value $\langle \vec{S}^z_{1,2} \rangle (t_{\text{low}}) = 0.2$ for different spin-spin interactions K.

a triplet and hence the second part of the interaction between the impurity spins and the conduction bands in Eq. (2.14), which is proportional to $\propto (\vec{S}_1 - \vec{S}_2)$, is suppressed [103] while for antiferromagnetic correlations the first part $\propto (\vec{S}_1 + \vec{S}_2)$ is suppressed. In both cases the effective coupling to the conduction band decreases and, therefore, also the Kondo temperature decreases.

Figure 6.7 shows the time-dependent expectation value $\langle S^z_{1/2} \rangle (t)$ vs. the rescaled time tT_K. For long times, the data for zero and ferromagnetic spin-spin interactions $K \leq 0$ (solid lines) fall onto one universal curve. The long-time behavior is determined by the Kondo effect and the relevant time scale is given by $t_K = 1/T_K$. The same behavior has been observed for the standard Kondo model with just one impurity spin coupling to the conduction band [88]. However, in Ref. [88] the change of the Kondo temperature T_K has been induced by directly changing the Kondo coupling to the conduction band J while in our case the effective coupling to the conduction band is changed by varying the spin-spin interaction K.

In contrast, antiferromagnetic spin-spin interactions $K < 0$ (dashed lines) amplify the decay of the polarization additionally to the decay caused by the Kondo effect since for antiferromagnetic interactions a formation of a singlet between the impurity spins is favored. Therefore, a rescaling with T_K only does not yield universal behavior as it was the case for ferromagnetic interactions.

To investigate the behavior for antiferromagnetic interactions, we define a new time scale t_{low} at which the polarization reaches 40% of its initial value $\langle S^z_{1,2} \rangle (t_{\text{low}}) = 0.2$.

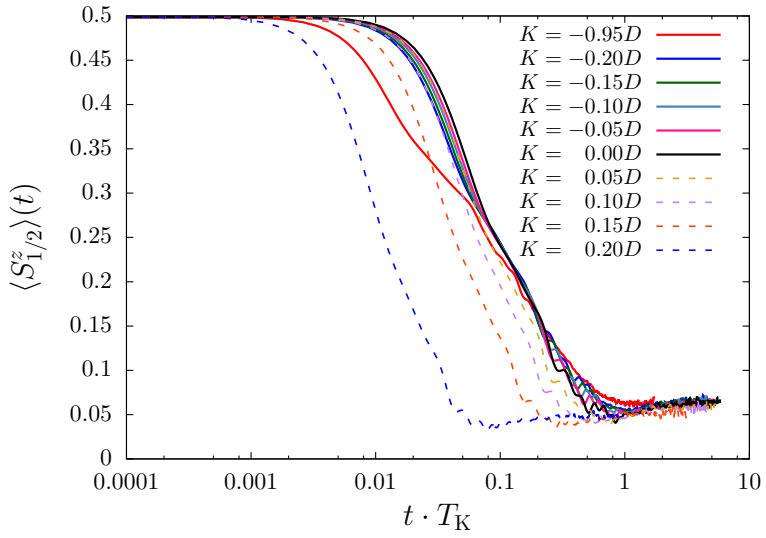

Figure 6.7: The time-dependent expectation value $\langle S^z_1\rangle(t) = \langle S^z_2\rangle(t)$ for the same parameters as in Fig. 6.6a rescaled with the Kondo temperature T_K. Solid lines indicate spin-spin interactions $K \leq 0$ while the dashed lines mark antiferromagnetic interactions. For $K \leq 0$ the long-time value of $\langle S^z_{1/2}\rangle(t)$ shows universal behavior. NRG parameters are $\Lambda = 3$, $N_s = 1500$ and $N_z = 16$.

The obtained values t_{low} are listed in Tab. 6.2 and the time-dependent polarization is plotted against the rescaled time t/t_{low} in Fig. 6.8 for different interactions K. In contrast to the rescaling with T_K only, the rescaling with the new time scale t_{low} yields also universal long-time behavior for up to the medium antiferromagnetic interaction $K = 0.30D$. In this regime the long-time behavior is determined by both the Kondo effect and the spin-spin interaction.

For larger antiferromagnetic interactions the behavior starts to differ from the universal long-time behavior until for very large interactions $K \geq 0.60D$ universal behavior is found again not only for the long-time behavior but for the entire decay of the polarization. Furthermore, after the decay of the polarization for these very large interactions damped oscillations are observed which will be discussed later in more detail.

The reason for the universal behavior for the entire decay is that the polarization does not decrease faster anymore with increasing antiferromagnetic interaction K. This can be seen in the inset of Fig. 6.8 where the time scale t_{low} is plotted against the interaction K. For up to medium antiferromagnetic interactions the time scale t_{low} decreases with increasing antiferromagnetic K while for $K > 0.5D$ the time scale approaches the fixed value $t_{\text{low}}D \approx 2.5$. For such interactions the time is only rescaled with a constant which means that the decay of the polarization must also show universal behavior even without any rescaling as shown in Fig. 6.10a.

The constant time scale $t_{\text{low}}D$ for large interactions is caused by the fact that the short-time behavior is independent of K and, therefore, the coupling to the conduction band J acts as a bottleneck for the decay.

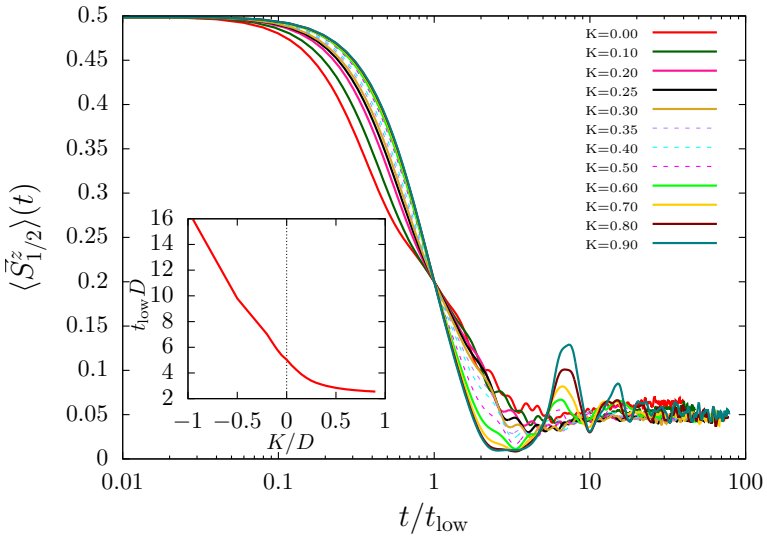

Figure 6.8: The time-dependent polarization $\langle S^z_{1/2} \rangle (t)$ rescaled with $t_{\rm low}$. For up to the medium antiferromagnetic interaction $K \leq 0.30D$ the long-time behavior of the decay shows universal behavior. For very large interactions $K \geq 0.60D$ universal behavior is found for the entire decay of the polarization. Dashed lines show no universal behavior. The inset shows the time scale $t_{\rm low}$ vs. the spin-spin interaction K.

The time-dependent spin-spin correlation function $\langle \vec{S}_1 \vec{S}_2 \rangle (t)$ is plotted for $\rho J = 0.4$ and different interactions K in Fig. 6.9. Since in the initial state the two impurities form a triplet, the correlation function starts at the maximal value $\langle \vec{S}_1 \vec{S}_2 \rangle (t) = 0.25$. As for the polarization, the short-time behavior is independent of the interaction K and the correlation decreases quadratically with time. For ferromagnetic and moderate antiferromagnetic spin-spin interactions $K < K_c$ the correlation function $\langle \vec{S}_1 \vec{S}_2 \rangle (t)$ reaches its equilibrium value for $t \to \infty$ which is indicated by arrows in the right of Fig. 6.9. For larger antiferromagnetic interactions, thermalization is not observed anymore. For such large antiferromagnetic K, the system is quenched from the Kondo phase over the QCP at $K_c = 0.241D$ into the decoupled singlet phase. In the decoupled singlet phase, the two impurity spins form a singlet and the Kondo coupling is renormalized to zero $J \to 0$. Due to the renormalization $J \to 0$ for times $t \to \infty$, the impurity spins are no longer coupled to the conduction band, the decrease of the correlation function $\langle \vec{S}_1 \vec{S}_2 \rangle (t)$ stops and, consequently, the system does not thermalize. A similar effect has been recently observed and extensively discussed for the pseudogap single impurity Anderson model (SIAM) [176]. In the pseudogap SIAM a Coulomb interaction quench over the QCP also leads to a decoupling of an effective local magnetic moment which prevents the thermalization of the system.

Most interestingly, however, is the occurrence of oscillations in the polarization and correlation function for large antiferromagnetic interactions K as shown in Fig. 6.10. These damped oscillations have the same frequency for $\langle S^z_{1/2} \rangle (t)$ and $\langle \vec{S}_1 \vec{S}_2 \rangle (t)$ and the

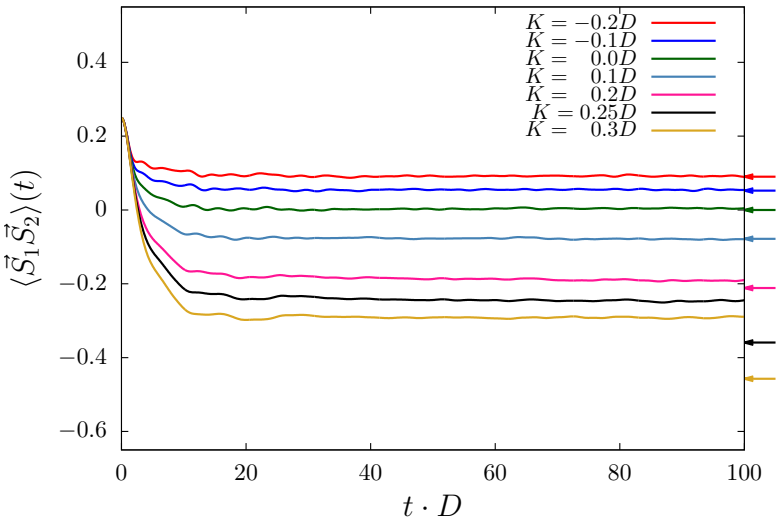

Figure 6.9: The time-dependent spin-spin correlation function $\langle \vec{S}_1 \vec{S}_2 \rangle (t)$ for $\rho J = 0.4$ and different interactions K. The arrows indicate the equilibrium value of $\langle \vec{S}_1 \vec{S}_2 \rangle$ calculated with the equilibrium NRG. For ferromagnetic and moderate antiferromagnetic interactions $K < K_c$ the correlation function $\langle \vec{S}_1 \vec{S}_2 \rangle (t)$ reaches its equilibrium value for large times. As soon as K exceeds the critical value $K_c = 0.241D$, the correlation function $\langle \vec{S}_1 \vec{S}_2 \rangle (t)$ no longer thermalizes. NRG parameters are $\Lambda = 3$, $N_s = 1500$ and $N_z = 16$.

amplitude increases with increasing interaction K. Since these oscillations only occur for very large interactions K, it is obvious that they must be caused by the first few Wilson sites which account for the high energy part of the NRG.

Therefore, we plotted the time-dependent polarization and spin-spin correlation function for different numbers of NRG-iterations N_{Iter} in Figs. 6.11a and b, respectively. Note that we used $\beta D = 10^5$ in the TD-NRG calculations instead of the usual $\beta D = 1$ in order to obtain results for $T \approx 0$ even for the first iterations. Since the polarization for $N_{\text{Iter}} = 0$ does not oscillate with a fixed frequency and shows a chaotic behavior, we omit this curve in Fig. 6.11a for clarity.

In contrast to the polarization, the spin-spin correlation function shows an oscillation with a constant frequency for $N_{\text{Iter}} = 0$, however, this oscillation is much faster than the oscillations observed for the full TD-NRG calculations shown in Fig. 6.10. Adding a second Wilson site at iteration $N_{\text{Iter}} = 1$ changes the picture. Now the time-dependent polarization and spin-spin correlation function show undamped oscillations with the same frequency. This frequency, however, is still 1.5 times larger than the one observed in Fig. 6.10. If we add a third Wilson site at iteration $N_{\text{Iter}} = 2$ the oscillations are damped and the frequency is lowered. Adding further Wilson sites increase the damping and the frequency further decreases. At $N_{\text{Iter}} \geq 7$ the polarization and spin-spin correlation both converge and the frequency coincides exactly with the frequency observed in the full TD-NRG calculations. Therefore, we can conclude that the oscillations

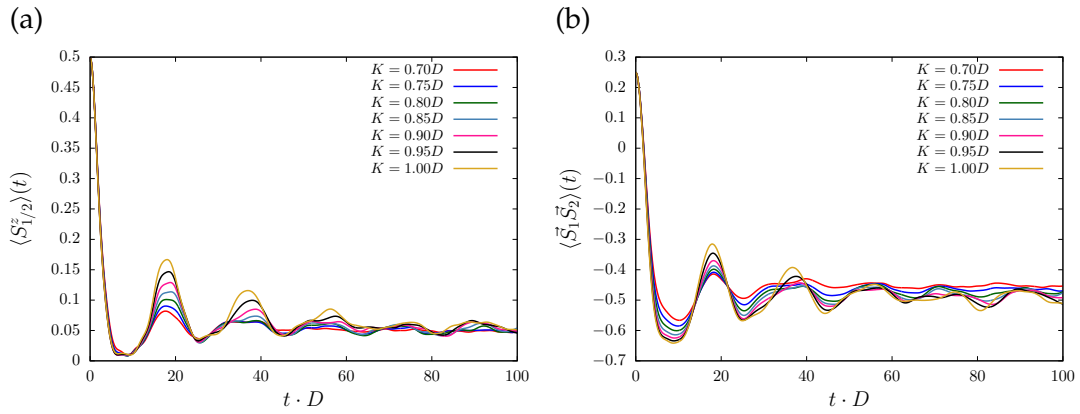

Figure 6.10: (a) The time-dependent polarization $\langle S^z_{1/2}\rangle(t)$ and (b) spin-spin correlation function $\langle \vec{S}_1\vec{S}_2\rangle(t)$ for $\rho J = 0.4$ and different large spin-spin-interactions K. For both expectation values damped oscillations with the same frequency are observed. NRG parameters are $\Lambda = 3$, $N_s = 1500$ and $N_z = 16$.

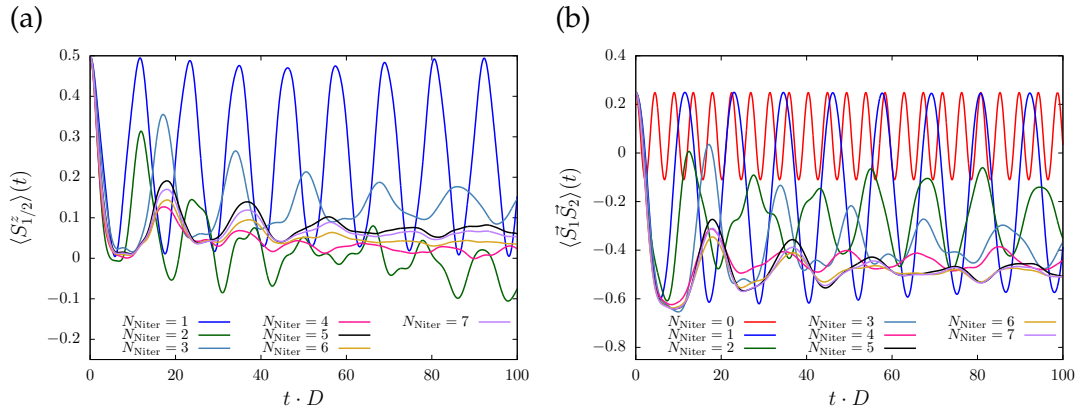

Figure 6.11: (a) The time-dependent polarization $\langle S^z_{1/2}\rangle(t)$ and (b) spin-spin correlation function $\langle \vec{S}_1\vec{S}_2\rangle(t)$ for $\rho J = 0.4$, $K = 1.0D$ and different numbers of NRG-iterations N_{Iter}.

for large interactions K are caused by the first two Wilson sites. Adding further Wilson sites only results in a damping of the oscillations and a small shift of the frequency.
To further investigate these oscillations and their precise origin, we plotted the frequency f of the oscillations for $N_{\text{Iter}} = 1$ against the spin-spin interaction for different Kondo couplings in Fig. 6.12a. The frequency decreases with increasing K until f has a minimum at $K = 2t_0$ for all Kondo couplings ρJ and afterwards it is increasing again. The decay of the frequency becomes stronger with decreasing coupling ρJ. Here $t_0 = 0.577D$ is the hopping between the zeroth and first Wilson site. For the Kondo coupling[4] $\rho J = 5 \cdot 10^{-4} \approx 0$ we can identify a $f(K) = |2t_0 - K|$ behavior for the K

[4] Since the initial state where both impurity spins point upwards is an eigenstate of $K\vec{S}_1\vec{S}_2$, the Kondo coupling must be finite $\rho J \neq 0$ in order to obtain a dynamic for the impurity spins. Therefore, we use $\rho J = 5 \cdot 10^{-4}$ to approximate the $\rho J = 0$ solution.

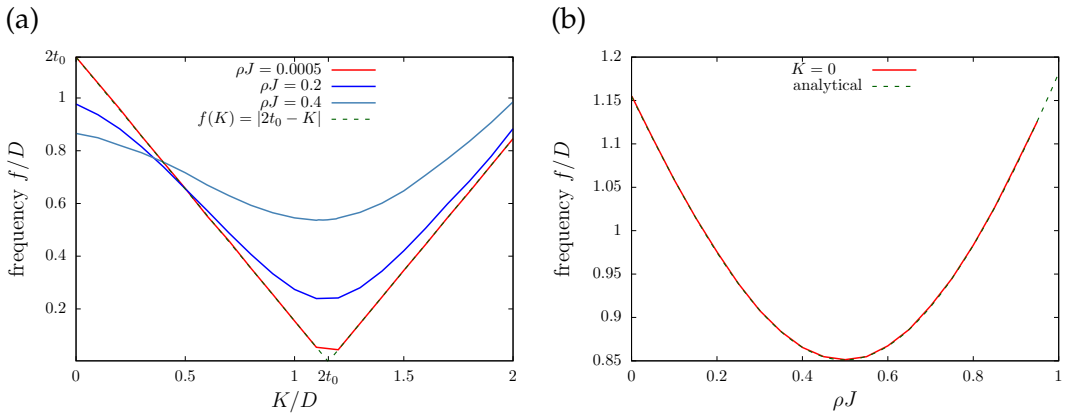

Figure 6.12: (a) The frequency f of the oscillations in the polarization and spin-spin correlation function for $N_{\text{Iter}} = 1$ vs. the interaction K for different Kondo couplings. For $\rho J = 0.0005 \approx 0$ the dependence of the frequency from the interaction is given by $f(K) = |2t_0 - K|$. (b) The measured frequency (red solid line) for $K = 0$ and $N_{\text{Iter}} = 1$ plotted against the Kondo coupling ρJ. The analytically calculated frequency (green dashed line) agrees perfectly with the measured frequency.

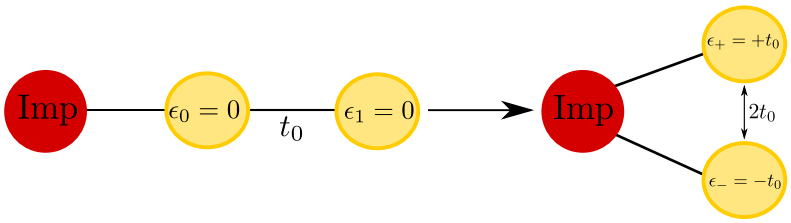

Figure 6.13: In the simplified model one impurity spin couples to a Wilson chain consisting of just two sites which are coupled via the hopping t_0. The bath can be diagonalized by the linear combinations $c_{\pm,\sigma} = 1/\sqrt{2}(c_{0,\sigma} \pm c_{1,\sigma})$ with the new onsite energies $\epsilon_\pm = \pm t_0$.

dependent frequency.

To explain this behavior for $\rho J \approx 0$, we consider a simplified model where at first only one impurity spin couples to a Wilson chain with only two sites which corresponds to $N_{\text{Iter}} = 1$. The two Wilson sites are coupled via the hopping $t_0 \approx 0.577D$. In a particle-hole symmetric case the onsite energies $\epsilon_{0/1} = 0$ are zero and the subsystem of the bath with the two sites can be diagonalized by the linear combinations $c_{\pm,\sigma} = 1/\sqrt{2}(c_{0,\sigma} \pm c_{1,\sigma})$ where $c_{i,\sigma}$ annihilates an electron of the i-th Wilson site with spin σ. The onsite energy of the new sites is given by $\epsilon_\pm = \pm t_0$ so that the difference between them is $\epsilon_+ - \epsilon_- = 2t_0$. The simplified model and the diagonalization of the bath is shown in Fig. 6.13.

In the initial ground state the $|-\rangle$-site is doubly occupied because ϵ_- is negative while the $|+\rangle$-site is unoccupied which means that the electrons in the bath form a singlet. Since the impurity spin points upwards and both the particle number and the z-component of the total spin are conserved quantities, the relevant subspace for the dynamics is given by $Q = 0$ and $S_z = +1/2$ where Q measures the particle number

from half-filling and S_z is the z-component of the total spin.
In order for the impurity spin to flip, the down-spin of the bath must also flip due to spin conservation. Because of the Pauli principle, this is only possible if the bath spin is excited into the $|+\rangle$-site, so that both $|\pm\rangle$-sites are occupied with an up-spin. This state, however, is separated by $\epsilon_+ - \epsilon_- = 2t_0$ from the ground state. Therefore, we observe for $K = 0$ a frequency of $2t_0 \approx 1.155D$ for the oscillations.
If we also consider a finite spin-spin interaction K between the two impurity spins, the energy difference between the impurity triplet and singlet is given by K. Since the impurities can be regarded as almost uncoupled from the conduction band ($\rho J \approx 0$), the total energy difference to the ground state after an impurity spin flip is simply given by $2t_0 - K$ so that we finally obtain $f(K) = |2t_0 - K|$ for the K-dependent frequency. At $K = 2t_0$ the spin-spin interaction compensates the energy difference $\epsilon_+ - \epsilon_-$ and consequently the oscillations vanish as shown in Fig. 6.12a.
For $\rho J > 0$ the model becomes more complicated and the K dependence deviates from the simple $f(K) = |2t_0 - K|$ behavior. Although the frequency no longer vanishes, it still has a minimum at $K = 2t_0$ for $\rho J > 0$.
Furthermore, for finite ρJ and $K = 0$ the frequency also differs from $2t_0$, however, for the simple case of vanishing spin-spin interaction the problem can be solved analytically since the two impurity spins are completely independent. For this purpose we consider the same simplified model as before where only one impurity spin couples to a single Wilson chain consisting of two sites as shown in Fig. 6.13. As already mentioned above, only the $Q = 0$ and $S_z = 1/2$ subspace is relevant because of particle and spin conservation. This subspace has only a dimension of 5×5 and can, hence, be diagonalized analytically with a computer algebra system. As it turns out, the frequency for $K = 0$ coincides exactly with the energy difference between two eigenstates. However, the analytical formula is very cumbersome, therefore, we only plot the result together with the measured frequency against the Kondo coupling in Fig. 6.12b. The measured (red solid line) and the analytically calculated frequency (green dashed line) are in a perfect agreement. Note that the dependence of the frequency from the Kondo coupling shown in Fig. 6.12b is not a parabola.
Therefore, we can conclude that the oscillations for large antiferromagnetic spin-spin interactions are a remnant of the oscillations for $N_{\text{Iter}} = 1$ where the system oscillates between two states and the frequency not only depends on ρJ and K but also on the hopping t_0 between the zeroth and first Wilson site.

6.2.2 Antiparallel aligned impurity spins

We now turn to the investigation of a different initial condition where the impurity spins are antiparallel aligned. As before, the two magnetic fields $H_1 = -10D$ and $H_2 = 10D$ that act locally on the z-component of the two impurity spins S_1^z and S_2^z are switched off and the spin-spin interaction is switched on at time $tD = 0$.

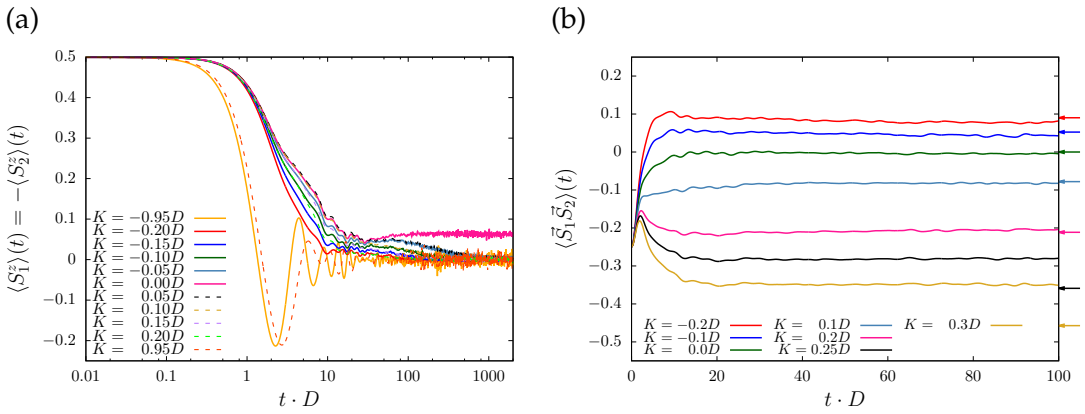

Figure 6.14: (a) The time-dependent spin polarization $\langle S_1^z\rangle(t) = -\langle S_2^z\rangle(t)$ for $\rho J = 0.4$ and different interactions K. For larger ferromagnetic (solid lines) as well as for larger antiferromagnetic (dashed lines) interactions K the polarization decays faster. The short-time behavior is K dependent. (b) The spin-spin correlation function $\langle \vec{S}_1 \vec{S}_2\rangle(t)$ for $\rho J = 0.4$ and different interactions K. The arrows indicate the equilibrium value of the correlation function. Only for interactions $K \leq K_c = 0.241D$ the correlation function thermalizes for long times. The short-time behavior is independent of the interaction K. NRG parameters are $\Lambda = 3$, $N_s = 1500$ and $N_z = 16$.

Figure 6.14a shows the time-dependent spin polarization of the two impurities for $\rho J = 0.4$ and different spin-spin interactions K. In comparison to the case discussed above, here, the time-evolution of the polarization of the two impurity spins is antisymmetrical $\langle S_1^z\rangle(t) = -\langle S_2^z\rangle(t)$ due to the antisymmetrical initial condition.
In contrast to the case where both spins are parallel aligned, we find that the polarization now decays faster for antiferromagnetic as well as for ferromagnetic interactions K. The reason for this is that the initial state, where one impurity is in a spin up state and the other in a spin down state, is not an eigenstate to the interaction $K\vec{S}_1\vec{S}_2$ anymore. Unlike the case where both spins were parallel aligned and spin flips could only be caused by the bath coupling, spin flips can now be performed locally on the impurity sites. This is also the reason why, in contrast to the case discussed above, the short-time behavior is dependent of the spin-spin interaction as the curves for $K = \pm 0.95D$ show. Without a coupling to the conduction band one would observe oscillations of the spin polarizations between the values -0.5 and 0.5 with the frequency $|K|$ so that it would make no difference if the interaction is ferro- or antiferromagnetic.
A notable effect is that for every finite interaction K the long-time value of the spin polarization reaches the expected value of $\langle S_i^z\rangle(t = \infty) = 0$ and, therefore, the system thermalizes. However, for small interactions the polarization first reaches a plateau and further decreases for larger times which can be seen most clearly for $K = \pm 0.05D$. This behavior is unphysical and must be a feature of the TD-NRG because there is no reason why the decay of the polarization should stop at a certain value and decrease later on. An explanation for this effect is that due to the antiparallel aligned impurity

K/D	-1.0	-0.9	-0.15	-0.10	-0.05	0.00	0.05	0.10	0.15	0.9	1.0
$t_{\mathrm{low}}D$	0.91	0.99	3.12	3.73	4.45	5.03	5.20	4.96	4.41	1.11	1.01

Table 6.3: The time scale t_{low} of the antiparallel aligned impurity spins at which the polarization reaches 40% of its initial value $|\langle\vec{S}^z_{1,2}\rangle(t_{\mathrm{low}})| = 0.2$ for different spin-spin interactions K. The time scale t_{low} in dependence of the interaction K is also depicted in the inset of Fig. 6.15a.

spins, there emerge overdamped oscillations locally on the impurity sites which cause the further decreases of the polarization. The fact that the curves for K and $-K$ fall onto one curve for large times supports this assumption because the frequency of these local oscillations is only determined by the absolute value of the interaction $|K|$.
The time-dependence of the spin-spin correlation function $\langle\vec{S}_1\vec{S}_2\rangle(t)$ is shown in Fig. 6.14b for different interactions K. For long times we observe the same behavior as for the case where both spins are parallel aligned. For interactions $K < K_c = 0.241D$ the system reaches the equilibrium value that is marked by the arrows while for large antiferromagnetic interactions $K > K_c$ the system does not thermalize. As before the reason for this is that the system is quenched into the decoupled singlet phase where the coupling to the bath J is renormalized to zero which prevents thermalization.
Unlike the spin polarization, the short-time behavior of the correlation function is independent of K. For all interactions the correlation function first increases until for large antiferromagnetic interactions $\langle\vec{S}_1\vec{S}_2\rangle(t)$ starts to decrease. The time at which the correlation starts to decrease depends on the interaction K.
To understand this short-time behavior one can perturbatively calculate $\langle\vec{S}_1\vec{S}_2\rangle(t)$ by expanding the time-dependent density operator in orders of J similar to the perturbative calculation of the correlation function $\langle\vec{S}_{\mathrm{imp}}\vec{s}(\vec{r},t)\rangle$ in Sec. 4.3.2. It is straight forward to see that an interaction $K\vec{S}_1\vec{S}_2$ has no influence on the correlation function for short times because the commutator $\left[K\vec{S}_1\vec{S}_2, \vec{S}_1\vec{S}_2\right]$ vanishes.
As it turns out, a rescaling of the time with the Kondo temperature T_{K} only never yields universal behavior since due to the antiparallel initial configuration, the interaction K always has a direct impact on the decay of $|\langle S^z_i\rangle(t)|$. This is in contrast to the case with parallel aligned impurity spins where ferromagnetic interactions only influence the Kondo temperature and, therefore, a rescaling with T_{K} leads to universal long-time behavior.
As before, we hence define a new time scale $|S^z_i(t_{\mathrm{low}})| = 0.2$ at which the polarization reaches 40% of its initial value in order to investigate the decay of the spin polarization in more detail.
The obtained time scales t_{low} for the different spin interactions K are listed in Tab. 6.3 and shown in the inset of Fig. 6.15a. Unlike before, the time scale does not reach a constant value for large interactions but continues to decrease. The inset also shows that the maximum of t_{low} is not exactly located at $K = 0$ but slightly shifted to small antiferromagnetic interactions $K > 0$. An explanation for this will be discussed below

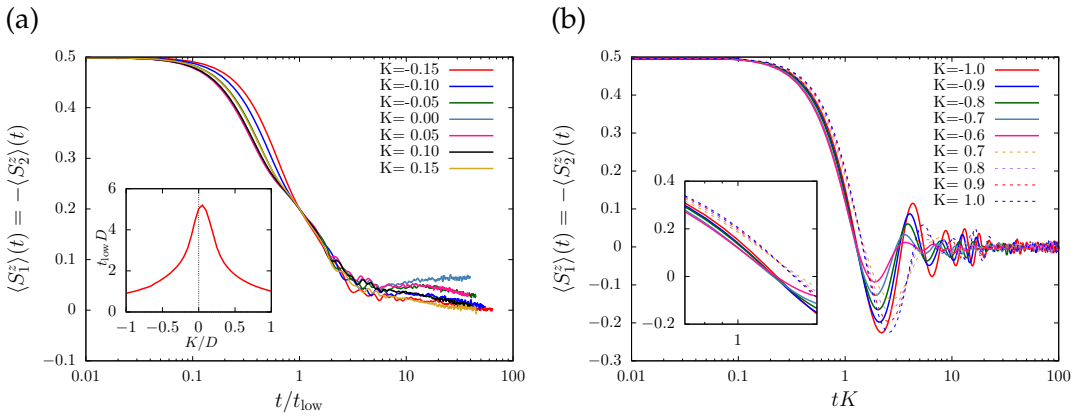

Figure 6.15: (a) The spin polarization $\langle S_1^z\rangle(t) = -\langle S_2^z\rangle(t)$ for $\rho J = 0.4$ vs. the rescaled time t/t_{low}. For small spin-spin interactions $|K| \leq 0.15D$ universal long-time behavior is found. The inset shows the time scale $t_{\mathrm{low}}D$ versus the interaction K/D. (b) The polarization plotted against tK for different large interactions K. The inset shows the decay in more detail and reveals a slight shift between the ferromagnetic (solid lines) and antiferromagnetic (dashed lines) interactions. NRG parameters are $\Lambda = 3$, $N_s = 1500$ and $N_z = 16$.

in the context of the oscillations that arise for large spin-spin interactions.

The spin polarization $|\langle S_i^z\rangle(t)|$ versus the rescaled time t/t_{low} is depicted in Fig. 6.15a for different small interactions. As for the parallel aligned impurity spins, universal long-time behavior is found for ferro- as well as for antiferromagnetic interactions. In this regime the long-time behavior is determined by both the Kondo effect and the spin-spin interaction.

Figure 6.15b shows the time-dependent polarization for larger interactions plotted against the rescaled time tK. For such large interactions the decay is dominated by the local oscillations of the two impurity spins with frequency K. Therefore, after a rescaling of time with the interaction K the curves almost fall onto one curve and universal behavior is found for the entire decay of the polarization. However, the inset, which shows the decay in more detail, reveals that there is a slight shift between the ferromagnetic (solid lines) and antiferromagnetic (dashed lines) interactions. This asymmetry between ferromagnetic and antiferromagnetic interactions can already be seen in Fig. 6.14a where a slight shift between the curves for $K = -0.95D$ and $K = 0.95D$ can be observed and is also reflected in the asymmetric shape of the time scale t_{low} shown in the inset of Fig. 6.15a.

Furthermore, the asymmetry is also visible in the damped oscillations for large interactions K which are shown in Fig. 6.16a for ferromagnetic and in Fig. 6.16b for antiferromagnetic interactions. The frequency of both oscillations slightly differ with the oscillations for ferromagnetic interactions being a little bit faster. Both frequencies, however, are much faster than the frequency of the oscillations observed in the parallel aligned case for large ferromagnetic spin-spin interactions. Once again the reason for

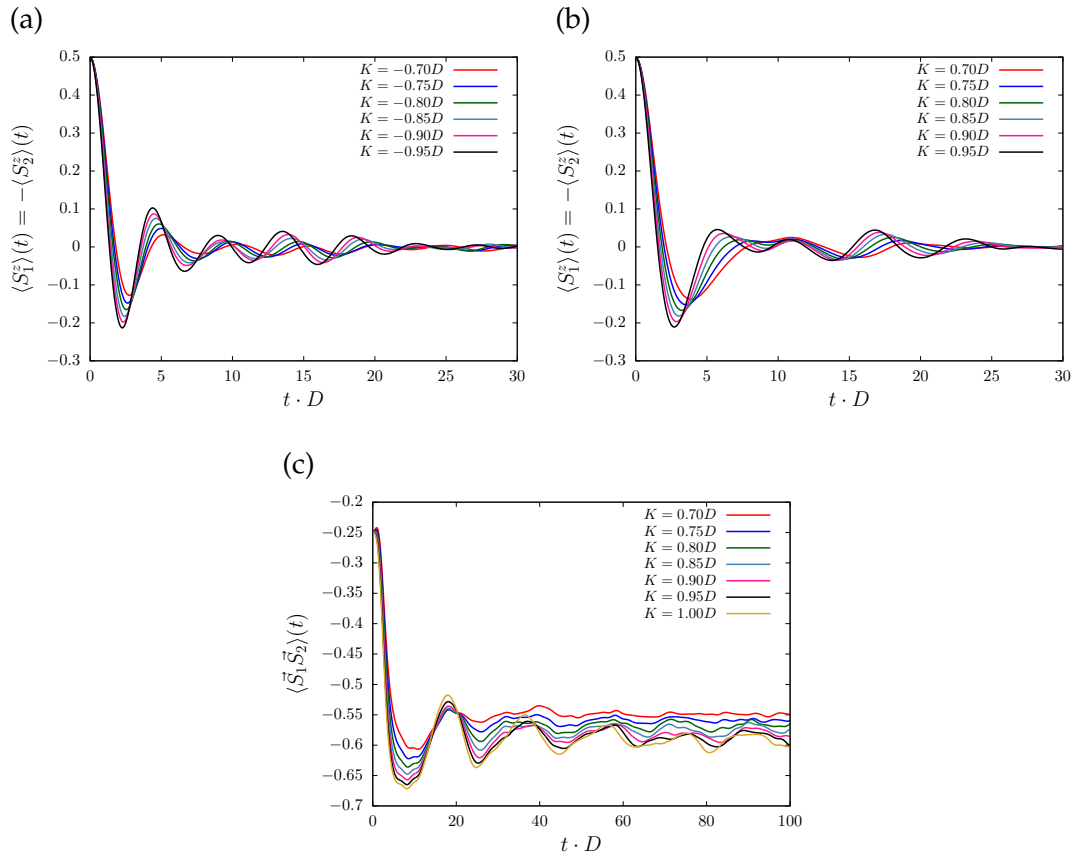

Figure 6.16: The spin polarization $\langle S_1^z \rangle(t) = -\langle S_2^z \rangle(t)$ for large (a) ferromagnetic and (b) antiferromagnetic spin-spin interactions K. In both cases damped oscillations are observed, however, the frequency is slightly different. In comparison to Fig. 6.10a the oscillations are much faster. (c) The spin-spin correlation function $\langle \vec{S}_1 \vec{S}_2 \rangle(t)$ for large antiferromagnetic spin-spin interactions. Damped oscillations with the same frequency as in Fig. 6.10b are observed. NRG parameters are $\Lambda = 3$, $N_s = 1500$ and $N_z = 16$.

this is that the antiparallel aligned initial condition gives rise to another spin flip process locally on the impurity sites that occurs on the time scale $1/|K|$ which can be very short for large $|K|$.

The slight frequency shift between the two oscillations indicates that depending on the sign of the K once the interaction is added and once subtracted from another occurring frequency. This suggestion is supported by the fact that the oscillations look more complicated in comparison to the case discussed above and differ from a simple cosine shape which is also an indication that multiple frequencies are involved. The frequency shift as well as the more complicated structure of the oscillations are already visible at the first iteration $N_{\text{Iter}} = 1$ and one could now carry out a similar investigation as it has been done for the parallel aligned case. However, this investigation will be even more complicated than the already long and cumbersome discussion of the parallel aligned case so that we omit a detailed analysis of the frequencies.

In contrast to the spin polarization, oscillations in the time-dependent spin-spin correlation function $\langle \vec{S}_1 \vec{S}_2 \rangle(t)$ are only observed for large antiferromagnetic interactions $K \gg 0$ which is depicted in Fig. 6.16c. The frequency coincides exactly with the frequency observed for the polarization and spin correlation function in the parallel aligned case. The reason is that a change of the correlation function $\langle \vec{S}_1 \vec{S}_2 \rangle(t)$ cannot be caused by an interaction of the form $K\vec{S}_1\vec{S}_2$ and must happen via the interaction with the conduction band. Therefore, the fast local oscillations, which originate from the antiparallel initial configuration, do not have a direct influence on $\langle \vec{S}_1 \vec{S}_2 \rangle(t)$ and we observe the same oscillations as for the parallel aligned case discussed above.

6.3 Nonequilibrium TIKM with restored QCP

In the following we investigate the nonequilibrium dynamics of the model with full energy-dependent DOSs after the QCP has been restored. In contrast to Sec. 6.2 where we have adjusted the constant $N_o/N_e = 1$ so that the RKKY interaction vanishes at all energy scales, in this section the RKKY interaction at low temperatures is given by[5] $K_{\mathrm{RKKY}} \approx -0.072D$ for $\rho J = 0.4$, $k_{\mathrm{F}}R/\pi = 0.59$, $V_e = 0.54D$. Therefore, the total effective spin-spin interaction for times $tD \geq 0$ is given by the sum of the direct and RKKY interaction $K_{\mathrm{eff}} = K + K_{\mathrm{RKKY}}$.

6.3.1 Parallel aligned impurity spins

We again start with the initial condition where the impurity spins are parallel aligned. With two magnetic fields $H_1^z = H_2^z = -10D$ that act locally on the z-component of the impurity spin both spins are fully polarized. These magnetic fields are switched off and the direct spin-spin interaction K is turned on at time $tD = 0$.
Figure 6.17a shows the time-dependent polarization $\langle S_{1/2}^z \rangle(t)$. As before, the time-evolution of both impurities is also symmetrical $\langle S_1^z \rangle(t) = \langle S_2^z \rangle(t)$ due to the symmetrical initial condition. The short-time behavior is once again independent of the spin-spin interaction since the initial state is an eigenstate of the interaction $K\vec{S}_1\vec{S}_2$. Similar to the case of constant DOSs, for short time scales the polarization decreases quadratically with time.
For medium and larger time scales we observe the same behavior as in Sec. 6.2.1, for antiferromagnetic effective spin-spin interactions the polarization decreases faster while for ferromagnetic interactions $\langle S_{1/2}^z \rangle(t)$ decreases more slowly. As for constant DOSs the decrease of the polarization stops at a finite value $\langle S_{1/2}^z \rangle(t \to \infty) \neq 0$ which can be traced back to discretization errors of the TD-NRG. However, a comparison with Fig. 6.6a shows that the long-time value of the polarization is slightly larger compared to

[5] The RKKY interaction is determined from the spin-spin correlation function $\langle \vec{S}_1 \vec{S}_2 \rangle$ shown in Fig. 6.5. For $K = -K_{\mathrm{RKKY}}$ the direct interaction compensates the RKKY interactions and, consequently, the correlation function vanishes $\langle \vec{S}_1 \vec{S}_2 \rangle = 0$.

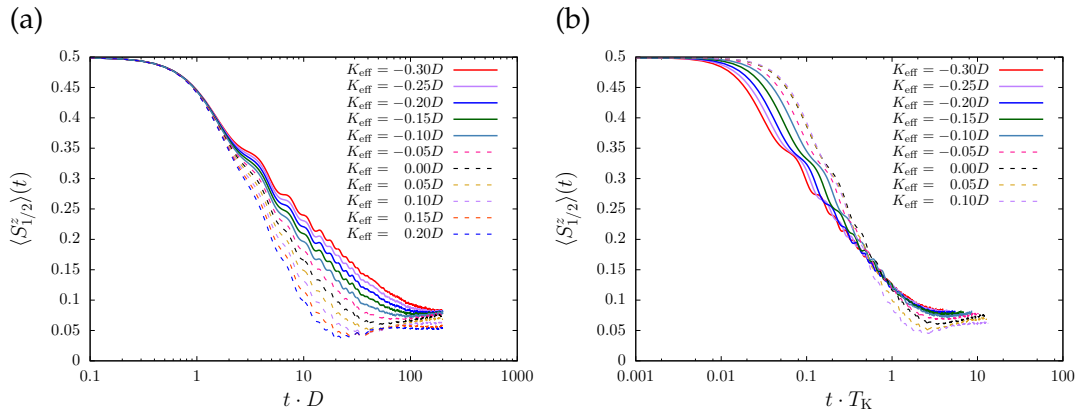

Figure 6.17: (a) The time-dependent expectation value $\langle S_1^z\rangle(t) = \langle S_2^z\rangle(t)$ for $\rho J = 0.4$, $k_F R/\pi = 0.59$, $V_e = 0.54D$ and different effective spin-spin interactions $K_{\text{eff}} = K + K_{\text{RKKY}}$. With increasing antiferromagnetic K_{eff} the polarization decreases faster. The short-time behavior is independent of the spin-spin interaction K_{eff}. (b) Same data as in (a) plotted against the rescaled time tT_K. Only for ferromagnetic interactions $K_{\text{eff}} \leq -0.10D$ (solid lines) universal long-time behavior is observed. NRG parameters are $\Lambda = 3$, $N_s = 1500$ and $N_z = 16$.

the case of constant DOSs. This will be discussed in more detail later on.

In order to investigate the long-time behavior of $\langle S^z_{1/2}\rangle(t)$, we rescale the time with the Kondo temperature T_K. As before, the Kondo temperature is defined by the energy scale at which the first excitation of the even iterations reaches 80% of its fixed point value. The obtained Kondo temperatures T_K are listed for the different effective interactions K_{eff} in Tab. 6.4. The time-dependent polarization $\langle S^z_{1/2}\rangle(t)$ versus the rescaled time tT_K is shown in Fig. 6.17. For ferromagnetic interactions $K_{\text{eff}} \leq -0.10D$ (solid lines) the polarization shows universal long-time behavior. In contrast, for the constant DOSs we have found universal long-time behavior for all ferromagnetic interactions $K \leq 0$ and only the data for antiferromagnetic interactions $K > 0$ have not shown universal behavior when rescaled with T_K. The reason for this is that we must adjust an antiferromagnetic direct spin interaction $K = -K_{\text{RKKY}} = 0.072D$ to achieve that the total effective interaction $K_{\text{eff}} = K + K_{\text{RKKY}}$ vanishes. However, since the RKKY interaction only emerges at low energy scales, at medium and high energy scales the total effective spin-spin interaction K_{eff} is antiferromagnetic. Therefore, we only observe universal long-time behavior if for the direct interaction $K \leq 0$ applies since only in this case the total effective spin-spin interaction K_{eff} is not antiferromagnetic for all energy scales.

Figure 6.18a shows a comparison between the time-dependent polarization with energy-dependent DOSs (red curve) and with constant DOSs (blue curve) for a vanishing total effective spin-spin interaction $K_{\text{eff}} = 0$. The naive expectation would be that the polarization for energy-dependent DOSs decreases faster because the effective interaction at high and medium energy scales is slightly antiferromagnetic which amplifies the

K_{eff}/D	-0.30	-0.25	-0.20	-0.15	-0.10	-0.05	0.00	0.05	0.10
$T_{\text{K}}/D \cdot 10^2$	2.00	2.32	2.71	3.41	4.30	5.07	6.25	6.39	6.67

Table 6.4: Kondo temperatures T_{K} for the different effective spin-spin interactions K_{eff}.

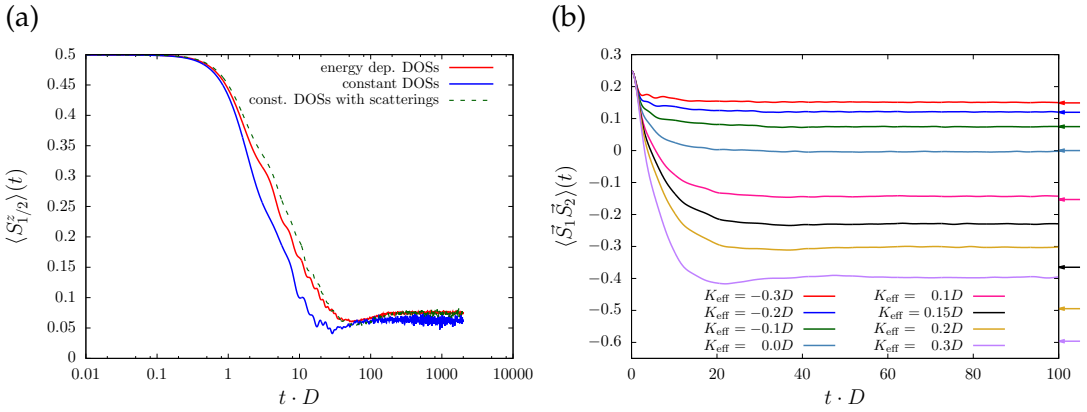

Figure 6.18: (a) A comparison between the time-dependent polarization with energy-dependent DOSs (red curve) and constant DOSs (blue curve) for a vanishing total effective spin-spin interaction $K_{\text{eff}} = 0$. The dashed green curve for constant DOSs and $V_e = V_o = 0.4D$ shows that the scattering terms are responsible for the slower decay. (b) The time-dependent spin-spin correlation function $\langle \vec{S}_1 \vec{S}_2 \rangle(t)$. For effective spin-spin interactions larger than the critical interaction $K_{\text{eff},c} \approx 0.138D$ the system does not thermalize. The arrows on the right indicate the equilibrium value. NRG parameters are $\Lambda = 3$, $N_s = 1500$ and $N_z = 16$.

decrease. In contrast to this expectation, the polarization value for constant DOSs decreases faster. Even for short time scales the two curves differ from each other which indicates that not the effective spin-spin interaction is responsible for the two different decays since the short-time behavior is independent of K.

The green dashed line in Fig. 6.18a shows the time-dependent polarization with constant DOSs and initial potential scatterings[6] $V_e = 0.4D$ and $V_o = 0.4D$. The effective spin-spin interaction is the same as for the blue curve ($K_{\text{eff}} = 0$) since for $N_o/N_e = 1$ and $V_e = V_o$ the RKKY interaction is not changed [64, 168]. Although the effective interactions K_{eff} are equal, the polarization of the green dashed curve decreases slower than the one of the blue curve even for short times and also the long-time value $\langle S_i^z(t \to \infty) \rangle$ is slightly larger. Due to the scattering terms, the occupation of the first Wilson sites differs from half-filling and, therefore, the transport of the polarization to the bath is suppressed which leads to a slower decay of the polarization and the previously mentioned slight increase of the long-time value $\langle S_i^z(t \to \infty) \rangle$.

The time-dependent spin-spin correlation function $\langle \vec{S}_1 \vec{S}_2 \rangle(t)$ is depicted in Fig. 6.18b.

[6] We have chosen $V_e = V_o = 0.4D$ as the potential scatterings because for energy-dependent DOSs, $k_{\text{F}}R/\pi = 0.59$ and $V_e = 0.54D$ the potential scatterings of the zeroth even and odd Wilson sites are also around $\approx 0.4D$.

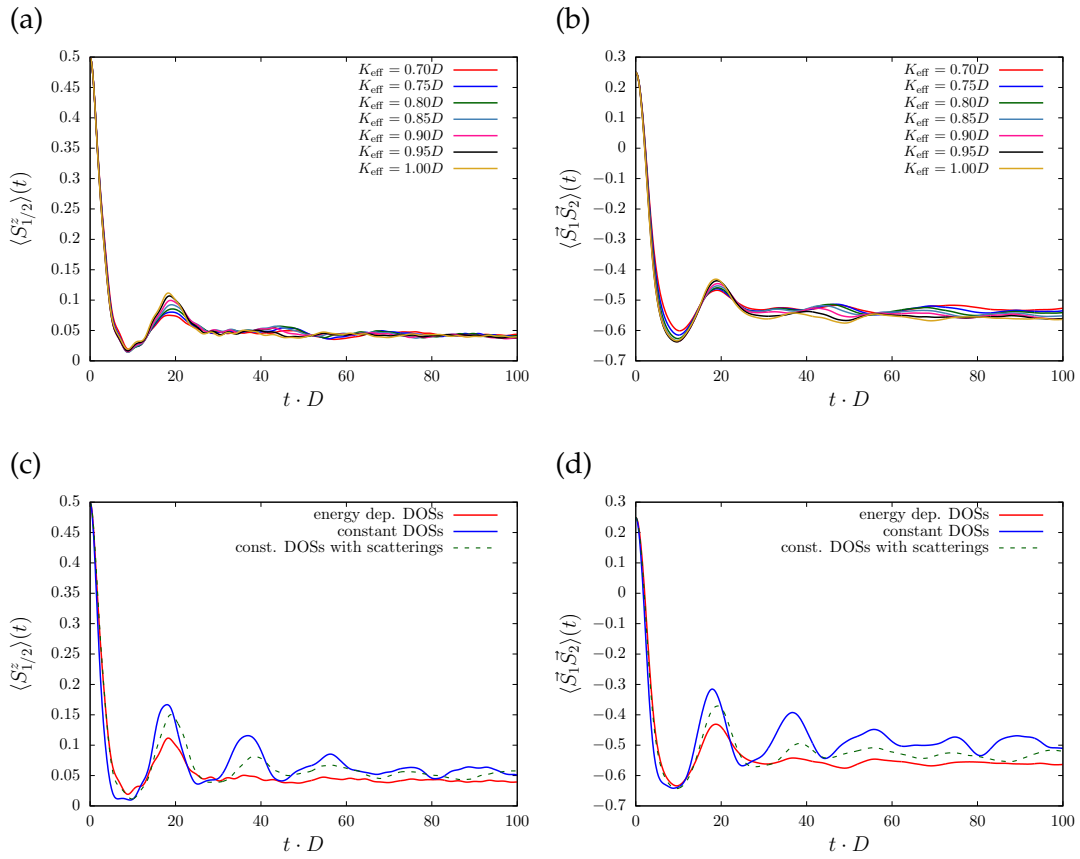

Figure 6.19: (a) The time-dependent polarization $\langle S^z_{1/2}\rangle(t)$ and (b) spin-spin correlation function $\langle \vec{S}_1\vec{S}_2\rangle(t)$ for $\rho J = 0.4$, $k_{\rm F}R/\pi = 0.59$, $V_e = 0.54D$ and different large antiferromagnetic effective spin-spin-interactions $K_{\rm eff}$. For both expectation values only the first maximum of the damped oscillations is visible. (c) Comparison between the polarization for energy-dependent DOSs (red line), constant DOSs (blue line) and constant DOSs with additional initial scattering terms $V_e = V_o = 0.4D$ (green dashed line). (d) The same comparison for the spin-spin correlation function. NRG parameters are $\Lambda = 3$, $N_s = 1500$ and $N_z = 16$.

We observe exactly the same behavior as for the constant DOSs. For spin-spin interactions $K < K_{\text{eff},c} \approx 0.138D$ the equilibrium value is reached as indicated by the arrows on the right of Fig. 6.18b. However, if we quench the system over QCPs into the decoupled singlet phase, the system does not thermalize anymore. As before, the reason for this is that in the decoupled singlet phase the Kondo coupling is renormalized to zero $J \to 0$. Therefore, the impurities decouple from the conduction band which prevents thermalization.

Figures 6.19a and 6.19b show the time-dependent polarization $\langle S^z_{1/2}\rangle(t)$ and spin-spin correlation function $\langle \vec{S}_1\vec{S}_2\rangle(t)$ for different large antiferromagnetic effective spin-spin-interactions $K_{\rm eff}$. For short times the behavior is the same as in Sec. 6.2.1 for constant DOSs, the entire decay of the polarization and correlation function is independent of the large effective interaction. As before, the reason for this is that the short-time be-

havior for both expectation values is completely independent of K and, therefore, the coupling to the conduction band J works as a bottleneck for the decay.
In contrast to the case for constant DOSs where we have observed damped oscillations with the same frequency for the expectation values $\langle S^z_{1/2}\rangle(t)$ and $\langle \vec{S}_1\vec{S}_2\rangle(t)$, for the energy-dependent DOSs only the first maximum is visible. Figure 6.19c shows a comparison between the polarization for energy-dependent DOSs (red line), constant DOSs (blue line) and constant DOSs with additional initial scattering terms $V_e = V_o = 0.4D$ (green dashed line) while Fig. 6.19d shows the same comparison for the spin-spin correlation function. While the first few maxima of the blue curves are clearly pronounced, the damping for the curves with potential scatterings (red and green dashed lines) is much stronger and, therefore, only the first maximum of the oscillations is clearly visible. We can, therefore, again trace the origin of the increased damping back to the potential scattering terms.
Here the oscillations of the red curves are even stronger suppressed than those of the green dashed curves because for energy-dependent DOSs scattering terms emerge at every Wilson site. In contrast, for the green dashed curve we have only introduced potential scatterings on the zeroth Wilson sites and in Sec. 6.2.1 we have shown that not only the zeroth sites are important for the occurring oscillations but also the first few following Wilson sites.

6.3.2 Antiparallel aligned impurity spins

We now turn to the investigation of the initial condition where the impurity spins are antiparallel aligned. We only briefly discuss the obtained results since they are very similar to the results for the constant DOSs in Sec. 6.2.2 and the influence of the potential scatterings have already been discussed in the previous section 6.3.1.
Figure 6.20a shows the time-dependent polarization $\langle S^z_1\rangle(t) = -\langle S^z_2\rangle(t)$ for different effective spin-spin interactions K_{eff}. As before, the polarization decreases faster for antiferromagnetic interactions. In contrast to the initial condition where the impurity spin are parallel aligned, the short-time behavior depends on the effective interaction K_{eff} which can be seen most clearly for $K_{\text{eff}} = -0.95D$ and $K_{\text{eff}} = 0.95D$. As already discussed in Sec. 6.2.2 for constant DOSs, the reason for the different short-time behavior is that the initial state is not an eigenstate to the interaction $K\langle \vec{S}_1\vec{S}_2\rangle$ anymore.
Furthermore, the long-time value $\langle S^z_i\rangle(t \to \infty) = 0$ vanishes which has also already been observed in Sec. 6.2.2 and can again be traced back to the local oscillations of the two impurities. However, in contrast to the case of constant DOSs, even the long-time value of $K_{\text{eff}} = 0$ vanishes because the RKKY interaction only emerges at low temperatures so that the effective interaction K_{eff} is finite at higher energy scales.
The time-dependent spin-spin correlation function $\langle \vec{S}_1\vec{S}_2\rangle(t)$ for different interactions is shown in Fig. 6.20b. The behavior is exactly the same as for the constant DOSs shown in Fig. 6.14b. For short times the correlation function is independent of the interaction

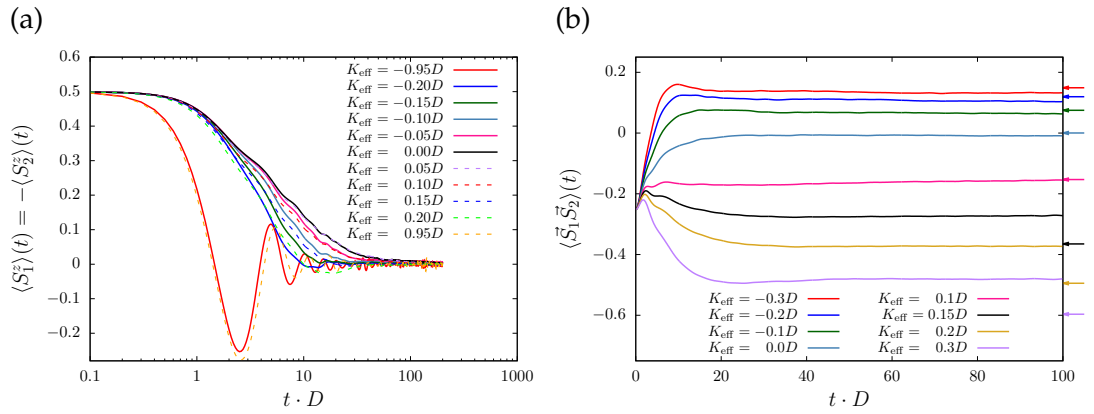

Figure 6.20: (a) The polarization $\langle S_1^z\rangle(t) = -\langle S_1^z\rangle(t)$ for $\rho J = 0.4$, $k_{\rm F}R/\pi = 0.59$, $V_e = 0.54D$ and different effective interactions $K_{\rm eff}$. With increasing antiferromagnetic interaction the polarization decays faster. The short-time behavior depends on $K_{\rm eff}$. (b) The time-dependent correlation function $\langle \vec{S}_1\vec{S}_2\rangle(t)$ for $\rho J = 0.4$, $k_{\rm F}R/\pi = 0.59$, $V_e = 0.54D$ and different effective interactions $K_{\rm eff}$. The arrows on the right indicate the equilibrium value. For times $tD \to \infty$ the system thermalizes only for interactions $K_{\rm eff} < K_{{\rm eff},c} \approx 0.138D$. NRG parameters are $\Lambda = 3$, $N_s = 1500$ and $N_z = 16$.

$K_{\rm eff}/D$	-1.00	-0.90	-0.15	-0.10	-0.05	0.00	0.05	0.10	0.15	0.90	1.00
$t_{\rm low}D$	0.99	1.09	4.51	5.23	5.92	6.40	6.14	5.40	4.55	1.04	0.95

Table 6.5: The time scale $t_{\rm low}$ at which the polarization reaches 40% of its initial value for different effective interactions $K_{\rm eff}$. The time scale is shown in the inset of Fig. 6.21a plotted against $K_{\rm eff}$.

$K_{\rm eff}$ and always increases. As before, for long times $t \to \infty$ and interactions smaller than the critical interaction $K_{\rm eff} < K_{{\rm eff},c} = 0.138D$ the correlation function reaches its equilibrium value which is indicated by the arrows on the right of Fig. 6.20b. However, for larger interactions $K_{\rm eff} > K_{{\rm eff},c}$ the system is quenched into the decoupled singlet phase and does not thermalize anymore.

Figure 6.21a depicts the time-dependent polarization $\langle S_1^z\rangle(t)$ plotted against the rescaled time $t/t_{\rm low}$. Again, $t_{\rm low}$ is the time at which the polarization reaches 40% of its initial value $\langle S_1^z\rangle(t_{\rm low}) = 0.2$ and the obtained values for $t_{\rm low}$ are listed in Tab. 6.5 for different interactions $K_{\rm eff}$. In contrast to Sec. 6.2.2, for energy-dependent DOSs no universal long-time behavior is found.

The inset of Fig. 6.21a shows the time scale $t_{\rm low}$ plotted against the effective interaction $K_{\rm eff}$. As before, the shape of the time scale is not symmetrical in $K_{\rm eff}$ but slightly shifted to antiferromagnetic interactions with the peak at $K_{\rm eff} \approx 0.025D$. However, the observed shift is smaller than the shift for constant DOSs shown in the inset Fig. 6.15a. A comparison between TD-NRG calculations for constant DOSs with and without initial potential scattering terms $V_e = V_o$ on the zeroth Wilson sites reveals that the decreasing asymmetry is caused by the potential scattering terms which occur in

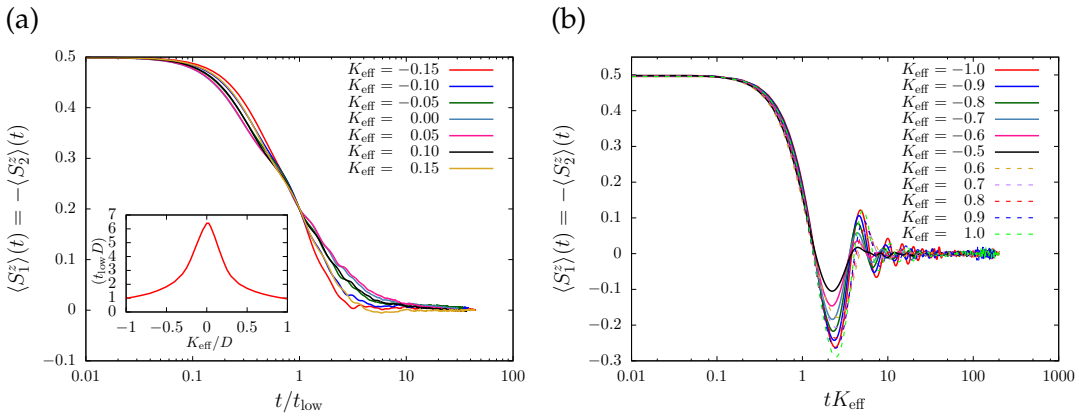

Figure 6.21: (a) The time-dependent polarization versus the rescaled time t/t_{low}. In contrast to the case with constant DOSs no universal behavior is found. The inset shows the time scale t_{low} plotted against the effective interaction K_{eff}. (b) The time-dependent polarization for large interaction K_{eff} versus the rescaled time tK_{eff}. For such large interactions the decay is dominated by the local oscillations of the impurity spins with frequency K_{eff}. NRG parameters are $\Lambda = 3$, $N_s = 1500$ and $N_z = 16$.

the energy-dependent model. Due to these scatterings, the occupation of the zeroth Wilson sites differs from half filling and, consequently, the influence of the conduction bands on the local spin-flip processes, which are symmetrical in K_{eff}, is weakened. For $V_{e/o} \to \pm\infty$ the zeroth Wilson sites would be unoccupied/doubly occupied and, therefore, spin-flips between the impurity spins and conduction band electron spins would be completely suppressed so that only the local oscillations occur.

This smaller shift is also noticeable in Fig. 6.21b where the time-dependent polarization is depicted versus the rescaled time tK_{eff} for large interactions. As for constant DOSs, the decay for such large interactions is dominated by the local oscillations of the impurities with frequencies K_{eff} and, therefore, a rescaling with K_{eff} leads to universal behavior. However, since the shift between ferromagnetic and antiferromagnetic interactions is much smaller, an offset between the curves for ferromagnetic (solid lines) and antiferromagnetic (dashed lines) is not visible as it was the case in Fig. 6.15b.

The time-dependent polarization $\langle S_i^z\rangle(t)$ is shown for different large ferro- (solid lines) and antiferromagnetic (dashed lines) interactions K_{eff} in Fig. 6.22a. As for the constant DOSs the observed frequencies are much faster than those for parallel aligned impurity spins shown in Fig. 6.19a because of the fast local oscillations. In contrast to the case of parallel aligned spins and energy-dependent DOSs where only the first maximum is visible, here, the oscillations are clearly visible since the potential scattering terms, which are responsible for the increased damping in the parallel aligned case, do not influence the local oscillations of the impurity spins.

The asymmetry for ferro- and antiferromagnetic interactions K_{eff} is also visible in the frequency of the oscillations. For the same absolute value of the effective interac-

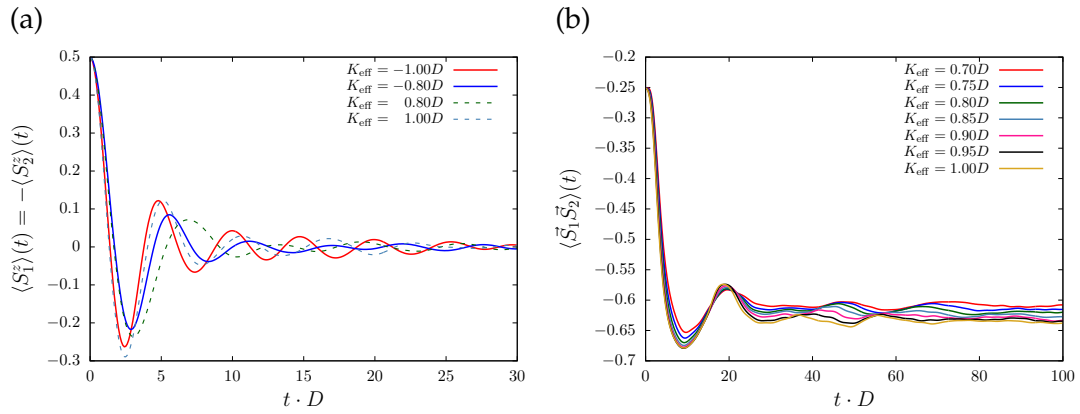

Figure 6.22: (a) The time-dependent polarization for $\rho J = 0.4$, $k_F R/\pi = 0.59$, $V_e = 0.54D$ and different large ferro- (solid lines) and antiferromagnetic (dashed lines) interactions K_{eff}. For the same absolute value of the interaction $|K_{\text{eff}}|$, the damped oscillations for ferromagnetic interactions are slightly faster. (b) The time-dependent correlation function $\langle \vec{S}_1 \vec{S}_2 \rangle(t)$ for different large antiferromagnetic interactions. Only the first maximum of the damped oscillation is visible and its position coincides exactly with the one observed in Fig. 6.19b.

tion $|K_{\text{eff}}|$, the frequencies of the oscillations for ferromagnetic interactions are slightly faster than the frequencies for antiferromagnetic interactions. This has also been observed and discussed for constant DOSs, however, since the asymmetry here is smaller, the difference between the frequencies is also reduced.

Figure 6.22b depicts the time-dependent correlation function $\langle \vec{S}_1 \vec{S}_2 \rangle(t)$ for different large ferromagnetic interactions K_{eff}. As it has been the case for constant DOSs, the frequency of the oscillations coincides with the frequency of the oscillations in the polarization and correlation function for parallel aligned impurity spins which have been shown in Fig. 6.19a and Fig. 6.19b respectively. The reason for this is that a change of the correlation can only be caused by a coupling to the conduction band. Therefore, the potential scattering terms once again increase the damping and, consequently, only the first maximum of the oscillation is visible.

6.4 Summary and outlook

The QCP of the TIKM is often considered to be artificial [67, 68] due to the approximation of energy independent DOSs. In this chapter, however, we have been able to demonstrate that it is actually possible to restore the QCP in the full energy-dependent TIKM using initial potential scattering terms. Instead of restoring the full particle-hole symmetry of the model, it has turned out that it is sufficient to shift the Kondo resonances of the even and odd conduction band again on top of each other in the vicinity of the QCP.

The QCP has the same properties as the QCP of the model with constant DOSs since

the spin-spin correlation function between the two impurity spins $\langle \vec{S}_1 \vec{S}_2 \rangle$ changes continuously and the staggered susceptibility diverges at the QCP. A remaining task is to ensure that also the linear coefficient of the specific heat diverges at the QCP [62, 63], cf. Sec. 2.3.

In reality, however, the direct tuning of the even and odd potential scattering terms V_e and V_o is impossible. Nevertheless, in experiment there are two options to shift the two Kondo resonances on top of each other. At first, the energy level of both impurities can be changed via a gate voltage which, if mapped to even and odd conduction bands, would at first sight only shift both Kondo resonances equally $V_e = V_o = V$ [27]. However, it has been shown that such a term would also generate scattering terms in second order of the Kondo coupling J of the form $V_e - V_o \propto J^2 V$ [168]. Such a generated potential scattering could in principle shift the Kondo resonances back on top of each other.

A second method would be to tune the tunneling between the two impurities. This would shift the energy levels of the even and odd linear combinations of the impurities differently and, therefore, also generate different potential scattering terms $V_e \neq V_o$. Consequently, it should be in principle possible to shift the even and odd Kondo resonances back on top of each other using the tunneling.

It would be, therefore, interesting to investigate the TIAM and examine if it is possible to restore the QCP with the methods described above and estimate the magnitude of the tunneling and gate voltage required for this purpose.

After discussing the restoration of the QCP we have investigated the nonequilibrium dynamics of the TIKM exhibiting a QCP for two different initial conditions. For the first one the impurity spins have been parallel and for the second one antiparallel aligned. To set the stage for the full energy-dependent model, at first we have studied the TIKM with constant DOS and no initial potential scatterings.

For the parallel aligned initial condition we have discovered that for ferromagnetic interactions $K \geq 0$ between the two impurity spins the long-time behavior of the time-dependent polarization is determined by the Kondo effect. Furthermore, it has turned out that the time-dependent spin-spin correlation function $\langle \vec{S}_1 \vec{S}_2 \rangle(t)$ reaches the equilibrium value for times $t \to \infty$ only if the interaction is smaller than the critical interactions $K < K_c$ since for larger interactions the system is driven to the decoupled singlet phase where the impurity spins decouple from the conduction band preventing thermalization. Interestingly, we have observed coherent oscillations for large antiferromagnetic interactions in the polarization and correlation function with the same frequency. These oscillations could be connected to the local oscillations which already occur for the first NRG iteration $N_{\text{Iter}} = 1$.

For the initial condition of antiparallel aligned impurities, all differences in the time-dependent spin polarization compared to the case of parallel aligned spins originate from the local oscillations of the two impurity spins which emerge due to the fact that

the initial state is not an eigenstate to the interaction $K\vec{S}_1\vec{S}_2$ anymore. These local oscillations are clearly visible in the spin polarization for large antiferromagnetic as well as ferromagnetic interactions K and are much faster than the oscillations observed for parallel aligned impurity spins. However, the behavior of the time-dependent spin-spin correlation function has been the same as for parallel aligned spins since a change of the correlation function cannot be caused by the direct interaction K but must happen via a coupling to the conduction band.
Moreover, we have investigated the TIKM with full energy-dependent DOSs after the QCP has been restored. The nonequilibrium dynamics of the system have been essentially the same as for the TIKM with constant DOSs. The slightly different short-time behavior and increased damping of the oscillations could be traced back to the potential scattering terms whereas the differences in the universal long-time behavior of the polarization for weak ferromagnetic effective interactions has been related to the fact that in contrast to the direct interaction K, the RKKY interaction only emerges at low energy scales.
However, the nonequilibrium results presented in this chapter are only the outcome of a first investigation and it would be interesting to examine also different initial conditions and different types of quenches. An alternative quench would be a change of the distance R between the two impurities which changes the RKKY interaction and could, therefore, also drive the system from the decoupled singlet phase to the Kondo phase or vice versa. Another example would be a quench in the Kondo coupling J. Since the position of the QCP depends on the ratio between the effective spin-spin interaction and the Kondo temperature $K_{\text{eff}}/T_{\text{K}}$ [62, 63] and since the Kondo temperature changes exponentially in J whereas the RKKY interaction depends quadratically on the Kondo coupling, it is possible to drive the system from one phase to another by changing the Kondo coupling J. In an experiment the Kondo coupling could be controlled by an external gate voltage [71].
It would also be worthwhile to study the differences between the time-dependent behavior of the full energy-dependent TIKM with and without restored QCP. In this way one could directly observe the influence of the QCP on the nonequilibrium dynamics.
Furthermore, it would be very interesting to investigate how the correlations between the two impurity spins propagate through the system for different types of quenches and initial conditions as it has been done in Sec. 4 for the correlations between an impurity spin and the spin density of the conduction band at a certain distance.

Chapter 7

Conclusion

In this thesis we have investigated the equilibrium and nonequilibrium properties of different fermionic quantum impurity systems, employing the numerical renormalization group (NRG) and time-dependent numerical renormalization group (TD-NRG).
In particular, we have studied the spatial and temporal propagation of Kondo correlations for ferro- and antiferromagnetic Kondo couplings J. For this purpose we have investigated the time-dependent spin-spin correlation function between the impurity spin and the spin density of the conduction band at a certain distance R.
To set the stage for the nonequilibrium calculations, we have first measured the equilibrium spin-spin correlation function. Surprisingly, for antiferromagnetic Kondo couplings we have found significant deviations from previous NRG results by Borda [47] where only antiferromagnetic correlations have been observed. In contrast, our results have shown distance dependent oscillations between ferromagnetic and antiferromagnetic correlations for small distances compared to the size of the Kondo screening cloud $v_\mathrm{F}/T_\mathrm{K}$ in accordance with analytical calculations by Affleck *et al.* [125]. The quality of our results has been checked by an analytically known sum rule from which our numerical data deviates by less than 2% in 1D. For large distances our equilibrium results agree with the observations in Ref. [47].
Inside the Kondo screening cloud the spin-spin correlation function decreases slowly with a powerlaw decay of $1/R^D$ while outside of the screening cloud a $1/R^{D+1}$ decay of the correlations has been found, with D being the dimension. In the case of a ferromagnetic Kondo coupling, we have observed oscillations between ferromagnetic and antiferromagnetic correlations and a $1/R^D$ decay for all distances since for a ferromagnetic coupling the size of the screening cloud diverges. At finite temperature a new length scale has emerged beyond which the correlations are exponentially cut off.
For the full time-dependent correlation function we have found that most of the correlations propagate within a light cone defined by the Fermi velocity v_F. Precisely on the light cone a ferromagnetic wave propagates away from the impurity location. The correlations inside the light cone develop rather quickly towards their equilibrium value.
Surprisingly, we have seen for ferro- as well as for antiferromagnetic Kondo couplings

the buildup of correlations outside of the light cone that do not decay exponentially. As a main result of our investigations, we have been able to trace back these correlations to the intrinsic entanglement of the Fermi sea using a second-order perturbative expansion in the Kondo coupling J.
Furthermore, we have calculated the retarded susceptibility describing the response of the conduction band spin density at certain distance to a magnetic field applied to the impurity spin. We have used this susceptibility to calculate the response of the spin-density polarization induced by a very weak magnetic field. For the real-time response we have found no correlations outside of the light cone. However, a benchmark calculation with the analytically known retarded equilibrium host spin-density susceptibility has revealed that this method is limited to short distances.
Moreover, we have demonstrated in this thesis that the NRG is capable to reproduce the data of a scanning tunneling spectroscopy (STS) experiment with excellent agreement. For this purpose we have used the results of a density functional theory (DFT) calculation as a first principle input for the NRG calculations. In particular, we have investigated the adsorption of single Au atoms on a PTCDA monolayer physisorbed on an Au(111) surface. The chemical reaction between the Au atom and PTCDA leads to the formation of a metal-molecule complex occupied with an unpaired spin. In the experiment this radical formation has been observed as an additional zero-bias differential conductance peak in the STS spectra originating from the Kondo effect. In order to describe the electronic properties of the Au-PTCDA complex, including the low energy physics, we have applied the above mentioned combined DFT+NRG approach. It has turned out to be crucial to employ the full energy-dependent hybridization function for a correct quantitative description of the system.
Furthermore, we have carried out a careful analysis of the scaling behavior of various definitions of the Kondo temperature using the NRG in order to provide a systematical way to extract the Kondo temperature reliably from an experiment for a particle-hole asymmetric system. We have found that a temperature dependent fit to the zero-bias conductance is the best way to extract the Kondo temperature since it is not affected by nonuniversal aspects of the lineshape. Remarkably, we have found a Kondo temperature from our combined DFT+NRG approach that deviates only 1 K from the experimentally measured T_{K}.
A special feature of the Au-PTCDA complex is that the local moment resides in a π-orbital which is delocalized over the entire complex. The advantage of such an extended orbital is its increased probability to interact with neighbors, offering the possibility to use this interaction for spintronics.
Such an interaction between two adjacent Au-PTCDA complexes has been revealed in the experiment by the observation of a gap in the measured STS spectra. Mapping the system onto a two impurity Anderson model (TIAM), we have been able to trace back this effect to a strong direct tunneling between both complexes. Usually, the formation

of a gap in the spectrum of adatoms on a metallic surface is often associated with the competition between the Ruderman-Kittel-Kasuya-Yosida (RKKY) interaction and the Kondo effect. In our case, however, the ordinary chemical hybridization between the molecular monomers is sufficient to drive a quantum phase transition (QPT) between a partially Kondo-screened local triplet and a local singlet.
The QPT originates from a competition between the kinetic energy gain due to the entanglement with the substrate and the binding energy gain due to the chemical interaction between the moment-carrying orbitals. In the experiment the strength of the tunneling is determined by the specific adsorption sites of the Au atoms on the PTCDA molecules. While for a dimer configuration with a weak tunneling a Kondo resonance has been observed, the particularly strong interactions of specific dimer configurations have led to a formation of a gap in the STS spectra. As for a single noninteracting Au-PTCDA complex, we have found an excellent agreement between the results of the combined DFT+NRG approach and the experimental data. In particular, we have been able to predict the formation of a gap for the correct dimer configurations without any fitting parameters. Furthermore, we have revealed that only in the parity-broken case the gap can be observed in the STS spectra.
We have also investigated the equilibrium and nonequilibrium properties of the two impurity Kondo model (TIKM). This model exhibits a QPT if the energy-dependence of the coupling constants is artificially neglected. However, we have shown that it is possible to restore the QPT with potential scattering terms even in the full energy dependent model. In the experiment these potential scattering terms could, in principle, be generated by applying a gate voltage to the impurities or by changing the tunneling between both impurities.
Next, we have examined the nonequilibrium dynamics of the TIKM exhibiting a QPT for two different initial conditions, namely for parallel and antiparallel aligned impurity spins. In the case of constant couplings, we have revealed that for a ferromagnetic direct spin-spin interaction the decay of the spin-polarization is only determined by the Kondo effect for long times. An antiferromagnetic interaction leads to an increased decay of the polarization since for an antiferromagnetic interaction a singlet ground state is favorable. We have been able to relate the coherent oscillations that emerge for very large antiferromagnetic interactions in the spin-polarization as well as in the correlation function to the oscillations that already occur for the first NRG iteration.
All differences between the initial conditions of parallel and antiparallel aligned impurities have been connected to the local oscillations between both impurity spins. These local oscillations occur since the antiparallel aligned initial condition is not an eigenstate of the direct spin-spin interaction anymore. As a result, we have observed a spin-spin interaction dependent short-time behavior and fast coherent oscillations in the spin-polarization for large ferro- as well as antiferromagnetic interactions. The time dependence of the spin-spin correlation function, however, has been essentially

the same as for the parallel aligned initial conditions because a change of the correlation function cannot be caused by a direct interaction between the impurity spins but must happen via a coupling to the conduction band.
The nonequilibrium dynamics of the full energy-dependent TIKM have been very similar to the case of constant couplings. We have been able to relate the slightly different short-time behavior and increased damping to the potential scattering terms occurring in the energy-dependent model. The different universal long-time behavior has been associated with the circumstance that the indirect RKKY interaction only emerges at low energy scales.
In all cases discussed above, we have found that the time-dependent spin-spin correlation function only thermalizes if the system is quenched into the Kondo phase while for a quench into the decoupled singlet phase both impurities decouple from the conduction band preventing a thermalization.
However, our nonequilibrium results of the TIKM are only the outcome of a first investigation and it would be interesting to examine also different initial conditions and different types of quenches. Furthermore, it would be very interesting to analyze the spatial and temporal propagation of the correlations between both impurity spins similar to our studies of the correlations between the impurity spin and the conduction band spin density at a certain distance in the Kondo model.

Appendix A

Mapping the TIKM to even and odd parity states

In order to solve the two impurity Kondo model (TIKM) using the numerical renormalization group (NRG), the conduction band operators that couple to the impurities must be orthogonal. Therefore, we derive in this appendix the Hamiltonian of the TIKM in an orthogonal even-odd parity basis [61, 62, 64].
The TIKM Hamiltonian can be divided into three terms

$$H_{\mathrm{TIKM}} = H_0 + H_{\mathrm{int}} + H_{\mathrm{imp}}, \tag{A.1}$$

where $H_0 = \sum_{\vec{k}\sigma} \epsilon(\vec{k}) c^\dagger_{\vec{k}\sigma} c_{\vec{k}\sigma}$ accounts for the conduction band with the dispersion $\epsilon(\vec{k})$ and H_{imp} contains all interactions which only act on the impurities, e.g. a direct spin-spin interaction between the impurity spins $H_{\mathrm{imp}} = K\vec{S}_1\vec{S}_2$. H_{int} describes the interaction between the conduction band and the impurity spins and can be written as

$$H_{\mathrm{int}} = J\left(\vec{S}_1 s_c(\vec{R}_1) + \vec{S}_2 s_c(\vec{R}_2)\right), \tag{A.2}$$

where $\vec{S}_i$ is an impurity spin located at position $\vec{R}_i$ coupled via the effective Heisenberg coupling J to the unit-cell volume averaged conduction electron spin $s_c(\vec{r}) = V_u \vec{s}(\vec{r})$. Here, $\vec{s}(\vec{r})$ is the conduction band spin density operator expanded in planar waves

$$\vec{s}(\vec{r}) = \frac{1}{2}\frac{1}{NV_u}\sum_{\sigma\sigma'}\sum_{\vec{k}\vec{k}'} c^\dagger_{\vec{k}\sigma}[\underline{\vec{\sigma}}]_{\sigma\sigma'} c_{\vec{k}'\sigma'} e^{i(\vec{k}'-\vec{k})\vec{r}}, \tag{A.3}$$

with N being the number of unit cells in the volume V, $V_u = V/N$ the volume of such a unit cell, $\vec{k}$ a momentum vector and $\underline{\vec{\sigma}}$ a vector of the Pauli matrices.
In the following, we set the origin of the coordinate system in the middle of the two impurities such that $\vec{R}_1 = \vec{R}/2$ and $\vec{R}_2 = -\vec{R}/2$. In order to employ the NRG, the

Hamiltonian has to be transformed into energy-space. For this purpose, we define new energy-dependent field operators that also include the spatial dependence

$$c_{\epsilon\sigma,\pm} = \frac{1}{\sqrt{N\rho(\epsilon)}} \sum_{\vec{k}} \delta(\epsilon - \epsilon(\vec{k})) c_{\vec{k}\sigma} e^{\pm i\vec{k}\vec{R}/2}, \tag{A.4}$$

with the dispersion $\epsilon(\vec{k})$ and the density of states (DOS) $\rho(\epsilon)$ of the conduction band. These new operators can be combined to even (e) and odd (o) parity eigenstates

$$\begin{aligned} c_{\epsilon\sigma,e} &= \frac{1}{N_e(\epsilon)} \left(c_{\epsilon\sigma,+} + c_{\epsilon\sigma,-} \right) \\ c_{\epsilon\sigma,o} &= \frac{1}{N_o(\epsilon)} \left(c_{\epsilon\sigma,+} - c_{\epsilon\sigma,-} \right). \end{aligned} \tag{A.5}$$

The normalization factors $N_{e/o}(\epsilon)$ are chosen such that they fulfill the standard anti-commutator relation $\{c_{\epsilon\sigma,\alpha}, c^\dagger_{\epsilon'\sigma',\alpha'}\} = \delta(\epsilon - \epsilon')\delta_{\alpha\alpha'}\delta_{\sigma\sigma'}$:

$$\begin{aligned} \{c_{\epsilon\sigma,e/o}, c^\dagger_{\epsilon'\sigma',e/o}\} =& \frac{1}{N^2_{e/o}(\epsilon)} \frac{1}{N\rho(\epsilon)} \sum_{\vec{k}\vec{k}'} \delta(\epsilon - \epsilon(\vec{k}))\delta(\epsilon' - \epsilon(\vec{k}')) \\ & \cdot \left| e^{i\vec{k}\vec{R}/2} \pm e^{-i\vec{k}\vec{R}/2} \right|^2 \underbrace{\{c_{\vec{k}\sigma}, c^\dagger_{\vec{k}'\sigma'}\}}_{\delta_{\vec{k},\vec{k}'}\delta_{\sigma,\sigma'}} \qquad \text{(A.6)} \\ =& \frac{\delta_{\sigma,\sigma'}}{N^2_{e/o}(\epsilon)} \frac{1}{N\rho(\epsilon)} \sum_{\vec{k}} \underbrace{\delta(\epsilon - \epsilon(\vec{k}))\delta(\epsilon' - \epsilon(\vec{k}))}_{\delta(\epsilon-\epsilon')\delta(\epsilon-\epsilon(\vec{k}))} \left| e^{i\vec{k}\vec{R}/2} \pm e^{-i\vec{k}\vec{R}/2} \right|^2 \qquad \text{(A.7)} \\ =& \delta(\epsilon - \epsilon')\delta_{\sigma,\sigma'} \frac{1}{N^2_{e/o}(\epsilon)} \frac{1}{N\rho(\epsilon)} \sum_{\vec{k}} \delta(\epsilon - \epsilon(\vec{k})) \left| e^{i\vec{k}\vec{R}/2} \pm e^{-i\vec{k}\vec{R}/2} \right|^2. \qquad \text{(A.8)} \end{aligned}$$

A comparison of Eq. (A.8) with the standard anticommutator yields for the two normalization factors

$$\begin{aligned} N^2_e(\epsilon) &= \frac{4}{N\rho(\epsilon)} \sum_{\vec{k}} \delta(\epsilon - \epsilon_{\vec{k}}) \cos^2\left(\frac{\vec{k}\vec{R}}{2}\right), \\ N^2_o(\epsilon) &= \frac{4}{N\rho(\epsilon)} \sum_{\vec{k}} \delta(\epsilon - \epsilon_{\vec{k}}) \sin^2\left(\frac{\vec{k}\vec{R}}{2}\right). \end{aligned} \tag{A.9}$$

Note that both normalizations depend on the distance $\vec{R}$ between the two impurities. If we consider the case that the dispersion depends only on the absolute value of the momentum vector $\epsilon(\vec{k}) = \epsilon(|\vec{k}|) = \epsilon(k)$, we can perform the angular integration in the continuum limit $\sum_{\vec{k}} \to \frac{N}{(2\pi)^3} \int d^3k$. This yields in 1D

$$N^2_{e/o}(\epsilon)\rho(\epsilon) = 2\rho(\epsilon) \left[1 \pm \cos\left(k(\epsilon)R\right)\right] \tag{A.10}$$

with $R = |\vec{R}|$ and $k(\epsilon)$ being the inverse function of $\epsilon(k)$. For the simple case of a linear dispersion $\epsilon(k) = v_F(k - k_F)$, the inverse function is for example given by $k(\epsilon) = k_F + \frac{\epsilon}{v_F} = k_F(1 + \frac{\epsilon}{D})$. Here, v_F is the Fermi velocity, k_F the length of the Fermi wave vector and $D = v_F k_F$ the half bandwidth. In 2D we obtain after the integration over the angular

$$N^2_{e/o}(\epsilon)\rho(\epsilon) = 2\rho(\epsilon)\left[1 \pm J_0\left(k(\epsilon)R\right)\right] \tag{A.11}$$

where $J_0(x)$ is the zeroth Bessel function and for 3D the integration gives

$$N^2_{e/o}(\epsilon)\rho(\epsilon) = 2\rho(\epsilon)\left[1 \pm \frac{\sin\left(k(\epsilon)R\right)}{k(\epsilon)R}\right]. \tag{A.12}$$

Inserting $c_{\epsilon\sigma,\pm}$ into the Hamiltonian Eq. (A.2) yields

$$H_{\text{int}} = \frac{J}{2}\int\int\sum_{\sigma\sigma'}\sqrt{\rho(\epsilon)\rho(\epsilon')}\left(c^\dagger_{\epsilon\sigma,+}\vec{\sigma}_{\sigma\sigma'}c_{\epsilon'\sigma',+}\vec{S}_1 + c^\dagger_{\epsilon\sigma,-}\vec{\sigma}_{\sigma\sigma'}c_{\epsilon'\sigma',-}\vec{S}_2\right)\, d\epsilon\, d\epsilon' \tag{A.13}$$

which can be further rewritten in terms of the parity eigenoperators $c_{\epsilon\sigma,e}$ and $c_{\epsilon\sigma,o}$

$$\begin{aligned} H_{\text{int}} = &\frac{J}{8}\int\int\sum_{\sigma\sigma'}\sqrt{\rho(\epsilon)\rho(\epsilon')}\vec{\sigma}_{\sigma\sigma'} \\ &\Big[(\vec{S}_1 + \vec{S}_2)\left(N_e(\epsilon)N_e(\epsilon')c^\dagger_{\epsilon\sigma,e}c_{\epsilon'\sigma',e} + N_o(\epsilon)N_o(\epsilon')c^\dagger_{\epsilon\sigma,o}c_{\epsilon'\sigma',o}\right) \\ &+(\vec{S}_1 - \vec{S}_2)N_e(\epsilon)N_o(\epsilon')\left(c^\dagger_{\epsilon\sigma,e}c_{\epsilon'\sigma',o} + c^\dagger_{\epsilon'\sigma,o}c_{\epsilon\sigma',e}\right)\Big]\, d\epsilon\, d\epsilon'. \end{aligned} \tag{A.14}$$

We finally obtain for the Hamiltonian of the TIKM

$$H_{\text{TIKM}} = \sum_{\alpha=e,o}\sum_{\sigma}\int \epsilon c^\dagger_{\epsilon\sigma,\alpha}c_{\epsilon\sigma,\alpha}\, d\epsilon + H_{\text{int}} + H_{\text{imp}}, \tag{A.15}$$

where the first term describes the conduction band that has been divided into two conduction bands with even and odd parity symmetry and H_{int} is given by Eq. (A.14).

Appendix B

RKKY interaction

In this appendix, we briefly summarize the perturbative calculation of the RKKY interaction between two impurity spins mediated by a conduction band in second-order in the Kondo coupling J. The interaction part of the Hamiltonian, which describes the interaction between the impurity spins and the conduction band electron spins, can be expanded in even (e) and odd (o) parity states, cf. appendix A, and is given by

$$\begin{aligned} H_{\text{int}} =& \frac{J}{8} \sum_{\sigma,\sigma'} \int\int d\epsilon\, d\epsilon'\, \sqrt{\rho(\epsilon)\rho(\epsilon')}\vec{\sigma}_{\sigma,\sigma'} \\ & \times \Big[\left(\vec{S}_1 + \vec{S}_2\right) \left(N_e(\epsilon)N_e(\epsilon')c^\dagger_{\epsilon\sigma,e}c_{\epsilon'\sigma',e} + N_o(\epsilon)N_o(\epsilon')c^\dagger_{\epsilon\sigma,o}c_{\epsilon'\sigma',o} \right) \\ & + \left(\vec{S}_1 - \vec{S}_2\right) \left(N_e(\epsilon)N_o(\epsilon')c^\dagger_{\epsilon\sigma,e}c_{\epsilon'\sigma',o} + N_o(\epsilon)N_e(\epsilon')c^\dagger_{\epsilon\sigma,o}c_{\epsilon'\sigma',e} \right) \Big]. \end{aligned} \tag{B.1}$$

The normalization factors $\sqrt{\rho(\epsilon)}N_{e/o}(\epsilon)$ have been defined in appendix A and are given by Eq. (A.10) in 1D, by Eq. (A.11) in 2D and by Eq. (A.12) in 3D. The RKKY interaction is generated by a propagation of spin excitations in the conduction band between the two impurities. The second-order Feynman diagram generating the lowest order contribution to the RKKY interaction is shown in Fig. B.1. Integrating out the conduction electron degrees of freedom leads to the effective RKKY interaction

$$H_{\text{RKKY}} = \frac{1}{\beta} \sum_{i\omega_n} \int\int d\epsilon\, d\epsilon \sum_{\alpha,\alpha'} G^0(\omega_n,\epsilon)G^0(\omega_n,\epsilon')V^{\vec{R}_1}_{\alpha,\alpha'}(\epsilon,\epsilon')V^{\vec{R}_2}_{\alpha',\alpha}(\epsilon',\epsilon). \tag{B.2}$$

This expression is exact up to second-order in the coupling J. The vertex function $V^{\vec{R}_i}_{\alpha,\alpha'}(\epsilon,\epsilon')$ at the position $\vec{R}_i$ of the impurity spin $\vec{S}_i$ can be deduced from the Hamiltonian H_{int} in Eq. (B.1) and is given by

$$V^{\vec{R}_i}_{\alpha,\alpha'}(\epsilon,\epsilon') = c^i_{p,p'} \frac{J}{8} \sqrt{\rho(\epsilon)\rho(\epsilon')} N_p(\epsilon)N'_p(\epsilon')\vec{\sigma}_{\sigma,\sigma'}\vec{S}_i. \tag{B.3}$$

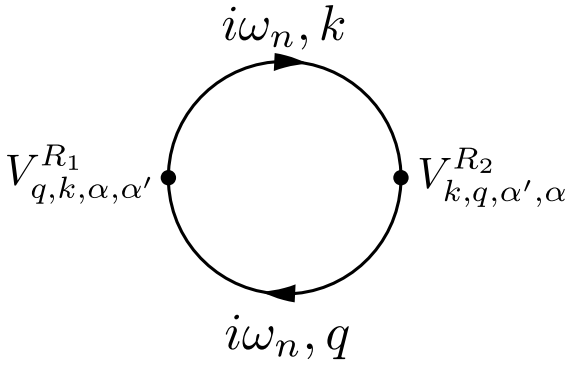

Figure B.1: The Feynman diagram of the leading second-order contribution to the RKKY interaction between localized spins mediated by a spin excitation propagating through the conduction band. Figure taken from [177].

The index $\alpha = (\sigma, p)$ combines the spin index σ and parity index p and the sign factor $c^i_{p,p'}$ is defined as

$$c^i_{p,p'} = \begin{cases} -1 & \text{if } p \neq p' \text{ and } i = 2 \\ 1 & \text{otherwise} \end{cases}. \tag{B.4}$$

$G^0(\omega_n, \epsilon) = \frac{1}{i\omega_n - \epsilon_k + i\delta}$ denotes the Green's function of a free conduction electron and $i\omega_n$ is the fermionic Matsubara frequency. A standard evaluation of the summation over the Matsubara frequencies [178] yields

$$\frac{1}{\beta}\sum_{i\omega_n} G^0(\omega_n, \epsilon) G^0(\omega_n, \epsilon') = \frac{f(\epsilon) - f(\epsilon')}{\epsilon - \epsilon'}, \tag{B.5}$$

where $f(\epsilon)$ is simply the Fermi-Dirac distribution function. For $T = 0$ Eq. (B.5) vanishes if both energies ϵ and ϵ' are above or below the Fermi energy. Therefore, we obtain for a particle-hole symmetric conduction band at $T = 0$

$$H_{\text{RKKY}} = \sum_{\alpha,\alpha'} \int_{-D}^{0} d\epsilon \int_{0}^{D} d\epsilon' \left(\frac{V^{\vec{R}_1}_{\alpha,\alpha'}(\epsilon, \epsilon') V^{\vec{R}_2}_{\alpha',\alpha}(\epsilon', \epsilon)}{\epsilon - \epsilon'} + \frac{V^{\vec{R}_2}_{\alpha,\alpha'}(\epsilon, \epsilon') V^{\vec{R}_1}_{\alpha',\alpha}(\epsilon', \epsilon)}{\epsilon - \epsilon'} \right). \tag{B.6}$$

Performing the spin and parity summation yields for the effective spin-spin interaction

$$H_{\text{RKKY}} = \int_{-D}^{0} d\epsilon \int_{0}^{D} d\epsilon' \, \rho(\epsilon)\rho(\epsilon') \frac{J^2}{16} \left(\frac{N_e^2(\epsilon) N_e^2(\epsilon') + N_o^2(\epsilon) N_o^2(\epsilon')}{\epsilon - \epsilon'} - \frac{N_e^2(\epsilon) N_o^2(\epsilon') + N_o^2(\epsilon) N_e^2(\epsilon')}{\epsilon - \epsilon'} \right) \vec{S}_1 \vec{S}_2, \tag{B.7}$$

from which we can read the distance dependent effective RKKY interaction constant

$$K_{\mathrm{RKKY}} = \int_{-D}^{0} d\epsilon \int_{0}^{D} d\epsilon' \, \rho(\epsilon)\rho(\epsilon')\frac{J^2}{16} \times \left(\frac{N_e^2(\epsilon)N_e^2(\epsilon') + N_o^2(\epsilon)N_o^2(\epsilon')}{\epsilon - \epsilon'} - \frac{N_e^2(\epsilon)N_o^2(\epsilon') + N_o^2(\epsilon)N_e^2(\epsilon')}{\epsilon - \epsilon'} \right). \tag{B.8}$$

The distance dependence is implicitly encoded in the distance dependent parity densities $N_e(\epsilon)$ and $N_o(\epsilon)$. In general, the integration over the energies in Eq. (B.8) has to be performed numerically. In the simple case that the energy dependent parity densities are replaced by constants $\rho(\epsilon)N_p^2(\epsilon) = \rho_0 N_p^2$, we recover the approximation of Jones and Varma [61]

$$\frac{K_{\mathrm{RKKY}}}{D} = -\frac{J^2\rho_0^2}{16} 2\ln(2) \left(N_e^2 - N_o^2\right)^2. \tag{B.9}$$

However, this RKKY interaction remains ferromagnetic for all distances R and is, therefore, insufficient to capture the correct spatial dependent RKKY interaction which should oscillate between ferro- and antiferromagnetic interactions as a function of the distance R between the impurities. As pointed out by Affleck and co-workers [64], it is crucial to maintain the energy dependence to gain the alternating ferro- and antiferromagnetic interaction between the impurity spins.

Appendix C

Perturbative approach of spin-spin correlation function $\chi(\vec{r},t)$

In this section, we will show how to calculate the time-dependent correlation function $\chi(\vec{r},t)$ perturbatively up to second-order in J. Therefore, the Hamiltonian is divided into two parts $H = H_0 + H_K$ with $H_0 = \sum_{\sigma,\vec{k}} \epsilon_{\vec{k}}\, c^{\dagger}_{\vec{k}\sigma} c_{\vec{k}\sigma}$, the free conduction band dispersion $\epsilon_{\vec{k}}$ and $H_K = J\vec{S}_{\text{imp}}\vec{s}_c(0)$. The time-dependent spin correlation function $\chi(\vec{r},t) = \langle \vec{S}_{\text{imp}}\vec{s}(\vec{r})\rangle(t)$ can be written as

$$\langle \vec{S}_{\text{imp}}\vec{s}(\vec{r})\rangle(t) = \text{Tr}\left[\rho^I(t)\vec{S}_{\text{imp}}\vec{s}^I(\vec{r},t)\right], \tag{C.1}$$

where the index I means that the operator is transformed into the interaction picture which is defined for any operator A as

$$A^I(t) = \mathrm{e}^{iH_0t} A \mathrm{e}^{-iH_0t}. \tag{C.2}$$

Since the impurity spin commutes with H_0, $\vec{S}_{\text{imp}}$ remains time-independent. The real-time evolution of $\rho^I(t)$ is derived from the von Neumann equation

$$\partial_t \rho^I(t) = i\left[\rho^I(t), H_K^I(t)\right], \tag{C.3}$$

which is integrated to

$$\rho^I(t) = \rho_0 + i\int_0^t \left[\rho_0, H_K^I(t_1)\right]\, dt_1 - \int_0^t \int_0^{t_1} \left[\left[\rho^I(t_2), H_K^I(t_2)\right], H_K^I(t_1)\right]\, dt_2\, dt_1, \tag{C.4}$$

where we used the boundary condition $\rho^I(0) = \rho_0$. Replacing $\rho^I(t_2)$ by ρ_0 in the second integral yields an approximate solution in $O(J^2)$. If we substitute (C.4) into (C.1) and cyclically rotate the operators under the trace, we obtain

$$\begin{aligned}\langle \vec{S}_{\text{imp}}\vec{s}(\vec{r})\rangle(t) \approx &\text{Tr}\left[\rho_0 \vec{S}_{\text{imp}}\vec{s}_I(\vec{r},t)\right] + i\int_0^t \text{Tr}\left[\rho_0\left[H_K^I(t_1), \vec{S}_{\text{imp}}\vec{s}_I(\vec{r},t)\right]\right] dt_1 \\ &- \int_0^t\int_0^{t_1} \text{Tr}\left[\rho_0\left[H_K^I(t_2),\left[H_K^I(t_1), \vec{S}_{\text{imp}}\vec{s}^I(\vec{r},t)\right]\right]\right]\, dt_2\, dt_1. \end{aligned} \tag{C.5}$$

This expression contains only expectation values that involve the initial density operator ρ_0 in which the impurity spin and the conduction electrons factorize since in H_0 the impurity spin is decoupled from the conduction band. In the absence of magnetic fields the first term vanishes, and the initial correlation function is zero at $t = 0$.
The calculation of the first-order and especially the second-order contribution is, however, a cumbersome task. In the following, we will, therefore, only present the final results of the first and second-order integral kernel.
Calculating the commutator of the first order yields

$$\text{Tr}\left[\rho_0\left[H_K^I(t_1), \vec{S}_{\text{imp}}\vec{s}^I(\vec{r},t)\right]\right] = -\frac{3}{4}\frac{J}{V_u N^2}\sum_{\vec{k},\vec{q}} f(\epsilon_{\vec{k}+\vec{q}})\sin\left(\vec{q}\vec{r} + (\epsilon_{\vec{k}+\vec{q}} - \epsilon_{\vec{k}})(t_1 - t)\right). \tag{C.6}$$

For a linear dispersion in 1D, the argument of the sine contains $(\epsilon_{k+q} - \epsilon_k) = v_{\text{F}}q$ contributions. The kernel remains phase coherent on the light cone $q(r - v_{\text{F}}t)$ and, thus, generates the response on this light cone line.
The second-order correction is given by

$$\begin{aligned}&\text{Tr}\left[\rho_0\left[H_K^I(t_2),\left[H_K^I(t_1), \vec{S}_{\text{imp}}\vec{s}^I(\vec{r},t)\right]\right]\right] \\ &= \frac{3}{8}\frac{J^2}{V_u N^3}\sum_{\vec{k},\vec{q}_1,\vec{q}_2} f(\epsilon_{\vec{k}+\vec{q}_1}) f(-\epsilon_{\vec{k}-\vec{q}_2}) \\ &\times\Big\{\cos\left[\vec{q}_1\vec{r} + (\epsilon_{\vec{k}+\vec{q}_1} - \epsilon_{\vec{k}-\vec{q}_2})t_1 \;+(\epsilon_{\vec{k}-\vec{q}_2} - \epsilon_{\vec{k}})t_2 + (\epsilon_{\vec{k}} - \epsilon_{\vec{k}+\vec{q}_1})t\right] \\ &\quad+\cos\left[\vec{q}_2\vec{r} + (\epsilon_{\vec{k}+\vec{q}_1} - \epsilon_{\vec{k}-\vec{q}_2})t_1 \;+(\epsilon_{\vec{k}} - \epsilon_{\vec{k}+\vec{q}_1})t_2 + (\epsilon_{\vec{k}-\vec{q}_2} - \epsilon_{\vec{k}})t\right] \\ &\quad-\cos\left[(\vec{q}_1+\vec{q}_2)\vec{r} - (\epsilon_{\vec{k}+\vec{q}_1} - \epsilon_{\vec{k}-\vec{q}_2})t \;-(\epsilon_{\vec{k}-\vec{q}_2} - \epsilon_{\vec{k}})t_2 - (\epsilon_{\vec{k}} - \epsilon_{\vec{k}+\vec{q}_1})t_1\right] \\ &\quad-\cos\left[(\vec{q}_1+\vec{q}_2)\vec{r} - (\epsilon_{\vec{k}+\vec{q}_1} - \epsilon_{\vec{k}-\vec{q}_2})t \;-(\epsilon_{\vec{k}} - \epsilon_{\vec{k}+\vec{q}_1})t_2 - (\epsilon_{\vec{k}-\vec{q}_2} - \epsilon_{\vec{k}})t_1\right]\Big\}. \end{aligned} \tag{C.7}$$

Due to the simple sine and cosine structure, the time-integration can be done analytically for both the first and second-order contribution. For the momentum integrations over $\vec{k}$, $\vec{q}_1$ and $\vec{q}_2$ we insert a 1D linear dispersion for $\epsilon_{\vec{k}}$. If we expand (C.6) and (C.7) for small times around $t = 0$, the momentum integrations can also be calculated analytically otherwise a numerical integration has to be performed.

Appendix D

Intrinsic spin-spin correlation function of the Fermi sea $\langle \vec{s}(0)\vec{s}(R)\rangle$

In the following, we will briefly derive an analytical expression for the intrinsic host spin-spin correlation function of the decoupled Fermi sea $\langle \vec{s}(0)\vec{s}(\vec{r})\rangle$. If we insert the definition of the host spin density

$$\vec{s}(\vec{r}) = \frac{1}{2V_u N}\sum_{\vec{k},\vec{k}'}\sum_{\sigma,\sigma'}\vec{\sigma}_{\sigma,\sigma'}c^{\dagger}_{\vec{k},\sigma}c_{\vec{k}',\sigma'}e^{i(\vec{k}'-\vec{k})\vec{r}}, \tag{D.1}$$

into $\langle \vec{s}(0)\vec{s}(\vec{r})\rangle$, we obtain for the intrinsic correlation

$$\langle \vec{s}(0)\vec{s}(\vec{r})\rangle = \frac{1}{4N^2V_u^2}\sum_{\substack{\vec{k}_1\vec{k}_1'\\ \sigma_1\sigma_1'}}\sum_{\substack{\vec{k}_2\vec{k}_2'\\ \sigma_2\sigma_2'}}\vec{\sigma}_{\sigma_1,\sigma_1'}\vec{\sigma}_{\sigma_2,\sigma_2'}\langle c^{\dagger}_{k_1,\sigma_1}c_{k_1',\sigma_1'}c^{\dagger}_{k_2,\sigma_2}c_{k_2',\sigma_2'}\rangle e^{i(\vec{k}_2'-\vec{k}_2)\vec{r}}. \tag{D.2}$$

Since we consider only the decoupled $J = 0$ case, the Hamiltonian describing this system is given by the bilinear Hamiltonian of a free electron gas $H_0 = \sum_{\vec{k},\sigma}\epsilon_{\vec{k}}c^{\dagger}_{\vec{k},\sigma}c_{\vec{k},\sigma}$. Therefore, we can apply Wick's theorem to simplify the expectation value of Eq. (D.2)

$$\begin{aligned}\langle c^{\dagger}_{k_1,\sigma_1}c_{k_1',\sigma_1'}c^{\dagger}_{k_2,\sigma_2}c_{k_2',\sigma_2'}\rangle =& \langle c^{\dagger}_{k_1,\sigma_1}c_{k_1',\sigma_1'}\rangle\langle c^{\dagger}_{k_2,\sigma_2}c_{k_2',\sigma_2'}\rangle \\ &- \langle c^{\dagger}_{k_1,\sigma_1}c^{\dagger}_{k_2,\sigma_2}\rangle\langle c_{k_1',\sigma_1'}c_{k_2',\sigma_2'}\rangle + \langle c^{\dagger}_{k_1,\sigma_1}c_{k_2',\sigma_2'}\rangle\langle c_{k_1',\sigma_1'}c^{\dagger}_{k_2,\sigma_2}\rangle \qquad \text{(D.3)}\\ =& f(\epsilon_{\vec{k}_1})\delta_{\vec{k}_1,\vec{k}_1'}\delta_{\sigma_1,\sigma_1'}f(\epsilon_{\vec{k}_2})\delta_{\vec{k}_2,\vec{k}_2'}\delta_{\sigma_2,\sigma_2'} \\ &+ f(\epsilon_{\vec{k}_1})\delta_{\vec{k}_1,\vec{k}_2'}\delta_{\sigma_1,\sigma_2'}f(-\epsilon_{\vec{k}_2})\delta_{\vec{k}_1',\vec{k}_2}\delta_{\sigma_1',\sigma_2}. \qquad \text{(D.4)}\end{aligned}$$

Equation (D.4) has two contributions to the intrinsic correlation function. While executing the spin summation over the first term yields

$$\sum_{\sigma_1,\sigma_1'}\sum_{\sigma_2,\sigma_2'} = \delta_{\sigma_1,\sigma_1'}\delta_{\sigma_2,\sigma_2'}\vec{\sigma}_{\sigma_1,\sigma_1'}\vec{\sigma}_{\sigma_2,\sigma_2'} = \sum_{\sigma_1,\sigma_2}\vec{\sigma}_{\sigma_1,\sigma_1}\vec{\sigma}_{\sigma_2,\sigma_2} = 0 \tag{D.5}$$

the summation over the spin in the second line of (D.4) results in

$$\sum_{\sigma_1,\sigma_1'}\sum_{\sigma_2,\sigma_2'} = \delta_{\sigma_1,\sigma_2'}\delta_{\sigma_1',\sigma_2}\vec{\sigma}_{\sigma_1,\sigma_1'}\vec{\sigma}_{\sigma_2,\sigma_2'} = \sum_{\sigma_1,\sigma_1'}\vec{\sigma}_{\sigma_1,\sigma_1'}\vec{\sigma}_{\sigma_1',\sigma_1} = \mathrm{Tr}\left[\sigma_x^2+\sigma_y^2+\sigma_z^2\right] = 6. \tag{D.6}$$

Thus, only the second term of the expectation value contributes to the intrinsic spin-spin correlation function. Inserting the results of Eqs. (D.4)-(D.6) into Eq. (D.2) yields

$$\begin{aligned}\langle \vec{s}(0)\vec{s}(\vec{r})\rangle =& \frac{3}{2N^2V_u^2}\sum_{\vec{k}_1\vec{k}_1'}\sum_{\vec{k}_2\vec{k}_2'}\delta_{\vec{k}_1,\vec{k}_2'}\delta_{\vec{k}_1',\vec{k}_2}f(\epsilon_{\vec{k}_1})f(-\epsilon_{\vec{k}_2})e^{i(\vec{k}_2'-\vec{k}_2)\vec{r}}\\ =& \frac{3}{2V_u^2}\left[\frac{1}{N}\sum_{\vec{k}_1}f(\epsilon_{\vec{k}_1})e^{i\vec{k}_1\vec{r}}\right]\left[\frac{1}{N}\sum_{\vec{k}_2}f(-\epsilon_{\vec{k}_2})e^{-i\vec{k}_2\vec{r}}\right].\end{aligned} \tag{D.7}$$

The two summations over the momenta factorize and can be carried out independently of each other. If we use a particle-hole symmetric 1D linear dispersion $\epsilon_k = v_\mathrm{F}(|k|-k_\mathrm{F})$ and transform the discrete summation over k into a continuous integral $\frac{1}{N}\sum_k \to \frac{V_u}{2\pi}\int dk$, we obtain at $T=0$ for both momenta summations

$$\frac{1}{N}\sum_k f(\epsilon_k)e^{ikr} = \frac{V_u}{2\pi}\int_{-k_\mathrm{F}}^{k_\mathrm{F}} e^{ikr}\,dk = \frac{V_u}{\pi r}\sin(k_\mathrm{F}r) \tag{D.8}$$

and

$$\begin{aligned}\frac{1}{N}\sum_{\vec{k}_2}f(-\epsilon_{\vec{k}_2})e^{-i\vec{k}_2\vec{r}} =& \frac{V_u}{2\pi}\int_{-2k_\mathrm{F}}^{-k_\mathrm{F}} e^{-ikr}\,dk + \frac{V_u}{2\pi}\int_{k_\mathrm{F}}^{2k_\mathrm{F}} e^{-ikr}\,dk\\ =& \frac{V_u}{\pi r}\left[\sin(2k_\mathrm{F}r)-\sin(k_\mathrm{F}r)\right].\end{aligned} \tag{D.9}$$

Inserting these terms into Eq. (D.7) results in

$$\langle \vec{s}(0)\vec{s}(r)\rangle = \frac{3}{8V_u^2}\frac{1}{(k_\mathrm{F}r)^2}\sin(k_\mathrm{F}r)\left[\sin(2k_\mathrm{F}r)-\sin(k_\mathrm{F}r)\right], \tag{D.10}$$

where we have used that the Fermi wave vector for a 1D linear dispersion is given by $k_\mathrm{F} = \frac{\pi}{2V_u}$. With the addition theorem $\sin(2k_\mathrm{F}r)-\sin(k_\mathrm{F}r) = 2\cos(\frac{3}{2}k_\mathrm{F}r)\sin(\frac{1}{2}k_\mathrm{F}r)$ the expression for $\langle \vec{s}(0)\vec{s}(r)\rangle$ can be further simplified and we finally obtain

$$\langle \vec{s}(0)\vec{s}(r)\rangle = \frac{3}{4V_u^2}\frac{1}{(k_\mathrm{F}r)^2}\sin(k_\mathrm{F}r)\cos(\frac{3}{2}k_\mathrm{F}r)\sin(\frac{1}{2}k_\mathrm{F}r). \tag{D.11}$$

This analytical known expression for $\langle \vec{s}(0)\vec{s}(r)\rangle$ provides an excellent tool to check the accuracy of our NRG mapping to the even and odd parity states and, indeed, we find a perfect agreement between the analytical calculated $\langle \vec{s}(0)\vec{s}(r)\rangle$ and the one calculated with the NRG, cf. Fig. 4.12a.

Appendix E

Retarded host spin-spin susceptibility $\chi^r_{c-c}(R,t)$

In this appendix, we will derive the analytical spectral function $\rho^r_{c-c}(R,\omega)$ of the retarded host spin-spin correlation function

$$\chi^r_{c-c}(R,t) = -i\langle\left[s^z(R,t), s^z(0,0)\right]\rangle\theta(t). \tag{E.1}$$

The time-dependent spin density operator in the Heisenberg picture is given by

$$s^z(R,t) = \frac{1}{2V_u N}\sum_{k_1,k_2}\sum_{\alpha,\beta}\sigma^z_{\alpha,\beta}c^\dagger_{k_1,\alpha}c_{k_2,\beta}e^{-i(k_1-k_2)R}e^{i(\epsilon_{k_1}-\epsilon_{k_2})t}. \tag{E.2}$$

The insertion of $s^z(R,t)$ into Eq. (E.1) yields

$$\chi^r_{c-c}(R,t) = \frac{-i\theta(t)}{4V_u^2N^2}\sum_{\substack{k_1,k_2\\k_3,k_4}}\sum_{\substack{\alpha,\beta\\\alpha',\beta'}}\sigma^z_{\alpha,\beta}\sigma^z_{\alpha',\beta'}e^{-i(k_3-k_4)R}e^{i(\epsilon_{k_3}-\epsilon_{k_4})t}\langle[c^\dagger_{k_3,\alpha'}c_{k_4,\beta'}, c^\dagger_{k_1,\alpha}c_{k_2,\beta}]\rangle. \tag{E.3}$$

Using Wick's theorem or the rule for commutators

$$[AB,CD] = A\{B,C\}D - AC\{B,D\} - C\{A,D\}B + \{A,C\}DB, \tag{E.4}$$

we can simplify the expecation value to

$$\langle[c^\dagger_{k_3,\alpha'}c_{k_4,\beta'}, c^\dagger_{k_1,\alpha}c_{k_2,\beta}]\rangle = \delta_{\alpha,\beta'}\delta_{\beta,\alpha'}\delta_{k_1,k_4}\delta_{k_2,k_3}\left[f(\epsilon_{k_2}) - f(\epsilon_{k_1})\right], \tag{E.5}$$

where we have used $\{c_{k_1,\alpha}, c^\dagger_{k_2,\beta}\} = \delta_{\alpha,\beta}\delta_{k_1,k_2}$ and $\langle c^\dagger_{k_1,\alpha}c_{k_2,\beta}\rangle = \delta_{\alpha,\beta}\delta_{k_1,k_2}f(\epsilon_{k_1})$. After carrying out the spin and k_3, k_4 summations, the retarded susceptibility is given by

$$\chi^r_{c-c}(R,t) = \frac{-i\theta(t)}{2V_u^2N^2}\sum_{k_1,k_2}e^{-i(k_2-k_1)R}e^{i(\epsilon_{k_2}-\epsilon_{k_1})t}\left[f(\epsilon_{k_2}) - f(\epsilon_{k_1})\right]. \tag{E.6}$$

By a Fourier transformation the analytical expression

$$\chi^r_{c-c}(R,z) = \frac{-i}{2V_u^2N^2}\sum_{k_1,k_2}\int_0^\infty e^{izt}e^{-i(k_2-k_1)R}e^{i(\epsilon_{k_2}-\epsilon_{k_1})t}\left[f(\epsilon_{k_2})-f(\epsilon_{k_1})\right]\,dt \tag{E.7}$$

$$= \frac{1}{2V_u^2N^2}\sum_{k_1,k_2}\frac{\left[f(\epsilon_{k_2})-f(\epsilon_{k_1})\right]e^{-i(k_2-k_1)R}}{z-(\epsilon_{k_1}-\epsilon_{k_2})} \tag{E.8}$$

is gained, where the θ-function entered in the lower bound of the integral and a slight imaginary frequency $\mathrm{Im}\, z > 0$ was used to guarantee the convergence of the intergral. Due to the complex phase factor $\exp[-i(k_2-k_1)R]$, the spectral function $\rho^r_{c-c}(R,\omega)$ defined as

$$\rho^r_{c-c}(R,\omega) = -\frac{1}{\pi}\lim_{\delta\to 0}\mathrm{Im}[\chi^r_{c-c}(R,\omega+i\delta)], \tag{E.9}$$

has two contributions. The first contribution originates from the delta function stemming from the $\lim_{\delta\to0}\mathrm{Im}\frac{1}{\omega+i\delta-\epsilon} = -\pi\delta(\omega-\epsilon)$ term and the second originates from $\mathrm{Im}\exp[-i(k_2-k_1)R] = -\sin[(k_2-k_1)R]$. For the spectral function we finally obtain

$$\rho^r_{c-c}(R,\omega) = \frac{1}{2\pi V_u^2N^2}\sum_{k_1,k_2}\left[f(\epsilon_{k_2})-f(\epsilon_{k_1})\right] \times\left[\pi\cos[(k_2-k_1)R]\delta(\omega-(\epsilon_{k_1}-\epsilon_{k_2}))+\frac{\sin[(k_2-k_1)R]}{\omega-(\epsilon_{k_1}-\epsilon_{k_2})}\right]. \tag{E.10}$$

If we measure the momenta in units of k_F, it becomes clear that Eq. (E.10) contains the dimensionless frequency $k_\mathrm{F}R$, which is directly related to the increasing oscillations with increasing distance R.

Appendix F

The long-time value of the spin polarization $\langle s^z(R,t)\rangle$

In the following, we will briefly show how to calculate the long-time limit of the spin polarization $\langle s^z(R,t)\rangle$. In linear response theory the polarization is given by

$$\langle s^z(R,t)\rangle = \langle s^z(R,t=-\infty)\rangle + \int_{-\infty}^{\infty} \chi^r(R,t-t')\Delta(t')\,dt' \tag{F.1}$$

where $\langle s^z(R,t=-\infty)\rangle$ vanishes if no magnetic field is applied. For a Zeeman splitting $\Delta(t) = \Delta_0\theta(t) = g\mu_B B\theta(t)$ and no magnetic field, Eq. (F.1) can be written as

$$\langle s^z(R,t)\rangle = \Delta_0 \int_0^{\infty} \chi^r(R,t-t')\,dt'. \tag{F.2}$$

For simplicity we set $\Delta_0 = 1$ in the following because $\langle s^z(R,t)\rangle$ is trivially proportional to the applied field.
The long-time value of the spin polarization $\langle s^z(R,t\to\infty)\rangle = \overline{\langle s^z(R)\rangle}$ is obtained from

$$\overline{\langle s^z(R)\rangle} = \lim_{T\to\infty} \frac{1}{T}\int_0^T dt \int_0^{\infty} dt'\ \chi^r(R,t-t'). \tag{F.3}$$

Since the spectral function of this susceptibility defined as

$$\rho^r(\omega) = \lim_{\delta\to 0^+} -\frac{1}{\pi}\mathrm{Im}\chi^r(R,\omega+i\delta) \tag{F.4}$$

has to be an odd function $\rho^r(\omega) = -\rho^r(-\omega)$ [127], we can write $\chi^r(R,t)$ as a purely real integral

$$\chi^r(R,t) = -2\int_0^{\infty} \rho^r(R,\omega)\sin(\omega t)\theta(t)\,d\omega. \tag{F.5}$$

Inserting this expression for the susceptibility into Eq. (F.3) yields

$$\overline{\langle s^z(R)\rangle} = -2\int_0^\infty d\omega \rho^r(R,\omega)\lim_{T\to\infty}\frac{1}{T}\int_0^T dt\int_0^t dt' \sin(\omega(t-t')), \tag{F.6}$$

where we have made explicit use of the θ-function of Eq. (F.5). Since the spectral function is independent of the time, the time-integrations can easily be performed analytically which results in

$$\overline{\langle s^z(R)\rangle} = 2\int_0^\infty d\omega \left[-\frac{1}{\omega}\rho^r(R,\omega) + \lim_{T\to\infty}\rho^r(R,\omega)\frac{\sin(\omega T)}{\omega^2 T}\right]. \tag{F.7}$$

Using a representation for the delta distribution

$$\lim_{T\to\infty}\frac{\sin(\omega T)}{\pi\omega} = \delta(\omega) \tag{F.8}$$

we obtain for the second part of Eq. (F.7) in the long-time limit $T\to\infty$

$$\int_{-\infty}^\infty d\omega\, \rho^r(R,\omega)\frac{\sin(\omega T)}{\omega^2 T} \approx \int_{-\infty}^\infty d\omega\, \frac{\rho^r(R,\omega)}{\omega T}\delta(\omega). \tag{F.9}$$

Since at $\omega = 0$ the spectral function vanishes $\rho^r(R,\omega=0)=0$, the second contribution of Eq. (F.7) must also vanish for times $T\to\infty$. Finally the long-time value of the spin polarization is given by

$$\overline{\langle s^z(R)\rangle} = -2\int_0^\infty d\omega\, \frac{\rho^r(R,\omega)}{\omega}. \tag{F.10}$$

As described in appendix E, the retarded host spin-spin susceptibility $\chi^r_{c-c}(R,t)$ can be calculated analytically and is, therefore, suitable as a benchmark for Eq. (F.10). If we substitute $\chi^r_{c-c}(R,t-t')$ for $\chi^r(R,t-t')$ in Eq. (F.1) and perform the convolution for large times $t\to\infty$, we find a perfect agreement between $\langle s^z(R,t\to\infty)\rangle$ calculated with Eq. (F.1) and the long-time value $\overline{\langle s^z(R)\rangle}$ computed with Eq. (F.10).

Appendix G

Derivation of NRG parameters from a mean field spectrum

In this appendix we show how the energy level ϵ_0 and the hybridization strength $\Gamma(E)$ can be extracted from the DFT mean field spectrum and Coulomb repulsion U of a single impurity Anderson model (SIAM).
The Hamiltonian of the SIAM is given by

$$H = \sum_{\vec{k},\sigma} \epsilon_{\vec{k}} c^\dagger_{\vec{k},\sigma} c_{\vec{k},\sigma} + \sum_{\vec{k},\sigma} [V_{\vec{k}} c^\dagger_{\vec{k},\sigma} d_\sigma + V^*_{\vec{k}} d^\dagger_\sigma c_{\vec{k},\sigma}] + \epsilon_0 n_d + U n_{d,\uparrow} n_{d,\downarrow}, \tag{G.1}$$

with $n_d = n_{d,\uparrow} + n_{d,\downarrow}$ and $n_{d,\sigma} = d^\dagger_\sigma d_\sigma$. Here, $\epsilon_{\vec{k}}$ is the dispersion of the conduction band, $c^\dagger_{\vec{k},\sigma}$ the creation operator of a conduction band electron and $d^\dagger$ creates an electron on the impurity. In a mean field approximation the last term $U n_{d,\uparrow} n_{d,\downarrow}$ simplifies to

$$U n_{d,\uparrow} n_{d,\downarrow} \to U n_{d,\uparrow} \langle n_{d,\downarrow} \rangle + U \langle n_{d,\uparrow} \rangle n_{d,\downarrow} - U \langle n_{d,\uparrow} \rangle \langle n_{d,\downarrow} \rangle. \tag{G.2}$$

Therefore, we obtain a shift of the energy level according to

$$\epsilon_0 \to \epsilon_{\mathrm{MF},\sigma} = \epsilon_0 + U \langle n_{d,-\sigma} \rangle. \tag{G.3}$$

With the equation of motion technique (c.f. Sec. 3.3.3) it is straight forward to derive the Green's function of the impurity in mean field approximation

$$G_d(z) = \frac{1}{z - \epsilon_{\mathrm{MF},\sigma} - \Delta(z)} = \frac{1}{z - \epsilon_0 - U \langle n_{d,-\sigma} \rangle - \Delta(z)}. \tag{G.4}$$

Here, $\Delta(z) = \int d\omega \frac{1}{\pi} \frac{\Gamma(\omega)}{z-\omega}$ denotes the complex coupling function where the hybridization strength is given by $\Gamma(\omega) = \pi \rho(\omega) V^2(\omega)$, with $\rho(\omega)$ being the DOS of the conduction band.
For a NRG calculation the parameters ϵ_0, U and $\Gamma(E)$ are required. The Coulomb interaction U is received directly from the density functional theory (DFT) calculations via Eq. (5.3) while the energy level ϵ_0 and the hybridization strength $\Gamma(E)$ have to be

extracted from the DFT spectrum $\rho_{\mathrm{DFT}}(E)$ and the Coulomb interaction U.
The Green's function in mean field approximation is calculated from the mean field DFT spectrum $\rho_{\mathrm{DFT}}(E)$ via a Hilbert transformation

$$G_d(z) = \frac{1}{\pi} \int d\epsilon \frac{\rho_{\mathrm{DFT}}(\epsilon)}{z - \epsilon}. \tag{G.5}$$

The level energy ϵ_0 is computed according to

$$\epsilon_0 = \epsilon_{\mathrm{MF},\sigma} - U\langle n_{d,-\sigma}\rangle = \int_{-D}^{D} \rho_{\mathrm{DFT}}(\omega)\omega \, d\omega - U\langle n_{d,-\sigma}\rangle, \tag{G.6}$$

where the occupation number is given by $\langle n_{d,-\sigma}\rangle = \int_{-D}^{0} \rho_{\mathrm{DFT}}(\omega) \, d\omega$. The hybridization function $\Gamma(E)$ is finally obtained from the imaginary part of the coupling function $\Delta(z)$

$$\Gamma(E) = -\lim_{\delta \to 0} \mathrm{Im}[\Delta(E + i\delta)], \tag{G.7}$$

where the complex coupling function can be calculated from the mean field energy level $\epsilon_{\mathrm{MF},\sigma}$ and Green's function $G_d(z)$ using Eqs. (G.4) and (G.5)

$$\Delta(z) = z - \epsilon_{\mathrm{MF},\sigma} - G_d^{-1}(z). \tag{G.8}$$

Bibliography

[1] Parr, R.G.: *Density-Functional Theory of Atoms and Molecules*. Oxford University Press, USA, 1989 (International Series of Monographs on Chemistry). – ISBN 9780195357738

[2] Gross, E.K.U. ; Dreizler, R.M.: *Density Functional Theory*. Springer US, 2013 (Nato Science Series B:). – ISBN 9781475799750

[3] Hohenberg, P. ; Kohn, W.: Inhomogeneous Electron Gas. In: *Phys. Rev.* 136 (1964), p. B864–B871. doi: 10.1103/PhysRev.136.B864

[4] Kohn, W. ; Sham, L. J.: Self-Consistent Equations Including Exchange and Correlation Effects. In: *Phys. Rev.* 140 (1965), p. A1133–A1138. doi: 10.1103/PhysRev.140.A1133

[5] Kohn, W.: *Nobel Lectures in Chemistry 1996-2000*. Chap. Electronic Structure of Matter - Wave Functions and Density Functionals. Singapore : World Scientific Publishing Co, 2003, http://www.nobelprize.org/nobel_prizes/chemistry/laureates/1998/kohn-lecture.html

[6] Stewart, G. R.: Heavy-fermion systems. In: *Rev. Mod. Phys.* 56 (1984), p. 755–787. doi: 10.1103/RevModPhys.56.755

[7] Cyrot, M. ; Pavuna, D.: *Introduction to Superconductivity and High-Tc Materials*. World Scientific, 1992. – ISBN 9789810201449

[8] Bose: Plancks Gesetz und Lichtquantenhypothese. In: *Zeitschrift fur Physik* 26 (1924), p. 178–181. doi: 10.1007/BF01327326

[9] Einstein, Albert: Quantentheorie des einatomigen idealen Gases – Zweite Abhandlung. In: *Sitzungsberichte der preussischen Akademie der Wissenschaften* Volume 1, 1925, p. 3–10. – http://www.lorentz.leidenuniv.nl/history/Einstein_archive/Einstein_1925_publication/index.html

[10] MOTT, N. F.: Metal-Insulator Transition. In: *Rev. Mod. Phys.* 40 (1968), p. 677–683. doi: 10.1103/RevModPhys.40.677

[11] Hellberg, C. S. ; Erwin, Steven C.: Strongly Correlated Electrons on a Silicon Surface: Theory of a Mott Insulator. In: *Phys. Rev. Lett.* 83 (1999), p. 1003–1006. doi: 10.1103/PhysRevLett.83.1003

[12] Greiner, Markus ; Mandel, Olaf ; Esslinger, Tilman ; Hansch, Theodor W. ; Bloch, Immanuel: Quantum phase transition from a superfluid to a Mott insulator in a gas of ultracold atoms. In: *Nature* 415 (2002), No. 6867, p. 39–44. doi: 10.1038/415039a. – ISSN 0028-0836

[13] Gebhard, F.: *The Mott Metal-Insulator Transition: Models and Methods*. Springer Berlin Heidelberg, 2003 (Springer Tracts in Modern Physics). – ISBN 9783540148586

[14] Liechtenstein, A. I. ; Anisimov, V. I. ; Zaanen, J.: Density-functional theory and strong interactions: Orbital ordering in Mott-Hubbard insulators. In: *Phys. Rev. B* 52 (1995), p. R5467–R5470. doi: 10.1103/PhysRevB.52.R5467

[15] Hewson, A. C.: *The Kondo Problem to Heavy Fermions*. Cambridge : Cambridge University Press, 1993

[16] de Haas, W. J. ; de Boer, J. ; van dën Berg, G. J.: The electrical resistance of gold, copper and lead at low temperatures. In: *Physica* 1 (1934), p. 1115–1124. doi: 10.1016/S0031-8914(34)80310-2

[17] Kondo, J.: Resistance Minimum in Dilute Magnetic Alloys. In: *Progress of Theoretical Physics* 32 (1964), No. 1, p. 37–49. doi: 10.1143/PTP.32.37

[18] Goldhaber-Gordon, D. ; Shtrikman, Hadas ; Mahalu, D. ; Abusch-Magder, David ; Meirav, U. ; Kastner, M. A.: Kondo effect in a single-electron transistor. In: *Nature* 391 (1998), No. 6663, p. 156–159. doi: 10.1038/34373. – ISSN 0028-0836

[19] Cronenwett, Sara M. ; Oosterkamp, Tjerk H. ; Kouwenhoven, Leo P.: A Tunable Kondo Effect in Quantum Dots. In: *Science* 281 (1998), No. 5376, p. 540–544. doi: 10.1126/science.281.5376.540

[20] Wiel, W. G. van der ; Franceschi, S. D. ; Fujisawa, T. ; Elzerman, J. M. ; Tarucha, S. ; Kouwenhoven, L. P.: The Kondo Effect in the Unitary Limit. In: *Science* 289 (2000), No. 5487, p. 2105–2108. doi: 10.1126/science.289.5487.2105

[21] Park, Hongkun ; Park, Jiwoong ; Lim, Andrew K. L. ; Anderson, Erik H. ; Alivisatos, A. P. ; McEuen, Paul L.: Nanomechanical oscillations in a single-C60 transistor. In: *Nature* 407 (2000), No. 6800, p. 57–60. doi: 10.1038/35024031. – ISSN 0028-0836

[22] Yu, Lam H. ; Natelson, Douglas: Transport in single-molecule transistors: Kondo physics and negative differential resistance. In: *Nanotechnology* 15 (2004), No. 10, p. S517. http://stacks.iop.org/0957-4484/15/i=10/a=004

[23] Yu, L. H. ; Keane, Z. K. ; Ciszek, J. W. ; Cheng, L. ; Tour, J. M. ; Baruah, T. ; Pederson, M. R. ; Natelson, D.: Kondo Resonances and Anomalous Gate Dependence in the Electrical Conductivity of Single-Molecule Transistors. In: *Phys. Rev. Lett.* 95 (2005), p. 256803. doi: 10.1103/PhysRevLett.95.256803

[24] Reed, M. A. ; Randall, J. N. ; Aggarwal, R. J. ; Matyi, R. J. ; Moore, T. M. ; Wetsel, A. E.: Observation of discrete electronic states in a zero-dimensional semiconductor nanostructure. In: *Phys. Rev. Lett.* 60 (1988), p. 535–537. doi: 10.1103/PhysRevLett.60.535

[25] Anderson, P. W.: Localized Magnetic States in Metals. In: *Phys. Rev.* 124 (1961), p. 41–53. doi: 10.1103/PhysRev.124.41

[26] Krishna-murthy, H. R. ; Wilkins, J. W. ; Wilson, K. G.: Renormalization-group approach to the Anderson model of dilute magnetic alloys. I. Static properties for the symmetric case. In: *Phys. Rev. B* 21 (1980), p. 1003–1043. doi: 10.1103/PhysRevB.21.1003

[27] Krishna-murthy, H. R. ; Wilkins, J. W. ; Wilson, K. G.: Renormalization-group approach to the Anderson model of dilute magnetic alloys. II. Static properties for the asymmetric case. In: *Phys. Rev. B* 21 (1980), p. 1044–1083. doi: 10.1103/PhysRevB.21.1044

[28] DiVincenzo, David P.: The Physical Implementation of Quantum Computation. In: *Fortschritte der Physik* 48 (2000), No. 9-11, p. 771–783. doi: 10.1002/1521-3978(200009)48:9/11<771::AID-PROP771>3.0.CO;2-E. – ISSN 1521-3978

[29] Hanson, R. ; Kouwenhoven, L. P. ; Petta, J. R. ; Tarucha, S. ; Vandersypen, L. M. K.: Spins in few-electron quantum dots. In: *Rev. Mod. Phys.* 79 (2007), p. 1217–1265. doi: 10.1103/RevModPhys.79.1217

[30] Stolze, J. ; Suter, D.: *Quantum Computing: A Short Course from Theory to Experiment*. Wiley, 2008. – ISBN 9783527617777

[31] Ladd, T. D. ; Jelezko, F. ; Laflamme, R. ; Nakamura, Y. ; Monroe, C. ; O'Brien, J. L.: Quantum computers. In: *Nature* 464 (2010), No. 7285, p. 45–53. http://dx.doi.org/10.1038/nature08812. – ISSN 0028-0836

[32] Deutsch, David ; Jozsa, Richard: Rapid Solution of Problems by Quantum Computation. In: *Proceedings of the Royal Society of London A: Mathematical, Physical and Engineering Sciences* 439 (1992), No. 1907, p. 553–558. doi: 10.1098/rspa.1992.0167. – ISSN 0962-8444

[33] Coppersmith, D.: *An Approximate Fourier Transform Useful in Quantum Factoring*. IBM Research Report No. RC19642, 1994

[34] Shor, P.W.: Algorithms for quantum computation: discrete logarithms and factoring. In: *Foundations of Computer Science, 1994 Proceedings., 35th Annual Symposium on*, Nov 1994, p. 124–134

[35] Shor, Peter W.: Polynomial-Time Algorithms for Prime Factorization and Discrete Logarithms on a Quantum Computer. In: *SIAM Review* 41 (1999), No. 2, p. 303–332. doi: 10.1137/S0036144598347011

[36] Hackmann, Johannes ; Anders, Frithjof B.: Spin noise in the anisotropic central spin model. In: *Phys. Rev. B* 89 (2014), p. 045317. doi: 10.1103/PhysRevB.89.045317

[37] Uhrig, Götz S. ; Hackmann, Johannes ; Stanek, Daniel ; Stolze, Joachim ; Anders, Frithjof B.: Conservation laws protect dynamic spin correlations from decay: Limited role of integrability in the central spin model. In: *Phys. Rev. B* 90 (2014), p. 060301. doi: 10.1103/PhysRevB.90.060301

[38] Hackmann, J. ; Glasenapp, Ph. ; Greilich, A. ; Bayer, M. ; Anders, F. B.: Influence of the Nuclear Electric Quadrupolar Interaction on the Coherence Time of Hole and Electron Spins Confined in Semiconductor Quantum Dots. In: *Phys. Rev. Lett.* 115 (2015), p. 207401. doi: 10.1103/PhysRevLett.115.207401

[39] Dietl, T. ; Awschalom, D.D. ; Kaminska, M. ; Ohno, H.: *Spintronics*. Elsevier Science, 2009 (Semiconductors and Semimetals). – ISBN 9780080914213

[40] Bogani, Lapo ; Wernsdorfer, Wolfgang: Molecular spintronics using single-molecule magnets. In: *Nat Mater* 7 (2008), No. 3, p. 179–186. http://dx.doi.org/10.1038/nmat2133. – ISSN 1476-1122

[41] Zabel, H. ; Farle, M.: *Magnetic Nanostructures: Spin Dynamics and Spin Transport*. Springer Berlin Heidelberg, 2012 (Springer Tracts in Modern Physics). – ISBN 9783642320422

[42] Wolf, S. A. ; Awschalom, D. D. ; Buhrman, R. A. ; Daughton, J. M. ; Molnár, S. von ; Roukes, M. L. ; Chtchelkanova, A. Y. ; Treger, D. M.: Spintronics: A Spin-Based Electronics Vision for the Future. In: *Science* 294 (2001), No. 5546, p. 1488–1495. doi: 10.1126/science.1065389

[43] Baibich, M. N. ; Broto, J. M. ; Fert, A. ; Van Dau, F. N. ; Petroff, F. ; Etienne, P. ; Creuzet, G. ; Friederich, A. ; Chazelas, J.: Giant Magnetoresistance of (001)Fe/(001)Cr Magnetic Superlattices. In: *Phys. Rev. Lett.* 61 (1988), p. 2472–2475. doi: 10.1103/PhysRevLett.61.2472

[44] Binasch, G. ; Grünberg, P. ; Saurenbach, F. ; Zinn, W.: Enhanced magnetoresistance in layered magnetic structures with antiferromagnetic interlayer exchange. In: *Phys. Rev. B* 39 (1989), p. 4828–4830. doi: 10.1103/PhysRevB.39.4828

[45] Butler, W. H. ; Zhang, X.-G. ; Schulthess, T. C. ; MacLaren, J. M.: Spin-dependent tunneling conductance of Fe|MgO|Fe sandwiches. In: *Phys. Rev. B* 63 (2001), p. 054416. doi: 10.1103/PhysRevB.63.054416

[46] Mathon, J. ; Umerski, A.: Theory of tunneling magnetoresistance of an epitaxial Fe/MgO/Fe(001) junction. In: *Phys. Rev. B* 63 (2001), p. 220403. doi: 10.1103/PhysRevB.63.220403

[47] Borda, László: Kondo screening cloud in a one-dimensional wire: Numerical renormalization group study. In: *Phys. Rev. B* 75 (2007), p. 041307. doi: 10.1103/PhysRevB.75.041307

[48] Sachdev, S.: *Quantum Phase Transitions*. Cambridge University Press, 2001. – ISBN 9780521004541

[49] Vojta, Matthias: Quantum phase transitions. In: *Reports on Progress in Physics* 66 (2003), No. 12, p. 2069. http://stacks.iop.org/0034-4885/66/i=12/a=R01

[50] Vojta, M.: Impurity quantum phase transitions. In: *Philosophical Magazine* 86 (2006), p. 1807–1846. doi: 10.1080/14786430500070396

[51] Anderson, P. W. ; Yuval, G. ; Hamann, D. R.: Exact Results in the Kondo Problem. II. Scaling Theory, Qualitatively Correct Solution, and Some New Results on One-Dimensional Classical Statistical Models. In: *Phys. Rev. B* 1 (1970), p. 4464–4473. doi: 10.1103/PhysRevB.1.4464

[52] Ashcroft, N.W. ; Mermin, N.D.: *Solid state physics*. Saunders College, 1976 (Science: Physics). – ISBN 9780030493461

[53] Wilson, K. G.: The renormalization group: Critical phenomena and the Kondo problem. In: *Rev. Mod. Phys.* 47 (1975), p. 773–840. doi: 10.1103/RevModPhys.47.773

[54] Wilson, K. G.: *Nobel Lectures in Physics 1981-1990*. Chap. The Renormalization Group and Critical Phenomena. Singapore : World Scientific Publishing Co, 1993, http://www.nobelprize.org/nobel_prizes/physics/laureates/1982/wilson-lecture.html

[55] Andrei, N.: Diagonalization of the Kondo Hamiltonian. In: *Phys. Rev. Lett.* 45 (1980), No. 5, p. 379–382. doi: 10.1103/PhysRevLett.45.379

[56] P.B., Vigman: Exact solution of s-d exchange model at T = 0. In: *JETP Lett.* 31 (1980), No. 7, p. 364–370. http://www.jetpletters.ac.ru/ps/1353/article_20434.shtml

[57] Bethe, H.: Zur Theorie der Metalle. In: *Zeitschrift für Physik* 71, No. 3, p. 205–226. doi: 10.1007/BF01341708. – ISSN 0044-3328

[58] Ruderman, M. A. ; Kittel, C.: Indirect Exchange Coupling of Nuclear Magnetic Moments by Conduction Electrons. In: *Phys. Rev.* 96 (1954), p. 99–102. doi: 10.1103/PhysRev.96.99

[59] Kasuya, T.: A Theory of Metallic Ferro- and Antiferromagnetism on Zener's Model. In: *Progress of Theoretical Physics* 16 (1956), p. 45–57. doi: 10.1143/PTP.16.45

[60] Yosida, Kei: Magnetic Properties of Cu-Mn Alloys. In: *Phys. Rev.* 106 (1957), p. 893–898. doi: 10.1103/PhysRev.106.893

[61] Jones, B. A. ; Varma, C. M.: Study of two magnetic impurities in a Fermi gas. In: *Phys. Rev. Lett.* 58 (1987), p. 843–846. doi: 10.1103/PhysRevLett.58.843

[62] Jones, B. A. ; Varma, C. M. ; Wilkins, J. W.: Low-Temperature Properties of the Two-Impurity Kondo Hamiltonian. In: *Phys. Rev. Lett.* 61 (1988), p. 125–128. doi: 10.1103/PhysRevLett.61.125

[63] Jones, B. A. ; Varma, C. M.: Critical point in the solution of the two magnetic impurity problem. In: *Phys. Rev. B* 40 (1989), p. 324–329. doi: 10.1103/PhysRevB.40.324

[64] Affleck, Ian ; Ludwig, Andreas W. W. ; Jones, Barbara A.: Conformal-field-theory approach to the two-impurity Kondo problem: Comparison with numerical renormalization-group results. In: *Phys. Rev. B* 52 (1995), p. 9528–9546. doi: 10.1103/PhysRevB.52.9528

[65] Gan, Junwu: Solution of the two-impurity Kondo model: Critical point, Fermi-liquid phase, and crossover. In: *Phys. Rev. B* 51 (1995), p. 8287–8309. doi: 10.1103/PhysRevB.51.8287

[66] Fye, R. M. ; Hirsch, J. E. ; Scalapino, D. J.: Kondo effect versus indirect exchange in the two-impurity Anderson model: A Monte Carlo study. In: *Phys. Rev. B* 35 (1987), p. 4901–4908. doi: 10.1103/PhysRevB.35.4901

[67] Fye, R. M. ; Hirsch, J. E.: Quantum Monte Carlo study of the two-impurity Kondo Hamiltonian. In: *Phys. Rev. B* 40 (1989), p. 4780–4796. doi: 10.1103/PhysRevB.40.4780

[68] Fye, Richard M.: "Anomalous fixed point behavior" of two Kondo impurities: A reexamination. In: *Phys. Rev. Lett.* 72 (1994), p. 916–919. doi: 10.1103/PhysRevLett.72.916

[69] Silva, J. B. ; Lima, W. L. C. ; Oliveira, W. C. ; Mello, J. L. N. ; Oliveira, L. N. ; Wilkins, J. W.: Particle-Hole Asymmetry in the Two-Impurity Kondo Model. In: *Phys. Rev. Lett.* 76 (1996), p. 275–278. doi: 10.1103/PhysRevLett.76.275

[70] Mermin, N. D. ; Wagner, H.: Absence of Ferromagnetism or Antiferromagnetism in One- or Two-Dimensional Isotropic Heisenberg Models. In: *Phys. Rev. Lett.* 17 (1966), p. 1133–1136. doi: 10.1103/PhysRevLett.17.1133

[71] Schrieffer, J. R. ; Wolff, P. A.: Relation between the Anderson and Kondo Hamiltonians. In: *Phys. Rev.* 149 (1966), p. 491–492. doi: 10.1103/PhysRev.149.491

[72] Bruus, H. ; Flensberg, K.: *Many-body Quantum Theory in Condensed Matter Physics: An Introduction*. Oxford University Press, 2004 (Oxford graduate texts)

[73] Kopley, T. E. ; McEuen, P. L. ; Wheeler, R. G.: Resonant Tunneling through Single Electronic States and Its Suppression in a Magnetic Field. In: *Phys. Rev. Lett.* 61 (1988), p. 1654–1657. doi: 10.1103/PhysRevLett.61.1654

[74] Grabert, H. ; Devoret, M.H. ; Division, North Atlantic Treaty Organization. Scientific A.: *Single Charge Tunneling: Coulomb Blockade Phenomena in Nanostructures*. Springer, 1992 (Advances in Experimental Medicine & Biology). – ISBN 9780306442292

[75] Coleman, P.: *Introduction to Many-Body Physics*. Cambridge University Press, 2015. – ISBN 9780521864886

[76] Langreth, David C.: Friedel Sum Rule for Anderson's Model of Localized Impurity States. In: *Phys. Rev.* 150 (1966), p. 516–518. doi: 10.1103/PhysRev.150.516

[77] Gruner, G ; Zawadowski, A: Magnetic impurities in non-magnetic metals. In: *Reports on Progress in Physics* 37 (1974), No. 12, p. 1497. http://stacks.iop.org/0034-4885/37/i=12/a=001

[78] Falicov, L.M. ; Hanke, W. ; Maple, M.B.: *Valence fluctuations in solids: Santa Barbara Institute for Theoretical Physics Conferences, Santa Barbara, California, January 27-30, 1981*. North-Holland, 1981. – ISBN 9780444862044

[79] Anders, F.B. ; Grewe, N. ; Lorek, A.: On the validity of sum rules and Fermi-liquid properties in calculations for strongly correlated electrons. In: *Zeitschrift für Physik B Condensed Matter* 83 (1991), No. 1, p. 75–83. doi: 10.1007/BF01314400. – ISSN 0722-3277

[80] Bulla, R. ; Costi, T. A. ; Pruschke, T.: Numerical renormalization group method for quantum impurity systems. In: *Rev. Mod. Phys.* 80 (2008), p. 395–450. doi: 10.1103/RevModPhys.80.395

[81] Bulla, R. ; Tong, N.-H. ; Vojta, M.: Numerical Renormalization Group for Bosonic Systems and Application to the Sub-Ohmic Spin-Boson Model. In: *Phys. Rev. Lett.* 91 (2003), p. 170601. doi: 10.1103/PhysRevLett.91.170601

[82] Bulla, R. ; Lee, H.-J. ; Tong, N.-H. ; Vojta, M.: Numerical renormalization group for quantum impurities in a bosonic bath. In: *Phys. Rev. B* 71 (2005), p. 045122. doi: 10.1103/PhysRevB.71.045122

[83] Glossop, Matthew T. ; Ingersent, Kevin: Kondo physics and dissipation: A numerical renormalization-group approach to Bose-Fermi Kondo models. In: *Phys. Rev. B* 75 (2007), p. 104410. doi: 10.1103/PhysRevB.75.104410

[84] Bulla, R. ; Pruschke, T. ; Hewson, A. C.: Anderson impurity in pseudo-gap Fermi systems. In: *Journal of Physics: Condensed Matter* 9 (1997), No. 47, p. 10463. doi: 10.1088/0953-8984/9/47/014

[85] Campo, V. L. ; Oliveira, L. N.: Alternative discretization in the numerical renormalization-group method. In: *Phys. Rev. B* 72 (2005), p. 104432. doi: 10.1103/PhysRevB.72.104432

[86] Weichselbaum, A.: Discarded weight and entanglement spectra in the numerical renormalization group. In: *Phys. Rev. B* 84 (2011), p. 125130. doi: 10.1103/PhysRevB.84.125130

[87] Anders, F. B. ; Schiller, A.: Real-Time Dynamics in Quantum-Impurity Systems: A Time-Dependent Numerical Renormalization-Group Approach. In: *Phys. Rev. Lett.* 95 (2005), p. 196801. doi: 10.1103/PhysRevLett.95.196801

[88] Anders, F. B. ; Schiller, A.: Spin precession and real-time dynamics in the Kondo model:Time-dependent numerical renormalization-group study. In: *Phys. Rev. B* 74 (2006), p. 245113. doi: 10.1103/PhysRevB.74.245113

[89] Nghiem, H. T. M. ; Costi, T. A.: Generalization of the time-dependent numerical renormalization group method to finite temperatures and general pulses. In: *Phys. Rev. B* 89 (2014), p. 075118. doi: 10.1103/PhysRevB.89.075118

[90] Eidelstein, Eitan ; Schiller, Avraham ; Güttge, Fabian ; Anders, Frithjof B.: Coherent control of correlated nanodevices: A hybrid time-dependent numerical renormalization-group approach to periodic switching. In: *Phys. Rev. B* 85 (2012), p. 075118. doi: 10.1103/PhysRevB.85.075118

[91] Güttge, Fabian ; Anders, Frithjof B. ; Schollwöck, Ulrich ; Eidelstein, Eitan ; Schiller, Avraham: Hybrid NRG-DMRG approach to real-time dynamics of quantum impurity systems. In: *Phys. Rev. B* 87 (2013), p. 115115. doi: 10.1103/PhysRevB.87.115115

[92] Yoshida, M. ; Whitaker, M. A. ; Oliveira, L. N.: Renormalization-group calculation of excitation properties for impurity models. In: *Phys. Rev. B* 41 (1990), p. 9403–9414. doi: 10.1103/PhysRevB.41.9403

[93] Bulla, R. ; Costi, T. A. ; Vollhardt, D.: Finite-temperature numerical renormalization group study of the Mott transition. In: *Phys. Rev. B* 64 (2001), p. 045103. doi: 10.1103/PhysRevB.64.045103

[94] Hofstetter, Walter: Generalized Numerical Renormalization Group for Dynamical Quantities. In: *Phys. Rev. Lett.* 85 (2000), p. 1508–1511. doi: 10.1103/PhysRevLett.85.1508

[95] Costi, T. A.: Renormalization-group approach to nonequilibrium Green functionsin correlated impurity systems. In: *Phys. Rev. B* 55 (1997), p. 3003–3009. doi: 10.1103/PhysRevB.55.3003

[96] Costi, T A. ; Hewson, A C. ; Zlatic, V: Transport coefficients of the Anderson model via the numerical renormalization group. In: *Journal of Physics: Condensed Matter* 6 (1994), No. 13, p. 2519. http://stacks.iop.org/0953-8984/6/i=13/a=013

[97] Peters, Robert ; Pruschke, Thomas ; Anders, Frithjof B.: Numerical renormalization group approach to Green's functions for quantum impurity models. In: *Phys. Rev. B* 74 (2006), p. 245114. doi: 10.1103/PhysRevB.74.245114

[98] Sakai, Osamu ; Shimizu, Yukihiro ; Kasuya, Tadao: Single-Particle and Magnetic Excitation Spectra of Degenerate Anderson Model with Finite f–f Coulomb Interaction. In: *Journal of the Physical Society of Japan* 58 (1989), No. 10, p. 3666–3678. doi: 10.1143/JPSJ.58.3666

[99] Bulla, R ; Hewson, A C. ; Pruschke, Th: Numerical renormalization group calculations for the self-energy of the impurity Anderson model. In: *Journal of Physics: Condensed Matter* 10 (1998), No. 37, p. 8365. http://stacks.iop.org/0953-8984/10/i=37/a=021

[100] Metzner, Walter ; Vollhardt, Dieter: Correlated Lattice Fermions in $d = \infty$ Dimensions. In: *Phys. Rev. Lett.* 62 (1989), p. 324–327. doi: 10.1103/PhysRevLett.62.324

[101] Georges, A. ; Kotliar, G. ; Krauth, W. ; Rozenberg, M. J.: Dynamical mean-field theory of strongly correlated fermion systems and the limit of infinite dimensions. In: *Rev. Mod. Phys.* 68 (1996), p. 13–125. doi: 10.1103/RevModPhys.68.13

[102] Hewson, A.C. ; Oguri, A. ; Meyer, D.: Renormalized parameters for impurity models. In: *The European Physical Journal B - Condensed Matter and Complex Systems* 40 (2004), No. 2, p. 177–189. doi: 10.1140/epjb/e2004-00256-0. – ISSN 1434-6028

[103] Nevidomskyy, Andriy H. ; Coleman, P.: Kondo Resonance Narrowing in d- and f-Electron Systems. In: *Phys. Rev. Lett.* 103 (2009), p. 147205. doi: 10.1103/PhysRevLett.103.147205

[104] Schlottmann, P.: In: *Physics Rep.* 181 (1989), 1 p

[105] Costi, T. A.: Renormalization-group apprach to nonequilibrium Green functions in correlated impurity systems. 55 (1997), p. 3003

[106] Nordlander, P. ; Pustilnik, M. ; Meir, Y. ; Wingreen, N. S. ; Langreth, D. C.: How Long Does It Take for the Kondo Effect to Develop? 83 (1999), p. 808

[107] Paaske, J. ; Rosch, A. ; Wölfle, P.: Nonequilibrium transport through a Kondo dot in a magnetic field: Perturbation theory. In: *Phys. Rev. B* 69 (2004), No. 15, p. 155330. doi: 10.1103/PhysRevB.69.155330

[108] Kehrein, S.: Scaling and Decoherence in the Nonequilibrium Kondo Model. 95 (2005), p. 056602

[109] Schiró, Marco ; Fabrizio, Michele: Real-time diagrammatic Monte Carlo for nonequilibrium quantum transport. In: *Phys. Rev. B* 79 (2009), p. 153302. doi: 10.1103/PhysRevB.79.153302

[110] Werner, P. ; Oka, T. ; Millis, A. J.: In: *Phys. Rev. B* 79 (2009), 035320 p

[111] Schoeller, H.: A perturbative nonequilibrium renormalization group method for dissipative quantum mechanics. In: *Eur. Phys. J. Special Topics* 168 (2009), p. 179–266. doi: 10.1140/epjst/e2009-00962-3

[112] Pletyukhov, Mikhail ; Schoeller, Herbert: Nonequilibrium Kondo model: Crossover from weak to strong coupling. In: *Phys. Rev. Lett.* 108 (2012), p. 260601. doi: 10.1103/PhysRevLett.108.260601

[113] Schuricht, Dirk ; Schoeller, Herbert: Dynamical spin-spin correlation functions in the Kondo model out of equilibrium. In: *Phys. Rev. B* 80 (2009), No. 7, p. 075120. http://arxiv.org/abs/0905.3095

[114] Medvedyeva, M. ; Hoffmann, A. ; Kehrein, S.: Spatiotemporal buildup of the Kondo screening cloud. In: *Phys. Rev. B* 88 (2013), p. 094306. doi: 10.1103/PhysRevB.88.094306

[115] Nuss, Martin ; Ganahl, Martin ; Arrigoni, Enrico ; Linden, Wolfgang von der ; Evertz, Hans G.: Nonequilibrium spatiotemporal formation of the Kondo screening cloud on a lattice. In: *Phys. Rev. B* 91 (2015), p. 085127. doi: 10.1103/PhysRevB.91.085127

[116] Barzykin, Victor ; Affleck, Ian: Screening cloud in the k-channel Kondo model: Perturbative and large-k results. In: *Phys. Rev. B* 57 (1998), p. 432–448. doi: 10.1103/PhysRevB.57.432

[117] Affleck, Ian ; Simon, Pascal: Detecting the Kondo Screening Cloud Around a Quantum Dot. In: *Phys. Rev. Lett.* 86 (2001), p. 2854–2857. doi: 10.1103/PhysRevLett.86.2854

[118] Sørensen, Erik S. ; Affleck, Ian: Kondo Screening Cloud Around a Quantum Dot: Large-Scale Numerical Results. In: *Phys. Rev. Lett.* 94 (2005), p. 086601. doi: 10.1103/PhysRevLett.94.086601

[119] Affleck, Ian ; Borda, László ; Saleur, Hubert: Friedel oscillations and the Kondo screening cloud. In: *Phys. Rev. B* 77 (2008), p. 180404. doi: 10.1103/PhysRevB.77.180404

[120] Holzner, Andreas ; McCulloch, Ian P. ; Schollwöck, Ulrich ; Delft, Jan von ; Heidrich-Meisner, Fabian: Kondo screening cloud in the single-impurity Anderson model: A density matrix renormalization group study. In: *Phys. Rev. B* 80 (2009), p. 205114. doi: 10.1103/PhysRevB.80.205114

[121] Büsser, C. A. ; Martins, G. B. ; Costa Ribeiro, L. ; Vernek, E. ; Anda, E. V. ; Dagotto, E.: Numerical analysis of the spatial range of the Kondo effect. In: *Phys. Rev. B* 81 (2010), p. 045111. doi: 10.1103/PhysRevB.81.045111

[122] Mitchell, Andrew K. ; Becker, Michael ; Bulla, Ralf: Real-space renormalization group flow in quantum impurity systems: Local moment formation and the Kondo screening cloud. In: *Phys. Rev. B* 84 (2011), p. 115120. doi: 10.1103/PhysRevB.84.115120

[123] Barzykin, Victor ; Affleck, Ian: The Kondo Screening Cloud: What Can We Learn from Perturbation Theory? In: *Phys. Rev. Lett.* 76 (1996), p. 4959–4962. doi: 10.1103/PhysRevLett.76.4959

[124] Lechtenberg, Benedikt ; Anders, Frithjof B.: Spatial and temporal propagation of Kondo correlations. In: *Phys. Rev. B* 90 (2014), p. 045117. doi: 10.1103/PhysRevB.90.045117

[125] Affleck, I.: The Kondo screening cloud: what it is and how to observe it. In: *ArXiv e-prints* (2009)

[126] Ishii, H.: Spin correlation in dilute magnetic alloys. In: *Journal of Low Temperature Physics* 32 (1978), No. 3-4, p. 457–467. doi: 10.1007/BF00117963. – ISSN 0022-2291

[127] Anders, F. B.: *Quantum Field Theory in Solid State Physics*. 2008. – lecture notes

[128] Leuenberger, Michael N. ; Loss, Daniel: Quantum computing in molecular magnets. In: *Nature* 410 (2001), p. 789–793. doi: 10.1038/35071024

[129] Scott, Gavin D. ; Natelson, Douglas: Kondo Resonances in Molecular Devices. In: *ACS Nano* 4 (2010), No. 7, p. 3560–3579. doi: 10.1021/nn100793s. – PMID: 20568709

[130] Gatteschi, D. ; Sessoli, R. ; Villain, J.: *Molecular Nanomagnets*. Oxford : Oxford University Press, 2006 (Mesoscopic Physics and Nanotechnology). – ISBN 9780191620850

[131] Esat, Taner ; Deilmann, Thorsten ; Lechtenberg, Benedikt ; Wagner, Christian ; Krüger, Peter ; Temirov, Ruslan ; Anders, Frithjof B. ; Rohlfing, Michael ; Tautz, F. S.: Transfering spin into an extended π orbital of a large molecule. In: *Phys. Rev. B* 91 (2015), p. 144415. doi: 10.1103/PhysRevB.91.144415

[132] Kröger, J. ; Limot, L. ; Jensen, H. ; Berndt, R. ; Crampin, S. ; Pehlke, E.: Surface state electron dynamics of clean and adsorbate-covered metal surfaces studied with the scanning tunnelling microscope. In: *Progress in Surface Science* 80 (2005), No. 1–2, p. 26 – 48. doi: http://dx.doi.org/10.1016/j.progsurf.2005.10.002. – ISSN 0079-6816

[133] Perdew, John P. ; Burke, Kieron ; Ernzerhof, Matthias: Generalized Gradient Approximation Made Simple. In: *Phys. Rev. Lett.* 77 (1996), p. 3865–3868. doi: 10.1103/PhysRevLett.77.3865

[134] Ruiz, Victor G. ; Liu, Wei ; Zojer, Egbert ; Scheffler, Matthias ; Tkatchenko, Alexandre: Density-Functional Theory with Screened van der Waals Interactions for the Modeling of Hybrid Inorganic-Organic Systems. In: *Phys. Rev. Lett.* 108 (2012), p. 146103. doi: 10.1103/PhysRevLett.108.146103

[135] Hedin, Lars: New Method for Calculating the One-Particle Green's Function with Application to the Electron-Gas Problem. In: *Phys. Rev.* 139 (1965), p. A796–A823. doi: 10.1103/PhysRev.139.A796

[136] Rohlfing, Michael: Electronic excitations from a perturbative LDA + *GdW* approach. In: *Phys. Rev. B* 82 (2010), p. 205127. doi: 10.1103/PhysRevB.82.205127

[137] Greuling, A ; Temirov, R. ; Lechtenberg, B. ; Anders, F. B. ; Rohlfing, M. ; Tautz, F. S.: Spectral properties of a molecular wire in the Kondo regime. In: *physica status solidi (b)* 250 (2013), No. 11, p. 2386–2393. doi: 10.1002/pssb.201349238. – ISSN 1521-3951

[138] Greuling, A. ; Rohlfing, M. ; Temirov, R. ; Tautz, F. S. ; Anders, F. B.: *Ab initio* study of a mechanically gated molecule: From weak to strong correlation. In: *Phys. Rev. B* 84 (2011), p. 125413. doi: 10.1103/PhysRevB.84.125413

[139] Mohn, Fabian ; Repp, Jascha ; Gross, Leo ; Meyer, Gerhard ; Dyer, Matthew S. ; Persson, Mats: Reversible Bond Formation in a Gold-Atom–Organic-Molecule Complex as a Molecular Switch. In: *Phys. Rev. Lett.* 105 (2010), p. 266102. doi: 10.1103/PhysRevLett.105.266102

[140] Temirov, R ; Lassise, A ; Anders, F B. ; Tautz, F S.: Kondo effect by controlled cleavage of a single-molecule contact. In: *Nanotechnology* 19 (2008), No. 6, p. 065401. http://stacks.iop.org/0957-4484/19/i=6/a=065401

[141] Nagaoka, K. ; Jamneala, T. ; Grobis, M. ; Crommie, M. F.: Temperature Dependence of a Single Kondo Impurity. In: *Phys. Rev. Lett.* 88 (2002), p. 077205. doi: 10.1103/PhysRevLett.88.077205

[142] Lambe, J. ; Jaklevic, R. C.: Molecular Vibration Spectra by Inelastic Electron Tunneling. In: *Phys. Rev.* 165 (1968), p. 821–832. doi: 10.1103/PhysRev.165.821

[143] Goldhaber-Gordon, D. ; Göres, J. ; Kastner, M. A. ; Shtrikman, Hadas ; Mahalu, D. ; Meirav, U.: From the Kondo Regime to the Mixed-Valence Regime in a Single-Electron Transistor. In: *Phys. Rev. Lett.* 81 (1998), p. 5225–5228. doi: 10.1103/PhysRevLett.81.5225

[144] Meir, Yigal ; Wingreen, Ned S.: Landauer formula for the current through an interacting electron region. In: *Phys. Rev. Lett.* 68 (1992), p. 2512–2515. doi: 10.1103/PhysRevLett.68.2512

[145] Schiller, Avraham ; Hershfield, Selman: Theory of scanning tunneling spectroscopy of a magnetic adatom on a metallic surface. In: *Phys. Rev. B* 61 (2000), p. 9036–9046. doi: 10.1103/PhysRevB.61.9036

[146] Haldane, F. D. M.: Scaling Theory of the Asymmetric Anderson Model. In: *Phys. Rev. Lett.* 40 (1978), p. 416–419. doi: 10.1103/PhysRevLett.40.416

[147] Merker, L. ; Kirchner, S. ; Muñoz, E. ; Costi, T. A.: Conductance scaling in Kondo-correlated quantum dots: Role of level asymmetry and charging energy. In: *Phys. Rev. B* 87 (2013), p. 165132. doi: 10.1103/PhysRevB.87.165132

[148] Muñoz, Enrique ; Bolech, C. J. ; Kirchner, Stefan: Universal Out-of-Equilibrium Transport in Kondo-Correlated Quantum Dots: Renormalized Dual Fermions on the Keldysh Contour. In: *Phys. Rev. Lett.* 110 (2013), p. 016601. doi: 10.1103/PhysRevLett.110.016601

[149] Friedel, J.: XIV. The distribution of electrons round impurities in monovalent metals. In: *The London, Edinburgh, and Dublin Philosophical Magazine and Journal of Science* 43 (1952), No. 337, p. 153–189. doi: 10.1080/14786440208561086

[150] Henze, S.K.M. ; Bauer, O. ; Lee, T.-L. ; Sokolowski, M. ; Tautz, F.S.: Vertical bonding distances of {PTCDA} on Au(1 1 1) and Ag(1 1 1): Relation to the bonding type. In: *Surface Science* 601 (2007), No. 6, p. 1566 – 1573. doi: http://dx.doi.org/10.1016/j.susc.2007.01.020. – ISSN 0039-6028

[151] Rohlfing, Michael ; Temirov, Ruslan ; Tautz, Frank S.: Adsorption structure and scanning tunneling data of a prototype organic-inorganic interface: PTCDA on Ag(111). In: *Phys. Rev. B* 76 (2007), p. 115421. doi: 10.1103/PhysRevB.76.115421

[152] Fu, Ying-Shuang ; Xue, Qi-Kun ; Wiesendanger, Roland: Spin-Resolved Splitting of Kondo Resonances in the Presence of RKKY-Type Coupling. In: *Phys. Rev. Lett.* 108 (2012), p. 087203. doi: 10.1103/PhysRevLett.108.087203

[153] Tsukahara, Noriyuki ; Shiraki, Susumu ; Itou, Saika ; Ohta, Naoka ; Takagi, Noriaki ; Kawai, Maki: Evolution of Kondo Resonance from a Single Impurity Molecule to the Two-Dimensional Lattice. In: *Phys. Rev. Lett.* 106 (2011), p. 187201. doi: 10.1103/PhysRevLett.106.187201

[154] Prüser, Henning ; Dargel, Piet E. ; Bouhassoune, Mohammed ; Ulbrich, Rainer G. ; Pruschke, Thomas ; Lounis, Samir ; Wenderoth, Martin: Interplay between the Kondo effect and the Ruderman–Kittel–Kasuya–Yosida interaction. In: *Nat Commun* 5 (2014), p. 5417. doi: 10.1038/ncomms6417

[155] Wahl, P. ; Simon, P. ; Diekhöner, L. ; Stepanyuk, V. S. ; Bruno, P. ; Schneider, M. A. ; Kern, K.: Exchange Interaction between Single Magnetic Adatoms. In: *Phys. Rev. Lett.* 98 (2007), p. 056601. doi: 10.1103/PhysRevLett.98.056601

[156] Minamitani, Emi ; Nakanishi, Hiroshi ; Diño, Wilson A. ; Kasai, Hideaki: Effect of RKKY Interaction on the Scanning Tunneling Spectra of a Classic Kondo System –Two Magnetic Atoms Adsorbed on a Metal Surface–. In: *Journal of the Physical Society of Japan* 78 (2009), No. 8, p. 084705. doi: 10.1143/JPSJ.78.084705

[157] Sachdev, Subir: Quantum Criticality: Competing Ground States in Low Dimensions. In: *Science* 288 (2000), No. 5465, p. 475–480. doi: 10.1126/science.288.5465.475

[158] Franke, K. J. ; Schulze, G. ; Pascual, J. I.: Competition of Superconducting Phenomena and Kondo Screening at the Nanoscale. In: *Science* 332 (2011), No. 6032, p. 940–944. doi: 10.1126/science.1202204

[159] Esat, Taner ; Lechtenberg, Benedikt ; Deilmann, Thorsten ; Wagner, Christian ; Krüger, Peter ; Temirov, Ruslan ; Anders, Frithjof B. ; Rohlfing, Michael ; Tautz, F. S.: *A chemically driven quantum phase transition in a two-molecule Kondo system*. – submitted to Nature Physics

[160] Anderson, Philip W.: Theory of Magnetic Exchange Interactions: Exchange in Insulators and Semiconductors. In: Seitz, Frederick (Editor) ; Turnbull, David (Editor): *Solid State Physics* Volume 14. Academic Press, 1963, p. 99 – 214. doi: 10.1016/S0081-1947(08)60260-X. – ISSN 0081-1947

[161] Pavarini, E ; Koch, E ; Anders, F ; Jarrell, M: *Correlated electrons: from models to materials*. Volume 2. 2012

[162] Bork, Jakob ; Zhang, Yong-hui ; Diekhoner, Lars ; Borda, Laszlo ; Simon, Pascal ; Kroha, Johann ; Wahl, Peter ; Kern, Klaus: A tunable two-impurity Kondo system in an atomic point contact. In: *Nat Phys* 7 (2011), No. 11, p. 901–906. http://dx.doi.org/10.1038/nphys2076. – ISSN 1745-2473

[163] Hofstetter, Walter ; Schoeller, Herbert: Quantum Phase Transition in a Multilevel Dot. In: *Phys. Rev. Lett.* 88 (2001), p. 016803. doi: 10.1103/PhysRevLett.88.016803

[164] Nishimoto, Satoshi ; Pruschke, Thomas ; Noack, Reinhard M.: Spectral density of the two-impurity Anderson model. In: *Journal of Physics: Condensed Matter* 18 (2006), No. 3, p. 981. http://stacks.iop.org/0953-8984/18/i=3/a=015

[165] Jayaprakash, C. ; Krishna-murthy, H. R. ; Wilkins, J. W.: Two-Impurity Kondo Problem. In: *Phys. Rev. Lett.* 47 (1981), p. 737–740. doi: 10.1103/PhysRevLett.47.737

[166] Oles, A. M.: Antiferromagnetism and correlation of electrons in transition metals. In: *Phys. Rev. B* 28 (1983), p. 327–339. doi: 10.1103/PhysRevB.28.327

[167] NOZIÈRES, P. ; DE DOMINICIS, C. T.: Singularities in the X-Ray Absorption and Emission of Metals. III. One-Body Theory Exact Solution. In: *Phys. Rev.* 178 (1969), p. 1097–1107. doi: 10.1103/PhysRev.178.1097

[168] Zhu, L. ; Varma, C. M.: Coherence in the Two Kondo Impurity Problem. In: *eprint arXiv:cond-mat/0607426* (2006)

[169] Lechtenberg, Benedikt: *Zeitabhängige Dynamik des Zwei-Störstellen-Modells*. Germany, Technische Univerität Dortmund, Diplomarbeit, 2011

[170] Sakai, Osamu ; Shimizu, Yukihiro: Excitation Spectra of the Two Impurity Anderson Model. I. Critical Transition in the Two Magnetic Impurity Problem and the Roles of the Parity Splitting. In: *Journal of the Physical Society of Japan* 61 (1992), No. 7, p. 2333–2347. doi: 10.1143/JPSJ.61.2333

[171] Sakai, Osamu ; Shimizu, Yukihiro: Excitation Spectra of the Two Impurity Anderson Model. II. Interplay between the Kondo Effect and the Inter Site Interactions. In: *Journal of the Physical Society of Japan* 61 (1992), No. 7, p. 2348–2358. doi: 10.1143/JPSJ.61.2348

[172] Georges, Antoine ; Meir, Yigal: Electronic Correlations in Transport through Coupled Quantum Dots. In: *Phys. Rev. Lett.* 82 (1999), p. 3508–3511. doi: 10.1103/PhysRevLett.82.3508

[173] Zaránd, Gergely ; Chung, Chung-Hou ; Simon, Pascal ; Vojta, Matthias: Quantum Criticality in a Double-Quantum-Dot System. In: *Phys. Rev. Lett.* 97 (2006), p. 166802. doi: 10.1103/PhysRevLett.97.166802

[174] Malecki, Justin ; Sela, Eran ; Affleck, Ian: Prospect for observing the quantum critical point in double quantum dot systems. In: *Phys. Rev. B* 82 (2010), p. 205327. doi: 10.1103/PhysRevB.82.205327

[175] Jayatilaka, Frederic W. ; Galpin, Martin R. ; Logan, David E.: Two-channel Kondo physics in tunnel-coupled double quantum dots. In: *Phys. Rev. B* 84 (2011), p. 115111. doi: 10.1103/PhysRevB.84.115111

[176] Kleine, Christian ; Musshoff, Julian ; Anders, Frithjof B.: Real-time dynamics induced by quenches across the quantum critical points in gapless Fermi systems with a magnetic impurity. In: *Phys. Rev. B* 90 (2014), p. 235145. doi: 10.1103/PhysRevB.90.235145

[177] Lechtenberg, Benedikt ; Anders, Frithjof B.: Erratum: Spatial and temporal propagation of Kondo correlations [Phys. Rev. B 90, 045117 (2014)]. In: *Phys. Rev. B* 91 (2015), p. 039907. doi: 10.1103/PhysRevB.91.039907

[178] Mahan, G.: *Many-Particle Physics*. New York : Plenum Press, 1981

Acknowledgments

Als allererstes bedanke ich mich bei Frithjof Anders, der mir die Möglichkeit gegeben hat diese Arbeit in seiner Gruppe anzufertigen. Wenn es mal wieder nicht weiter ging, hatte er immer einen hilfreichen Rat für mich.
Auch möchte ich mich bei Joachim Stolze dafür bedanken, dass er sich freundlicherweise dafür bereit erklärt hat als zweiter Gutachter dieser Arbeit zu fungieren.
Am meisten bedanke ich mich jedoch bei meiner Freundin Rebecca Weinert, die mich in den vergangenen nunmehr fast zehn Jahren immer unterstützt hat. Auch wenn sie mich in den letzten Monaten manchmal kaum gesehen hat, hat sie (meistens) Verständnis und Geduld mit mir gehabt. Man kann wohl kaum eine bessere Frau auf dieser Welt finden.
Zudem geht ein großer Dank an meine Eltern, die mich immer finanziell und menschlich unterstützt haben. Auch heute noch stehen sie mir mit Rat und Tat bei.
Bei meiner Lieblingsschwester Katharina bedanke ich mich ganz herzlich für die Suche nach Fehlern in dieser Arbeit und natürlich dafür, dass sie immer die anspruchsvolle Aufgabe übernimmt, Familiengeschenke zu besorgen.
Darüber hinaus bedanke ich mich bei meinen Freunden in Dortmund und im Kreis Borken, mit denen ich immer eine gute Zeit hatte. Obwohl ich sie in letzter Zeit nicht mehr häufig zu Gesicht bekommen habe, zeigten sie immer Verständnis für meine Situation.
Dank geht auch an Fabian Güttge, der ein tolles Layout für eine Dissertation erstellt hat und so freundlich war, es mir zur Verfügung zu stellen.
Zuletzt möchte ich mich bei all meinen Arbeitskollegen für das tolle Arbeitsklima bedanken. Hierbei sind ganz besonders meine Bürokollegen Christian Kleine und Johannes Hackmann zu nennen, mit denen ich zahlreiche Diskussionen über alle möglichen Themen (außer Physik) hatte und viele lustige Stunden verbracht habe.